Flow Topology & Large-Scale Wake Structures Around Elite Cyclists

by

Timothy Crouch

A Thesis submitted to Monash University
for the degree of
Doctor of Philosophy

September 2013

Department of Mechanical Engineering
Monash Universty

To my father.

Statement of Originality

This thesis contains no material that has been accepted for the award of a degree or diploma in this or any other university. To the best of the candidate's knowledge and belief, this thesis contains no material previously published or written by another person except where due reference is made in the text of this thesis.

Candidate: Timothy N. Crouch

<September 2013>

Abstract

This work, for the first time, shows the dominant flow structures in the wake of a competitive cyclist geometry, and provides a general picture of the steady and unsteady near wake flow topology, in considerable detail and from a fundamental perspective. In contrast to accepted practices in the sport, wind tunnel investigations with a full-scale anthropometric cycling mannequin show that the fundamental flow physics is the dominant driver of the drag experienced by a cyclist, rather than just the frontal area. With cycling currently at the point where even small reductions in drag are required to be competitive at the elite level, more efficient means of optimising the aerodynamics of cyclists are required. This research shows that a comprehensive understanding of the nature of the flow around cyclist geometries can be gained by investigating the wake structures, and the degree to which they influence surface pressures and the aerodynamic forces acting on the rider. In doing so, a more systematic approach to reducing the aerodynamic drag force of cyclists can now be sought by targeting high drag areas associated with the large-scale flow structures through adjustments to rider position and modifications to equipment.

Wake structures are identified and investigated using a series of detailed three-dimensional velocity field wake surveys and flow visualisation studies for the time-trial racing position. The aerodynamic forces and wake structure variants are considered for static leg positions around a full 360° crank cycle. It is found that there are significant variations in the drag force with leg position associated with different flow regimes. Thus, these different flow regimes must be considered when optimising the aerodynamics of cyclists. Two characteristic flow regimes are identified, corresponding to symmetrical low drag and asymmetrical high drag regimes. The primary feature of the wake is shown to be a large trailing counter-rotating streamwise vortex pair, orientated asymmetrically in the centre plane of the mannequin. The primary flow structures in the wake are the dominant mechanism driving the large variations in the aerodynamic drag force around the crank cycle. This is also found in numerical flow simulations that were performed in parallel with this experimental research. From the analysis of time-averaged skin-friction patterns, topological critical points have also been identified on the suction surface of the mannequin's back. These are discussed with velocity field measurements to elucidate the time-averaged flow topologies, showing the origin of the primary flow structures for the low and high drag regimes.

The proposed flow topologies are related to the measured surface pressures acting on the mannequin's back. These measurements show that most of the variation in drag is due to changes in the pressure distribution acting on the lower back, where the large-scale flow structures develop that have the greatest impact on drag. The influence of changes to rider position (e.g., arm and torso angles) and Reynolds number on time-averaged force and surface pressure measurements are also investigated to see how resilient the dominant flow structures are to these changes. Findings show that the aerodynamic drag force can effectively be reduced by influencing the formation of the large trailing streamwise vortices. Specifically, drag is influenced by changes in the magnitude of the pressure distribution where vortices originate. Despite these changes, the overarching shape of the distributions are preserved and the dominant wake structures are present for all positions and test velocities analysed. This suggests that the dominant wake structures identified in this thesis are a critical feature applicable to a wide range of positions and cycling speeds.

A frequency analysis of wake probe data and time-accurate surface pressure measurements have revealed a complex wake exhibiting a variety of time and length scales associated with unsteady wake structures. This is expected considering the relatively high Reynolds numbers involved and the complex three-dimensional geometry of the mannequin and bicycle. Areas on the body and in the wake are associated with dominant shedding frequencies that are found to be significantly higher than typical pedalling frequencies. Due to the fact that the speed of the legs during pedalling is slow relative to the forward speed of the cyclist, the different wake states corresponding to different static leg positions analysed in this thesis are still likely to be representative of the pedalling case.

Acknowledgements

I have thoroughly enjoyed my studies at Monash University which is largely due to the amazing people I have met, who have been at my side throughout the project, and who I owe many thanks. If it were not for the opportunities, guidance and support provided to me by my supervisors, co-workers, friends and family this thesis would not have been possible.

I feel very honoured and fortunate to have been supervised by Prof. John Sheridan (main), Prof. Mark C. Thompson and Dr. Nicholas A.T. Brown. I thank you all for your guidance, support and encouragement throughout the project and for giving me the opportunity to be a part of an outstanding collaboration between Monash University and the Australian Institute of Sport. I owe a special thanks to David Burton, Manager of the Monash University Wind Tunnels who in many ways has acted as a fourth supervisor. I am grateful for your time, advice and willingness to critique all aspects of my studies which has had a profound impact on research directions and final outcomes.

It has been a pleasure to work with the other members of our Cycling Research Group at Monash, Nathan Barry and Dr. Martin Griffith whose assistance and weekly discussions I have benefited from immensely. I have also enjoyed working with Dr. David Martin from the AIS whose sharp insight into the performance of elite cycling has proved invaluable. Your enthusiasm is truly infectious and makes long days in the wind tunnel a breeze.

I also offer an ardent thank you to the Monash Wind Tunnel technical staff for your assistance and expertise in the preparation of wind tunnel experiments. I thank Steven Dunell for your input into the design of much of the equipment used in this thesis, Don McMaster, Michael Easton and Andrew Smith, who have all been heavily involved in many aspects of the design, construction and wind tunnel testing of the cycling mannequin and Greg Hewes for your expertise in the wind tunnel electrical systems/equipment and software. I look forward to many more discussions over 9:30am coffee with all of you in the future.

I also thank Narendra Babu and Santhosh Babu from the Mechanical engineering workshop for the construction of many of the mannequins components. I also owe a great debt of gratitude to Dr. Scott Wordley, Dr. Nicholas Boustead, Raoul Luescher, Jarryd Van Steenis and Luke Lenard who during the early stages of the project provided significant assistance with the design, development and construction of the very first prototypes of the cycling mannequin.

I would like to thank my post-graduate and post-doctoral friends especially the wind tunnel group Robert Harbig, James Venning, Damien McArther and James Bell who apart from providing me with many necessary distractions (beer and table-tennis), have also been directly involved either with the setting-up and running of experiments or the analysis of data.

To my wonderful girlfriend and best friend Lizzy who has supported me throughout all my time at Monash, I can't thank you enough, and for the tireless hours you have spent reading and editing my work. I am very lucky to have met you and the Marsh family, who I also thank for your support during my time as a post-graduate student. Finally I would like to thank my parents Barry and Michelle and my siblings Ben, Sam and Rommi for giving me the opportunity to pursue my endeavours and for making me the person that I am today.

I acknowledge the Department of Aerospace and Mechanical Engineering at Monash University for their financial support and also the Australian Research Council's Linkage Project scheme (project number LP100200090) who partially funded the project.

Publications

Crouch, T.N., Burton, D., Brown, N.A.T., Thompson, M.C. & Sheridan, J. 2012 Dominant flow structures in the wake of a cyclist. *In proceedings of the 30th AIAA Applied Aerodynamics Conference*, New Orleans, Louisiana, U.S.A, June 2012.

Crouch, T.N., Burton, D., Brown, N.A.T., Thompson, M.C. & Sheridan, J. 2012 A quasi-static investigation of the effect of leg position on cyclist aerodynamic drag. *Procedia Engineering* **34**, 3–8.

Barry, N., Burton, D.,Crouch, T.N., Sheridan, J. & Luescher, R. 2012 Effect of crosswinds and wheel selection on the aerodynamic behavior of a cyclist. *Procedia Engineering* **34**, 20–25.

Griffith, M. D., Crouch, T. N., Thompson, M.C., Burton, D., & Sheridan, J. 2012 Elite Cycling Aerodynamics: Wind Tunnel Experiments and CFD. *In proceedings of the 18th Australasian Fluid Mechanics Conference.*, Launceston, Tasmania, Australia, December 2012

Crouch, T.N., Burton, D., Brown, N.A.T., Thompson, M.C. & Sheridan, J. 2003 Flow topology in the wake of a cyclist and its effect on aerodynamic drag. *J. Fluid Mech.* (recommended for publication, reviewers comments received 23/08/2013).

Nomenclature

Symbol	**Description**
A	Projected Frontal Area
c	Torso Chord Length
C	Closed Wind Tunnel Test Section Cross Sectional Area
C_D	Drag coefficient
C_DA	Drag Area
C_p	Pressure Coefficient
$C_{xy}(f)$	Real Component of the Cross Power Spectral Density Estimate
$c_{xy}(f)$	Convection Velocity
D	Aerodynamic Drag Force
d	Spacing Between Any Two Pressure Taps
ES	Elbow Spacing
f	Frequency
$F_{arm\phi}$	Forearm Diameter
F_S	Separation Focus
$G_{xx}(f)$	Power Spectral Density Estimate Of Measured Time Signal $x(t)$ (single sided)
$G_{xy}(f)$	Cross Power Spectral Density Estimate Of Two Measured Time Signal $x(t)$ and $y(t)$ (single sided)
$G_{yy}(f)$	Power Spectral Density Estimate Of Measured Time Signal $y(t)$ (single sided)
HG	Head/Helmet Gap
$Hip_{x,y}$	Hip Joint Location Relative To Crank
$HipW$	Hip Width

Continued on the next page.

Continued from previous page.

Symbol	**Description**
HW	Maximum Helmet Width
I_u, I_v, I_w	Relative Turbulence Intensity in the x, y, z Directions to the Freestream Velocity
I_{uvw}	Resultant Principal Turbulence Intensity
$L_{leg\phi}$	Lower Leg Mean Diameter
L_A	Attachment Line
L_S	Separation Line
L_u, L_v, L_w	Integral Turbulence Length Scales Associated With Kármán Theoretical Estimates of u, v, w Spectra
n	Number Of Samples Recorded Over Sampling Period
N_S	Separation Node
N_A	Attachment Node
p'	Fluctuating Pressure Component
$P\#$	Traverse Plane Location
P_a	Barometric Pressure
P_s	Static Pressure
P_t	Total Pressure
$P_{Tap\#}$	Pressure At Surface Tap Location
q	Freestream Dynamic Pressure
$Q_{xy}(f)$	Imaginary Component of the Cross Power Spectral Density Estimate
$Re\#$	Reynolds Number
R_a	Specific Gas Constant For Dry Air
R_w	Specific Gas Constant For Water Vapour
S	Skewness Level
S_S	Separation Saddle
St	Strouhal Number
SW	Shoulder Width
t	Time
T	Ambient Air Temperature
T_s	Sampling Time

Continued on the next page.

Continued from previous page.

Symbol	**Description**
u, v, w	Relative Velocity Components in x, y, z Directions
u', v', w'	Fluctuating Velocity Components in x, y, z Directions
$U_{arm\phi}$	Upper Arm Mean Diameter
$U_{leg\phi}$	Upper Leg Mean Diameter
U_∞	Freestream Velocity
WB	Wheel Base
w_h	Humidity Ratio
x, y, z	Local Axis System
X, Y, Z	Wind Tunnel Axes
$x(t), y(t)$	Measured Signal Time History
$X_k(f, T_s)$	Finite Fourier Transform Of Time Signal $x(t)$
$X_k^*(f, T_s)$	Complex Conjugate Of The Finite Fourier Transform Of Time Signal $x(t)$
$Y_k(f, T_s)$	Finite Fourier Transform Of Time Signal $y(t)$

Subscript	**Description**
c	Corrected
u	Uncorrected
A	Attachment
S	Separation

Greek Symbols	**Description**
α	Angle-Of-Attack
η	Elbow Angle
δ^*	Displacement Thickness
Γ	Circulation of Streamwise Vortices
γ_{xy}^2	Coherence Estimate Between Two Signals $x(t)$ and $y(t)$
λ_{ci}	Imaginary Part of the Complex Eigenpairs Associated with the Velocity Gradient Tensor
μ	Neck Angle
ω	Streamwise Vorticity Component

Continued on the next page.

Continued from previous page.

Greek Symbols	Description
ϕ	Hip Angle
ψ	Knee Angle
ρ	Air Density
σ	Standard Deviation
τ	Upper Arm Angle
θ	Crank Angle and Leg Position
$\theta_{xy}(f)$	Phase Angle Between Two Signals $x(t)$ and $y(t)$
$\theta'_{xy}(f)$	Gradient Of The Phase Response Between Two Signals $x(t)$ and $y(t)$
ξ	Rib Angle Defining Pressure Tap Location

Abbreviations	Description
AIS	Australian Institute Of Sport
AOA	Angle Of Attack
CAD	Computer Aided Design
CFD	Computational Fluid Dynamics
CPSD	Cross Power Spectral Density
DPMS	Dynamic Pressure Measurement System
FFT	Finite Fourier Transform
MLWT	Monash Large Wind Tunnel
PDF	Probability Density Function
PSD	Power Spectral Density
RANS	Reynolds Averaged Navier Stokes
ROC	Radius Of Curvature
SAS	Scale Adaptive Simulation
SST	Shear Stress Transport
RPM	Revolutions Per Minute
UCI	Union Cycliste Internationale

Contents

Introduction

Cycling aerodynamics is a particularly interesting sub-class of bluff body aerodynamics because of the wide variety of flows and fluid mechanisms that must be considered to properly manage the effects of aerodynamic drag. The need to better understand these flows in the context of competitive cycling is clear when the impact that aerodynamic forces have on cycling performance is considered. Whether it be elite track, road or endurance cycling, the difference between first and second place is highly dependent on the aerodynamic efficiency of cyclists and teams. This realisation is largely responsible for the positions that cyclists adopt, as well as the design of equipment such as the bicycle frame, wheels, skin-suits and helmets. As a result of the emphasis placed on aerodynamics, the sport of cycling has now evolved to the point at which even small changes that result in minor reductions in drag must be taken seriously if one is to be competitive at the elite level.

Currently the vast majority of research on the aerodynamics of cyclists has addressed the issue of aerodynamic drag from the perspective of the rider through measurement of the aerodynamic forces acting on the cyclist system in a wind tunnel. Of all the rider positions used by cyclists the time-trial position common in road and track cycling events is the most widely investigated. This is primarily a result of restrictions placed on rider position by cycling's governing body, the Union Cycliste Internationale (UCI), which has effectively banned 'extreme' lower drag aerodynamic positions. This has led to particular emphasis placed on the streamlining of the time-trial position, which is the focus of this investigation. Wind tunnel studies on the time-trial position have shown that aerodynamic drag is highly dependent on rider shape, size and position (Zdravkovich *et al.* 1996). As athletes often find it difficult to exactly maintain and repeat positions during testing, which limits the ability to study flows around rider geometries, wind tunnel testing has incorporated the use of cycling mannequins that can accurately maintain a wide range of cyclist positions.

Although there have been many investigations into cycling aerodynamics, no consistent procedures concerning rider position and the design of cycling equipment to optimise aerodynamic performance are yet available. Currently the most widely practised method for optimising rider aerodynamics is through trial and error force measurement in a wind tunnel. Although this method of wind tunnel testing has demonstrated that there is a large potential to improve rider aerodynamics through small changes in position and optimised equipment choices, the physical fluid mechanisms that have the largest influence on drag are not yet understood. Currently, no picture of the gross wake structure, or more importantly, the large-scale flow structures which have a significant impact on the aerodynamic drag force of a cyclist, has yet emerged. This is a reflection of both the competitive nature of cycling, where withholding research can provide teams with a competitive advantage, and also a current lack in understanding of the nature of the very complex flow around cycling geometries.

In order to achieve more effective methods of reducing the aerodynamic drag of cyclists, a picture of the gross wake structure and flow topology is required. Efficient means of optimising rider aerodynamics will only come about if a greater understanding of the fundamental flow mechanisms that have the largest impact on the aerodynamic forces is divulged and not through trial and error techniques that are currently used to investigate rider aerodynamics. With this in mind the primary objectives of this thesis include:

- Identify the dominant flow mechanisms and structures in the wake of a cyclist whilst holding a time-trial position for a full 360° crank cycle.

- Relate wake structures directly to the surface pressure distributions where they originate on the body of the rider, and identify where the major flow separation regions occur and how they are influenced by leg position.

- Provide a means to validate and compare numerical simulations of the flow around similar cyclist geometries with experimental findings (Note: the experimental research presented in this thesis is a part of a wider research program that includes numerical investigations).

- Determine how resilient the proposed flow structures are to changes in rider position and Reynolds number, with particular emphasis placed on changes to rider position that have previously been identified to have a significant impact on aerodynamic drag.

- Highlight areas of high unsteadiness on the body and in the wake of rider geometries, and determine the time scales associated with dominant shedding frequencies so that they can be compared with typical pedalling frequencies (quasi-steady assumption).

- Provide a rigorous approach and a solid foundation for addressing the complex flows associated with cycling geometries so that future investigations may build on findings presented in this thesis. Also, further the body of knowledge of bluff body flows associated with highly 3-D geometries.

Findings relating to the objectives listed above are limited to a *quasi-steady assumption*, i.e., the flow is measured for static leg positions only. Although the flow dynamics induced by leg motion around the crank is included in the wider body of research that this study belongs to, the pedalling frequency (to forward motion) limit at which this assumption breaks down is outside the scope of this particular investigation. If the time scales associated with the pedalling frequency are of the order of the time scales associated with the large-scale flow structures, then different flow regimes are likely to occur which will undoubtedly require different aerodynamic solutions when optimising cyclist performance.

Pedalling frequencies characteristic of cyclists in typical road and time-trial races ($\approx$ 100 RPM) put the mean foot speed around the crank to be $< 12\%$ of typical forward cycling velocities for these events. Although the effects of cycling cadence on the aerodynamics of cyclists is largely unknown, given that the speed of the legs around the crank compared to that of the forward speed of a rider is small even for relatively high cadences, a quasi-steady assumption is likely to hold for a large range of typical pedalling frequencies and riding speeds. This is especially true for road cycling where gearing on the bicycle means that an increase in forward cycling speed is not necessarily associated with an increase in pedalling frequency. This research provides a solid foundation for investigating more complex flow phenomena such as the influence of cadence on time-averaged and unsteady flow phenomena. Further evidence in support of a quasi-steady assumption will be provided when analysing the unsteady characteristics of the wake flow, where it will be shown that dominant shedding frequencies are typically much higher than pedalling frequencies.

The organisation of this thesis, which provides, perhaps for the first time, a general picture of the near wake flow topology of an elite cyclist in a time-trial racing position and then uses this to develop a fundamental understanding of the flow physics, is briefly summarised below:

Chapter 1: Reviews the current literature related to bluff body cycling aerodynamics. A brief history of the development of aerodynamics in the sport of cycling is presented. This is followed by a discussion of previous results of wind tunnel testing of rider position, with particular emphasis placed on the time-trial position. Issues with current methods used to address cycling aerodynamics are highlighted, and ways in which these deficiencies can be rectified, are considered through a review of the progression of the much more developed field of bluff body road vehicle aerodynamics, which shares many analogous flow characteristics.

Chapter 2: The experimental methodology and equipment used in this investigation are discussed in detail.

Chapter 3: Discusses experimental results from wind tunnel studies into the time-averaged flow topology around a cyclist mannequin. The time-averaged results section is divided up into two sub-sections. The first develops a picture of the time-averaged flow topology and how the dominant flow structures influence the aerodynamic drag force as leg position is varied. The flow topology that is developed is also compared directly with numerical simulations of the flow. The second section presents results from rider position studies (i.e., arm and torso angles) and relates dominant near wake flow structures directly to the surface pressure on the body of the mannequin from where the structures originate.

Chapter 4: Covers the unsteady flow characteristics and dominant shedding frequencies. Velocities at points in the wake and time-accurate surface pressures on the body are associated with distinct spectral activity. Unsteady results are presented from similar experiments repeated in two separate wind tunnels. These independent sets of data are shown to be consistent.

Chapter 5: Summarises the major findings from experimental wind tunnel investigations presented in this thesis and makes recommendations for further studies that would contribute to further improvements in the understanding of flows around cyclist geometries at a fundamental level.

Appendices: Provides supplementary data and results from wind tunnel studies, and additional information regarding calibration and error/uncertainties associated with the equipment and analysis techniques.

Chapter 1

Literature Review

The importance of aerodynamics in cycling will become abundantly clear in this section which reviews literature on the subject. The development of aerodynamics in cycling is first addressed with particular attention placed on streamlining of the time-trial position and the limitations of methods that are currently used to assess the aerodynamic performance. Although there have been many investigations into cycling aerodynamics, there is little available literature discussing the dominant fluid mechanisms and flow structures that have a large influence on drag. This is identified as a major deficiency in our current understanding of the influence of different rider shapes, positions and equipment on aerodynamic drag. Analogies are drawn between the flows around other complex highly three-dimensional bluff bodies that share similar flow characteristics, namely automobiles. The large benefits gained in automotive aerodynamics by investigating wake structures is highlighted, and in doing so a clear direction for addressing many of the limitations associated with the current understanding of cycling aerodynamics is formulated.

1.1 Development of Cycling Aerodynamics

Over the past twenty-five years there have been significant increases in the speed of elite cyclists, mainly due to improved aerodynamics. To cycle fast riders must maximise their power output while minimising the resistive forces acting on them. Whilst travelling over flat surfaces, the total resistive forces consist of aerodynamic drag, rolling resistance, and drive-train/wheel-bearing frictional losses (Martin *et al.* 2007). Of these, it is the aerodynamic drag component that contributes the largest proportion to the total resistance. Unlike rolling resistance and bearing losses, which increase linearly with speed, the aerodynamic drag component increases with the square of a cyclist's speed.

Thus, at high cycling speeds, aerodynamics plays a vital role, as most of the power produced by the rider is used to overcome aerodynamic drag. This is especially true for elite athletes, where investigations into the power requirements of cyclists (Martin *et al.* 1998) have found that the aerodynamic drag component can account for as much as 96% of a cyclist's available power at constant speed on a flat surface.

In one of the first studies to highlight the importance of aerodynamics in cycling Kyle & Burke (1984) looked at ways to reduce the power requirements of cyclists by decreasing their aerodynamic drag. Using wind tunnel testing they found that at speeds above 8.9 m/s, the aerodynamic component of the total resistance was as much as 90%. They also concluded that the bicycle contributed 31–39% of the total aerodynamic drag, depending on rider position. Other authors have stated the drag component of the bicycle to be as little as 25–30% (Gross *et al.* 1983; Oggiano *et al.* 2008). The rider has a large effect on the flow field around the bicycle, and for this reason the drag component of the bicycle and rider cannot be separated and treated independently (Gibertini & Grassi 2008). Thus, the breakdown into contributions from the bicycle and rider serves only as an approximate indication of the contribution associated with each component. Despite this, studies by Kyle & Burke (1984) led them to develop a three-tier hierarchy for reducing cycling resistance:

1. The position of the rider
2. The geometry of the bicycle
3. Rolling resistance.

The large influence that rider position has on the aerodynamic drag force and the impact that this has on cycling performance is dramatically shown in the cycling em Hour Record (the greatest distance pedalled by an athlete in one hour). In this event, figure 1.1 shows that distances travelled over the hour period have more than doubled since its establishment in 1876. Since the 1980s, improvements to records in this event have been achieved predominantly through improvements in streamlined bicycle design, such as airfoil-shaped tubing and disc wheels. More recent records can be attributed to rider position, such as the time-trial position, and more extreme positions such as the Obree and Superman positions, which are now banned under current Union Cycliste Internationale (UCI) rules.

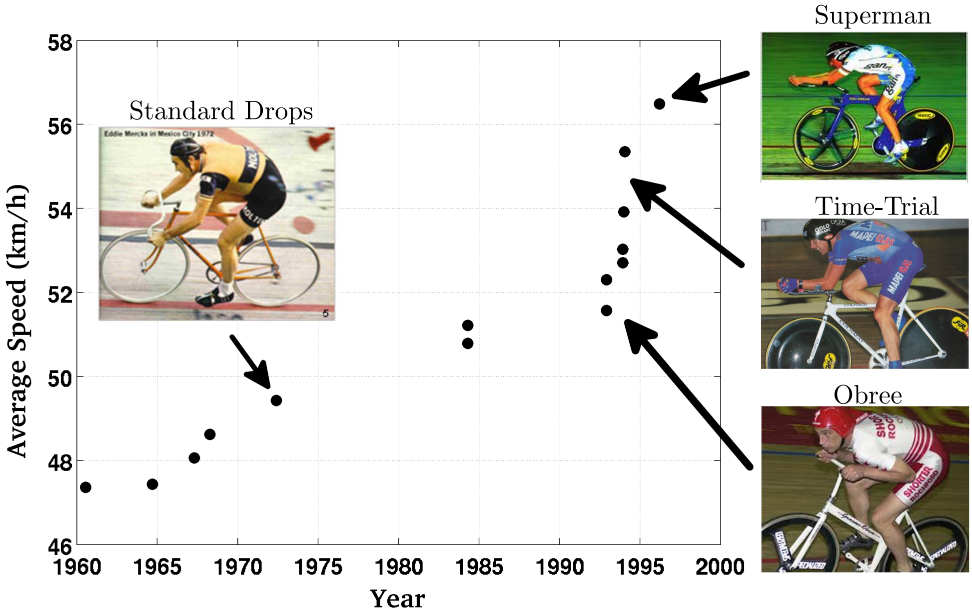

Figure 1.1: UCI Hour Records (Best Human Effort) and rider positions used in records.

The majority of the aerodynamic resistance experienced by riders is explained by bluff-body aerodynamics. Bluff-body flows are typically characterised by regions of separated flow that may or may not reattach to the body surface. Flow separation means that aerodynamic resistance is mainly pressure drag (Gibertini & Grassi 2008). Flow separation from bluff bodies leads to a turbulent low-pressure wake. This results in a pressure differential being generated between the low pressure regions of trailing surfaces and the high pressure regions of leading surfaces. This is experienced by a cyclist as pressure drag. The pressure drag can be decreased by either reducing the magnitude of the high pressure regions where flow stagnation occurs on leading surfaces or by increasing the pressure in the wake on trailing surfaces. Methods used to reduce the drag of bluff bodies differ from those of streamline bodies, such as airfoil-shaped geometries, where the dominant form of aerodynamic resistance is in the form of skin-friction due to wall shear stresses.

The degree to which a body is streamlined is essentially governed by the drag coefficient 'C_D' given in equation 1.1; where 'D' is the total aerodynamic drag consisting of pressure drag and skin-friction components, 'ρ' is the fluid density, 'U_∞' is the body's velocity relative to the freestream and 'A' is the projected frontal surface area of the body. Rearranging equation 1.1 for the total aerodynamic drag we see that the drag force is directly proportional to the projected frontal area and the drag coefficient in equation 1.2. As a result of this relationship, drag reductions on cyclists have been accomplished through both reductions in the projected area and through lowering the drag coefficient. Rider positions used to set records in the UCI Hour Record act to both minimise the projected area of the cyclist whilst also streamlining the shape of the cyclist. With the UCI placing restrictions on rider position, and banning extreme positions such as the Obree and Superman positions, aerodynamic gains in time-trial type cycling events currently focus on streamlining the time-trial position (also known as tri-position), which is the focus of this investigation.

$$C_D = \frac{D}{\frac{1}{2}\rho U_\infty^2 A} \tag{1.1}$$

$$D = C_D \frac{1}{2}\rho U_\infty^2 A \tag{1.2}$$

As flow separation largely dictates the magnitude of the pressure force that acts on bluff geometries, the drag coefficient is highly dependent on the location at which flow separation occurs on the body. Flow separation from bluff bodies may occur from sharp or continuous surfaces resulting from adverse pressure gradients imposed on the boundary layer that are too large to sustain attachment. The size of the wake is dependent on the location where flow separation occurs. Larger wakes are usually accompanied by an increase in the pressure drag component due to lower pressures acting in the wake. Flow separation from contoured surfaces, such as the body of a cyclist, is often difficult to predict, as it depends not only on the magnitude of the adverse pressure gradient but also the characteristics of the upstream boundary layer and flow structures in the near wake (Bearman 1997). The location at which flow separation occurs on a cyclist is dependent on a number of factors including: local geometry (dependent on rider shape/position, equipment selection), surface roughness (skin-suit type for example), Reynolds number (size of rider and velocity at which they are moving), and freestream conditions (road/track freestream turbulence levels, wind conditions on the road), to name a few. The position of the separation point (line) is also further complicated by unsteady flow structures arising from vortex shedding, which can cause the separation position to oscillate in response to fluctuating pressures in the wake.

By effectively managing the location at which flow separates from the cyclist, large reductions in the pressure drag can be obtained. This realisation has had a large impact on the development and design of cycling equipment. Airfoil shaped tubing and disk wheels all act to streamline the bicycle by delaying flow separation on the frame/wheels, which results in a reduction in the pressure forces acting on the bicycle compared to traditional round tube and spoked bicycles. The reductions in aerodynamic drag through shaping of the bicycle are ultimately limited however, as it is evident that most of the drag is caused by the rider (Zdravkovich *et al.* 1996). This is why streamlining the rider through position and/or equipment is the principal variable for drag reduction.

The drive to reduce the pressure drag force acting on the rider has resulted in not only the development of rider positions but also the design of cycling equipment with the aim of reducing the drag force associated with the rider. The design and set-up of the bicycle, such as the inclusion of time-trial bars, has enabled cyclists to achieve more aerodynamic positions and enabled them to maintain low drag positions for extended periods of time. Recently there has been a shift towards streamlining rider position through aerodynamically tear-shaped helmets and skin-suits. Unlike aero-helmets, which effectively streamline the shape of the head and reduce the size of the wake downstream of the helmet, skin-suit design has employed the use of textured fabrics to target the reduction of the pressure drag and skin-friction components of the total aerodynamic resistance. Projects such as the Nike Swift Spin (Brownlie *et al.* 2009) used textured fabrics in specific areas of the skin-suit in order to prematurely induce transition to a turbulent boundary layer before separation occurred in order to reduce the pressure drag on body segments. Compared to laminar boundary layers, which have only diffusive intermixing, turbulent boundary layers are characterised by intense small-scale structures that transfer momentum from the freestream to the viscous interface at the body's wall (Schlichting *et al.* 1968). The increased momentum at the body's surface gives turbulent boundary layers a greater ability to overcome adverse pressure gradients compared to laminar boundary layers. As a result, this can delay flow separation leading to reductions in pressure drag. The skin-friction component can also be reduced by maintaining an attached laminar boundary layer and the use of smooth surfaces in flow attached regions. However, as pressure drag is the largest component of aerodynamic drag, delaying separation will see the greatest reductions in drag.

1.2 Wind Tunnel Testing of Rider Position

The primary method used to investigate the aerodynamics of cyclists and the effect of rider position on aerodynamic drag, has been through force measurements in a wind tunnel testing environment. As the determination of the projected frontal surface for the complex geometries of the cyclist and bicycle system is difficult, drag measurements of cyclists in a wind tunnel are often reported not as a coefficient, but as the drag area 'C_DA'. The drag area, given in equation 1.3 as the ratio of the measured drag to the dynamic pressure, provides a means of eliminating the uncertainty associated with measuring frontal surface area (Hoerner 1965), while still providing a way of standardising drag measurements for variations in test speeds and atmospheric conditions (temperature, pressure, density). As aerodynamic drag is dependent on both the drag coefficient and frontal area, the drag area is also a more appropriate representation of the power requirements of riders to maintain a particular speed (ignoring other forms of cycling resistance).

$$C_DA = \frac{D}{\frac{1}{2}\rho U_\infty^2} \tag{1.3}$$

The importance of position has prompted many wind tunnel investigations into the five main positions used by elite cyclists, which are depicted in figure 1.2. Table 1.1 shows reported drag area and drag coefficients from the wind tunnel testing of cyclists in various positions. Average wind tunnel data suggests that the reduction in drag between an upright sitting position with straight arms (such as the *stem* and *hoods positions*) and a *drops position*, can be as much as 15–20%, and for the time-trial position as much as 30–35%. However, these are only average results and drag area and coefficient measurements for the time-trial position widely used today vary by as much as 40% between separate wind tunnel studies, and as much as 60% between wind tunnel studies and other indirect methods (Candau *et al.* 1999) of determining drag. Differences in atmospheric conditions, drag measurement devices, wind tunnel blockage ratios and freestream flow quality are all specific characteristics of the wind tunnel tested in and have been shown to affect drag measurements (Barlow *et al.* 1999; Mercker & Wiedemann 1996a). Although it is difficult to make direct comparisons between different wind tunnel studies, which often do not state the specifics of the wind tunnel testing environment, the greatest contribution to the dissimilarities in the

(a) Stem (b) Break Hoods (c) Drops

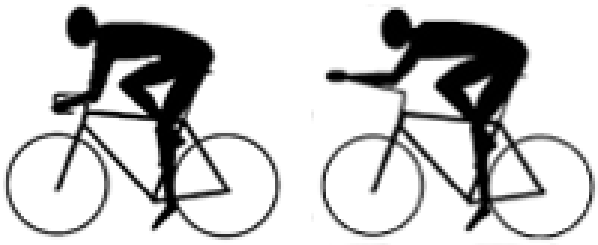

(d) Crouched Drops (e) Time-Trial

FIGURE 1.2: Five commonly used positions in cycling events, from Gibertini & Grassi (2008).

research are most likely due to rider aspects such as variation in rider position and anthropometric characteristics (rider shape).

A study by Zdravkovich *et al.* (1996) looked at the drag coefficient for two different athletes of a similar height and mass, and a 1:2.5 scale model of a bicycle and rider in the break hoods position, drops position, crouched drops position and the time-trial position. Wind tunnel measurements showed that the break hood position had the highest drag coefficient followed by the drops and crouch drops position, with the tri-position recording the lowest drag coefficient. However, there were large variations in the drag coefficient between each of the two athletes and the model for similar positions. This was most noticeable between the two athletes with the drag coefficient varying as much as 30% between them for the same position. This led Zdravkovich to conclude that a single value of drag coefficient cannot be specified for any one position, a result of the strong dependence of the drag coefficient on the size and shape of the rider. This finding is supported by Gibertini & Grassi (2008) who also looked at the effect that position can have on how streamlined a rider is. In contrast to findings by Zdravkovich *et al.* (1996), wind tunnel tests of an experienced rider in the stem, breaks hoods,

Studies	Measurement	Upright Position	Dropped Position	Tri-Position
Kawamura (1953)	C_D	1.140-0.912	N/A	N/A
Kyle (1979)	C_D	1.140-0.950	0.971-0.800	N/A
Zdravkovich *et al.* (1996)	C_D	0.750-0.600	0.690-0.540	0.600-0.490
Padilla *et al.* (2000)	C_D	N/A	N/A	0.650
Gibertini & Grassi (2008)	C_D	0.824-0.760	0.814	0.792
García-López *et al.* (2008)	C_D	1.33	N/A	0.99-0.96
Underwood & Jermy (2013)	C_D	N/A	N/A	0.864-0.803
Kyle & Burke (1984)	C_DA (m^2)	reference	-19.5%	N/A
Kyle (1989)	C_DA (m^2)	N/A	reference	-15.0%
Padilla *et al.* (2000)	C_DA (m^2)	N/A	N/A	0.244
Jeukendrup & Martin (2001)	C_DA (m^2)	0.358	0.307	0.269-0.244
García-López *et al.* (2008)	C_DA (m^2)	0.521-0.428	N/A	0.255-0.377
Gibertini & Grassi (2008)	C_DA (m^2)	0.318-0.282	0.289-0.275	0.235-0.223
Underwood & Jermy (2013)	C_DA (m^2)	N/A	N/A	0.296-0.226

TABLE 1.1: Reported drag coefficient and drag area measurements from wind tunnel testing of cyclist position.

drops and time-trial position revealed that the most streamlined position for this rider (indicated by the drag coefficient) was not that of the time trail position (0.792 m^2) but of the breaks hood position (0.760 m^2). This was despite the projected frontal surface area been 37% higher for the breaks hood position. Drag area measurement for the breaks hood position however were higher than the tri-position by 30%, indicating that it was more important to reduce frontal area for this particular rider.

Frontal surface area is not always the dominant factor when comparing the aerodynamic drag of different riders and positions. When considering the aerodynamic optimisation of rider position, changes to position that lead to reductions in frontal surface area must also take into account the drag coefficient. The effect of changing the cyclist position acts to alter both the frontal surface area while simultaneously altering the drag coefficient. This is due to different wake flow that may vary significantly from one position to another. The degree to which the drag coefficient can affect the performance of a cyclist is highlighted in two separate studies reported by Bassett JR *et al.* (1999). Both of these investigations involved measurements of drag and frontal surface area of cyclists in a wind tunnel at 13.3 m/s. The findings demonstrated only a weak correlation between measured drag and frontal area, of which the frontal area only accounted for $\approx$ 50% of the variation in drag between the different athletes and their positions.

Similar findings have also been found by wind tunnel studies reported by the author,

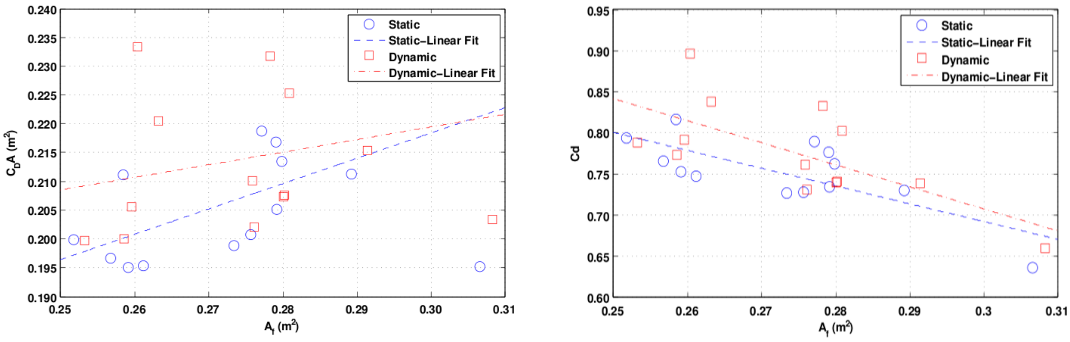

(a) C_DA V's A_f

(b) C_D V's A_f

FIGURE 1.3: Influence of rider projected frontal area on the drag area and drag coefficient (Crouch *et al.* 2010).

which looked at establishing parameters concerned with the shape of cyclists other than frontal area for predicting aerodynamic drag (Crouch *et al.* 2010). As part of a national selection camp with the Australian Institute of Sport (AIS), thirteen experienced female road cyclists were tested in the Monash Large Open-Jet Wind Tunnel whilst holding their standard time-trial position, under both pedalling and non-pedalling conditions. Force measurements were recorded with the same bicycle (and its set-up) and cycling equipment (helmet, skin-suit) so that any variation in force measurements between athletes was primarily a result of variations in body shape/size, which varied significantly between athletes, and their time-trial positions.

Wind tunnel test results showed that the measured drag varied significantly between the athlete's time-trial positions for both static and dynamic test conditions. Frontal area determined from video footage recorded simultaneously with force measurements, could not account for the large variations in drag that were measured between the athletes. Figure 1.3(a) shows the weak relationship established between the drag and frontal area, with frontal area only accounting for 37% and 27% of the variation in the drag for the static and dynamic test conditions, respectively. Interestingly, riders with higher projected frontal surface areas generally had lower drag coefficients. This can be seen in figure 1.3(b) and explains why some athletes that had high frontal surface areas achieved lower drag measurements than some of the smaller riders in the test group who were generally less streamlined.

From the weak correlations drawn between rider frontal area and aerodynamic drag, this led Crouch *et al.* (2010) to conclude that other rider characteristics must have a

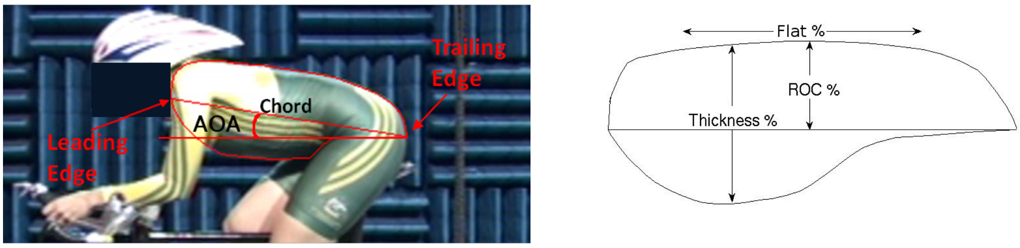

FIGURE 1.4: Cyclist position and side profile shape characteristics (Crouch *et al.* 2010).

large impact on the drag area of the cyclists. Instead of considering the frontal profile of athletes, the shape of the rider was considered from a side view perspective, which was recorded simultaneously with force measurements. The largest variation in the side profile between athletes was concerned with the shape and position of the torso. Figure 1.4 shows the outline of a test subject's torso from the side-view perspective, termed the athlete's profile. From these profiles the shape and orientation of the torso to the freestream was characterised for each athlete for both the static and dynamic pedalling conditions. These included the torso chord line defined as the line connecting the leading edge of the shoulders with the trailing edge of the base of the lower back; the torso angle-of-attack describing the angle made between the chord line and the freestream direction; torso thickness (as a percentage of the chord); radius of curvature (as a percentage of the chord), which defined the maximum displacement of the profile above and perpendicular to the chord line; and the relative flatness (as a percentage of the chord), which is the continuous section of the top surface of the profile that was parallel to the chord line within $\pm 5.0°$.

In characterising the shape of the torso it was found that athletes who had low measured drag, all had common traits regarding the shape of the side profiles. Figure 1.5 shows profiles for the three riders who had the lowest and the highest drag measurements for the static tests. In comparing the profiles it can be seen that riders who had a flat back generally had much lower drag compared to riders who had curved backs. This has been suggested by both Broker (2003) and Kyle (2003), who note that cyclists with a flat back, a tucked head and forearms positioned parallel to the bicycle frame are generally well streamlined. Of all the parameters used to describe the shape and orientation of the torso, the relative flatness of the back was found to be a much better predictor of aerodynamic drag than when considering frontal area alone. This can be

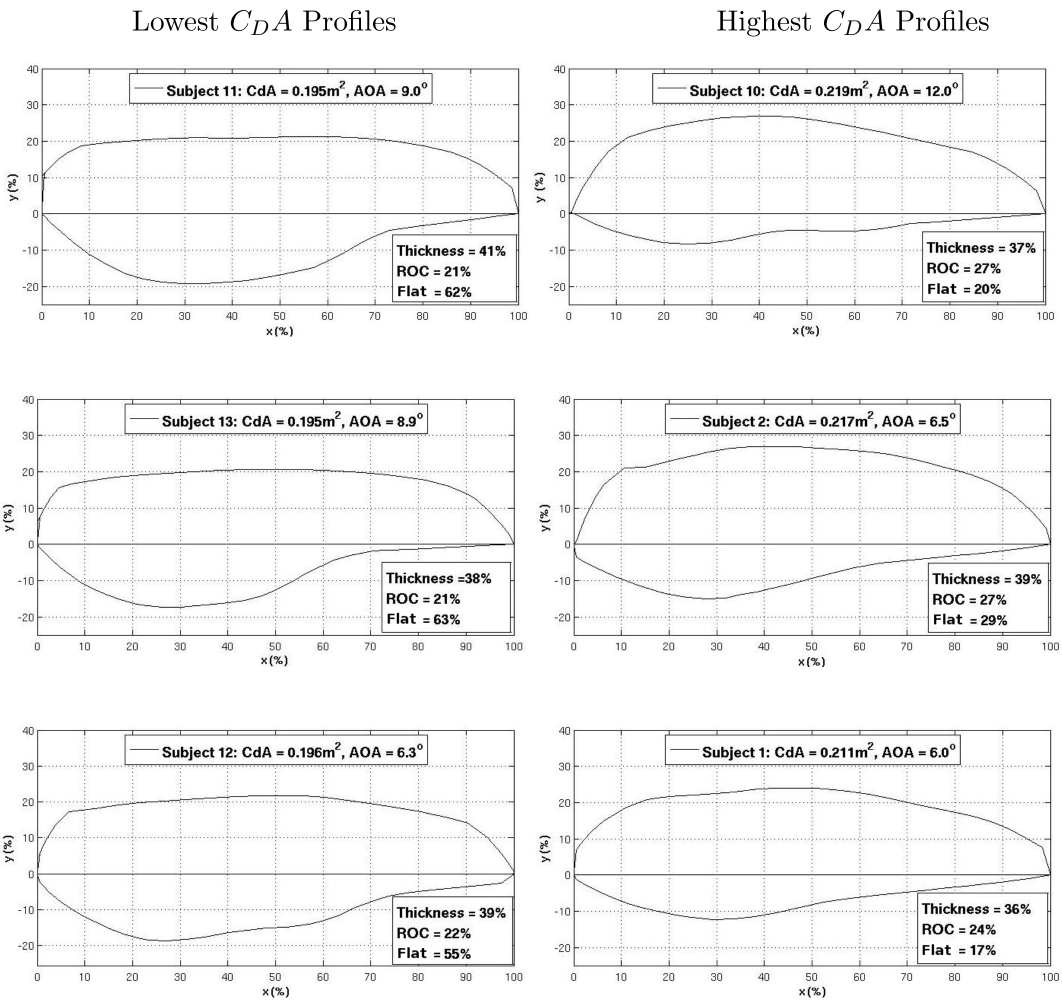

Figure 1.5: Comparison of low and high drag profiles. Left - high drag; Right - low drag profiles (Crouch *et al.* 2010).

seen in figure 1.6 for both pedalling and non-pedalling conditions. It was also shown that the change in the relative flatness of the back between static and dynamic tests could account for much of the variation in drag between these tests. The majority of athletes showed an increase in the curvature of their backs for dynamic testing, resulting in an overall increase in drag measured for the dynamic tests. The degree to which the back shape changed between static/dynamic tests for each athletes is shown in Appendix A that compares rider profiles between these test conditions.

1.2.1 Optimisation of Time-Trial Position

Although there have been many wind tunnel investigations into the aerodynamics of cyclists they have not been able to explain the large variation in drag that is observed between different rider geometries and positions. This is primarily a result of the strong

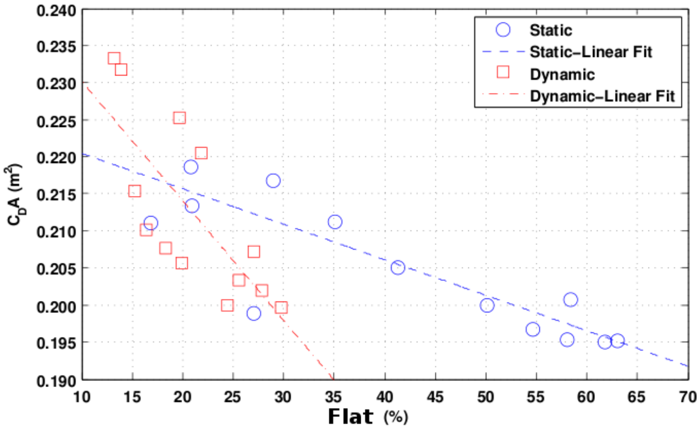

FIGURE 1.6: Correlation between drag area and relative flatness of the back from wind tunnel investigations performed by Crouch *et al.* (2010).

dependence of the drag on the shape/size and position of the rider. As the shape of the rider changes with position, these variables must be considered at the same time. Even relatively minor adjustments to position have been reported to have a large effect on drag (Jeukendrup & Martin 2001; Broker 2003). There have been many 'rules of thumb' developed regarding optimal positioning of the cyclist's arms, legs, torso and head (McLean *et al.* 1994; Jeukendrup & Martin 2001; Broker 2003; Kyle 2003). However, wind tunnel force measurements have shown that when a seemingly optimal position determined for one rider is implemented for another, this can actually have a detrimental effect on aerodynamic performance (Luca *et al.* 2008). As a result of this, optimal positional changes that result in drag reductions of the time-trial position are largely inconclusive.

Similar trends have also been observed when implementing different rider equipment, such as helmets, into the cyclist 'system' (García-López *et al.* 2008; Blair & Sidelko 2008; Chabroux *et al.* 2008). For these reasons the most effective method to evaluate a cyclist's aerodynamic performance to date has been largely by a trial and error approach to force measurements in a wind tunnel. The position of the cyclist, usually defined by the set-up of the bicycle (handle bar and seat positions) and cycling equipment are continually refined until rider position and equipment configurations are identified that result in a lower drag compared to baseline force measurements. It is apparent that defining rider position through the 'bike set-up' approach does not address the key parameters which determine the aerodynamic forces. This is the shape of the rider, which will change from athlete to athlete. Also, the trial and error approach to cycling aerodynamics severely limits the ability to identify what the fundamental fluid mechanisms are that are driving the variations.

In recent times, in order to achieve the types of gains now required to be competitive on the world stage, a vital element to evaluating and optimising aerodynamics has involved wind tunnel testing with mannequins. This can be seen in sports and research institutions that have performed testing with mannequins modelled on elite cyclists, such as British Cycling, who developed a replica Chris Hoy (an Olympic track cyclist champion) cycling mannequin, and equipment manufacturers such as Cervelo, who conduct testing using a mannequin modelled on David Zabriski (a seven-time national time-trial champion). Although athlete wind tunnel testing will always be an integral part of developing any aerodynamic package for elite sports, the major limitations with athletes is the repeatability of position during testing, and the accessibility of athletes for the long periods of time that are often required for detailed investigations. With mannequins, this can be avoided and also opens up a host of other experimental techniques (such as those utilised in this thesis) for investigating the aerodynamics of cyclists, which are simply not practical or would be impossible to perform with a real athlete. Despite the issues associated with studies involving athletes, wind tunnel testing of time-trial positions has pointed to key areas on the body and positional changes that potentially have a significant impact on aerodynamic drag and warrant further investigation.

1.2.1.1 Upper Body

One of the first wind tunnel studies to report the effects on drag due to small adjustments made to the tri-position was Kyle (1989). In tests conducted on a cyclist using tri-bars, it was found that as the cyclist's elbows moved together the drag decreased, and the drag was lowest when the forearms were positioned horizontally or raised thirty degrees. It was also found that for this particular cyclist, moving forward on the seat with the arms in the horizontal position decreased drag, however moving forward with the arms at thirty degrees had little effect for unknown reasons. From wind tunnel tests conducted on the U.S National Cycling Team in 1995, Broker (2003) explains the large potential for riders to improve their performance through relatively small adjustments in position. This was highlighted by drag measurements of cyclists in two separate positions, one that was assumed to replicate a particular cyclist position when fatigued, and another where the same cyclist's head and handle bar position were lowered and the handlebars were moved slightly forwards. The latter position resulted in a 5.3% reduction in measured drag, claimed to possibly reduce a 4000 m time-trial race by as much as 3.91 seconds. Jeukendrup & Martin (2001) also commented on wind tunnel testing of the Rabobank Professional Cycling Team, where similar adjustments made to the handle bars resulted in a 5.9% reduction in drag area compared to the cyclist's standard time-trial position.

More recent studies however, show that when it comes to bike set-up and the position of the handle bars, the optimisation of rider aerodynamics must be treated on an individual basis. Underwood & Jermy (2013) looked at the optimisation of the time-trial position by changing handle bar height and elbow spacing (pad spacing) in wind tunnel tests performed on seven male and female cyclists using their own cycling equipment. Force measurements showed that there was no one optimal position for the handle bars, with significant variations in drag forces recorded for both the male and female athletes for the different handle bar set-ups. Similar findings have also been reported on how the hands are positioned on the tri-bars, with some hand positions being advantageous for certain athletes but detrimental to the performance of others (Underwood & Jermy 2010). Broker (2003) draws on the fact that research findings are largely inconclusive in determining the best bike set up and arm position. As suggested by Broker (2003), with the arms together, most of the airstream is apparently directed around the body of the rider and as the forearms are separated, this flow is mainly directed underneath the rider's torso towards the rear wheel of the bicycle.

In a study by Oggiano *et al.* (2008), wind tunnel investigations were used to analyse the effect of slight adjustments to the standard position of nine male and two female elite athletes. For each cyclist, six positions were tested following adjustments made to the seat height and the position of the handle bars on the athletes' own time-trial bicycles. It was found that one particular position on average, achieved by maintaining the athlete's standard seat height and lowering and moving the handlebars forward by 20 mm resulted in the greatest drag reductions. However, not all the athletes tested had the same improvements in this position, and significant variations in measured drag were observed among the athletes for all positions tested. This was suggested to be a result of the fact that some cyclists already had optimised standard positions due to their riding experience.

The position of the head and the type of helmet used has also proved to be an important factor in the determination of the drag acting on a cyclist. Blair & Sidelko (2008) tested ten different aerodynamic helmets in three head positions (low, medium and high) on a mannequin in order to eliminate the inconsistencies in position between tests, which would likely occur with human subjects. Although helmets were tested for only one body position, results showed that the position of the head and the type of helmet had a large effect on drag measurements. Wind tunnel testing by García-López *et al.* (2008) on multiple riders in a time-trial position with and without helmets has also highlighted the fact that the selection of cycling equipment such as helmets must be treated on an individual basis, as not all athletes observed reductions in drag when an aero-helmet was used. The selection of other cycling equipment such as textured skin-suits, which have been shown to be an effective means of reducing cyclist aerodynamic drag (Kyle *et al.* 2004; Brownlie *et al.* 2009), will also likely require optimal solutions to be treated on an individual basis. As the relationship between surface roughness and the state of the boundary layer is highly dependent on the local Reynolds number, it is expected that the effectiveness of skin-suits to reduce aerodynamic drag, through prematurely inducing transition to a turbulent boundary layer, will be sensitive to the size, shape and speed at which the cyclists moves through the air.

1.2.1.2 Lower Body

Effects on drag due to the adjustment of the position of the legs in the vicinity of the bicycle frame have been examined by Parker *et al.* (1996). Using the lower half of a mannequin to model a cyclist's legs in a static horizontal pedalling position, the effects of the spacing between the legs and a closed and open bicycle frame were tested in a wind tunnel. It was found that the spacing between the legs and the frames influenced the drag measurement, which was also dependent on the type of frame tested. Figure 1.7 shows that as leg spacing decreased, a linear reduction in drag was observed for the open frame, however for the closed frame, drag initially increased before decreasing as leg spacing reduced.

This also provides further support for claims made earlier that the aerodynamics of the rider cannot be decoupled from the aerodynamics of the bicycle, and these must therefore be considered as one complete system when considering the total drag acting on a cyclist. Kyle *et al.* (2004) shows that the drag changes as the position of the leg

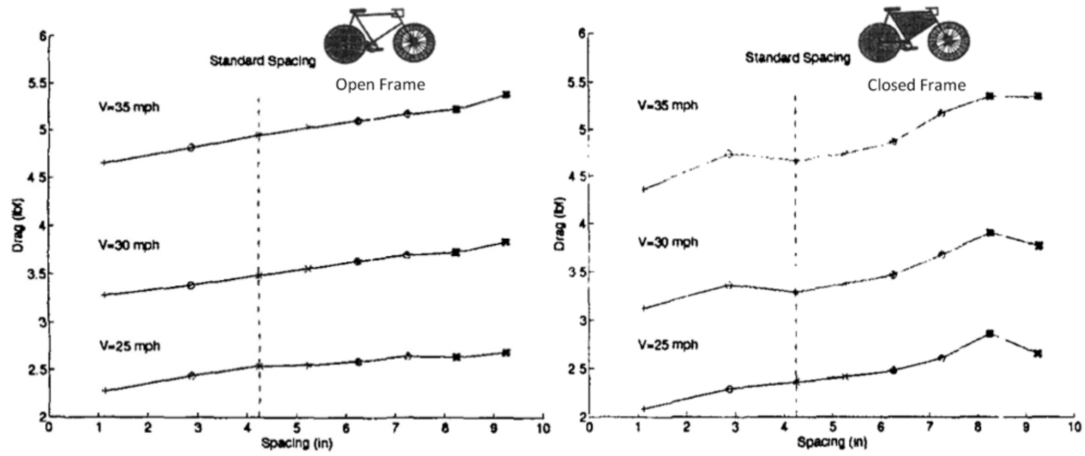

FIGURE 1.7: Influence of leg spacing for open and closed frames (Parker *et al.* 1996).

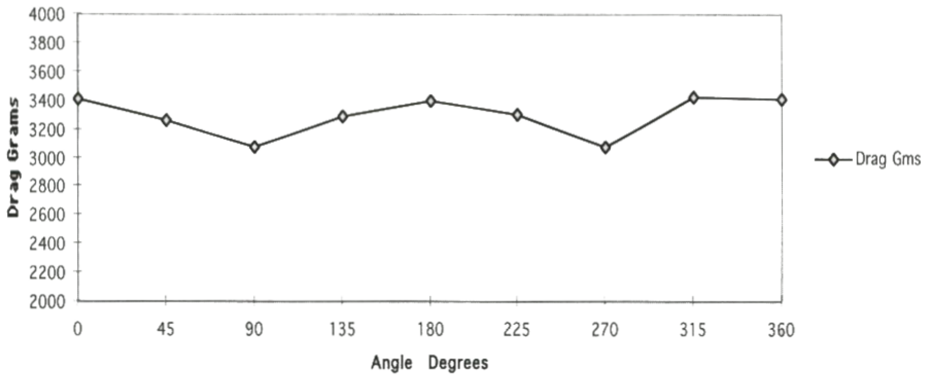

FIGURE 1.8: Effect of crank angle on drag, where 0° represents the vertical crank position (Kyle *et al.* 2004).

rotates around the crank, as shown in figure 1.8. Although these results do not take into account the effect of the pedalling motion and frequency on the aerodynamics and fluid mechanisms that influence drag, they do indicate the large influence that the position of the legs around the crank have on drag, with different crank angles resulting in changes in drag as high as 15%. As movement of the legs around the crank is a prerequisite for cycling, any detailed study into cycling aerodynamics must take into account how changes in leg position will affect the aerodynamics of cyclists.

1.3 Analogous Flows

There is little public literature discussing dominant fluid mechanisms and flow structures that have a large influence on a cyclist's drag. This is a reflection of the competitive nature behind the sport of cycling, where withholding research can provide athletes with a competitive 'edge'. Currently the vast majority of research on the aerodynamics of cyclists has addressed the issue of aerodynamic drag from the perspective of the rider through measurement of the aerodynamic forces acting on the cyclist system. However, aerodynamic drag can also be assessed from the perspective of the fluid through which the cyclist moves through (Newton's third law). Measurement techniques that take advantage of this fact often provide much more information regarding how and where the drag force is generated.

Previous investigations into highly three-dimensional bluff body flows, such as vehicle aerodynamics, have shown that investigating the wake structures can lead to a better understanding of how changes in vehicle geometry can affect the pressure distribution over the body, leading to changes in drag. Similarly by investigating the wake of cyclists and, in particular, identifying wake structures that have the largest impact on the aerodynamic drag force, this will lead to a better understanding of how variations in rider shape and position will affect drag. It also follows that knowing the locations on the body where flow separation occurs has the potential to have a significant impact on the design of cycling equipment with the goal of minimising aerodynamic drag on the rider. Currently, no picture of the gross wake structure has yet emerged.

Similar to cyclists, road vehicles are three-dimensional bluff bodies where vehicle performance is highly dependent on aerodynamics. Whether it be passenger cars and transport vehicles, where fuel efficiency and emissions is of primary concern, or racing cars, where the time taken to travel around the track has to be minimised, aerodynamics is of primary importance for maximising performance. Like the geometry of cyclists, many vehicles, and especially passenger cars, are of a relatively low aspect ratio and consist of complex curved three-dimensional shapes. This makes the location at which the flow separates hard to predict and results in a very complex wake structure. Also, from an aerodynamic point of view, not only is the aerodynamic drag mainly a result of pressure forces, but the dominant wake structures of passenger cars, for which there has been extensive research, are found in this thesis to share many similarities with the most important flow structures in the wake of a cyclist.

In a review of road vehicle aerodynamics, Hucho & Sovran (1993) notes that one of the most influential findings in vehicle research and development has been the identification of large trailing streamwise vortices as a primary feature of vehicle wakes. Passenger type vehicle geometries such as fast backs, hatch backs and notch backs all exhibit strong streamwise vortex structures that dominant the near wake flow. A sim-

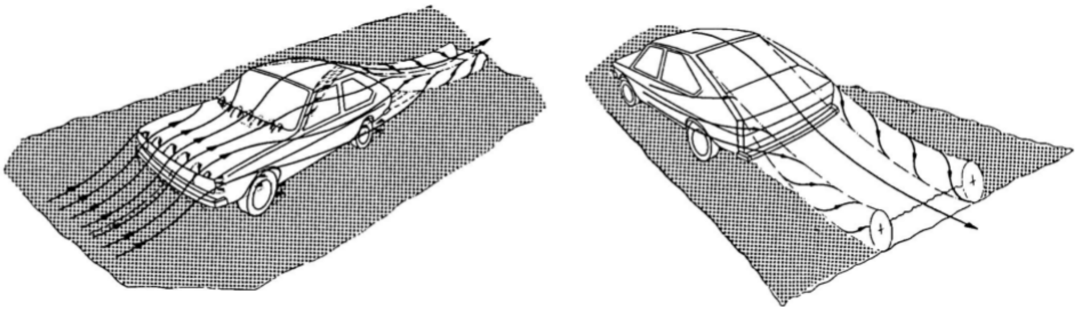

FIGURE 1.9: Simplified model of the flow field around fast back type passenger vehicles (Ahmed *et al.* 1985).

plified three-dimensional flow model depicting these vortices can be seen in figure 1.9. These primary structures originate when flow separates from the separation line along the C-pillar. The shear layer that develops over the backlight (rear window) of the vehicle rolls up to form strong streamwise vortices from each side of the vehicle. Hence the name *C-pillar vortices* by which they are commonly referred to.

It is hard to ignore the similarities between the formation of the C-pillar vortices and streamwise vortices that are generated at the tips of low aspect ratio wings. This has also been noted by many others (Ahmed *et al.* 1985; Hucho & Sovran 1993; Gilhome 2002). These structures shown in figure 1.10 for a low aspect ratio rectangular wing and a delta wing, develop as a result of a pressure differential generated between the underside and top of the wing surfaces. This pressure differential results in the separation of the flow off the wing tips of rectangular wings and from the swept leading edges of delta wing planforms. These separated flows roll up over the top of the wing to form large counter-rotating streamwise vortices. These primary vortices are the main feature of the flow and are present over the majority of the wing area and hence largely dictate the aerodynamic performance of low-aspect ratio wings. The rapid swirling motion of these vortices can induce lower pressures over the upper wing surfaces, leading to enhanced lift performance. Large angles-of-attack are also able to be obtained before the wing stalls, as a result of the additional downwards component of the flow (downwash) that is induced between primary streamwise vortices emerging from both sides of the wing. The downwash helps to maintain attached flow along the centreline, allowing much higher angles-of-attack to be achieved compared to wings of a higher aspect ratio.

Unlike low aspect ratio wings however, where low pressure vortices generated over

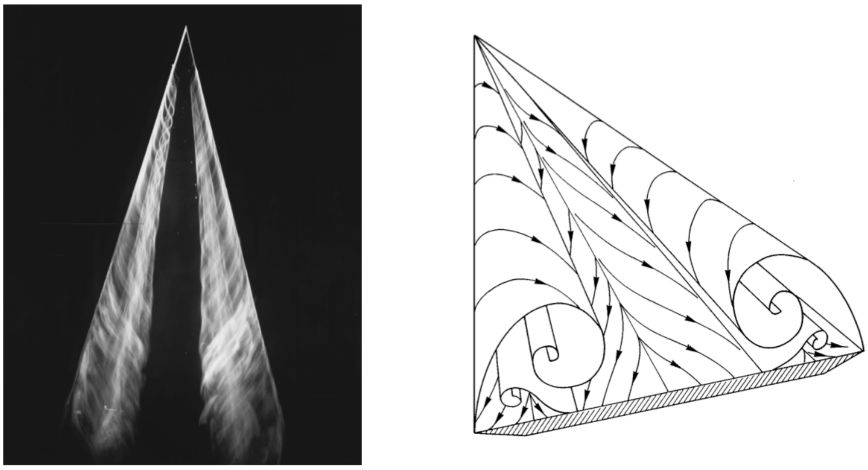

(a)

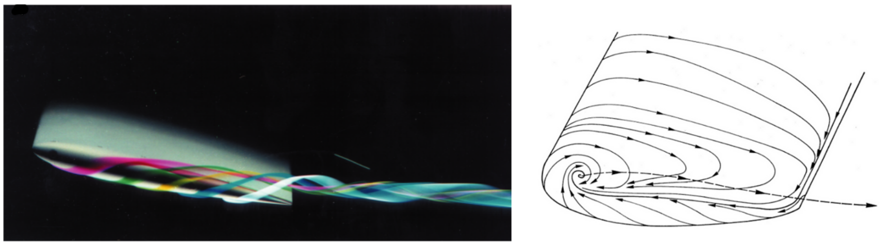

(b)

FIGURE 1.10: (a) Flow visualisation of vortices over a delta wing and corresponding schematic of the leading edge vortex structures (Délery 2001) (b) Flow visualisation of vortices forming at the tip of a low aspect ratio rectangular wing and the topological interpretation of corresponding skin-friction lines (Délery 2001).

the upper surface of the wing are desirable for enhanced lift and stall characteristics, for many bluff body geometries strengthening of streamwise vortices has the undesirable effect of reducing the base pressure and hence increasing the aerodynamic drag. For road vehicle geometries, the drag contribution of trailing streamwise vortices is significant and much of the work surrounding vehicle shape development has centred on ways in which the associated vortex drag can be minimised. This has been achieved through a focus on understanding the flow physics associated with the rear section of vehicles, where the primary flow structures originate and also where the majority of the drag is generated. For some passenger road vehicle geometries as much as 75% of the pressure drag is solely due to pressure forces acting on the rear of the vehicle (Beaudoin *et al.* 2004).

The importance of the vehicle wake structure on aerodynamic drag has led to many

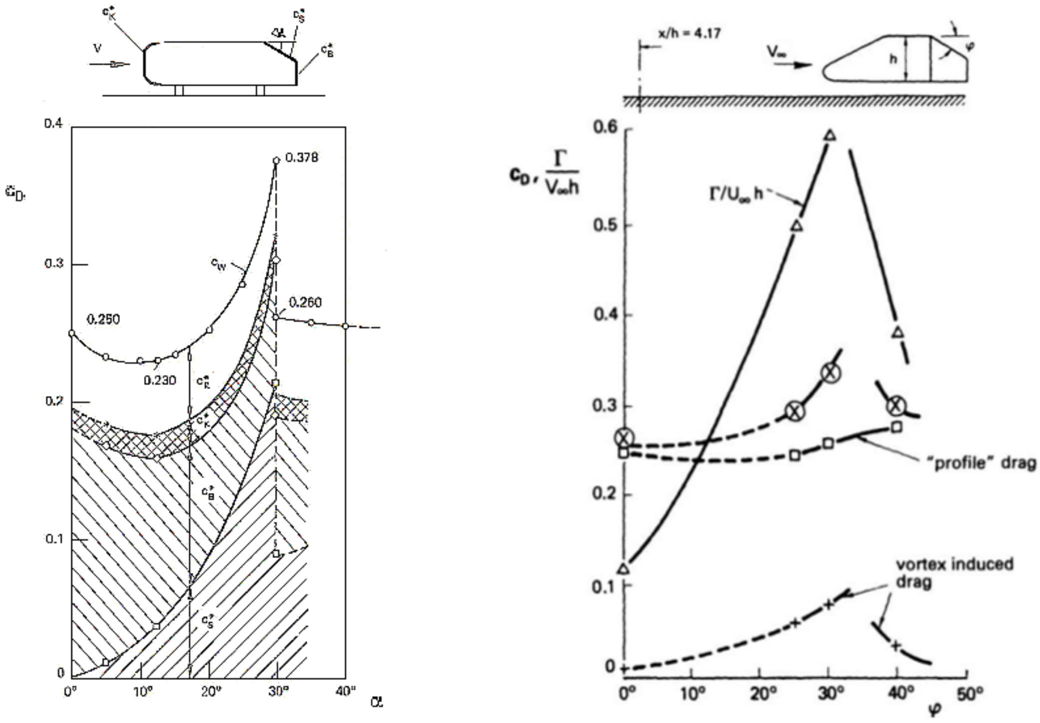

(a) (b)

FIGURE 1.11: Variation in aerodynamic drag with rear slant angle from (a) Ahmed *et al.* (1984) and (b) Bearman & Obasaju (1982) which also shows the circulation and contribution of C-pillar vortices to the total aerodynamic drag (taken from Hucho (1987)).

investigations performed on simplified vehicle geometries that reproduce the most essential flow features of real vehicle geometries (Le Good & Garry 2004). With the simplified vehicle geometries a greater understanding of the origin and nature of the aerodynamic drag force has been gained by making systematic parametric changes and observing not only how this affects the aerodynamic drag force but also the state of the structure of the flow in the near wake. One of the most widely investigated simplified geometries is that initially investigated by Ahmed *et al.* (1984), which is now known as the *Ahmed* vehicle or model (or body). This particular model is of a rectangular prism geometry with a rounded front-end shape (to minimise the influence of the front end on the wake structure) and a rear section that had a slant originating from the top surface of the model (with sharp edges) to simulate the angle of the backlight of a fast/hatch back type vehicle.

The study by Ahmed *et al.* (1984) is a very good example of how a deeper understanding of the most important aspects of vehicle geometry that influence the aerody-

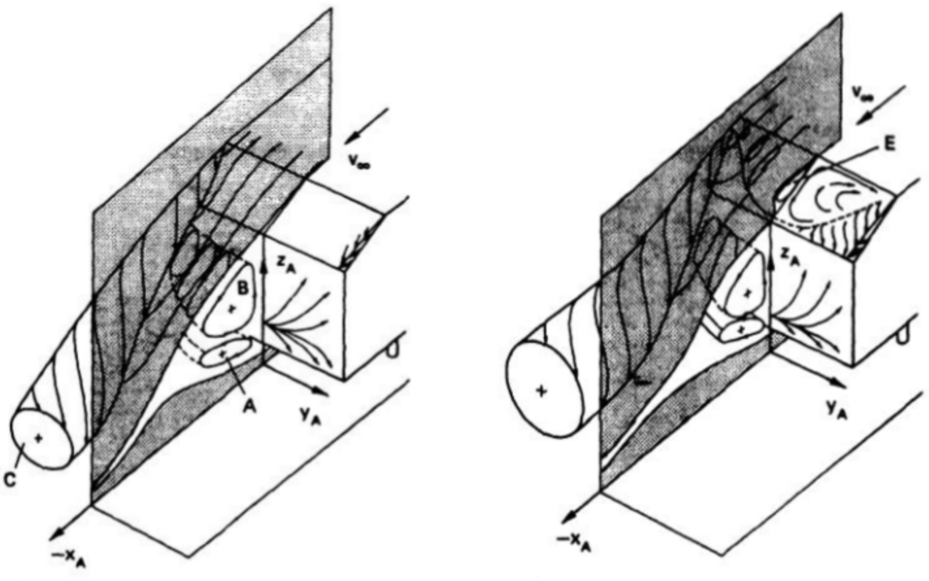

(a) (b)

FIGURE 1.12: Flow structure in the wake of the Ahmed model showing (a) Low and (b) High drag flow regimes (Ahmed *et al.* 1984).

namic drag force can be obtained, with a focus on investigating the large-scale wake structures. Ahmed *et al.* (1984) used his simplified vehicle model to demonstrate that the aerodynamic drag was primarily a result of the pressure drag acting on the rear surfaces and was highly dependent on the rear slant angle. This had also been previously shown in similar wind tunnel investigations into the influence of the rear slant-angle on drag(Janssen & Hucho 1975; Morel 1978b,a; Ahmed 1983). The variations in the total drag and surface pressures were determined for different slant angles, which enabled the aerodynamic drag to be decomposed into skin-friction 'C_R^*' (total body) and pressure drag components acting on the forebody 'C_K^*', vertical base 'C_B^*' and the rear slanted surface 'C_S^*', which are reproduced in figure 1.11(a).

The large variation in the pressure drag acting on the rear surfaces was a result of dramatic changes in the wake structure, which was associated with a low, high and post high drag flow regime (caused by changing the slant angle). The low drag flow regime was present for slant angles between 0° and 15°, as shown in figure 1.12(a). For this regime the flow remained attached over the majority of the slanted surface, with a pair of counter-rotating streamwise vortices originating from each side of the slanted edge (equivalent to C-pillar vortices). These streamwise vortices were found to be the primary wake structures influencing the variation in drag with slant angle. For slant angles between 15° and 30°, the flow transitioned to the high drag state, where the flow separated from the top edge of the slanted surface and subsequently reattached to it further down near the vertical base. This is shown in figure 1.12(b). As the base slant angle approached 30°, the recirculation region over the slanted surface was found to increase in size, which draws in and strengthens the C-pillar vortices. The strengthening of the vortices and the larger surface area they covered over the rear of the model resulted in a significant reduction in base pressures and hence an increase in drag. A more direct relationship between the strength of the C-pillar vortices and their impact on the drag was made by Bearman & Obasaju (1982) who showed the circulation of the streamwise vortices increased rapidly as the slant angle approached 30°, after which the strength of the vortices rapidly decreased. This can be seen in figure 1.11(b), which shows the majority of the variation in drag with slant angle is a result of the drag associated with the C-pillar vortices. For angles greater than 30° the separated flow from the top of the roof no longer reattaches down the slant surface. This resulted in a large reduction in the strength and area impacted by the C-pillar vortices. In turn this results in an increase in the base pressure and a significant reduction in drag for these slant angles. This can be seen in both figures 1.11(a) and (b).

1.4 Conclusion

In reviewing published literature on cycling aerodynamics, it is apparent that a more fundamental understanding of the flow around rider geometries would be useful to understand and improve aerodynamic performance. The sport of cycling is still at a point at which even small reductions in aerodynamic drag can make a substantial difference at the elite level. However, with the UCI placing rules restricting rider positions, large gains through 'extreme aero-positions' are no longer possible. Future improvements to rider aerodynamics will likely result from smaller adjustments to rider positions, such as the time-trial position, and the streamlining of the rider through equipment selection.

Wind tunnel testing has demonstrated the large potential to reduce the aerodynamic drag force on riders through relatively minor changes to the position of the arms, head and torso. However, wind tunnel testing to date has not been able to explain the large variation in measured force between different riders and their positions, and has shown the optimisation of rider aerodynamics seems to be best treated on an individual basis. As a result of this, rider position and equipment selection is currently assessed using a trial and error approach, which limits the ability to build a fundamental understanding of the influence or rider shape, position and equipment on cycling aerodynamics. In order to achieve a more efficient approach to optimising the aerodynamics of elite cyclists the focus must change from ad-hoc modifications to a more systematic targeted approach at reducing the pressure drag component on the rider in critical areas. This can only be achieved through a deeper understanding of how the pressure forces are imparted on the rider and by identifying what are the most important features of the flow affecting variations in drag.

Currently, the location of regions of the flow separation, the basic wake flow structures and where the majority of the drag originates from are not well understood. A review of road vehicle aerodynamics has demonstrated that a deeper understanding of how vehicle geometry influences drag can be gained through a focus on investigating the dominant large-scale flow structures in the wake, which have the largest impact on the aerodynamic forces. It is evident that the field of cycling aerodynamics could also benefit immensely from developing a greater understanding of how and where the aerodynamic forces are imparted on the rider through forming and shedding flow structures. In order to develop a more systematic and target approach to reducing the aerodynamic drag force, we first must identify where the large separated areas occur, where the majority of the pressure drag is generated on the body and what the large-scale flow structures look like. As a change in the position of the legs around the crank cycle is a prerequisite for sustained cycling, the investigation must also incorporate the effect of leg position.

In developing a generalised picture of the flow topology around a generalised rider geometry in a time-trial position, this study provides a basis for assessing rider position and the design of rider equipment with the aim of targeting the reduction of drag in specific areas associated with the dominant wake structures. This understanding also builds a solid foundation for addressing the influence variations in rider geometry and position have on the aerodynamic drag force through the effect that these variables have on the large-scale flow structures.

Chapter 2

Equipment & Experimental Method

This chapter discusses both the equipment and facilities utilised to investigate cycling aerodynamics in the Monash University wind tunnels. It also outlines the overall experimental methodology of the project. As the cycling mannequin was used across the majority of aerodynamic testing, particular emphasis is placed on its design, construction and capabilities.

2.1 Full-Scale Cycling Mannequin

The need for a cycling mannequin was recognised during the very early stages of the project. One of the major problems with athlete wind tunnel testing is the repeatability of rider position. The validity of assigning any aerodynamic quantity associated to a particular rider shape and position depends upon the ability of the rider to maintain their position throughout the testing period. As explained in Chapter 1, this is particularly true when taking force measurements of rider position, where small variations in position can have a large impact on the results. Repeated wind tunnel measurements of cyclists over long periods of time (months/years) are also subject to variations arising from fluctuations in rider body composition, which can alter the shape and position of the rider from test to test. By performing wind tunnel experiments on a mannequin, rider positions can be accurately repeated and maintained for extended periods of time. The ability to hold a particular position for long periods was especially important throughout this project with some wind tunnel tests lasting well over six hours. Over such a time it is clearly impractical for any individual to maintain their position. Figure 2.1 shows the full-scale cycling mannequin that was developed for this

FIGURE 2.1: Mannequin standard time-trial position.

project. It contributed to all the major findings presented in this thesis.

The mannequin also allows a systematic testing methodology to be developed to investigate the impact a specific variable has on the aerodynamics of the system, something that is not possible with real riders. Also, when a particular change is made to a rider's position it is usually also associated with a change in the "shape" of the cyclist being tested, a fact that is often not considered when testing riders in a wind tunnel. This was made particularly apparent in the wind tunnel tests performed on the AIS female National Squad Camp (section 1.2), where the large variations in rider position observed between static and dynamic testing were also associated with large changes in the shapes of the athletes' backs. Testing with the mannequin allows for the geometry and position to be decoupled. This capability was particularly important because it meant that position and geometric variables could be varied independently, and hence investigated, in a thorough and systematic way.

Apart from these benefits, the mannequin also bypasses any ethical or safety issues associated with the testing of athletes and allows for wind tunnel tests that are impossible to perform on real cyclists. Many of the wind tunnel experiments presented throughout this thesis could have been considered unsafe if performed on a real cyclist. This is particularly true for some of the flow visualisations, which involved the use of high powered lasers, volatile liquids, surface paints and smoke visualisations.

Although there are significant advantages in using a mannequin to model a cyclist a number of limitations must also be considered. These limitations are mainly concerned with its simplified geometry and range of motion. As movement of the human form is complicated, it was necessary to simplify the shape and the degrees of freedom of the mannequin's joints. These simplifications, to be addressed in detail in the following section, were needed to make the computer aided design (CAD) modelling and construction of the mannequin practical. The simplified design also ensured that the mannequin could be described in terms of simple geometrical shapes with a limited range of motion, effectively reducing the number of aerodynamic variables that may impact this complicated system.

2.1.1 Design & Capabilities

Prior to commencing the design of the mannequin a number of key design criteria were identified. These include;

1. The geometry of the mannequin must model the shape of elite cyclists to ensure that the aerodynamic characteristics represent those of a real cyclist. As a result of this project being part of a wider body of research into the understanding of cycling aerodynamics, the ability to adjust the shape of the mannequin was an important design feature due to the large impact that the shape of a cyclist has on aerodynamic drag. In designing the mannequin, special emphasis was placed on a design that allowed for a high degree of freedom to manipulate the shape of the mannequin's torso. This was largely initiated by outcomes from findings presented in Chapter 1, where the shape of a cyclist's torso was found to have a significant impact on drag.

2. The mannequin needed incorporate all the major anatomical joints to allow its position on the bicycle to be adjusted, with these positions being chosen to represent those typically used by elite cyclists. As noted above, these positions also need to be highly repeatable, to ensure the same position was tested throughout all wind tunnel experiments. This placed constraints on the structural integrity of the mannequin, so that positions would be maintained under typical wind loads experienced on the track or road.

3. The mannequin must be adaptable to meet the needs of a wide range of wind tunnel experiments. This will be further discussed when addressing wind tunnel testing involving surface oil flow visualisations and surface pressure measurements made on the back of the mannequin. This required a reconfiguration of the standard set-up, involving the addition of a rigid fibreglass skin torso.

Figure 2.2: Profiled athlete's standard time-trial positions.

To construct a cycling mannequin that represents a generalised cyclist geometry, the shape of three experienced male cyclists (two triathletes and one road cyclist) were analysed. These cyclists were aged between 21 and 35 years with a mean body mass and standing height of 73.3 kg and 1.82 m respectively, representative of elite road and track cyclist characteristics. A number of different techniques where considered to obtain a three-dimensional scan of the athletes but they proved to be prohibitively expensive or required the athletes to be in a standing position, which would not provide a representative geometry of a cyclist in a riding position. To overcome these issues a novel technique was developed that profiled two-dimensional sections of the athletes' bodies whilst holding their standard time-trial positions on their own personal bicycles, as shown in figure 2.2.

Figure 2.3 shows one example of how the shape of a sectional profile measurement made on the upper half of the back of the torso is characterised in terms of simple two-dimensional shapes. By breaking up sectional profiles of the torso into halves, the shape of each top (back) and bottom section (chest/stomach) can be described in terms of a series of ellipses and circles. From a number of these measurements made at regular intervals along the torso the three-dimensional shape of the torso could be built up and characterised in terms of simple two-dimensional shapes. The development of the geometry of the mannequin torso is described in more detail in Appendix B. Similar profiles were also completed on the athletes' upper and lower legs from which ellipses and circles were also used to construct the overall geometry of the legs. These measurements were performed on each of the cyclists and the results were then used to calculate an average rider geometry on which the shape of the fully-adjustable mannequin was based. This ensured that traits that were inherent to individual riders were averaged, providing

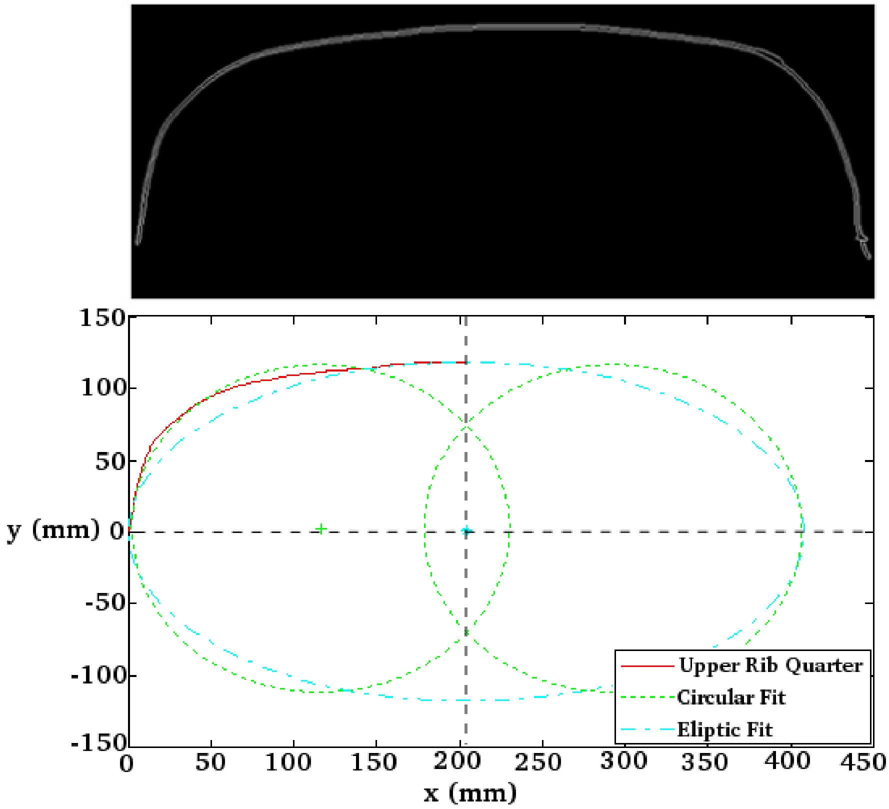

FIGURE 2.3: Example of a profiled torso rib section for mannequin geometry development.

a more generalised shape on which to base the geometry of the mannequin.

After a number of iterations the final design of the mannequin was developed in the 3-D modelling package Uni-Graphics NX.7. The CAD model allowed for the final design to be accurately evaluated for key design criteria prior to construction. The final design consisted of an internal jointed skeleton constructed of lightweight aluminium to which the external network of body parts that provide the mannequin with its overall form were fastened. To smooth out and fill any discontinuities and gaps in between body part sections, a wetsuit was stretched over the external frame providing the mannequin with a flexible air-tight skin that that does not limit the rotation of the legs around the crank. When additional material was required to fill gaps in areas where body parts intersected each other, a low density, highly compressible foam was used. Figure 2.4 shows a CAD model of the mannequin, showing the internal skeletal frame, joints and the external shape developed from mean athlete profiles. The compressible foam sections are coloured orange.

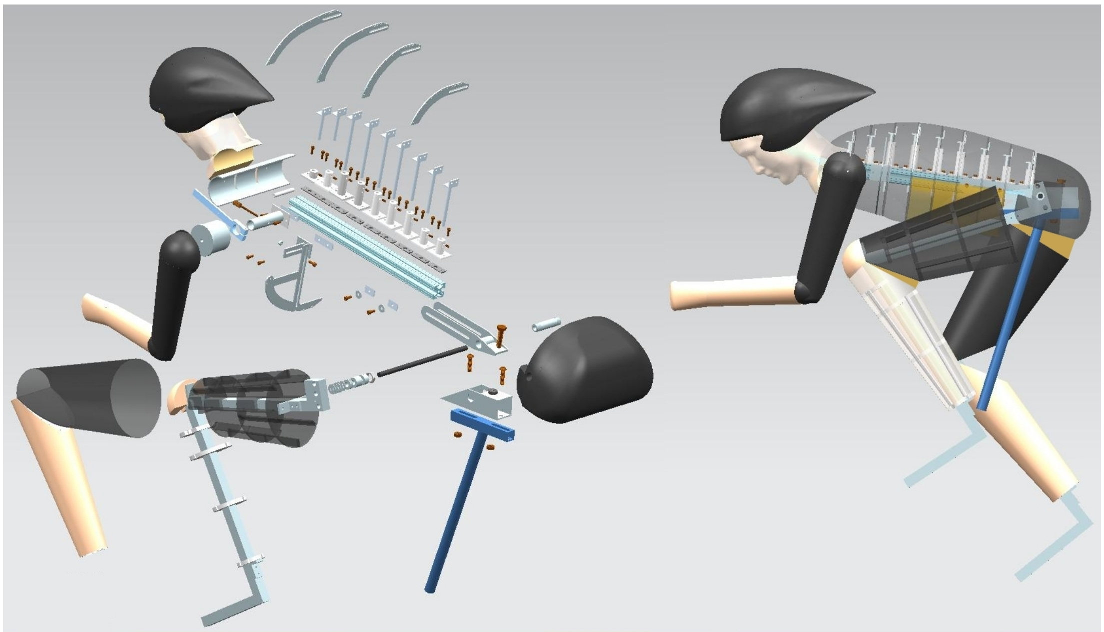

FIGURE 2.4: Mannequin CAD Model.

From detailed drawings developed from the CAD model the mannequin was built in-house at the Monash Mechanical and Aerospace Engineering Workshop and the Monash Wind Tunnel Wood Workshop. The main features of the mannequin consist of; independent joints at the base of the head and neck for accurate positioning of the head and helmet, adjustable shoulder joints to allow rotation and locking of the upper arms with the added ability to alter shoulder width, flexible arms so that a range of cycling positions can be achieved while still maintaining rigidity, hip joints that not only allow for the rotation of the upper legs but also allow for the angle of the torso (angle-of-attack) to be altered and locked in place and an adjustable ribbed torso design that allows for the shape, width and length of the torso to be adjusted. The completed mannequin without the foam inserts, wetsuit and the skin-suit stretched over the frame (shown previously in figure 2.1) is shown in figure 2.5. The figure also shows how the adjustable ribbed design of the torso allows the user to change the shape of the torso.

Although the standard mannequin set up, with the wetsuit and the cycling suit stretched over the ribbed frame was ideal for the majority of experiments, a fibreglass torso was also constructed to extend the testing capabilities of the mannequin to include surface pressure measurements and surface skin-friction flow visualisations. This was necessary as the wetsuit and skin-suit combination do not provide a rigid enough structure to fix pressure taps to or a surface finish that allows skin-friction flow visu-

FIGURE 2.5: Mannequin final assembly.

alisations. The fibreglass torso was completed using a hands lay-up technique applied directly onto the skin-suit on the back of the mannequin so that a hollow female shell of the geometry of the back could be formed. Figure 2.6 shows the fibreglass addition to the mannequin's back (outlined in red) which extends from the shoulders to the sides of the torso and down to the base of the mannequins back. With the skin-suit firmly fixed on the inside of the fibreglass the shell/skin-suit can be positioned on the ribs and used as a alternative to the standard set up with minimal variation in the physical geometry being tested (fibreglass provides an additional 3–4 mm thickness to glassed areas).

2.1.2 Mannequin Test Set Up

This section describes the position, cycling equipment and the overall shape and size of the mannequin that was tested throughout all wind tunnel studies with both the standard and fibreglass torso configurations. As reviewed in Chapter 1, the drag of a cyclist is very sensitive to their position, body shape and cycling equipment. It is therefore important to establish the geometry, cycling positions and mannequin cycling equipment tested. The majority of outcomes presented, particularly those concerned with the identification of flow structures, are a result of wind tunnel tests performed

FIGURE 2.6: Mannequin fitted with fibreglass torso over ribbed frame.

on the mannequin in the standard position.

Figure 2.7 shows the standard time-trial position and cycling equipment that was adopted for the majority of wind tunnel testing. The mannequin's position on the bicycle is representative of a low drag time-trial position that is typically used by cyclists during time-trial stages of road races, triathlon events, the UCI hour record and many track cycling events that do not involve sprints. The helmet, skin-suit and bicycle are typical of those used by elite cyclists competing in such events.

Figure 2.7 also depicts the parameters that describe the position of the mannequin on the bicycle and the main geometric properties that describe the overall shape and size of the mannequin. To ensure the repeatability of the positioning of the mannequin a system was developed to measure all independent parameters that determine its position so that they could be measured and checked against previous wind tunnel tests. Table 2.1 shows the standard positioning and overall shape and size of the mannequin that was employed throughout the majority of investigations into the aerodynamics of cyclists.

In identifying the primary flow structures of a cyclist, the main variable that was changed was the position of the mannequin's legs around the crank cycle. The position of the legs is defined by the angle of the crank 'θ' where the 0° crank position (pictured in figure 2.7) is when the crank is horizontal, with the right leg in a forward position and left leg back. This naming convention is adopted to describe the position of the legs throughout the entirety of this thesis. To simplify the dynamics of the legs the ankle angle, which typically only varies 5–10° throughout the pedal stroke, was locked

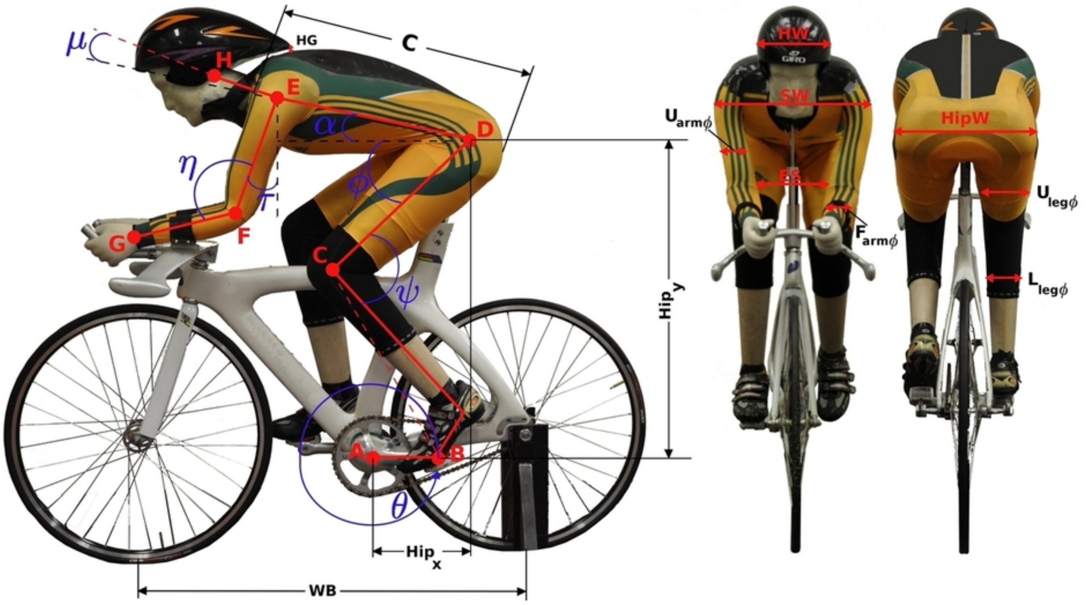

FIGURE 2.7: Standard mannequin time-trial position.

in place at 90° effectively constraining the motion of the upper leg, lower leg and crank in terms of a four bar linkage crank rocker mechanism. As the mannequin is mounted on a fixed gear track bicycle, with the motion of the legs fully constrained, the leg position could be changed by moving the rear wheel and locking it in place. Of key importance to the aerodynamics of the upper body of the mannequin is the position of the upper leg defined in terms of the hip angle 'ϕ'. Figure 2.8 shows how the hip angle of the mannequin varies throughout the pedal stroke while in the standard position.

2.2 Mannequin Wind Tunnel Testing Methodology

A range of wind tunnel investigations were performed to identify the dominant flow structures which predominantly influence drag and how they are affected by rider position. Experiments performed with the mannequin that investigated the effect of leg position on flow structures and the forces acting on the model include measurements of the aerodynamic drag force, time-averaged wake surveys, flow visualisations and measurements of the fluctuating pressures made on the back of the model. These studies were carried out in two separate wind tunnels located at Monash University; the Monash Large Wind Tunnel (MLWT) and the smaller 450kW wind tunnel which are described in detail in the following section. Table 2.2 shows a comparison of the main characteristics of the two wind tunnels. A breakdown of the experiments performed in

Name	Symbol	Standard Position
Crank Angle	θ	0°:15°:360°
Knee Angle	ψ	$f(\theta)$
Hip Angle	ϕ	$f(\theta)$
Angle-Of-Attack	α	12.5°
Upper Arm Angle	τ	20°
Elbow Angle	η	110°
Neck Angle	μ	5.0°
Head/Helmet Gap	HG	20 (mm)
Hip Location (x)	Hip_x	200 (mm)
Hip Location (y)	Hip_y	806 (mm)
Name	Symbol	Length (mm)
Wheel Base	WB	970
Crank	A→B	175
Torso Chord	c	640
Foot-Knee	B→C	558
Upper Leg	C→D	448
Torso	D→E	485
Upper Arm	E→F	300
Forearm	F→G	250
Neck	E→H	120
Helmet Width	HW	200
Shoulder Width	SW	420
Elbow Spacing	ES	160
Hip Width	HipW	350
Upper Arm Diameter	$U_{arm\phi}$	80
Forearm Diameter	$F_{arm\phi}$	72
Upper Leg Diameter	$U_{leg\phi}$	150
Lower Leg Diameter	$L_{leg\phi}$	90

TABLE 2.1: Mannequin geometry and standard positioning set-up.

Wind Tunnel	MLWT	450kW
Type	Return circuit open-jet & closed	Return circuit closed
Cross Sectional Area	2.6×4 m (jet exit)	2.0×2.0 m
Turbulence Intensity	$< 1.8\%$	$< 1.5\%$
Blockage (Mannequin)	$\approx 4\%$	$\approx 10\%$

TABLE 2.2: Comparison of main wind tunnel characteristics.

each wind tunnel is also shown in figure 2.9.

2.2.1 Monash Large Wind Tunnel & 450kW Wind Tunnel

The large wind tunnel located at Monash University (Clayton, Melbourne) is a return circuit wind tunnel consisting of multiple closed and open-jet test sections located around the tunnel circuit. Currently the Monash wind tunnel is the largest of its kind in the Southern Hemisphere, making it ideal for carrying out wind tunnel tests on large or full-scale models. The tunnel has three main test sections that are utilised for a

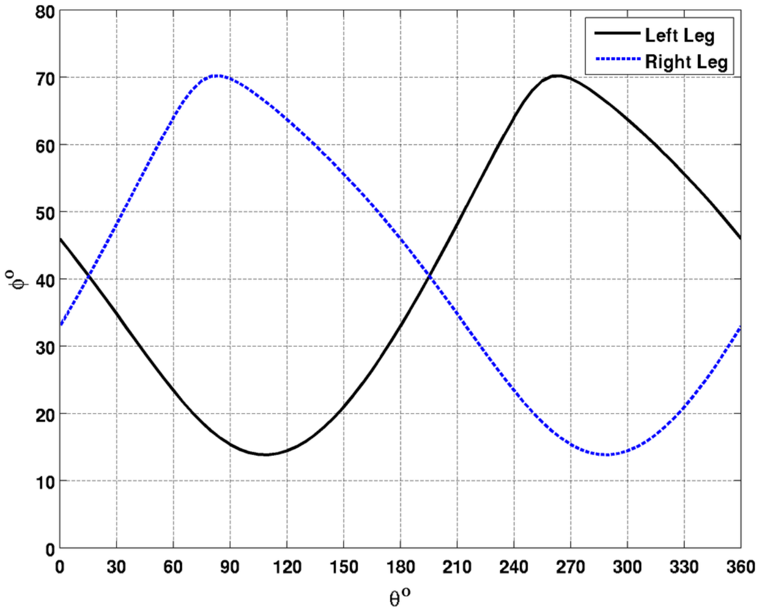

FIGURE 2.8: Left and right leg hip angle as a function of crank angle.

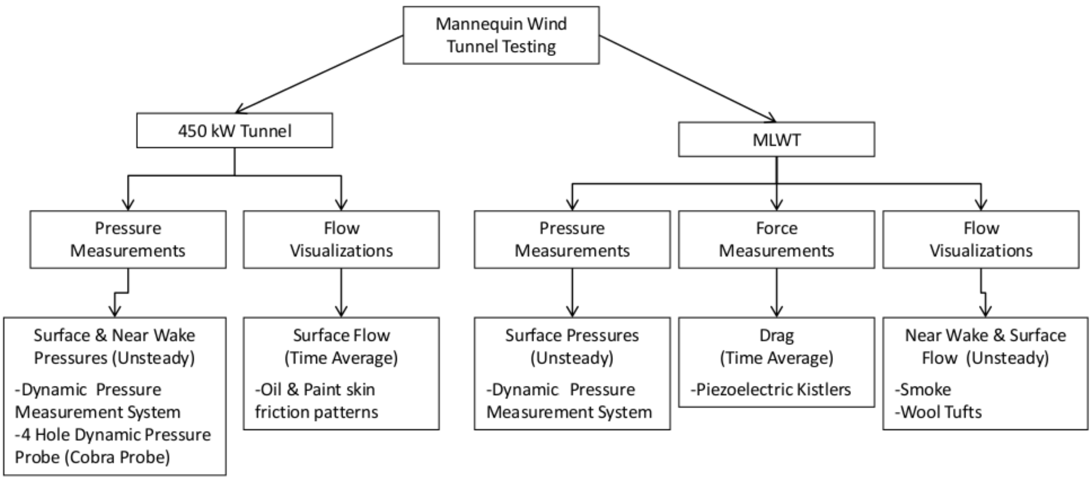

FIGURE 2.9: Wind tunnel testing flow chart.

diverse range of aerospace, automotive, and wind engineering projects. A schematic of the tunnel showing these test sections and the overall tunnel layout can be seen in figure 2.10. The upper section of the tunnel is mainly used for wind engineering proposes such as modelling atmospheric boundary layers and flows in built up areas for investigating wind loadings on buildings and bridges. The lower section consists of two main test areas; a high Reynolds number closed section and a three quarters open-jet

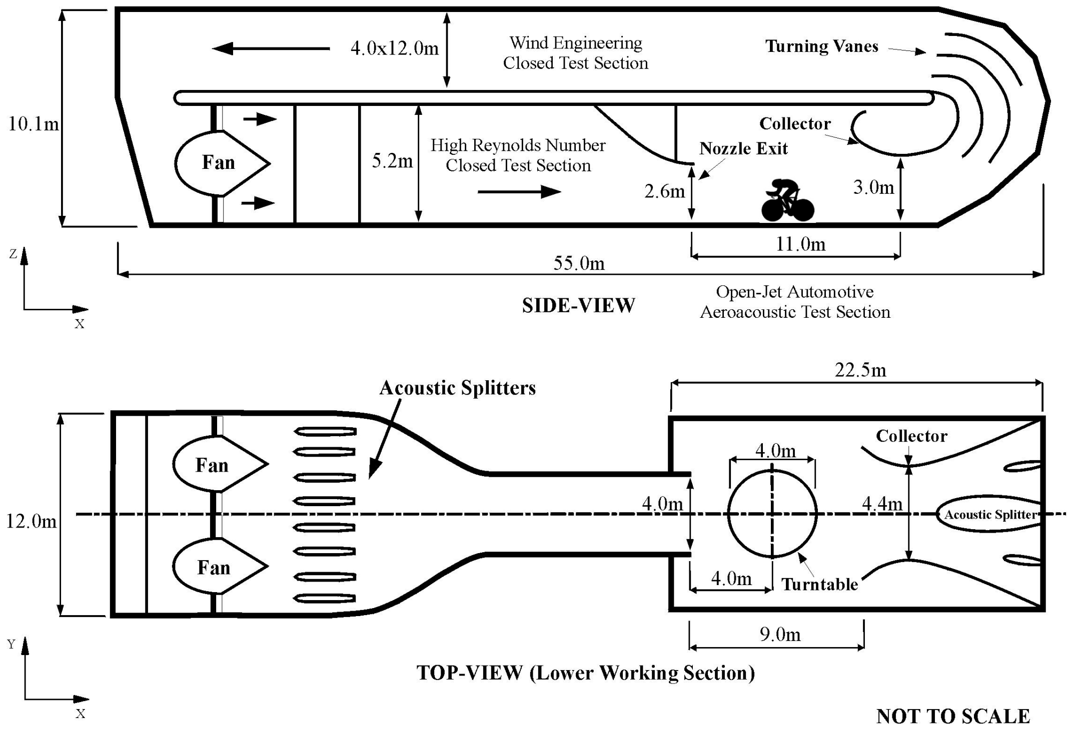

FIGURE 2.10: Schematic of the Monash Large Wind Tunnel, from Gilhome (2002).

section where all cycling experiments were performed. This particular section is the main test area of the tunnel and is predominantly used for aerodynamic and acoustic development of vehicles by Australian car manufacturers, acoustic and structural testing of facades, wind turbine performance and site evaluation and sports aerodynamic performance enhancement.

The wind tunnel is operated from a control room that is located just outside of the open-jet test section of the tunnel, where large windows allows for tests performed within this section to be directly observed. The flow speed in the tunnel is controlled via two 5 m diameter variable speed fans that are each driven by four 400 kW electrical motors (1.6 MW total). At maximum power flow speeds in the open-jet test section of the tunnel reach 180 km/h (50 m/s). The wind tunnel graphical user interface that controls systems surrounding the motors that drive the fans was developed in the instrument control software Lab View V8.20 running on Microsoft Windows XP. This signal processing and data acquisition software is also used to record atmospheric test conditions such as temperature and barometric pressure as well as the freestream velocity throughout the duration of wind tunnel tests.

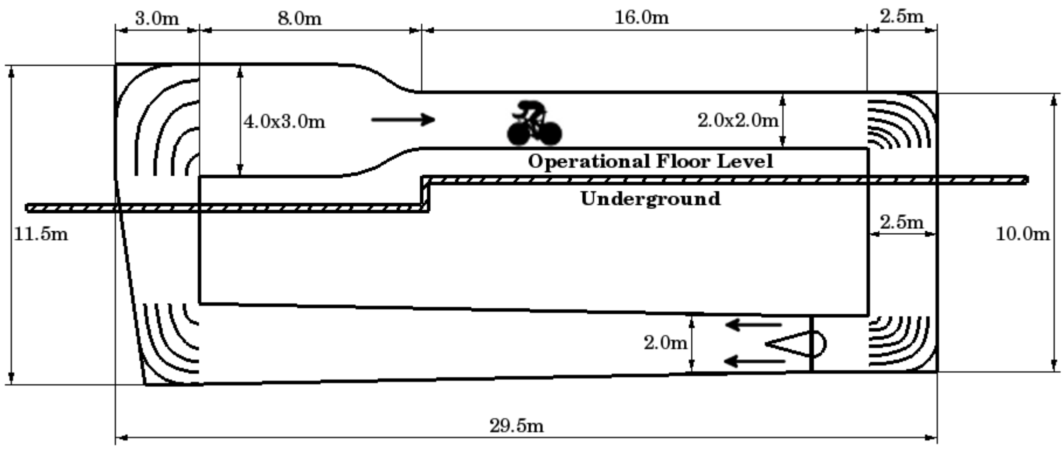

FIGURE 2.11: Schematic of the Monash 450kW Wind Tunnel.

The Monash 450kW wind tunnel is the second largest wind tunnel situated at Monash University Clayton. A schematic of this closed section return circuit wind tunnel is shown in figure 2.11. The flow speed in this wind tunnel is controlled via a variable pitch 2.0 m diameter fan that is driven by a 450 kW electrical motor. There are two main working sections on the upper level of the tunnel-circuit which consists of an upstream 4×3 m and a downstream 2×2 m section. The maximum speed in the 2.0 m test section where all experiments with the cycling mannequin were conducted is 40 m/s. Due to the smaller working section of this tunnel, compared to the large MLWT test section, blockage effects have been considered or corrected for in experiments performed in the 450kW tunnel which is covered in section 2.4.4.1. Similar experiments repeated in both wind tunnels are also compared and discussed in this section and throughout the results sections of this thesis and show that findings are consistent between both wind tunnel testing environments.

2.2.1.1 Wind Tunnel Speed Calibration

The wind tunnel speed of both wind tunnels is determined from the dynamic pressure and air density in the wind tunnel test section. The dynamic pressure is measured using a differential pressure transducer connected to a pitot-static tube. Prior to testing the pressure transducers were calibrated by applying a known reference pressure to the pressure transducer which can be compared with the corresponding voltage output. Reference pressures are applied to the transducer using a peristaltic pump and are measured using a Betz reference manometer. The calibration method consists of incrementally increasing the reference pressure supplied by the peristaltic pump and measuring the voltage output of the pressure transducer which is correlated with the reference pressure measured by the Betz manometer. The calibration was performed over the range of relevant pressures and is performed on a regular basis so that any drift in the pressure transducer can be identified. Calibration of the pressure transducers preformed over the duration of mannequin wind tunnel experiments is shown in Appendix C.

The air density in the wind tunnel test section is calculated using equation 2.1, which is based on the perfect gas law and is a function of the barometric pressure 'P_a', ambient air temperature 'T', specific gas constant for dry air 'R_a', specific gas constant for water vapour 'R_w' and the humidity ratio 'w_h'. For mannequin wind tunnel experiments the air density was take to be a constant throughout the test section and corrections for spatial variations in air density have not been applied. For both wind tunnels temperature was measured using thermocouple probes located in the test section, downstream of the test model. Barometric pressure was measured inside the wind tunnel control room. Temperature equations are used to determine saturation vapour pressure and the humidity ratio is then determined from relative humidity measurements. All pressure and temperature measurements are acquired using a National Instruments data acquisition system and are taken as an average reading throughout the duration of a particular test. The uncertainties associated with pressure and temperature measurements is a combination of data acquisition error and the sensor/system error and are summarised in Appendix D.

$$\rho = \frac{P_a.(1+w)}{R_a.T.(1+w_h.\frac{R_w}{R_a})} \tag{2.1}$$

In the 450kW wind tunnel the test section speed was determined from pitot-static measurements made in the test section a distance 3.0 m in front of the mannequin. This was determined to be far enough in front of the mannequin so that reference wind tunnel speed measurements were not effect by the presence of the model (change in velocity $< 0.5\%$). In the large open-jet test section of the MLWT however, which is often used to test models much larger than the mannequin, it is not ideal to measure velocities inside the test section during a test, as the model in the test section may influence the wind speed at the measurement point. To determine the flow speed in the MLWT a rake of three pitot-static tubes on either side of the settling chamber (six in total) are used to measure the reference dynamic pressure in the settling chamber (average of all pitot tubes). The calibration procedure of the test section wind speed involves measuring the dynamic pressure at the centre of turntable at a height of 435 mm above the ground plane using a pitot-static tube (calibration pitot-static tube) connected to a pressure transducer which is compared to the dynamic pressure upstream at the reference pitot-static tubes. The ratio of the flow speed in the test section centre of a clean wind tunnel (without models) to the flow speed upstream at the reference pitot-static tubes, known as the velocity calibration factor, is determined over a range of relevant wind speeds. An example of the calibration of the MLWT test section speed can be found in Appendix C. During wind tunnel testing of the mannequin the test section dynamic pressure (and velocity) is determined by applying the calibration factor to the velocity determined from the reference pitot-static tubes located in the upstream settling chamber. This method of calculating the flow speed at the test section centre does not take into account any blockage effects that may arise from the model being tested.

2.2.1.2 Wind Tunnel Test Section Flow Characterisation

It is important to characterise any flow properties in the test section that could influence the aerodynamics of the mannequin. Fluid mechanical process such as separation and the transition to turbulence are all influenced by freestream turbulence levels, flow uniformity, flow angularity and pressure gradients in the test section. As two wind tunnels have been utilised in this investigation it is also important to identify any large variations in the flow field that may result in findings from mannequin experiments being specific to a particular wind tunnel testing environment.

Currently there are no guidelines or standard wind tunnel testing conditions for the aerodynamic evaluation of cyclists. Previous investigations by Gilhome (2002) into vehicle aerodynamics, which are subjected to flow quality standards stipulated by the Society of Automotive Engineers, found no evidence that flow quality induced errors in the MLWT had significantly influenced the aerodynamics of sedan type vehicles compared to on-road conditions. Similarly it is not expected that flow quality issues will adversely affect aerodynamic testing of cyclists in the MLWT and 450kW tunnel. This is strengthened by the consistency in results from wind tunnel testing of the mannequin in both the MLWT and 450kW wind tunnel environments which will be shown throughout the results section of this thesis.

A four hole dynamic pressure probe was used to map the flow in MLWT and 450kW wind tunnel test sections at the representative cycling speed of 16 m/s. Measurements were also performed at selected locations at test speeds of 13 m/s and 19 m/s which represent low and high cycling velocities. The 'clean' test section flow was mapped using a two axis traverse that moved the probe within a plane normal to the mean flow in the centre of the test section. The test section centre is taken to be where the bicycle crank is located during testing with the mannequin in both wind tunnels. Both the probe and the automated traversing mechanism are described in detail in section 2.4. The grid resolution of probe measurements outside the boundary layer was 250×200 mm and the sample time and rate were 15 seconds and 1500 Hz respectively.

Flow Uniformity & Angularity:

Figures 2.12 and 2.13 show the uniformity in the mean velocity profile and angularity throughout the test section centres of both wind tunnels. The variation in the time-averaged velocity profile across the test section outside boundary and shear layers (for the open-jet tunnel) is $\pm 1.5\%$. An increase in the variation of the mean flow can be seen out towards the corners of the 450kW closed test section. The flow uniformity over the majority of both test section areas occupied by the mannequin is $< 1.0\%$. As expected due to the symmetrical wind tunnel geometry the angularity of the flow in the fully closed 450kW tunnel is more symmetrical about the centre planes compared to the 3/4 open test section in the MLWT. In both wind tunnels the flow angularity in the test section is not sever with maximum pitch and yaw angles relative to wind tunnel axes being less than $\pm 1.0°$ over the majority of the test section area. The highest flow angles can be seen to develop out towards the wind tunnel walls/floor and out towards the free shear layer in the MLWT. Repeated data points resulted in a maximum standard deviation of $0.1°$ for both pitch and yaw angles.

Turbulence Intensity:

Figure 2.14 compares the principal turbulence intensity components across the test section centres in the 450kW and MLWT. Turbulence intensities are defined in equations 2.2– 2.5. A summary of turbulence intensity components averaged over the test section area is shown in table 2.3. As a result of a single sided vertical (top) con-

Turbulence Intensity	MLWT (%)	450kW (%)
I_u	1.90	1.30
I_v	1.85	1.60
I_w	1.80	1.65
I_{uvw}	1.86	1.50

TABLE 2.3: Average turbulence levels across the MLWT and 450kW test sections.

traction at the nozzle exit in the MLWT turbulence levels are not isotropic and are lower in the z direction compared to the x and y directions. All turbulence levels increase towards the upper edges of the traverse plane as measurements approached the jet shear layer. Compared with the 450kW tunnel turbulence levels in the MLWT are typically 0.2–0.5% higher for all components over the area of the test section covered by the mannequin. Due to the 4-sided contraction leading into the 450kW test section the central areas (above 700 mm and below 1450 mm) turbulence levels (1.4%) are relatively uniform. This core area of the wind tunnel surrounds the vast majority of the mass and surface area of the mannequin. Towards the corners of the 450kW walls turbulence levels increase which is captured in the bottom corners of the traverse plane. These turbulent areas are expected to have little influence on the most critical aspects of the flow around the mannequin which are well outside of these regions.

$$I_u = \frac{\sqrt{\overline{u'^2}}}{U_\infty}, \tag{2.2}$$

$$I_v = \frac{\sqrt{\overline{v'^2}}}{U_\infty}, \tag{2.3}$$

$$I_w = \frac{\sqrt{\overline{w'^2}}}{U_\infty}, \tag{2.4}$$

$$I_{uvw} = \frac{\sqrt{\frac{1}{3}(\overline{u'^2} + \overline{v'^2} + \overline{w'^2})}}{U_\infty}. \tag{2.5}$$

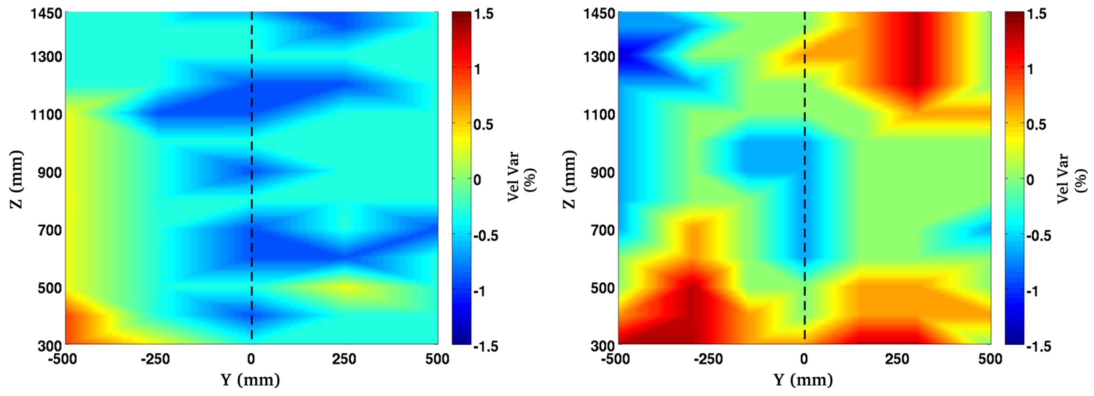

(a) MLWT (b) 450kW

FIGURE 2.12: Variation in the mean velocity profile at the test section centre in the MLWT and 450kW wind tunnels.

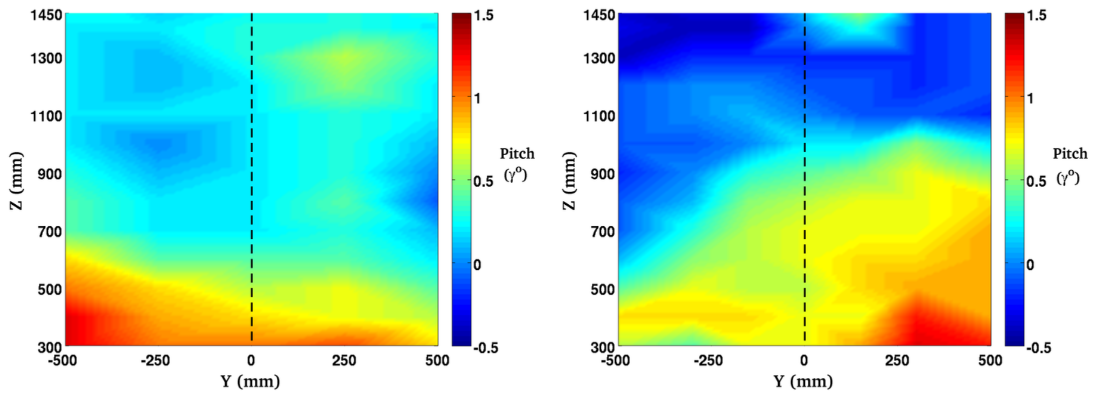

(a) MLWT (b) 450kW

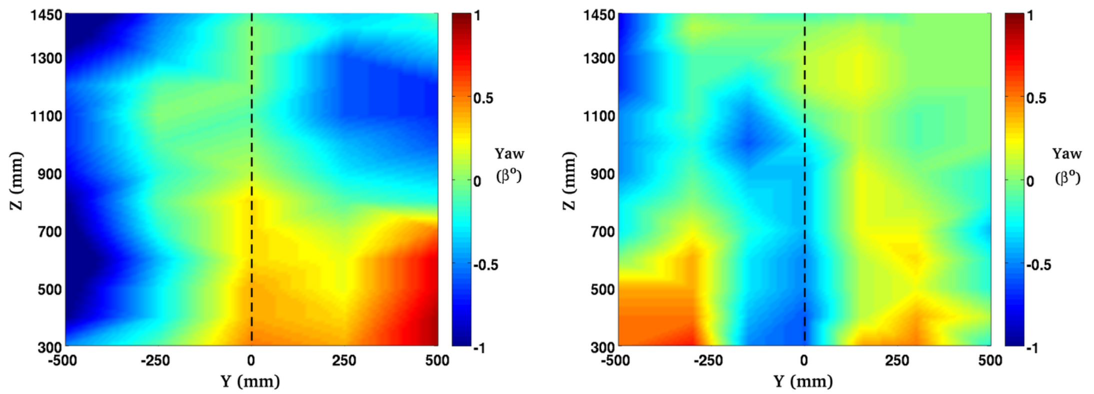

(c) MLWT (d) 450kW

FIGURE 2.13: Variation in pitch and yaw angles at the test section centre in the MLWT and 450kW wind tunnels.

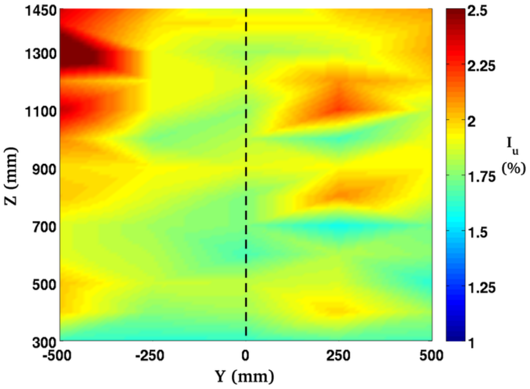

(a) MLWT

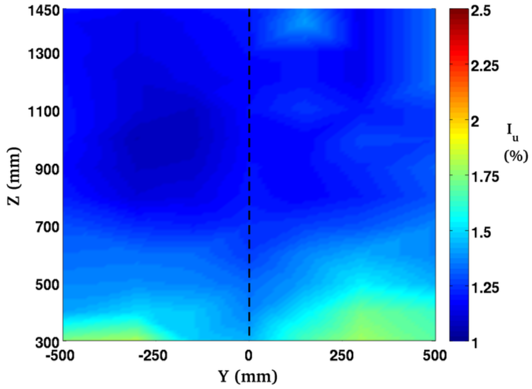

(b) 450kW

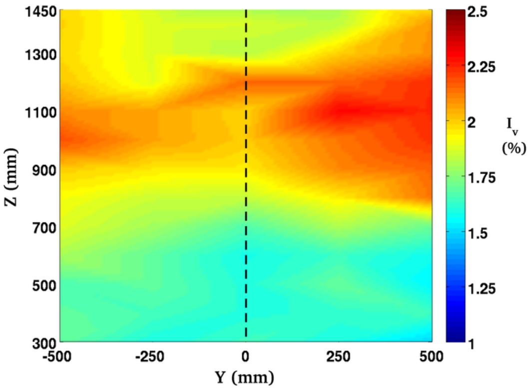

(c) MLWT

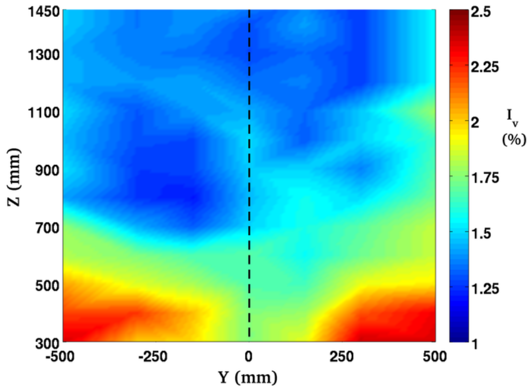

(d) 450kW

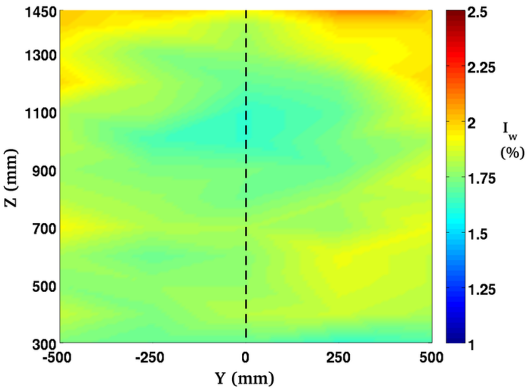

(e) MLWT

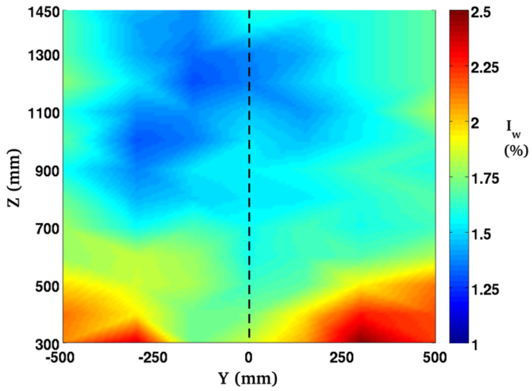

(f) 450kW

FIGURE 2.14: Principal turbulence intensity components across the test section centre in the MLWT and 450kW wind tunnels.

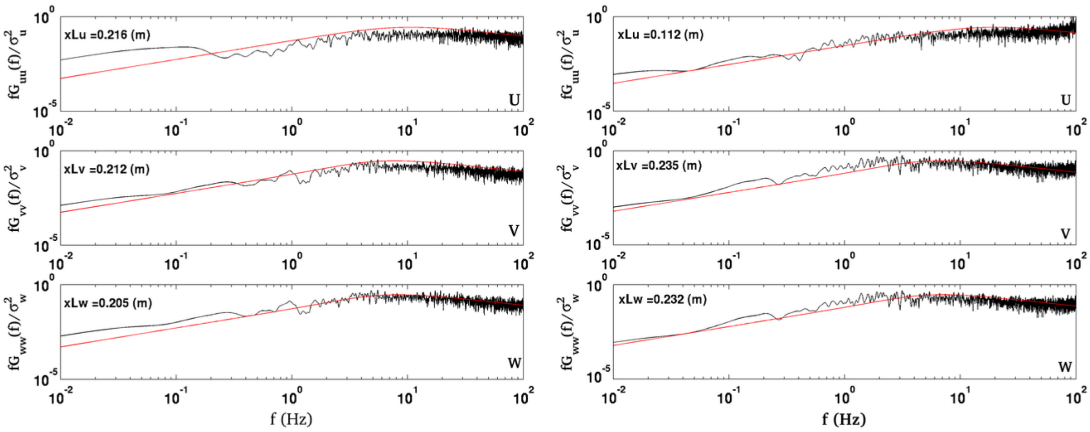

(a) MLWT (b) 450kW

FIGURE 2.15: Kármán spectra fit (red lines) to u, v, w auto-spectral estimates (black lines) in MLWT and 450kW wind tunnels.

Integral turbulence length scales associated with the typical size of the most energetic turbulent eddies have been estimated from Kármán turbulence spectra for each of the velocity components. The turbulence length scales L_u, L_v and L_w are found by fitting theoretical models of velocity power spectra developed by Von Kármán (1948) to u, v and w velocity spectra respectively. The least-squares fit of the Kármán spectra to the auto-spectral density estimates of the fluctuating velocity components and the corresponding integral turbulence length scales are shown in figure 2.15 for each wind tunnel. For equations describing the spectral estimates of probe velocity measurements see Chapter 4 section 4.1.2.

Boundary Layer:

Boundary layer profiles measured at test section centres are shown in figure 2.16 for MLWT and 450kW tunnels. The height and shape of the boundary layer is very similar in both wind tunnels. The boundary layer height, which is defined as the distance normal to the floor (or wall) at which the mean velocity reaches $0.99U_\infty$, is 180 mm at the test section centre in both wind tunnels. The displacement thickness, defined in equation 2.6, is 13.3 mm ± 0.5 mm and 14.0 mm ± 0.5 mm for the MLWT and 450kW tunnels respectively. As the majority of the drag and the large separated areas of the wake develop on the upper regions of the body (i.e., areas of the body above 700 mm from the ground plane) the size of the boundary layer is expected to be of little concern.

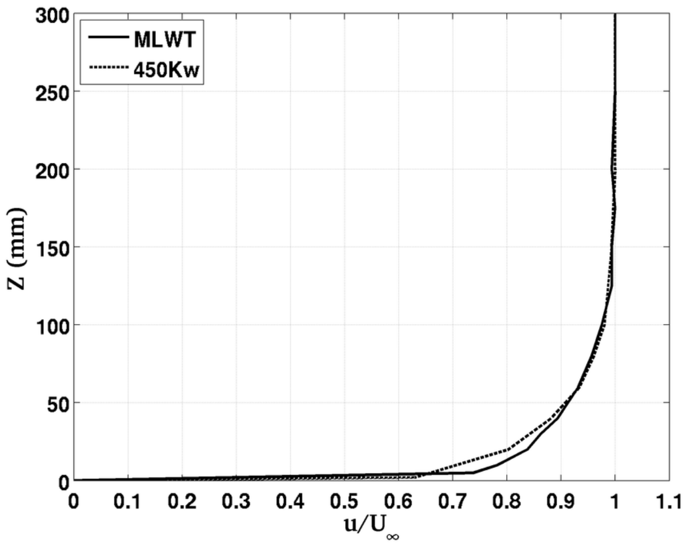

FIGURE 2.16: Boundary layer profiles in the centre of the MLWT and 450kW test sections.

$$\delta^* = \int_0^\infty 1 - \frac{u}{U_\infty} dZ \tag{2.6}$$

Axial Pressure Distribution:

Compared with full closed wind tunnels, open-jet facilities often possess large axial static pressure gradients across the length of the test section. These pressure gradients generate additional forces that are not present for real cycling conditions on the road or track. Forces resulting from static pressure gradients are often referred to as horizontal buoyancy forces and can be significant for long bluff bodies with large vertical surfaces at the frontal and rear ends of the model. Large pressure gradients can also influence the local flow field and the wake flow structure, resulting in non-linear aerodynamic effects which are difficult to take into account.

Figure 2.17 shows the static pressure distribution across the MLWT. The distribution is similar to static pressure distributions found in many other open-jet wind tunnels which have been compared by Wickern & Lindener (2000). As can be seen in the MLWT, the pressure gradient in open-jet tunnels generally falls following the jet exit, is flat over the centre of the test section and increases as the flow decelerates towards the collector. Various methodologies have been developed to correct for the influence static pressure gradients have on force measurements (Glauert 1933; Mercker

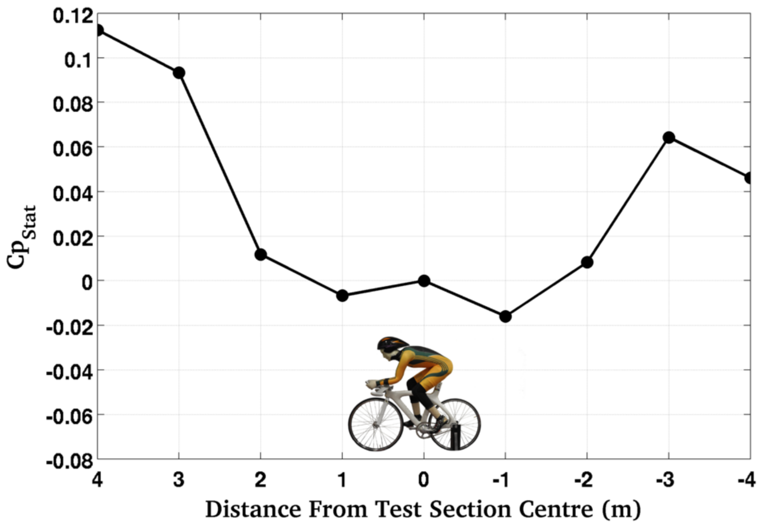

FIGURE 2.17: Axial pressure distribution in the MLWT open-jet test section.

& Wiedemann 1996b; Cooper 1998; Wickern 2001; Mercker *et al.* 2005). The corrections are dependent on the sign and magnitude of the pressure gradient acting over the front and rear halves of the wind tunnel model. Often the adverse pressure gradient due to the collector, that acts over the rear section and in the wake of wind tunnel models dominants and results in artificially low force measurements. As the pressure gradient over the length of the test section occupied by the mannequin in the MLWT is not severe being relatively flat, errors arising due to axial static pressure gradients are negligible and have been ignored. When horizontal buoyancy corrections, outlined by Mercker & Wiedemann (1996b), are applied to mannequin drag measurements, corrections result in a $< 0.5\%$ change in raw force measurements. Large errors arising due to wake distortion effects are also unlikely, as the flat section of the static pressure gradient extends into the wake areas of the test section behind the mannequin.

Open-Jet Wind Tunnel Low Frequency Background Noise:

In addition to static pressure gradients open-jet wind tunnels are also susceptible to low frequency pressure and velocity fluctuations. Separation lines may move in response to such background low frequency noise and change the time-averaged and or unsteady flow field characteristics. Although low frequency background noise is common in open-jet wind tunnels, driving many facilities to consider various active and passive methods

Open-Jet Wind Tunnel	Mode-1 (Hz)
Duct/Tube Response	1.8
Test-Leg Resonance	4.0
Plenum Resonance (lowest)	14.3

Table 2.4: Theoretical first resonant modes associated with the MLWT wind tunnel return circuit, open-jet test section and plenum.

to attenuate these noise sources, the exact fluid mechanisms driving these oscillations is not well understood. Various models have been proposed for predicting the frequency at which different resonant modes may be present in the test section based on the wind tunnel geometry and flow speed (Arnette *et al.* 1999; Gerhand *et al.* 2000; Rennie *et al.* 2004; Duell *et al.* 2010). For open-jet wind tunnels these models generally involve:

1. a forcing frequency associated with vortex shedding from the nozzle exit (Shear Layer Frequency), which is dependent on the mean freestream speed,
2. and can excite different resonant modes associated with the:
    - Geometry of the plenum which is often compared to a shallow cavity (Plenum Resonance Frequency),
    - Standing waves around the entire wind tunnel circuit (or tube) and in the open-jet test section (Test-Leg Resonance Modes).

Vortices that develop in the jet shear layer have been associated with an edge tone feedback mode mechanism (Duell *et al.* 2010), whereby vortices shed from the nozzle are carried downstream in the jet shear layer, where they impinge on the walls of the collector, which causes a pressure pulse to travel back upstream and trigger periodic vortices been shed from the nozzle.

For the MLWT geometry, table 2.4 shows the first resonant mode associated with the wind tunnel duct, test-leg and plenum sections calculated from equations used by Arnette *et al.* (1999) to predict low frequency pressure fluctuation in automotive open-jet wind tunnels. Table 2.5 shows the first three modes associated with the jet shear layer, for wind tunnel test speeds covering typical cycling velocities, that may excite resonance frequencies associated with the geometry of the MLWT. A summary of equations used to calculate resonant modes in tables 2.4 and 2.5 is given in Appendix E.

Test Speed (m/s)	Mode-1 (Hz)	Mode-2 (Hz)	Mode-3 (Hz)
13	0.5	1.3	2.0
16	0.7	1.6	2.4
19	0.8	1.8	2.9

TABLE 2.5: Theoretical resonance modes associated with vortices shed downstream of the MLWT nozzle in the jet shear layer for different test velocities.

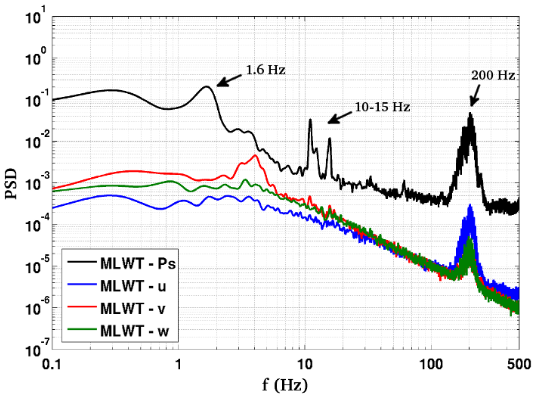

(a) MLWT background noise

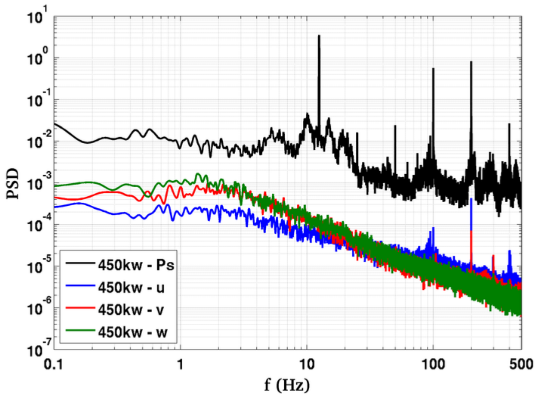

(b) 450kW background noise

FIGURE 2.18: Power spectra of static pressure (P_s) and velocity (u,v,w) fluctuations in the test section centres of the MLWT and 450kW wind tunnels at a test velocity of 16 m/s.

MLWT Low Frequency Pressure Fluctuations:

Low frequency fluctuations have been identified in the centre of the MLWT test section. Figure 2.18(a) shows power spectra of static pressure and the three velocity components from probe measurements recorded at 1000 Hz for 540 seconds at a test speed of 16 m/s in the MLWT. Background velocity and pressure fluctuations are not expected to have greatly influenced time-averaged forces and unsteady pressures measured in the MLWT. Although several peaks in the low frequency background noise spectra are evident, they are not expected to have significantly impacted findings from experiments with the mannequin. The energy content of these fluctuations are of a significantly lower magnitude than dominant pressure and velocity fluctuations measured on the surface and in the wake of the mannequin.

The dominant source of low frequency noise in the MLWT is a result of static pressure fluctuations around the 1.6 Hz peak which is highlighted in figure 2.18(a). Although the source of these pressure fluctuations is unknown it is close to the theoretical MLWT duct frequency (1.8 Hz) which may be excited by higher mode numbers identi-

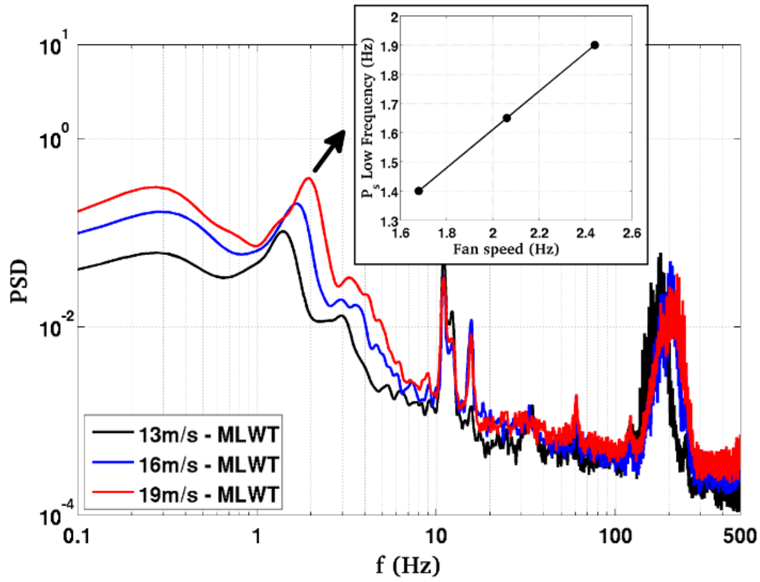

(a) MLWT - P_s background noise

FIGURE 2.19: Power spectra of static pressure (P_s) background noise fluctuations in the test section centre of the MLWT.

fied for the jet shear layer in table 2.5. Other potential sources for these low frequency fluctuations in the MLWT have been discussed by Gilhome (2002), who suggested low frequency noise arising from a possible fan unbalance. Figure 2.19 shows that a linear relationship exists between the rotational rate of the fans and the low frequency peak in static pressure spectra which are both of a similar frequency. As the flow speed also increases linearly with fan speed (in this velocity range) this can also be explained by increase in velocity. As many potential sources and feedback mechanisms may account for this peak in static pressure, additional measurements are required to properly define the exact nature of these low frequency pressure fluctuations.

Additional lower energy peaks in background noise spectra are also found at frequencies around 200 Hz and 10–15 Hz. Unsteadiness associated with these frequencies was not noticeable in time accurate pressure measurements performed in the wake and on the surface of the mannequin. It is expected that the broad peak around 200 Hz, which also has a linear relationship with the fan speed, is related to the fan rotor blades passing stator vanes. Possible noise sources for the peaks found between 10–15 Hz remain unknown.

Static pressure and velocity spectra for the 450kW tunnel are plotted alongside MLWT spectra in figure 2.18(b) for the test speed of 16 m/s. Compared to the MLWT, for frequencies < 10 Hz static pressure spectra measured in the 450kW show a relatively low power flat response. To investigate the influence of low frequency fluctuations, time accurate surface pressure measurements were repeated in the 450kW tunnel which lacks the low frequency background noise sources characteristic of the MLWT. By directly comparing time-averaged and unsteady pressures measured in each wind tunnel the effect of back ground static pressure fluctuations on measurements performed in the MLWT can be assessed. Results presented in Chapter 4 demonstrate that wind tunnel background noise levels are unlikely to have been significantly influenced both the time-averaged and unsteady flow field associated with the mannequin.

2.3 Time-Averaged Force Measurements

Time-averaged aerodynamic forces were measured in the MLWT for 15° increments in leg position around a complete crank cycle. Forces acting on the mannequin and bicycle system were measured using a six-component Kistler force balance of the piezoelectric type. The data acquisition system is a National Instruments PXI based system running on Lab View V8.20 software. The System uses six channels of a SCXI – 1102 card for acquiring force values from the six component Kistlers. Only measurements of the drag component of the aerodynamic force are reported in this study. The accuracy of the data acquisition system is outlined in Appendix D.

Prior to testing the force balance was calibrated over the relevant force range using dead weights of a known mass. The calibration weights were suspended on a right angle moment arm that transferred the load to the force balance in the drag direction. The moment arm had a counter balance that could be adjusted so that there was negligible load on the force balance prior to the application of the calibration weights. The calibration procedure involved applying the calibration weights in 3 *lbs* (1.36 *kg*) increments up to a maximum load of 15 *lbs* (6.81 *kg*) and then reducing the weight back down to zero to test for hysteresis in the system. This process was repeated three times to test the repeatability, sensitivity and linearity of the Kistler system. A typical Kistler calibration, which was performed prior to and after experiments to test for any drift in the calibration of the system, is shown in Appendix C. The error associated with the calibration of the Kistlers is outlined in Appendix D and is dependent on both the data acquisition error and the error induced due to the variability of the force data. The total bias and precision error associated with the Kistler calibration measurements

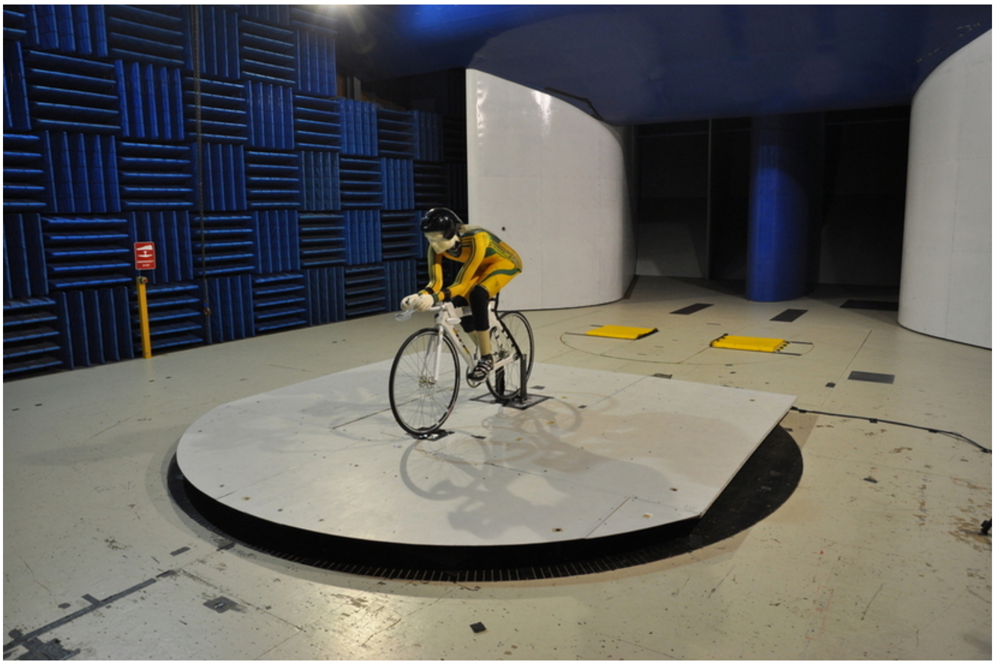

FIGURE 2.20: Mannequin Kistler force balance set-up.

was estimated to be $\pm 0.1\ N$.

Struts attached to either side of the rear axles were used to rigidly fix the mannequin system to the force balance housed underneath the wind tunnel floor. The mannequin was positioned on a raised box with a cantilevered splitter extending over the leading edge of the platform to limit the impact of the raised box and the wind tunnel floor boundary layer on force results as shown in figure 2.20. Force measurements at each crank angle are taken as the mean result of a minimum of three separate tests sampled at 500 Hz for 30 seconds. Measured forces have not been corrected for open-jet wind tunnel blockage effects which are shown to be negligible in section 2.4.4.1. Each test involved recording baseline measurements with no wind before and after force measurements of mannequin leg positions so that any drift in the force measurement system over the duration of a test could be monitored and corrected for. The two main sources of drift are;

1. Leakage of charge inherent in the charge amplifier, which causes the force signal to drift
2. Temperature variations throughout a test.

The maximum variation in each of the force measurements performed for varying leg positions was $< 0.5\%$ of the mean drag for all the leg positions tested. Baseline Kistler force measurements at leg positions that had the highest and lowest drag were repeated throughout each half of the crank cycle to test the repeatability of repositioning the legs. Baseline force measurements for the mannequin in the standard position configuration were also recorded before and after a change of rider upper body position (arm and torso). The combined error of the repeatability of static aerodynamic force measurements and the error associated with the repositioning of the mannequin throughout a particular test period is estimated to be $< 2.5\%$ of the mean drag. The accuracy of individual force measurements and coefficients for mannequin testing is outlined in Appendix D.

2.4 Pressure Measurement Systems

The time-averaged flow topology of the mannequin was primarily developed from pressures measured in the wake and on the surface of the mannequin. This section outlines the systems, accuracy, and the experimental method used in the measurement of wake and surface pressures. Pressures measured in the wake were performed using a four-hole dynamic pressure probe and surface pressures were measured using a Dynamic Pressure Measurement System (DPMS) both from Turbulent Flow Instrumentation Pty. Ltd (TFI). As the DPMS is capable of measuring simultaneously time-accurate surface pressures at multiple locations this allows for the time-dependent nature of flows to be investigated through unsteady surface pressure fluctuations. The pressure measurements not only reveal the dominant wake structures and unsteady flow characteristics, but also how they are affected by changes to rider position (both leg and upper body) and what impact this has on the aerodynamic drag force acting on the mannequin.

2.4.1 Four Hole Cobra Probe

The four-hole dynamic pressure probe, commonly referred to as a Cobra Probe due to its shape, provides high frequency local three component velocity and pressure measurements in real time. There are many variations in the types of these multi-hole pressure probes, which were originally developed by Shepherd (1981) and Hooper & Musgrove (1997). Multi-hole pressure probes have being utilised extensively to investigate many types of different flows, especially turbulent wakes of bluff bodies.

The Cobra Probe used to study the turbulent wake of a cyclist, was ideal for carry-

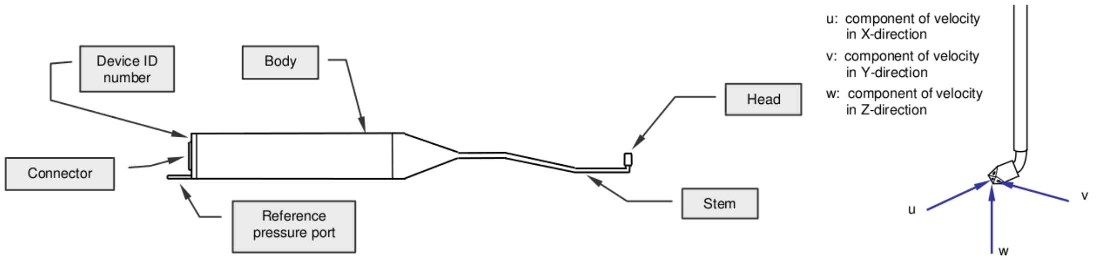

FIGURE 2.21: Four hole dynamic pressure probe main features, from (TFI 2011).

ing out detailed high frequency measurements in the near wake of the mannequin and also for characterising the flow quality in both the MLWT and the 450kW wind tunnels. By using a traversing mechanism to move the probe to multiple measurement locations within a plane, two-dimensional flow maps of the velocity field in the wake were constructed. These measurements were performed at multiple streamwise locations in the wake of the mannequin, revealing the nature of the turbulent wake flow through the identification of large-scale flow structures and the unsteady flow characteristics of the wake.

The Cobra Probe consists of a main steel body that houses four individual pressure transducers that are connected via steel tubing to holes located on each of the four flat faceted surfaces on the probe head. The measured fluctuating pressures acting on each of the surfaces are linearised to correct for amplitude and phase distortions caused by the size and length the tubing that connects these holes to their corresponding pressure transducer. The instantaneous three component velocity vectors and static pressures are determined by relating the pressures on each of the surfaces of the faceted head of probe to these quantities. The probe has a high linear frequency response of up to 2000 Hz allowing for high frequency measurements of fluctuating velocities between 2 m/s and 100 m/s whose direction lies within $\pm 45°$ of the probe axis (acceptance cone). A schematic of the Cobra Probe can be seen in figure 2.21.

The probes come pre-calibrated from TFI who recommend that the probes be re-calibrated on a yearly basis. The calibration procedure that is used to relate the pressure field at the head of the probe to the velocity vector field is described by Shepherd (1981) and Hooper & Musgrove (1997). Measurements are made through the TFI interface using the Device Control Software. The Cobra Probe outputs raw voltage data from each of the pressure transducers that is transferred to the computer using a 225 kHz,$\pm$10 V,

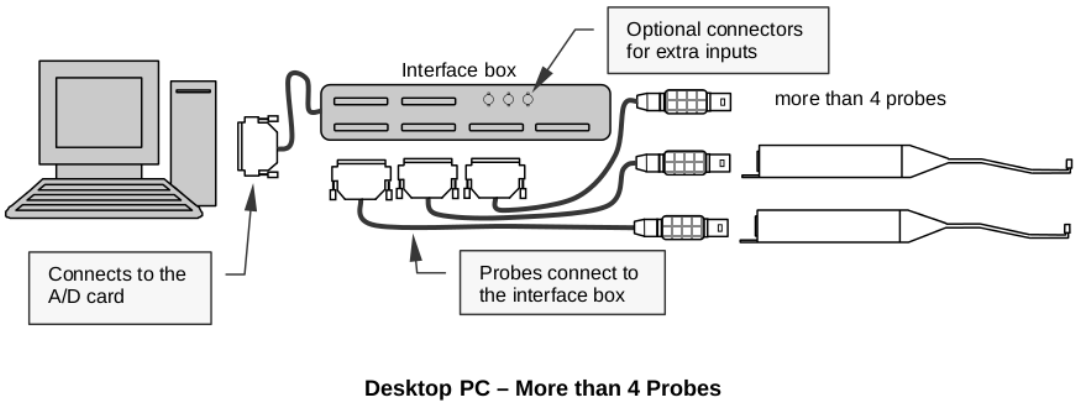

FIGURE 2.22: Cobra Probe and data acquisition system, from (TFI 2011).

12 channel analogue to digital DT9836-12-0 data acquisition system. The raw voltages are then processed into the three component velocity data by the Device Control Software. When a measurement is taken, data is output in the form of a summary file and a binary data time history file. Summary files contain mean data over the length of the sample whereas the time history files contain the complete data set (three velocity components and static pressure) recorded at the sampling rate. These files were post processed in MATLAB R2009a to analyse both the time-averaged and instantaneous data quantities of the mannequin wake. Simultaneous measurements with other systems (i.e., multiple probes, thermocouples, pitot-static tubes, surface pressure measurement systems and other pressure transducer related devices) can also be combined with the Cobra Probe using an interface box between the different measurement systems and the computer. A diagram showing the Cobra Probe system configuration is shown in figure 2.22.

The accuracy of the Cobra Probe depends on a number of factors that need to be considered when taking measurements and interpreting data. The Cobra Probe is limited to velocity measurements above 2 m/s that fall within the $\pm 45°$ acceptance cone. High turbulence levels or flow that is highly yawed or pitched may induce pressures on the faceted head of the probe that lie out of the calibration surface limits. This limitation of the Cobra Probe also means it can't perform measurements within flow reversal regions of the wake. The number of measurements that fell outside the limits of the probe was monitored carefully when investigating the wake of the mannequin. Regions of high turbulence intensity, yawed and pitched flow outside the probes mea-

Flow Quantity	Error
Velocities (U, V, W)	$\pm 1\%$ of total velocity
Yaw and Pitch angles	$\pm 0.5°$
Static Pressure	$\pm 1\%$ of dynamic head
Turbulence Intensity	$\pm 5\%$ of total turbulence level

Table 2.6: Estimated errors of Cobra Probe stated by manufacturer TFI Pty. Ltd

suring capabilities were constrained to relatively small areas of the wake and only for a small number of leg positions. The estimated error of probe measurements stipulated by the manufacturer is outlined in Table 2.6 for turbulence intensities less than 30%.

There are additional external factors that can provide a potential source of error that are not as easily quantified. These have been outlined by Gilhome (2002) and are summarised below;

1. Inaccuracies in calibration and dynamic response of the Cobra Probe
2. Pressure transducer accuracy
3. Initial alignment of the probe
4. Vibration of the probe
5. Atmospheric temperature and pressure variations throughout samples
6. Electrical noise.

Although it is hard to quantify the effect of these types of errors, wherever possible steps were taken to limit their effect as much as possible. To check the calibration and accuracy of average velocities prior to testing, probe measurements were performed in a clean wind tunnel (without model) and compared with that made by a pitot-static tube. Repeated measurements at selected locations in the wake were also performed throughout the duration of traverses to check the repeatability of measurements. The traversing mechanism was rigidly fixed to the wind tunnel walls and a carbon fibre rod was used to securely hold the probe in the flow to limit the vibration of the probe as much as possible throughout tests. To measure the degree of initial misalignment of the probe with the freestream, probe measurements where performed following a traverse along the centreline of a clean tunnel with and without the probe rotated through 180°. By comparing the yaw and pitch angles of the two centreline measurements the misalignment of the probe can be approximated and used to correct the yaw, pitch and the magnitude of the three velocity components measured during a traverse. A second probe located in the freestream, 3.0 m upstream of the mannequin, was also used as a reference. Reference probe measurements were recorded simultaneously throughout the duration of each traverse measurement and used to normalise any velocity or density variations resulting from changes in temperature and atmospheric pressure, over the duration of a traverse. The wind tunnel temperature and the atmospheric pressure were also measured throughout traverse measurements.

2.4.2 Traversing System & Flow Mapping

A two axis traverse enabled detailed flow mapping in planes both perpendicular to and in line with the mean freestream flow. Traverses were performed for multiple leg positions to show how flow structures evolve in the wake and how they influence the aerodynamic drag as the legs move around the crank. Measurements were also taken at traverse planes at multiple locations both over the body and in the near wake of the mannequin to show the spatial evolution of the time-averaged wake flow structure. Flow maps generated using this technique also served to validate numerical simulations of the flow over the mannequin, which were run in parallel with these experiments.

Figure 2.23 shows a diagram of the experimental set up and the traversing system used to map the wake flow behind the mannequin in the 450kW wind tunnel. Traverses were also performed in the MLWT to serve as a method of comparing flow maps with those obtained in the 450kW wind tunnel to ensure the same flow structures were being observed in the two wind tunnels. The vertical axis of the traverse is rigidly fixed to the roof and floor of the wind tunnel with the horizontal axis mounted to the vertical traverse so that the whole axis can be moved in the vertical direction. The vertical and horizontal axes of the traverse have a travel range of 1.65 m and 1.10 m respectively. A carbon fibre Cobra Probe holder extends out from the horizontal traverse into the flow that can be moved along the horizontal axis. Previous measurements using this arrangement have shown that the head of the Cobra Probe should be at least 600 mm (4 times the maximum thickness of the larger vertical traverse) in front of the horizontal traverse to avoid interference effects caused by the traverse. For all experiments the minimum distance between the probe head and the traverse was extended to 700 mm.

The traverse is controlled using the same TFI Pty. Ltd Device Control Software

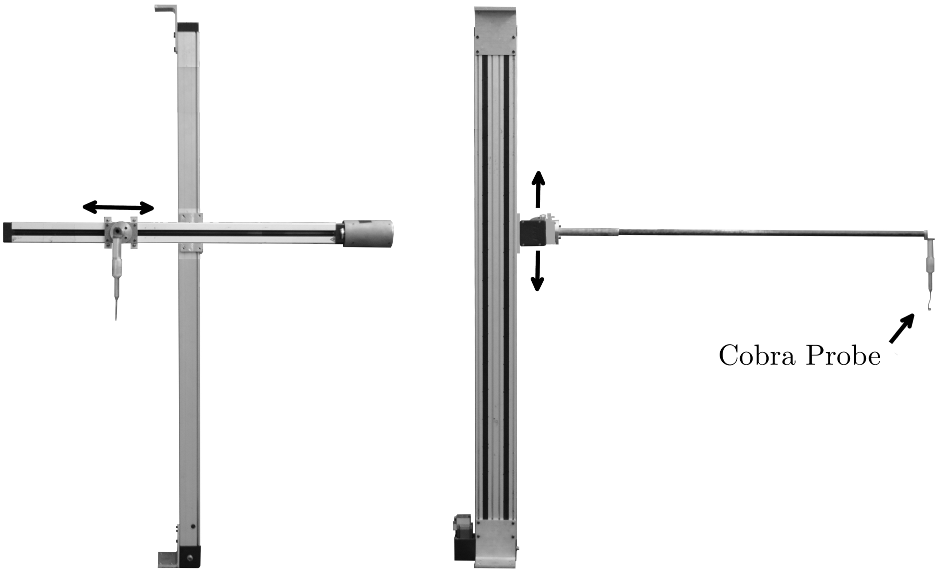

FIGURE 2.23: Two axis traverse mechanism for mapping the wake flow of the cycling mannequin.

used to record Cobra Probe measurements. Flow maps are created in the software that contain an array of (x,y) measurement locations within the traverse plane. The Cobra Probe is systematically driven and held stationary at each measurement location in the traversing plane for the duration of the sample. A typical traverse involves the following steps;

1. Zero Cobra Probe(s) (Record baseline probe measurement to serve as reference for when wind is turned on)

2. Ramp up wind tunnel and wait for flow to stabilise at the desired flow speed

3. Run flow mapping in the Device Control Software

4. Ramp down wind tunnel

5. Repeat process until traversing plane is complete.

The wake surveys were broken down into two main separate experiments to investigate specific aspects of the flow and the effect changes made to the positioning of the legs had on wake flow structures. The first consisted of traverses performed in a plane normal to the mean flow, one torso length (640 mm) behind the base of the mannequin (P–5) for static leg positions that were moved in 15° increments around a complete

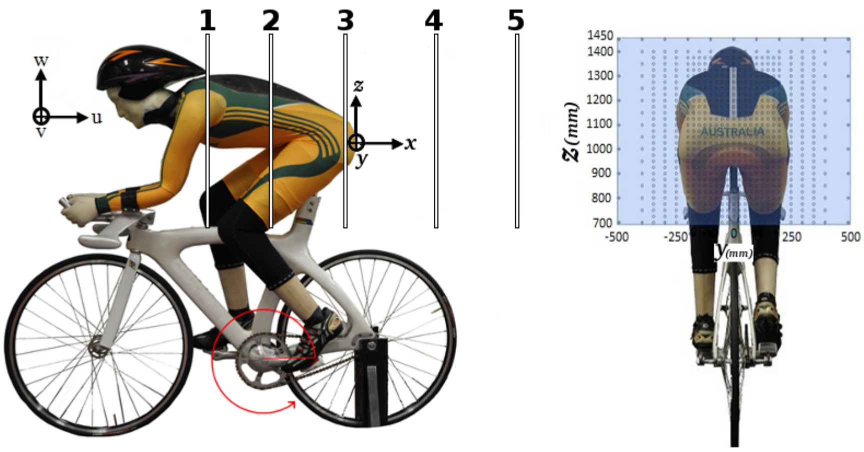

FIGURE 2.24: Cobra Probe wake survey locations and traversing area.

crank cycle. The second involved a series of traverses performed at different streamwise locations over the body of the mannequin and into the near wake for critical leg positions. By performing traverse planes for varying leg positions at multiple streamwise locations, changes how the flow evolves over the body and into the near wake can be identified. Figure 2.24 shows the measurement area and location of traverses completed in planes normal to the mean flow direction.

The wake surveys are constrained to a partial section of the wake capturing the flow over the upper body of the mannequin in a 1.0×0.75 m plane centred about the central plane of the mannequin, 0.7 m above the wind tunnel floor. The probe was traversed to capture the entire wake of the upper body with traverse measurements extending into the flow field that exhibited the same turbulence intensity as the freestream. There were two main reasons for investigating this particular section of the wake. The first was that it had previously been shown in the initial athlete investigations by Crouch *et al.* (2010) that the upper body of the cyclist was of particular importance due to the large effect that variations in back shape has on aerodynamic drag. The second being that this study is also a part of a wider investigation into cycling aerodynamics with the Australian Institute of Sport and Melbourne University (supported under Australian Research Council's Linkage Projects funding scheme project number LP100200090), where the aerodynamics of the lower body and legs are being investigated by Melbourne University. Due to the time consuming process of obtaining traverse measurements, the decision to constrain the traversing area to the upper body also meant that the quantity of measurements, in regions of the wake that have the largest impact on aerodynamic drag, could effectively be increased, providing much more detail of the structure of the wake in the most important areas.

The wake surveys consist of probe measurements sampled at 1250 Hz for 15 seconds (18,750 samples) at each measurement location in the traversing plane. Each traverse plane took approximately 6 hrs to complete. The sampling time was carefully considered with the total number of individual measurement locations required to properly resolve the key features of the wake. The final sample length selected was long enough to accurately define the mean flow quantities. This was checked against measurements made at similar locations in the turbulent wake for progressively increased sample durations.

The spatial resolution of measurements made in the traversing plane depended on the streamwise location of the traverse. For measurements made in the near wake of the mannequin the density of probe measurements was increased in areas of the wake that exhibited large velocity gradients. These areas were progressively refined throughout the traverse and were largely constrained to regions of the wake directly behind the mannequin. The final vertical and horizontal grid spacing between measurement points in this section of the wake was 25 mm and 20 mm respectively.

Despite the reduced total area traversed when performing measurements around the body of the mannequin, more grid points were required to resolve the areas of the flow close to the surfaces of the mannequin. These regions exhibited large velocity gradients and required a greater number of total measurements to properly define the formation regions of flow structures developing over the back. In these areas close to the surface the maximum vertical and horizontal grid spacing between measurement points was 10 mm and 20 mm respectively with measurements being refined to 5 mm from to the surface in the vertical direction for the first 20 mm away from the surface. A breakdown of the total number of Cobra Probe measurements made in each of the traverses completed is shown in table 2.7.

2.4.3 Dynamic Pressure Measurement System

The pressures acting on the body of a cyclist are of particular importance as it is the pressure drag component that contributes the greatest to the total aerodynamic resistance and indeed to the total resistance experienced by cyclists. The surface pressure distribution acting on a bluff body can reveal information about which parts of the body

Plane #	Location	# of points	Mean cm^2/point	Leg Positions
1	-3/4 c	1064	3.5	15°, 75°
2	-1/2 c	1125	3.8	15°, 75°
3	-1/16 c	1354	3.6	15°, 75°
4	1/2 c	924	8.1	15°, 75°
5	c	888	8.4	0°:15°:360°

Table 2.7: Breakdown of mannequin traverses performed in 450kW wind tunnel

Module	A-1335	B-1336
Type	Differential	Differential
No. Channels	64	64
Pressure Range	±3 kpa	±7 kpa
Accuracy	0.1% F.S.O	0.1% F.S.O

Table 2.8: Properties of DPMS modules

contribute the greatest to the aerodynamic drag and the nature of the flow close to the surface. Time-accurate surface pressures can lead to a more complete understanding of the time-averaged and unsteady nature of the near wake flow. By investigating the pressure footprints of flow structures, as they are formed and develop over the body, surface pressures can be associated with flow structures identified in the near wake leading to a better understanding of their formation and development and how they affect the pressure drag.

A multi-channel Dynamic Pressure Measurement System (DPMS) by TFI Pty. Ltd was used to investigate fluctuating and time-averaged surface pressures acting on the mannequin's back where dominant flow structures (identified in the near wake surveys) originate. Two rack mounted pressure modules were used in parallel to measure fluctuating pressures at 128 measurement locations simultaneously. Figure 2.25 shows a picture of the two pressure modules with tubing connected to measure fluctuating surface pressures on the mannequin in the MLWT. A summary of the specifications for the two pressure modules are outlined in table 2.8.

The DPMS comes pre-calibrated, however it was checked prior to performing experiments using a peristaltic pump to apply a known reference pressure across a Betz reference manometer and the channels of the DPMS. A typical calibration check of both DPMS modules can be found in Appendix C. The DPMS operates in much the same way as the Cobra Probes through TFI's Device Control Software. Measured fluctuating pressures from each channel were corrected in the software for amplitude and

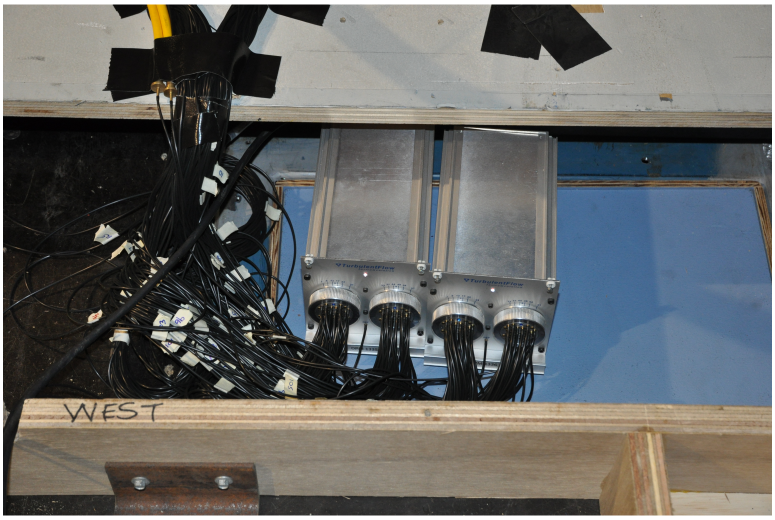

Figure 2.25: Pressure modules used to measure fluctuating surface pressures on the back of the mannequin.

phase distortion effects caused by the network of tubing that connects the surface of the model to the pressure transducers. The corrected pressures can by viewed in real time as contours in the software, which can also be used to check that each channel is operating correctly throughout measurements. The method used to correct the fluctuating component of the pressure signals (mean pressures are unaffected) is as follows;

1. Obtain the Fourier transform of the measured signal at each transducer

2. Signal, now in frequency domain, is divided by a complex transfer function that accounts for dynamic pressure amplitude and phase delay (property of tubing and transducer type)

3. Signal is transformed back into the time domain via an inverse Fourier transform.

The tubing transfer function was found in this investigation using a theoretical technique to model the response characteristics of the tubing system. This technique has been used extensively in a wide range of pressure measurements of bluff bodies and has been validated and compared with experimentally obtained transfer functions by Irwin *et al.* (1979) and Holmes & Lewis (1987). As all PVC tubes connecting the pressure modules to the pressure taps were of the same length a single tubing transfer function was applied to correct all channels used to measure surface pressures. For the tubing, which consisted of 1.2 mm internal diameter and 2500 mm length PVC tubes,

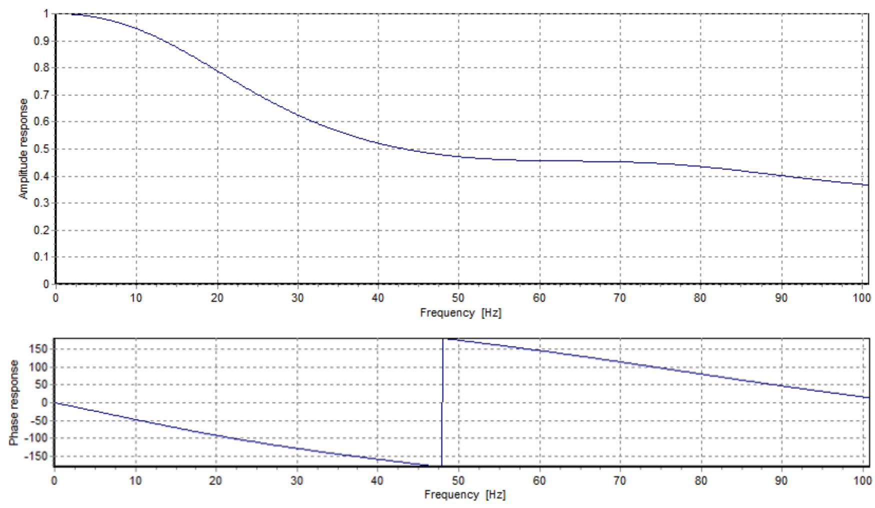

FIGURE 2.26: Theoretical tubing frequency response used to measure time-accurate surface pressures.

the calculated transfer function of the amplitude and phase responses output by the TFI software are shown in figure 2.26.

2.4.4 MLWT Surface Pressure Measurements

Surface pressure measurements were performed in the MLWT for static leg positions that were incremented every 15° around one complete crank cycle for a range of different forearm spacing and torso angle-of-attack positions as well as Reynolds numbers. Pressure taps were applied to the rigid fibreglass shell back section (as described in section 2.1.1). To address the potential impact of changes to the surface roughness of the mannequin's back on surface pressures, a number of comparative studies with and without of the fibreglass torso addition were performed. Smoke and surface flow visualisations using wool-tufts and oil (presented in Chapter 3) showed no significant difference in smoke patterns and flow separation lines/locations between the two configurations. Force measurements for leg positions around the crank cycle were also compared between the two set-ups, which is shown in figure 2.27. Despite a consistent offset of ≈ 23 counts (1 count $= 0.001\ m^2$ of $C_D A$) throughout the crank cycle between the two set-ups (fibreglass torso higher), force measurements agreed very well, with the same variation in drag observed throughout the crank cycle for both configurations. It is thought that the higher drag measurements with the fibreglass torso set up is primarily a result of the slight increase in size of the torso (due the addition of the 4–5 mm thick skin) and the pressure tap tubing that was exposed to the flow during force measurements with the fibreglass torso set-up.

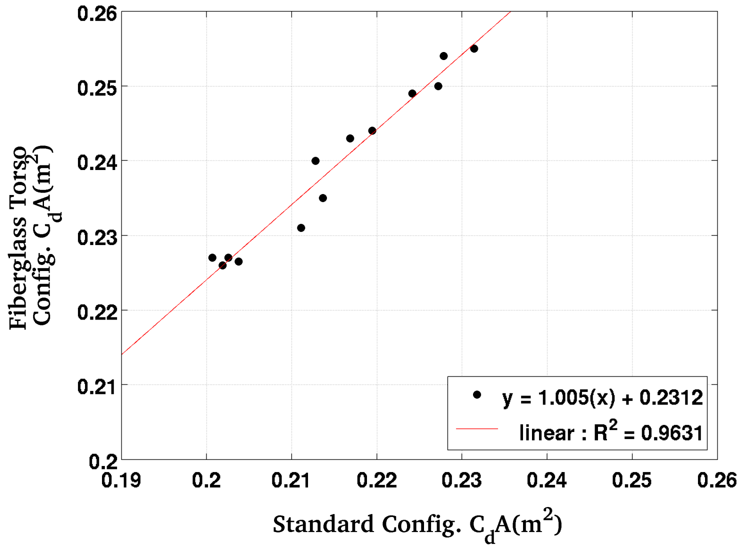

FIGURE 2.27: Comparison of force measurements between standard mannequin configuration and the addition of the fibreglass torso.

A network of tubing connects the pressure taps on the surface of the mannequin to the DPMS housed under the wind tunnel floor. Tubing runs through the hollow fibreglass torso shell out behind the seat-post along the seat stays to the rear axle and down the rear support struts to the DPMS, which is pictured in figure 2.28. Prior to connecting the tubing to the DPMS all tubes were checked for blockages or restrictions by clearing the lines with compressed nitrogen. Initially it was planned that all tubing and the DPMS modules would be fully contained within the hollow fibreglass torso. However due to the size and volume of the pressure modules and tubes this was not possible. Care was taken to ensure that the length of tubing exposed to the flow was positioned in the wake of bicycle components to minimise their impact on the flow. It is expected that the interference of the tubing, which is largely constrained to the lower wake regions, will have limited impact on the upper body surface pressure measurements.

Figure 2.29 shows the 125 tap locations on the mannequin's back where fluctuating surface pressures were measured for a range of different leg and cycling positions. For each leg position tested surface pressure measurements consist of three separate tests sampled at a rate of 1,500 Hz, each for 60 seconds (270,0000 samples in total for each leg position). Pressure taps are located on the left half of the mannequin's back along lines

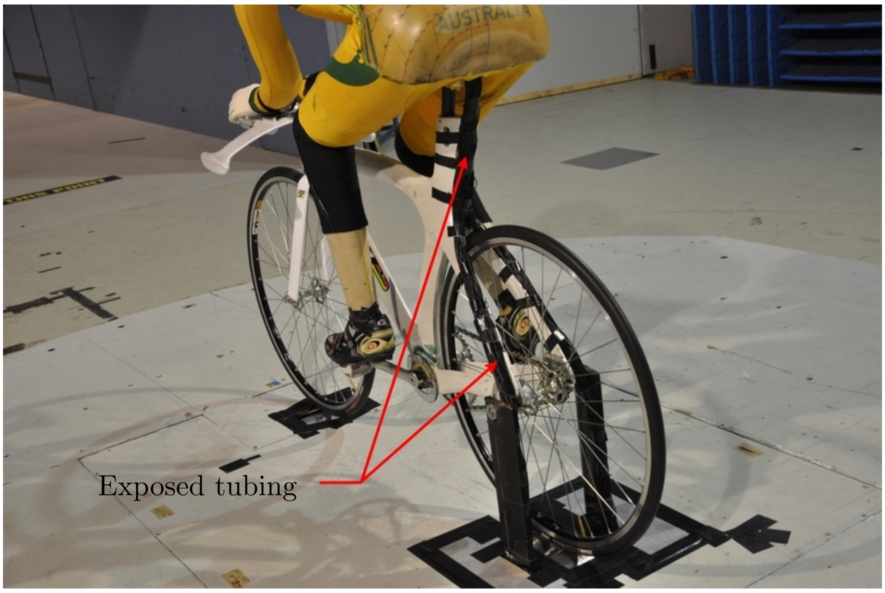

FIGURE 2.28: Exposed pressure tap tubing during surface pressure and force measurements with fibreglass torso.

projected on the surface (projection lines 1–14) that are perpendicular to the chord of the torso. Assuming the pressure distribution is symmetrical across the centreline for opposite leg positions the effective number of pressure tap locations can be doubled by tapping only one half of the model and repeating surface pressure measurements for opposite leg positions (i.e., 15 increments for a full revolution of the crank). This assumption was checked by comparing surface pressures of symmetry taps located at the mid torso and hips on the right side of the body, which are marked in green in figure 2.29. Surface pressures measured on the left-hand side of the body agree well with their symmetry tap counterpart on the right-hand side of the body, which are compared directly in figure 2.30 for surface pressure measurements performed around a full crank cycle.

The location of pressure taps is described by the projection line along the cord they lie on and how far along the line they are placed from the centreline. Projection lines (14 in total) are evenly spaced on the surface at 50 mm intervals and begin at the tip of the trailing edge of the helmet, finishing at the base of the lower back. By evenly distributing taps along these lines, at 40 mm intervals, a gridded arrangement of taps was generated on the three-dimensional curved surface of the mannequin's back, with only two coordinates being required to define the location of each tap on the surface. The optimal number of taps and their distribution along each projection line was found

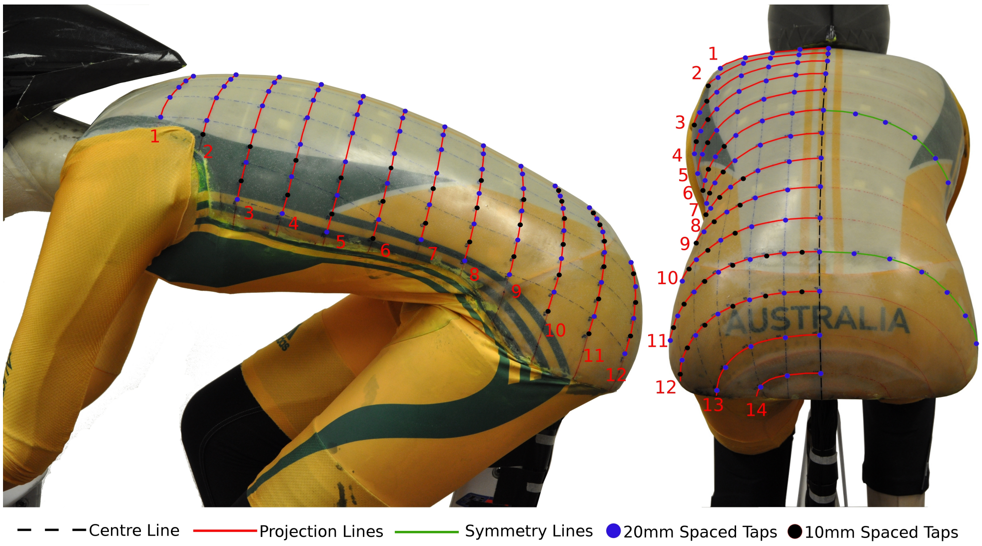

FIGURE 2.29: Pressure tap locations.

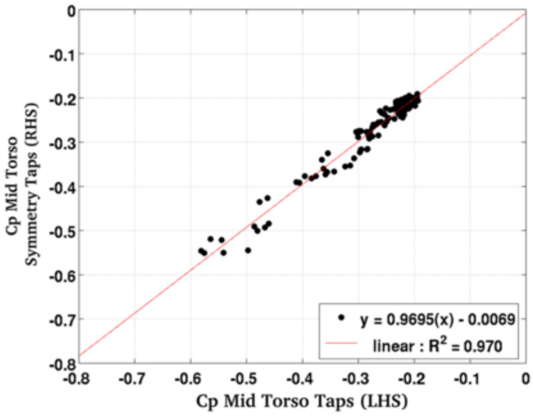

(a)

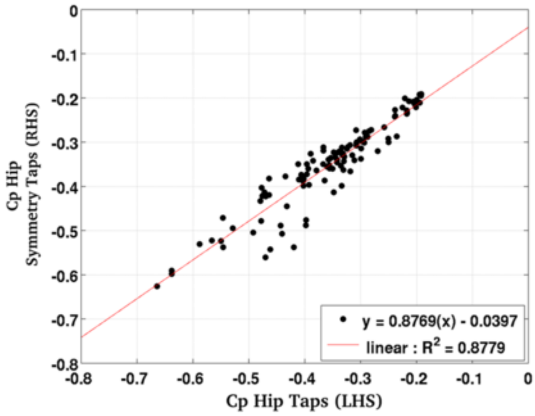

(b)

FIGURE 2.30: Comparison of surface pressures with symmetry taps located at the (a) Mid torso and (b) Hips.

by redistributing taps to areas where large pressure gradients existed. In these regions marked by the black circle taps in figure 2.29 the standard 40 mm spacing was halved to 20 mm between each tap.

As the DPMS measures differential pressures rather than absolute, an appropriate baseline pressure was required as a reference. Each channel was referenced to the pressure inside the plenum of the MLWT. The plenum pressure provides a relatively constant baseline to which surface pressure fluctuations can be referenced. This was checked by comparing the fluctuating pressures in the plenum with the wind tunnel at

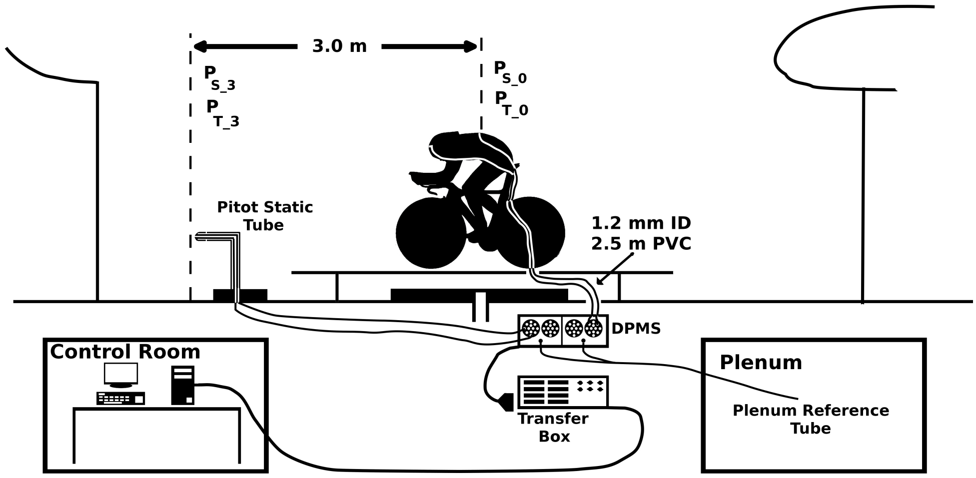

FIGURE 2.31: MLWT surface pressure measurement system experimental set-up.

speed, with those of the control room and under the wind tunnel floor.

Although pressures at the time of measurements were referenced to the pressure in the plenum all reported pressures however are given as surface pressure coefficients, shown in equation 2.7, that are referenced to the static pressure of the freestream at the test section centre '$P_{s,0}$', where '$P_{Tap\#}$' is the pressure acting at each pressure tap location, 'ρ' is the air density and 'U_∞' is the freestream velocity.

$$Cp = \frac{\mathrm{P}_{Tap\#} - \mathrm{P}_{s,0}}{\frac{1}{2}\rho \mathrm{U}_\infty^2} \tag{2.7}$$

Reference static '$P_{s,3}$ and total pressures '$P_{t,3}$' were measured by a pitot-static tube placed 3.0 m in front of the test section centre as shown in figure 2.31. As a result of the variation in the static pressure distribution across the test section, typical of open-jet wind tunnels (Mercker & Wiedemann 1996a), pitot-static reference measurements are corrected for their offset. This correction assumes that there is no loss in total pressure between the test centre and the location of the pitot-static tube. To check the validity of this assumption a pressure tap was located at the point at which flow stagnates on the helmet of the mannequin and compared with the total pressure measured simultaneously by the pitot-static tube.

2.4.4.1 Blockage Corrections

Ideally the MLWT would have been used to carry out all experiments due to its larger size and consequently lower blockage ratio. However due to the limited availability of the MLWT and the large amount of time required to complete velocity field measurements the use of the smaller 450kW was necessary. The major difference between the two wind tunnels is the blockage ratio of the mannequin and how open-jet and closed test sections respond to blockage (MLWT: $\approx 4\%$, 450kW: $\approx 10\%$).

High blockage ratios in both open-jet and fully closed wind tunnels have been shown to significantly affect force and pressure coefficients. In fully closed wind tunnels the rigid walls around the model prevent a free lateral displacement of the streamlines by the model and are compressed closer together. As a consequence the model effectively sees an increase in the freestream velocity (Garner *et al.* 1966). This form of blockage is a combination of the volume distribution of the model known as solid blockage and the displacement effect of the wake known simply as wake blockage.

In open-jet wind tunnels errors associated with blockage are generally less than in closed tunnel sections, meaning they can handle higher blockage ratios. Blockage errors in open-jet test sections arise due to an over expansion of the jet around the model due to the curvature of the jet boundary streamline over the test section being increased compared to an infinite flow case. The over expansion effectively results in reduced velocity over the model compared to the upstream reference velocity measurement and hence lower force coefficients and higher base pressure coefficients are measured compared to the infinite flow case. Based on the open-jet wind tunnel correction methodology of Mercker & Wiedemann (1996a); Mercker *et al.* (1997); Cooper (1998), which applies corrections based on the blockage ratio and volume of the model, the proximity of the model to the nozzle exit and collector as well as the static pressure variation in the test section, corrections to force and pressure coefficients measured in the MLWT are $< 0.2\%$. As a result of this it is expected that open-jet wind tunnel interference effects are negligible and are neglected in the MLWT.

For the wake traverses performed in the 450kW wind tunnel however the effect of the blockage ratio on the measured wake velocities and pressures becomes important, especially when wake integral techniques are used to approximate the drag from velocity field data. As a result of the speed up of the flow around the model the velocity deficit in the wake and the static pressure coefficient is reduced compared to an infinite flow case. Various closed-jet blockage corrections have been developed but the most widely used corrections for closed wind tunnels is those proposed by Maskell (1963). Maskell (1963) developed a theory for blockage corrections to force and pressure coefficients for bluff bodies where flow separation is the dominant form of drag (pressure drag). This theory is based on a momentum balance in the flow outside the wake and corrections are applied to drag and pressure coefficients in the form of a simple increase in the velocity of the undisturbed freestream upstream of the model. For a first order approximation which assumes '$\frac{A^2}{C^2}$' is small (the ratio of the model area to the wind tunnel test section cross-sectional area squared), the ratio of the corrected freestream dynamic pressure 'q_c' to the measured or uncorrected pressure 'q_u is given in equation 2.8. The correction is solved iteratively and assumes that the measured or uncorrected base pressure 'C_{p_u}' and drag 'C_{D_u}' coefficients are known and that the wall constraints do not affect the location of boundary layer separation/reattachment and the form of the pressure distribution on the body. Experiments performed on flat plates normal to the mean flow have shown that Maskell's corrections hold up to blockages of 15% (Awbi 1974, 1978), which is much higher than the blockage of the mannequin.

$$\frac{q_c}{q_u} = \frac{C_{D_u}}{C_{D_c}} = \frac{1 - C_{p_u}}{1 - C_{p_c}} = 1 - \frac{C_{D_u}}{C_{p_c}}.\frac{A}{C} \tag{2.8}$$

To quantify the effect of the 450kW wind tunnel wall constraint, surface pressure measurements were repeated in the smaller 450kW wind tunnel so that they could be compared with surface pressures measured in the MLWT. Although force measurements have not been performed in the 450kW wind tunnel, assuming that MLWT is relatively unaffected by blockage effects, surface pressures coefficients determined in MLWT can be used as an 'equivalent' corrected pressure coefficient and used to solve for a corrected value of the reference dynamic pressure. Equation 2.9 was applied to all tap locations numbered 1–125 and then averaged for a particular leg position to provide an estimate of the correction. This correction results in an average increase in the measured 450kW reference dynamic pressure of $\approx$ 8.0% for all leg positions around the crank cycle. When the correction is applied to surface pressures measured in the 450kW tunnel the maximum variation in the mean pressure distributions between each wind tunnel is $<$ 4.0%, with the majority of leg positions showing a $<$ 2.5% variation, which can be seen in figure 2.32. Measurements performed in each wind tunnel are highly correlated and no observable differences are found between the pressure distributions showing

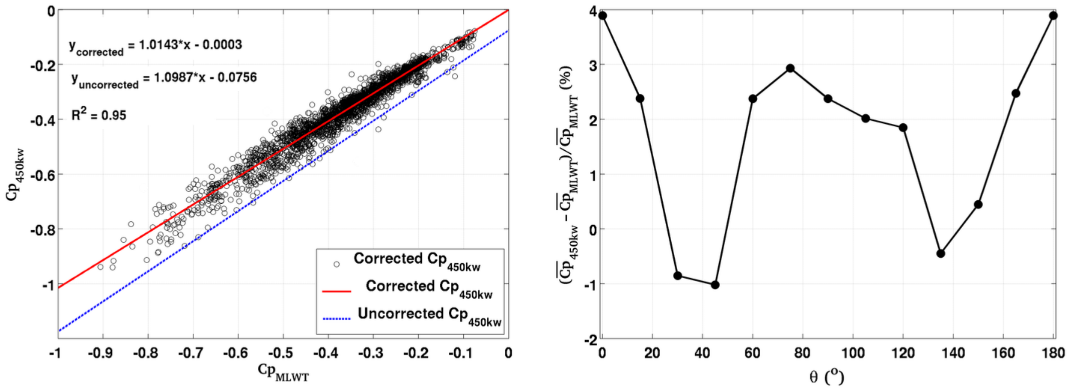

(a) (b)

FIGURE 2.32: (a) Comparison of surface pressure measured around a full crank cycle in the MLWT and 450kW wind tunnels (b) Variation in mean pressure distributions between the two wind tunnels.

that mean separation and reattachment lines were not noticeably affected by the higher blockage ratio. This is also supported by flow visualisations studies performed in each wind tunnel.

$$\frac{q_c}{q_u} = \frac{1 - C_{p(\#)_{450kW}}}{1 - C_{p(\#)_{MLWT}}} \tag{2.9}$$

To check the corrections made to the freestream dynamic pressure using the base pressures, the static pressure distribution on the 450kW wind tunnel walls around the model was also measured simultaneously during pressure measurements. The increase in the dynamic pressure around the model results in a drop in static pressure that is not only experienced by the model but also by the wind tunnel walls that surround the model. Figure 2.33 shows the location of wall static pressures that were measured in the middle of the side and top walls in line with the crank of the mannequin. Pressures measured on the walls were combined to provide a mean drop in static pressure at the wall measurement locations. Assuming losses in total pressure are negligible, the drop in static pressure between the reference pitot-static tube and the wind tunnel walls around the model is equal to the increase in the dynamic pressure correction. When the drop in static pressure at the walls is used to correct the measured dynamic pressure the difference in the correction using the two correction methodologies is $< 2.5\%$.

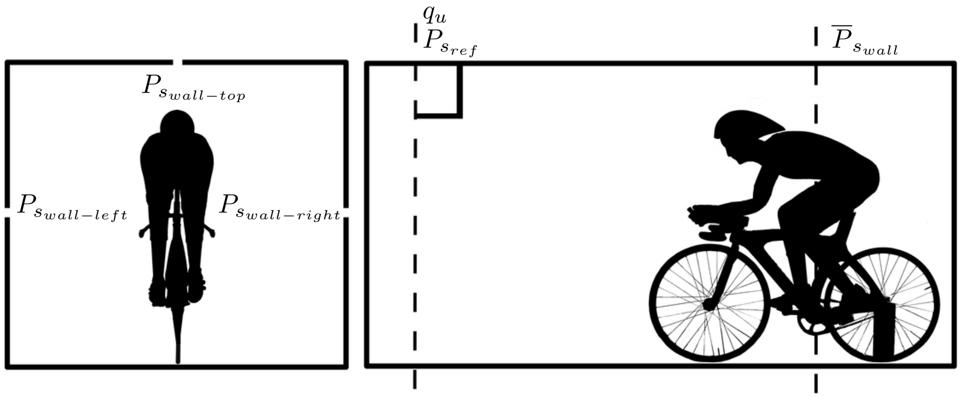

FIGURE 2.33: Schematic of wall static pressure measurement locations.

2.5 Flow Visualisations

To better understanding the types of flows under investigation it is important to try and visualise them. Flow patterns around even simple bodies are often very complicated. Visual representation of such flows can be very helpful in providing a deeper appreciation and understanding of the fluid mechanical processes that govern these flows.

Numerous wind tunnel flow visualisation techniques have been successfully used to provide insight into many complex fluid mechanical problems. In this wind tunnel investigation a range of different techniques were utilised to provide information on the nature of the surface flow topology and near wake flow structure for varying leg positions.

2.5.1 Smoke

The introduction of smoke (which is not restricted to combustible products but also includes vapours, mists, aerosols and other tracer gases) into the flow for purpose of flow visualisation has long been a standard tool in wind tunnel flow visualisation. As described in detail by Maltby (1962) the choice of 'smoke' used should be visible to the naked eye, neutrally buoyant, non-toxic and corrosive as well as being of a small particular size that does not condense out of the air stream upon release into the flow. The smoke released into the air-stream should also not have a sufficient velocity to disturb the flow being visualised.

In this investigation smoke flow visualisations were performed in the MLWT to visualise the flow in the near wake of the mannequin. The smoke was released at several locations around the mannequin to visualise different aspects of the flow over the body for different leg positions. The smoke patterns could be compared with the wake surveys and surface pressure distributions to build a more complete picture of the effect of leg position on the flow topology around the mannequin. Smoke was generated by a smoke machine that uses compressed air to drive mineral oil through a wand that has a heating element in the tip that vaporises the oil upon release into the freestream. The resulting flow patterns from the smoke released around the mannequin were recorded on high resolution photographs and high definition video from a range of different perspectives. Interpretation of smoke flow patterns requires care, especially if the flow is unsteady. Smoke injected at a single point in a steady flow traces the streamlines which are also streaklines and pathlines for a steady flow case. In unsteady flows however streamlines, streaklines and pathlines will not necessarily follow the same path and care must be taken when interpreting smoke trajectories.

The ability to identify coherent flow structures using the smoke flow visualisation technique depends not only on the method of generating and releasing the smoke into the flow but also on the flow quality of the freestream, the geometry and surface finish of the model being tested and the lighting being used to illuminate the smoke particles. For these reasons it is often difficult to obtain clear smoke flow visualisations in wind tunnels, especially for highly turbulent flows where the smoke diffuses rapidly. Extraordinary measures have been undertaken in order to obtain clear images of smoke flow visualisations. Although the quality of the images obtained from releasing smoke around the mannequin will be covered in more detail in the results section, attempts were made to improve the quality of the recorded images by addressing the method for illuminating the smoke particles and the post processing procedure of images. By using a laser sheet to illuminate the smoke in a plane at various locations in the wake and on the body of the mannequin details of the flow that were not observed under normal lighting conditions were revealed. The planes used were as close as possible to those used for Cobra Probe measurements.

2.5.2 Wool-Tufts

Wool-tufting is an inexpensive flow visualisation technique that is easy to set up and perform and can provide useful information about the nature of the flow over the surface of the model. Wool-tufts can be used to show both the time-averaged and time-dependent nature of the flow near the surface. In steady flows short wool-tufts attached to the model provide information about the local flow direction near the surface. In unsteady flows the rapid flapping of the tuft indicates that the flow is separated.

Short wool-tufts placed in a gridded pattern were used to show the near surface flow pattern over the arms, back, hips and upper legs. A short tuft of 0.03 m attached to the surface at one end was determined to be the best length to capture on high definition video without adversely affecting the local flow conditions. Areas of separated flow identified using the tufts could be compared with the surface pressure measurements and the near wake surveys to show where the large separated regions identified in the wake originate from. Wool-tufting also served as a preliminary method for evaluating the symmetry of the model by comparing wool-tuft patterns for opposing leg positions.

Other variations of different sized wool-tufts were also applied to the mannequin to provide additional information about the flow that the smaller wool-tufts failed to capture. Longer tufts of up to 1.5 m were tested to show features of the near wake flow, size of the large separated regions and symmetry of the flow over the mannequin. Long wool-tufts need to be applied and analysed carefully as they are susceptible to misinterpretation due to the additional mass of the tuft and the viscous forces acting along the length of the tuft that can influence its position in the flow.

2.5.3 Surface Oils & Paints

When oils and other viscous fluids are applied to the surface of a model in a flow, the shear stress from the local air flow near the surface causes the oil to flow in patterns that represent lines of surface sheer stress commonly referred to as the skin-friction surface pattern. This technique is particularly useful for revealing complex flow topologies that arise from highly three-dimensional flows. The skin-friction patterns reveal the time-averaged surface flow topology and can be interpreted as separation and attachment lines and other singularities. Critical point theory (as described by Peake & Tobak (1982); Hornung & Perry (1984); Perry & Chong (1987)) provides a framework for identifying these critical points allowing the shear stress patterns on the surface can be related to the time-averaged flow structures that ultimately develop in the near wake flow. Linking the skin-friction patterns to the developing near wake flow is not straight forward, and additional information regarding the overall structure of the near wake flow is often required to interpret the skin-friction patterns correctly. Similar to the other flow visualisation techniques described, when the skin-friction patterns are coupled with surface pressure measurements and velocity field measurements made in the near wake (as they are in this study), it can help to develop a clearer understanding of how the flow develops over the model and what the large-scale flow structures are.

To complement findings found from the near wake velocity field and surface pressure measurements, visualisation of the time-averaged skin-friction patterns were performed on the back surfaces of the mannequin's torso which was identified as being an important area of interest. As the surface oils and paints utilised to reveal the shear stress lines will not flow on the textured fabric of the skin-suit, surface oil flow visualisation was performed with the mannequin fitted with the smooth fibreglass torso prior to its use in the surface pressure measurements.

Although there are many different mixtures and techniques for producing skin-friction patterns which have been well covered by Maltby (1962) one technique that has been used successfully by many different authors is a mixture of kerosene, china clay and fluorescent paint and this was used here. The mixture was sprayed onto the surface using a hand pump spray gun so that an even distribution could be quickly applied. As it begins to flow over the surface as the wind tunnel is turned on, the kerosene evaporates out of the mixture leaving behind a fluorescent chalky residue that remains after the wind tunnel has been turned off. The resulting pattern can then be photographed for analysis. The exact ratio of the kerosene to china clay is found through trial and error. The ability of the mixture to flow on the surface is not only dependent on the type of surface being tested but also the velocity of the freestream and the viscosity of the oil. The viscosity can be fine-tuned by varying the ratio of the constituents in the mixture. Due to variations in the temperature that occur throughout testing, as the tunnel gradually heats up with use, the mixture must be constantly varied to compensate for this temperature variation and its effect on the viscosity of the mixture.

As the torso is a highly three-dimensional attempts were made to limit the effect of gravity on the resulting skin-friction patterns. To minimise this effect, the oil was sprayed on while the tunnel was running at a low speed to reduce the time required to reach the operational test speed where the motion of the fluid was primarily a result of the shear stress and not gravity. Multiple visualisations using oils of slightly different mixing ratios to change the viscosity (which alters the ability of the fluid to flow down surfaces under the influence of gravity) were also compared. Despite attempts to minimise the effect of gravity on the torso skin-friction patterns, care must be taken when analysing these especially in areas where the surface of the torso is highly aligned with the vertical.

2.6 Summary

In this chapter the experimental equipment and method used to investigate the structure of the cyclist wake and how it is influenced by rider position have been outlined. A model of the flow topology of a cyclist will be developed from velocities measured in the wake of mannequin using a pressure probe and from flow visualisations. Dominant flow structures are then related to the drag and pressure forces acting on the mannequin that are measured for a range of different leg and upper body positions. The nature of the unsteady wake is investigated through the analysis of measured fluctuating velocity components in the wake and time-resolved surface pressures that are measured on the back, where the dominant flow structures originate.

The major assumptions, limitations and the accuracy of equipment and measurement techniques associated with wind tunnel experiments of the cycling mannequin have been documented. Although two different wind tunnels have been utilised in this investigation the differences in the flow quality and blockage ratio of the mannequin are not expected to influence major findings relating to the flow topology and the influence of rider position on the aerodynamics of the mannequin. This is further strengthened in the results and discussion section that directly compares results from both wind tunnels and shows that findings are independent of the wind tunnel in which the results were obtained. This repeatability across different facilities builds further confidence in the results.

Chapter 3

Time-Averaged Experimental Results & Discussion

3.1 Development of the Wake Structure and its Effect on the Drag of a Cyclist

In this section, a model for the time-averaged wake structure of the mannequin is developed. The influence of leg position on the dominant flow structures is investigated through a series of wake traverses and flow visualisations. Different states in the wake flow structure are described by multiple flow regimes. These flow regimes are related to the variation in aerodynamic drag and surface pressure distributions that are measured around a complete crank cycle.

3.1.1 Aerodynamic Drag Measurements

The implications that variations in the wake flow topology and structures have on rider aerodynamics begins by considering the influence leg position has on the time-averaged drag force. Figure 3.1(a) shows how the drag force, represented by the drag area, varies as the legs are positioned around the crank cycle. The drag area varies significantly throughout the pedal stroke with a 20% variation in drag over both halves of the crank cycle. Note error bars include the uncertainty associated with repositioning of the mannequin.

The results for the two halves of the crank cycle are in reasonable agreement indicating good model symmetry, with a maximum variation in drag of opposite leg positions of $< 5\%$. Both halves show the drag does not change significantly over the first 15° of rotation, after which it increases rapidly for the next 60°, where it reaches a maximum at the 75° and 255° leg positions. Following the peak in drag in both halves of the crank cycle, the drag decreases at a reduced rate compared to the rate at which it increased. It can be seen that over the range of crank angles where the drag reduces, a more rapid reduction in drag occurs during the second half of the crank cycle. Traverse results and surface pressure measurements completed around a complete crank cycle, suggest that this difference can be attributed to small asymmetries in the geometry and positioning of the mannequin. These minor differences between opposite leg positions do not compromise the overall conclusions drawn and one half of the crank cycle is representative of the data trend throughout the complete crank cycle. Dominant flow mechanisms affecting the drag are also shown to be consistent in both halves of the crank cycle in all experiments performed with the mannequin.

The change in the drag area with crank angle can be explained by a variation in the frontal area, a change in the drag coefficient or a combination of both. In an initial attempt to explain the change in drag throughout the crank cycle the combined frontal area of the bicycle and mannequin system 'A' was determined for each leg position and is compared with the drag in figure 3.1(a). The projected frontal area was determined from photographs taken from 10 m in front of the mannequin, with a reference area held at the midpoint of the crank. The frontal area was then determined by counting pixels that lay within the boundaries of the bicycle and mannequin. The small change in frontal area, which varies $< 2\%$ over the crank cycle, does not account for the large variations in drag, despite the frontal area maxima and minima coinciding with the low and high drag crank positions. Figure 3.1(b) shows that when the variation in frontal area on drag is taken into account and extracted out of the drag area values, the drag coefficient is primarily responsible for the variations in drag. Trends in the drag coefficient are similar to drag area, which varies up to 15% with leg position. Interestingly figure 3.1(b) also shows that the minimum in the drag coefficient coincides with crank angles when the upper thighs of both legs are closely aligned ($\phi_{Left} = \phi_{Right}$) and the maximum occurs when one of the legs is at its most extended position corresponding to when the hip angle of that leg is at a maximum ($\max(\phi_{Left})$, $\max(\phi_{Right})$).

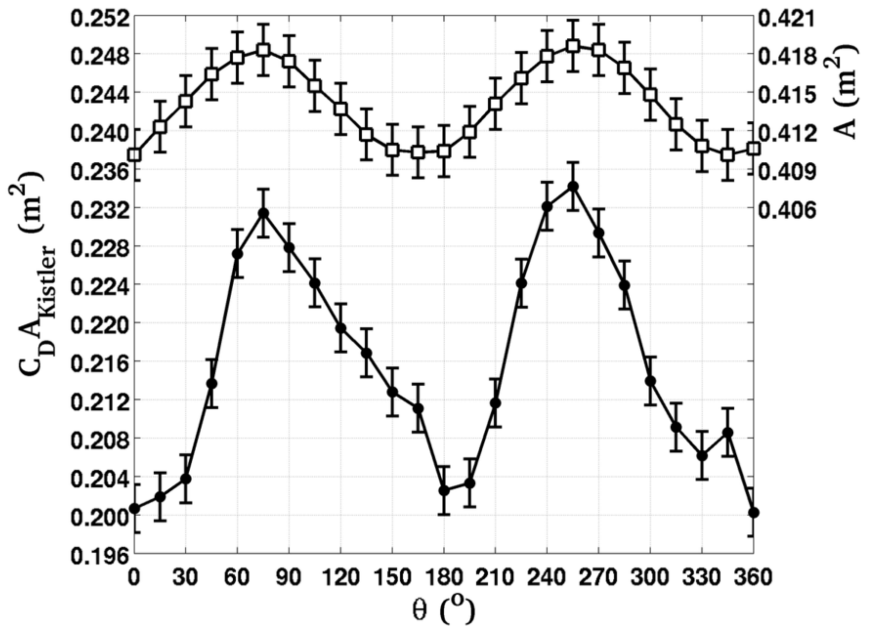

(a)

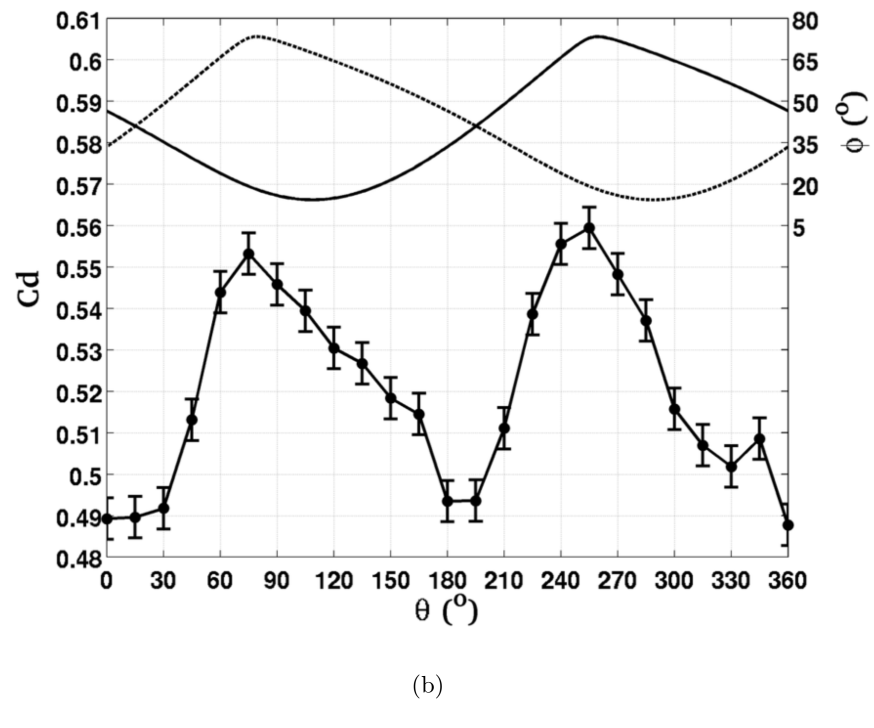

(b)

FIGURE 3.1: Variation in: (a) drag area (–•–left-hand axis) and projected frontal area (–□–right-hand axis); and (b) drag coefficient (–•–left-hand axis) and left (–) and right (···) leg hip angles (right-hand axis) with crank angle.

3.1.2 Near Wake Analysis

3.1.2.1 Characterisation of Flow Regimes

The large variation in the drag coefficient suggests that as the legs move around the crank there is a large change in the flow regime around the mannequin. Figure 3.2 and 3.3 show time-averaged contours of the out-of-plane non-dimensional streamwise velocity component and the resultant principal turbulence intensity. The contours produced from wake surveys performed at plane five (a torso chord length behind the mannequin) show large variations in the size and shape of the wake as the crank cycle progresses. It is clear that the effect of leg position on the structure of the wake is not constrained to regions near the legs where movement occurs, but the entirety of the upper wake is affected.

Contours of streamwise velocity and principal turbulence intensity identify two prominent flow regimes in each half of the crank cycle. For the 15° and 195° low drag leg positions, where the upper thighs are aligned ($\phi_{Left} = \phi_{Right}$), the wake is symmetrical about the centre plane of the mannequin. As the legs are moved around each half of the crank cycle the wake progressively undergoes a transition to an asymmetrical flow regime. Once this has occurred the defining features of this regime remain relatively stable and the high drag 75° and 255° leg positions are defined as being representative of the asymmetrical flow regime in each half of the crank cycle.

Compared with the low drag symmetrical flow regime turbulence levels and velocity deficits are much large for asymmetrical flow regime wake. The majority of the variation in the wake between the two flow regimes occurs below the hips. These differences are primarily a result of a variation in the location at which flow separates from the hips and lower back. For the symmetrical flow regime, flow separates evenly across the lower back resulting in the increase in the size of the wake above the hips. The asymmetries in the flow for the high drag flow regime develop due to a variation in the location at which the flow separates from the left and right sides of the hips and lower back. During this regime, flow remains largely attached over the side of the torso and hips where the leg is in a raised position, resulting in relatively high streamwise velocity and low turbulence in the wake downstream of this side of the torso. As the flow separates low on the rear base of the hip of the raised leg, large velocity defects and high turbulence levels are found below the hips. On the opposite side of the body, where the leg is extended, flow separates much earlier and higher on the hip resulting in an increase in the size of the wake above them.

It is also evident that the position of the legs significantly affects the location at which flow separates from other regions of the body. For crank angles 60°–75° and 150°–165° in the first half of the crank cycle, a turbulent low velocity separated region develops near the outer left hip, which is highlighted by the dashed lines in figure 3.2. In the first half of the crank cycle this separated region is initially isolated from the main body of the wake, it then progresses towards the centre plane of the mannequin and joins the main wake body, finally receding out towards the outer left hip. Section 3.1.3 will show that this particular region of the wake is associated with separated flow originating from the lower arm/elbow. This pattern is also observed in the second half of the crank cycle on the opposite side of the body. Here, the wake from the arms/elbow is more pronounced and we can clearly see that the position of the legs has a large impact how the wake that originates from the arms develops over the body and into the wake.

3.1.2.2 Identification of Large-Scale Structures

Contours of the out-of-plane streamwise vorticity component in figure 3.4 show that the time-averaged flow exhibits large-scale streamwise vortices whose formation, strength and interaction depend on leg position. These structures constitute the major separated flow regions in the wake of the mannequin and, as a result, have a large effect on the drag force throughout the pedal stroke. Similar to the characteristic flow regimes previously described, contours of streamwise vorticity exhibit a low vorticity, low drag symmetrical profile and an asymmetrical high drag profile where the large separated regions of the wake are characterised by regions of high streamwise vorticity.

Streamwise vortices in the traverse plane have been identified and are visualised in figure 3.4 using the swirling strength criterion to outline the boundaries of wake vortices. Derived from critical point analysis by Zhou *et al.* (1999) the swirling strength criterion delineates vortex structures based on the imaginary part (λ_{ci}) of the complex eigenpairs of the velocity gradient tensor. Vortex identification schemes based on the velocity gradient tensor have been shown to identify coherent vortex structures within shear flow regions. Structures outlined in the figure were identified as regions of ($\lambda_{c_i}^2$) being above a threshold level that was set as the square of the maximum swirling strength in a wind tunnel without the mannequin in the plane of the traverse. Other vortex identification schemes based on the velocity gradient tensor (see Chakraborty

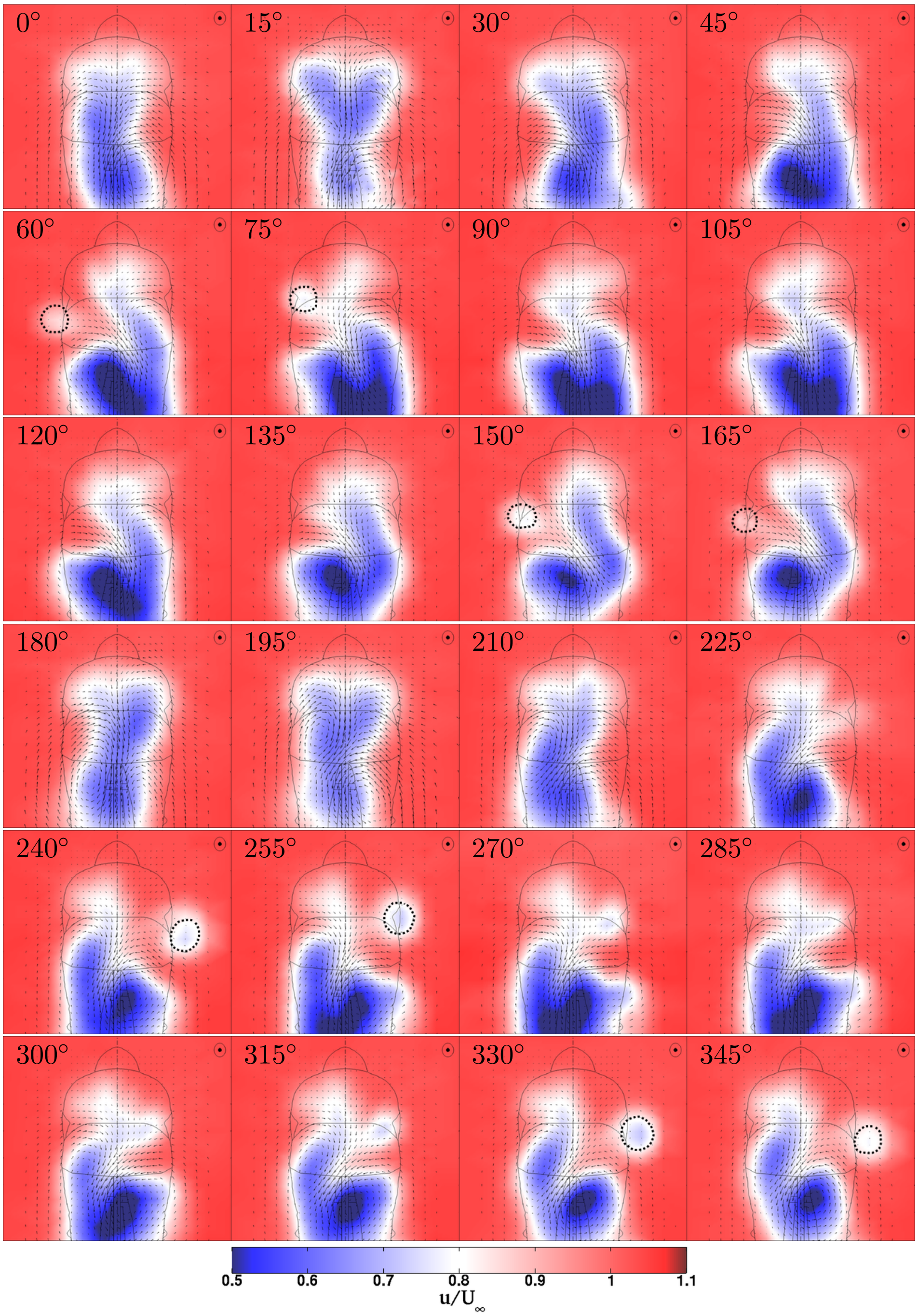

FIGURE 3.2: Contours of the streamwise velocity component with in-plane velocity vectors drawn for varying leg positions.

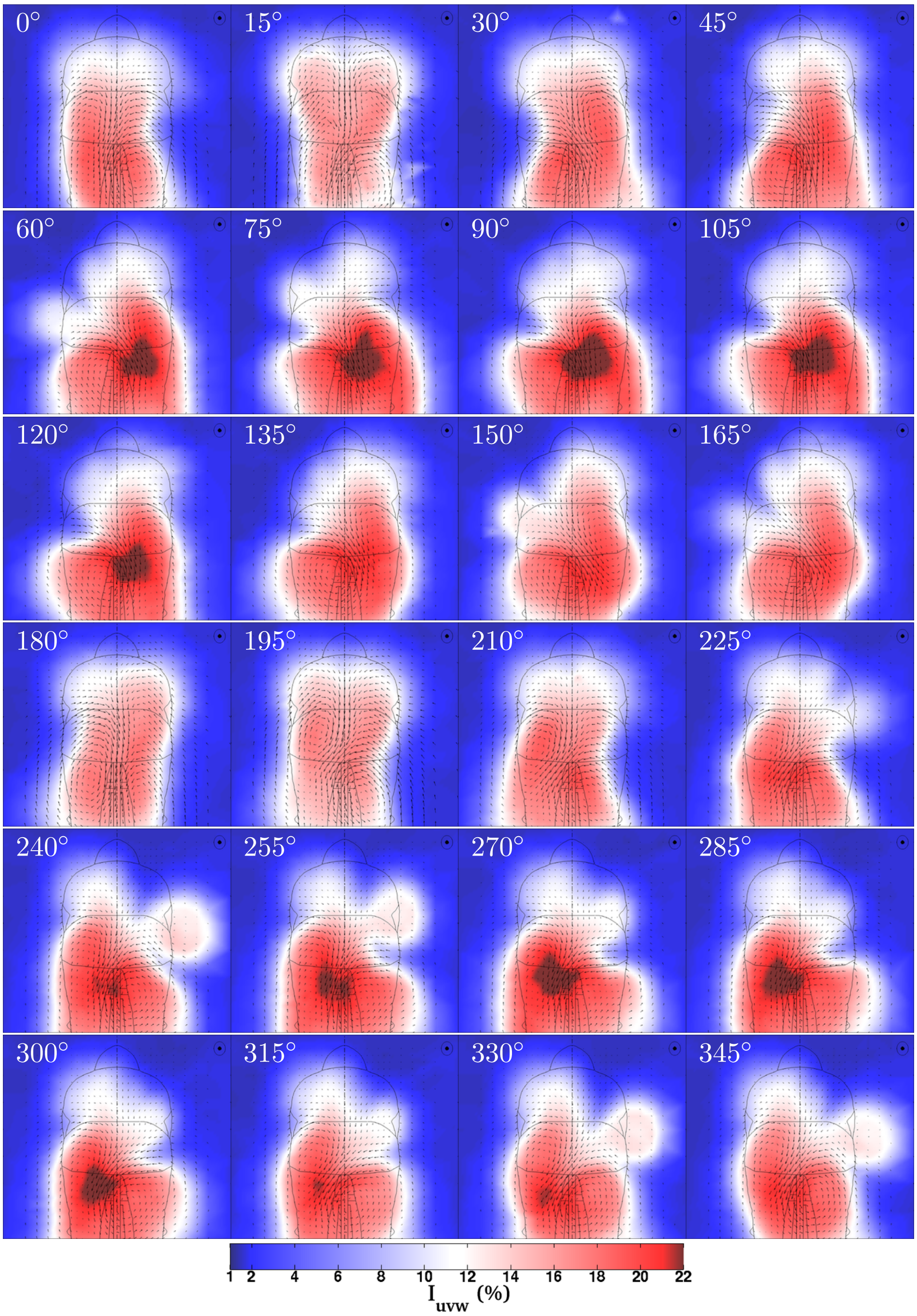

FIGURE 3.3: Contours of principal turbulence intensity with in-plane velocity vectors drawn for varying leg positions.

et al. (2005)) have also been considered and show that the large-scale flow structures are identified irrespective of the vortex identification scheme used.

The swirling strength criterion clearly identifies a large pair of counter-rotating streamwise vortices as the primary feature of the wake flow for the majority of leg positions. For the low drag regime in each half of the crank cycle, large coherent streamwise vortices are not present a torso length behind the mannequin. As the legs move around the crank and the flow transitions to the asymmetrical high drag regime, a large streamwise vortex pair forms. This vortex pair is orientated asymmetrically across the centre plane of the mannequin as a result of the asymmetries in flow separation from left and right sides of the body. A topological analysis of the near body flow presented in section 3.1.3 shows that these vortices result from vorticity that is fed into the wake as vortex sheets that roll up from flow that separates from:

- low on the base of the rear hip that is in a raised position, generating the vortex structure that is positioned lower in the wake (rear hip vortex),
- the upper hip and side of the torso where the leg is in an extended position, generating the vortex that is orientated higher in the wake (upper hip vortex).

To gain a clearer picture of the transition process throughout the full crank cycle, figure 3.5 shows the spatial development of primary vortices in traverse plane five for the different leg positions. This is represented as iso-surfaces drawn from different perspectives of regions of high vorticity within the boundaries of vortex regions identified using the swirling strength criterion. Two-dimensional contours of vorticity for the 75° and 195° positions are also included in the isometric view to highlight where the high drag and low drag leg positions lie within the visualisation of vortex structures. The location of primary streamwise vortices originating from each side of the body alternates between a low position in the wake, when the leg is raised, and a higher position in the wake, when the leg is extended. The lower vortex of the pair is also located closer to the centre plane than the higher of the pair which is positioned further out towards the edge of the hips. This orientation results in the flow being strongly yawed across the hip in the raised position and the downwash generated between the vortex pair being directed across the centre plane of the mannequin.

Another noticeable feature of the wake flow is a smaller streamwise vortex positioned below the outer hip of the raised leg, this can also be seen in figures 3.4 and 3.5. This

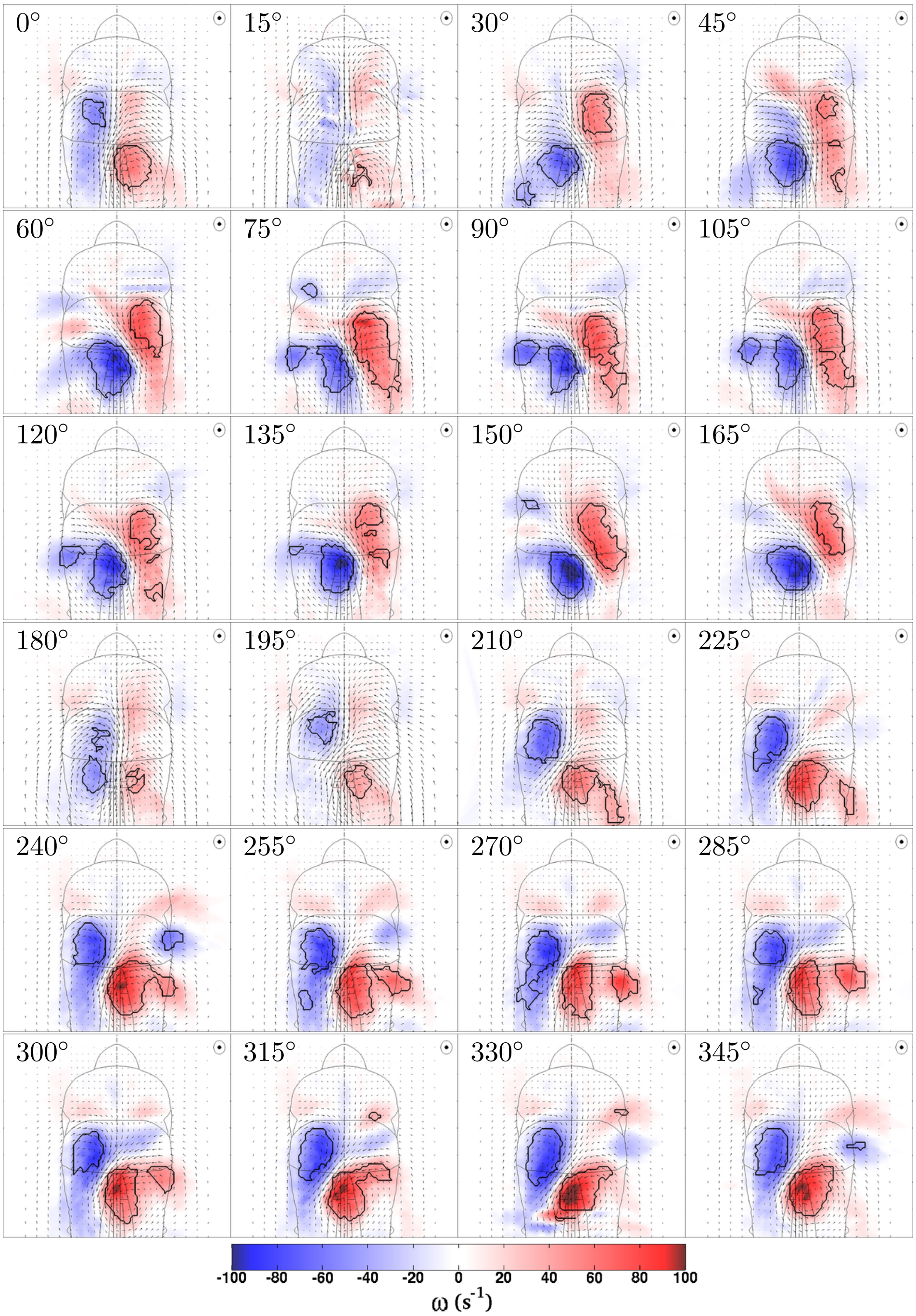

FIGURE 3.4: Contours of streamwise vorticity with vortex boundaries delineated by the swirling strength criterion.

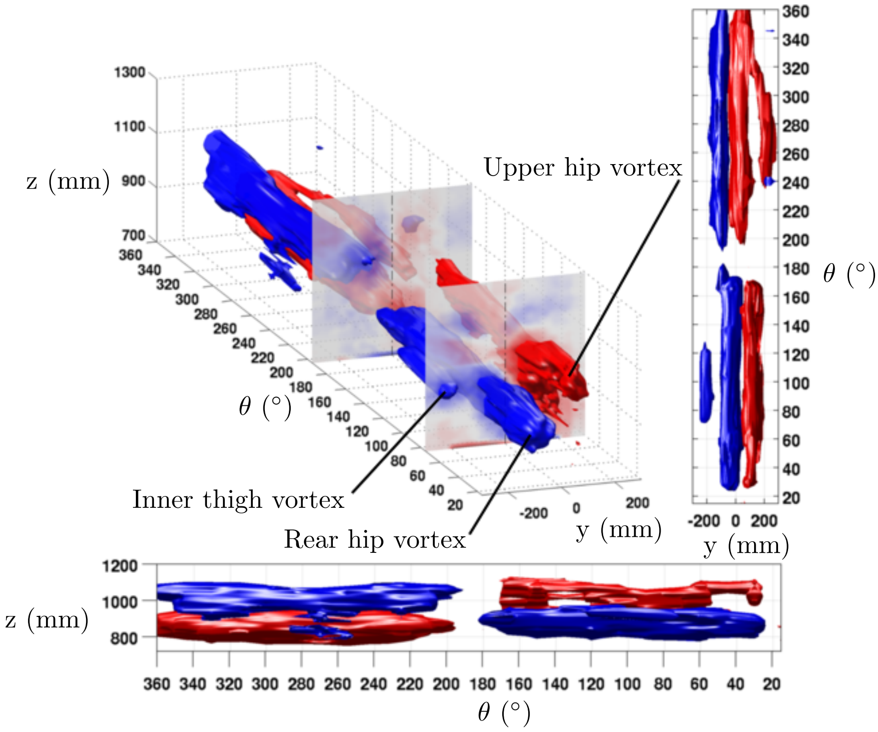

FIGURE 3.5: Primary vortex structures in the wake of the mannequin for varying leg positions. Vortex structures are visualised from different perspectives using surfaces of the swirling strength criterion throughout the crank cycle. Structures are coloured by streamwise vorticity, where blue and red colours represent clockwise and counter-clockwise rotation respectively.

vortex originates when flow separates from the inner thigh of the raised leg. The formation of this vortex is similar to that visualised by Ramberg (1983) for vortices that form at the upstream ends of inclined finite cylinders. Although similarities can be drawn between experiments performed on inclined cylinders, the presence of the torso and the opposite leg in the extended position have a large effect on the formation of streamwise vortices originating from the inner thigh of the raised leg, which is discussed in section 3.1.3.

3.1.2.3 Wake Integral Analysis

By analysing the wake and its constituent vortex structures identified in figure 3.5, the effect of leg position on the strength, merging and drag contribution of vortex structures is determined. The contribution of the drag from primary vortex structures can be estimated by performing a wake integral analysis developed by Maskell (1973) on the traverse planes discussed thus far. This method is an application of the momentum equation applied to a control volume that contains the model and assumes the flow is steady, incompressible, and gravity and turbulence effects are negligible compared to the pressure effect (Rouméas *et al.* 2009). The drag area can be calculated from the detailed wake surveys using equation 3.1 that contains three integral terms that takes into account defects in wake stagnation pressure, streamwise velocity and the drag contribution of the in-plane velocity components (Hucho & Sovran 1993). This method of determining the drag force has been used extensively in road vehicle aerodynamics, in investigations into the wake structures of vehicle geometries and the effectiveness of drag reduction mechanisms (Bearman 1984; Hackett & Sugavanam 1984; Onorato *et al.* 1984; Rouméas *et al.* 2009). The drag area can be approximated by

$$C_D A = \iint_A \frac{\mathrm{P}_{t\infty} - \mathrm{P}_t}{\frac{1}{2}\rho \mathrm{U}_\infty^2} da + \iint_A 1 - \left(\frac{\mathrm{u}}{\mathrm{U}_\infty}\right)^2 da + \iint_A \left(\frac{\mathrm{v}}{\mathrm{U}_\infty}\right)^2 + \left(\frac{\mathrm{w}}{\mathrm{U}_\infty}\right)^2 da. \quad (3.1)$$

Figure 3.6(a) compares the wake integral approach applied to the wake traverses performed a torso chord length in the wake '$C_D A_{Wake}$' with the drag force measured directly using the Kistler force balance '$C_D A_{Kistler}$'. As expected, forces calculated using this method are approximately 25% lower than the measured force results, mainly due to equation 3.1 being applied to only a partial section of the wake. Although absolute values cannot be directly compared, the variation in drag over the crank cycle for both force results is consistent. The minor asymmetries in force measurements across both halves of the crank cycle are also reflected in the wake integral analysis, providing further evidence of consistent results across both of the wind tunnels used in this investigation.

The agreement between the drag results also suggests that the most important features of the wake causing the changes in drag with leg position were captured in the traverse plane. Figure 3.7 shows a three-dimensional drag map of the value of the integrand of equation 3.1 normalised by the maximum value of the integrand throughout the pedal stroke for selected leg positions. For the low drag 15° and 195° leg positions a symmetrical drag profile can be seen. As the legs progress further into each half of the pedal stroke a significant increase in the value of the integrand can be observed in areas of the wake where the primary counter-rotating vortex pair is located. The contribution to the drag from the primary vortex structures '$C_D A_{Vortex}$' is also shown Figure 3.6(a). This has been calculated by applying equation 3.1 to areas of the wake within vortex boundaries identified in figure 3.4. Although the primary vortex structures in the asymmetrical flow regime only account for 20–30% of the total drag approximated by integrating the entire traverse plane, when present in the traverse plane they account for almost all of the variation in drag over the crank cycle. The drag force associated with streamwise vortices increases rapidly from when they first appear in the traverse plane and peaks at the high drag 75° and 255° leg positions. Following this peak, similar to the drag measured with the force balance, their contribution to the drag force decreases.

It is also evident that the wake the develops downstream from the arms contributes to the variation in both the total and the drag associated with primary vortices. For the 150° and the opposite 330° leg positions, a second peak in the vortex drag and a 'kink' in the total drag occurs in each half of the crank cycle. These leg positions correspond with crank angles where the wake immediately downstream of the arms was particularly evident in the flow field at traverse plane 5 (discussed in section 3.1.2.1). In the region of the wake that develops from the arm on the side of the body where the leg is in a raised position there is an increase in the magnitude of the wake integral. This isolated region of the wake can be seen in figure 3.7 on the side of the body where the leg is in a raised position. As shown previously in the contours of the streamwise velocity deficit (figure 3.2) the location and magnitude of this section of the wake is dependent on leg position and is much more pronounced in the second half of the crank cycle. This variation contributes to the minor asymmetries in the drag profile that are observed between each half of the crank cycle. For an animation showing the variation in the drag map for a complete crank cycle please refer to Appendix H.

The large variation in drag that results from streamwise vortices suggests that leg position not only dictates the flow regime but also the relative strength of wake structures. To quantify the effect of leg position on the strength of primary streamwise vortices, their circulation over the course of the pedal stroke has been calculated. Studies into drag reduction mechanisms of simplified vehicle geometries have shown that the streamwise circulation of trailing vortices in the wake are strongly correlated with the magnitude of the overall drag force acting on the body (Bearman & Obasaju 1982; Aider *et al.* 2010). As a result of this, the circulation of vortex structures determined from wake velocity field data has being used to indicate the drag state (low or high drag flow regime) of three-dimensional bluff bodies, such as the Ahmed vehicle. Figure 3.6(b) shows the circulation of streamwise vortices that comprise the main vortex pair and also the smaller inner thigh vortex throughout the crank cycle. The circula-

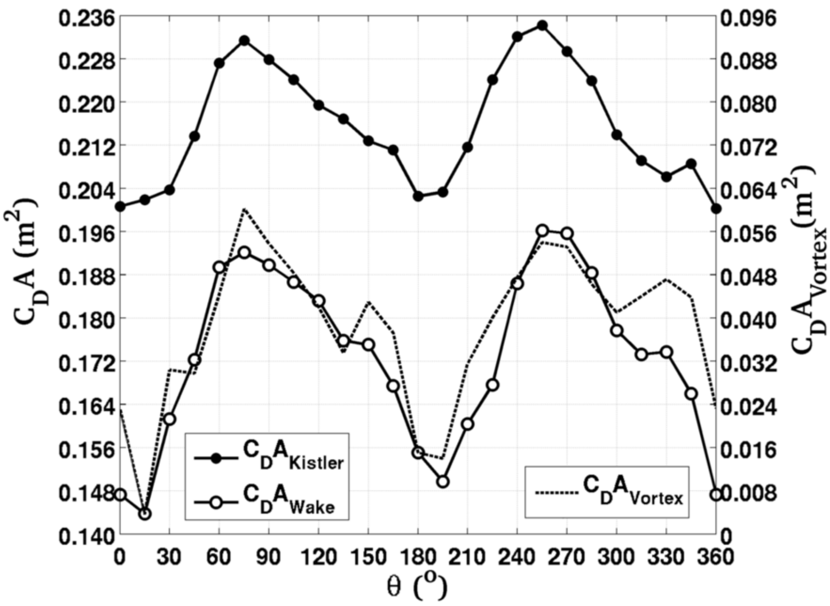

(a)

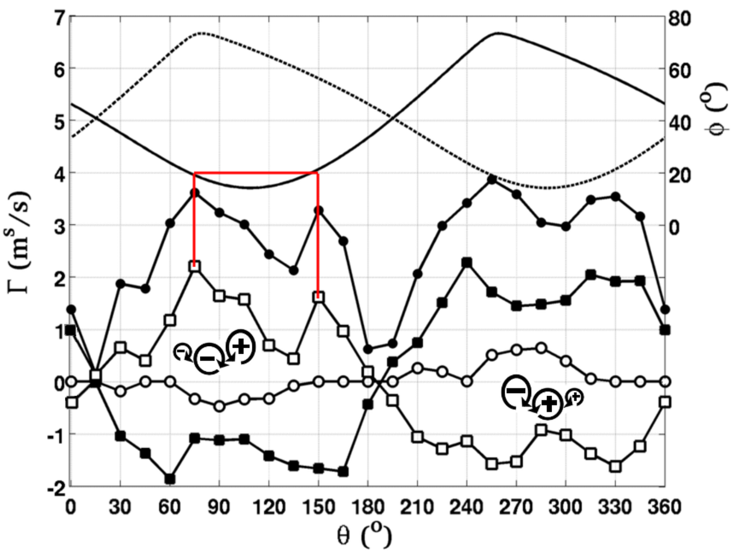

(b)

FIGURE 3.6: (a) Comparison of integrated wake and vortex drag approximations with drag measured using the Kistler force balance. Note both axes have the same scale. (b) Break down of circulation of primary vortex structures: (–■–) primary rear hip vortex,(–□–) primary upper hip vortex,(–○–) inner thigh vortex,(–●–) total sum of the absolute value of circulation from each vortex. Left (—) and right (· · ·) hip angles are plotted on the right-hand axis.

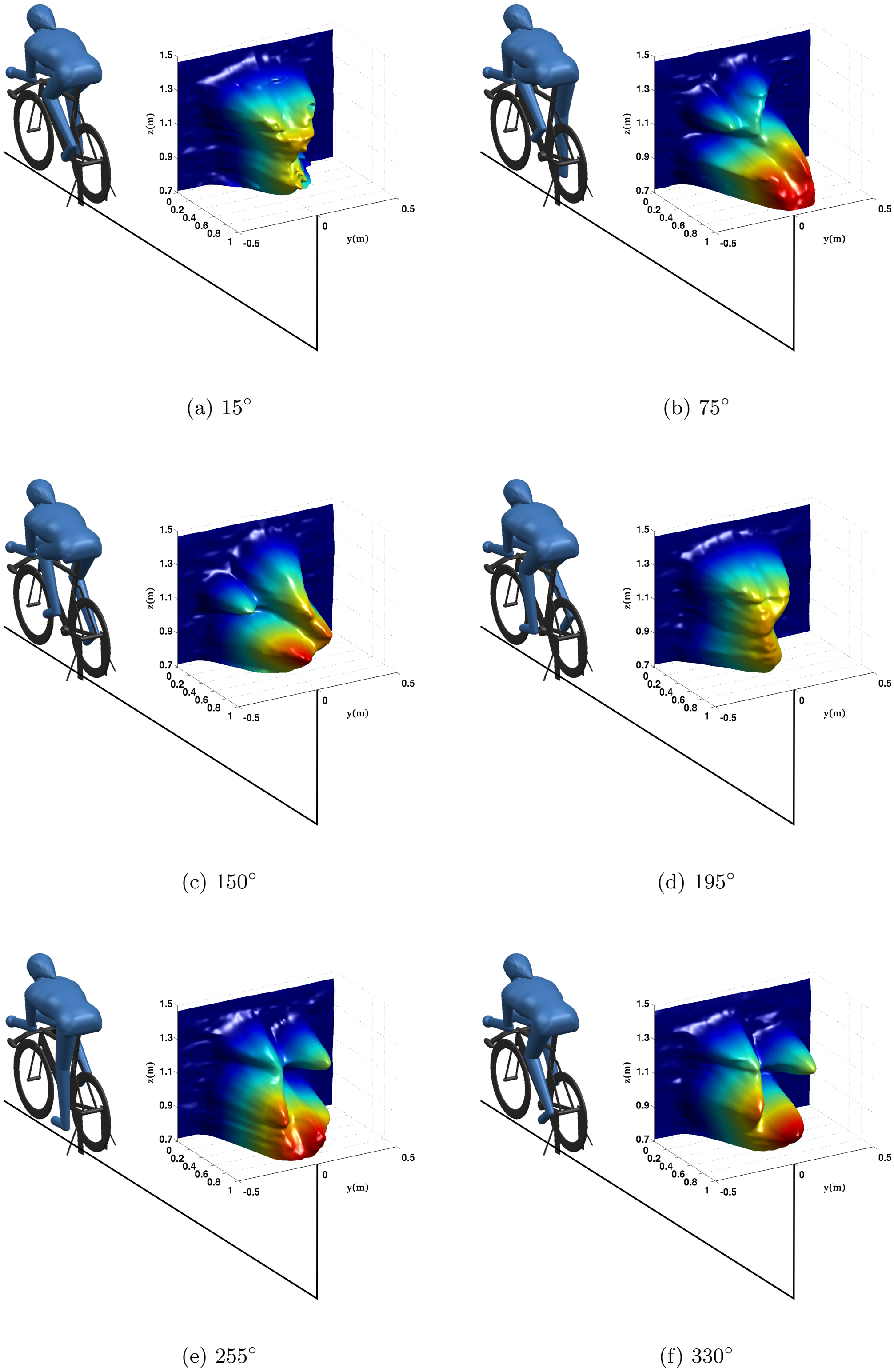

(a) 15°
(b) 75°
(c) 150°
(d) 195°
(e) 255°
(f) 330°

FIGURE 3.7: Three-dimensional representation of the drag map in the wake of the mannequin for selected leg position coloured by intensity of total drag. Drag maps represent the integrand of Maskell's equation evaluated at each measurement point in the wake normalised between 0–1 by the maximum value of the integrand measured throughout the crank cycle.

tion of each vortex was determined by evaluating the surface integral of the streamwise vorticity field within vortex boundaries $\Gamma_i = \iint_A \omega_x da$. The total circulation was found by summing the absolute value of the circulation from each vortex $\Gamma_{total} = \sum_n |\Gamma_i|$.

Despite minor asymmetries, the major trends in the circulation of each of the structures analysed is consistent in both halves of the crank cycle. In both halves of the crank cycle the circulation from the rear hip vortex peaks ($-$&$+$) at the 60° and opposite 240° leg positions, following this the circulation first decreases and then increases again until the 165° and 345° leg positions. Interestingly, over the crank angles at which the inner thigh vortex is identified in the traverse plane, an increase in the circulation of this vortex is associated with a decrease in the circulation of the rear hip vortex, and vice versa. When the circulation associated with these two vortices of the same sign are summed, this value remains relatively constant over leg positions 60° to 165° in the first half of the crank cycle and 240° to 345° in the second half, suggesting strong interaction between the two. Due to the close proximity at which these two structures form it is not surprising that they influence one another. Merging of these two vortices is also evident in figures 3.4 and 3.5, particularly in the second half of the crank cycle.

The circulation from the upper hip vortex also varies throughout the crank cycle in a similar manner to the rear hip vortex, with two key differences. Firstly, the initial peak occurs later in the crank cycle at the high drag 75° and 255° leg positions when the hip angle is at a maximum. Secondly, following a decrease in circulation, a clear second peak in the circulation of this vortex can be seen at the 150° and opposite 330° leg positions. Interestingly these two peaks in each half of the crank cycle (first: 75° & 150°, second: 255° & 330°) occur at approximately the same 20° hip angle of the opposite raised leg to where this vortex forms. This is highlighted for the first half of the crank cycle by the red lines in figure 3.6(b). When the raised left/right upper leg is at 20°, this also corresponds to crank angles where the wake that develops downstream of the arm, on the side of the body where the leg is in the raised position, is isolated from the main wake body. As you might expect with low aspect ratio bodies, this finding suggests that flow which develops on each side of the body affects the formation and strength of the primary vortex structures on both sides of the wake.

The vortex drag, which accounts for the majority of the variation in the drag over the crank cycle, is highly dependent on the relative strength of each of these vortex structures, which is shown to be closely related to where the leg is positioned around the crank cycle. When the total sum of the circulation of the primary vortex pair and the inner thigh vortex is compared with the vortex drag shown in figure 3.6(a), it is clear that the vortex drag varies with the strength of these vortices in the wake.

3.1.3 Development of Characteristic Flow Topologies

The flow topology depicting the origin and formation mechanisms of primary vortex structures around a rider is important to visualise for a number of reasons. Firstly, surface pressures which dictate the aerodynamic forces and contribute the greatest proportion to the total resistance are highly dependent on the local flow conditions near the surface of the rider, where large-scale flow structures develop. Secondly, the location of the large separated formation regions of the primary flow structures can isolate specific areas on the body where the greatest drag savings can be achieved. An understanding of both the location and flow mechanisms which describe where and how the large-scale flow structures develop will lead to informed and more efficient decisions on how better to minimise the effects of aerodynamic drag. Whether this be through the manipulation of both rider and cycling equipment geometry/position or the addition of other passive flow control mechanisms using known techniques in targeted areas to affect the formation and development of the large-scale flow structures that have the greatest impact on drag.

As is commonly the case with complex turbulent three-dimensional separated flows, a variety of techniques are required to deduce the overall structure of the flow. This is eloquently put by Délery (2001) who notes that when discussing the interpretation of three-dimensional separated flow fields: “The construction of separated three-dimensional fields is frequently an arduous task, visualisations often being too coarse to reveal all the topological features of the flow. To arrive at a rational construction, the fragmentary information must be complemented by a large dose of imagination, with the guide of logical rules, and the capacity to see objects in three dimensions.” To develop the time-averaged flow topology, several techniques were used to investigate the structure and formation of the flow over the body of the mannequin and into the near wake. This involved the additional streamwise traverses and multiple flow visualisation techniques including smoke, wool-tuft and skin-friction flow visualisations. These results are discussed in relation to the low drag symmetrical and high drag asymmetrical flow regimes to deduce the effect of leg position on the time-averaged characteristic flow

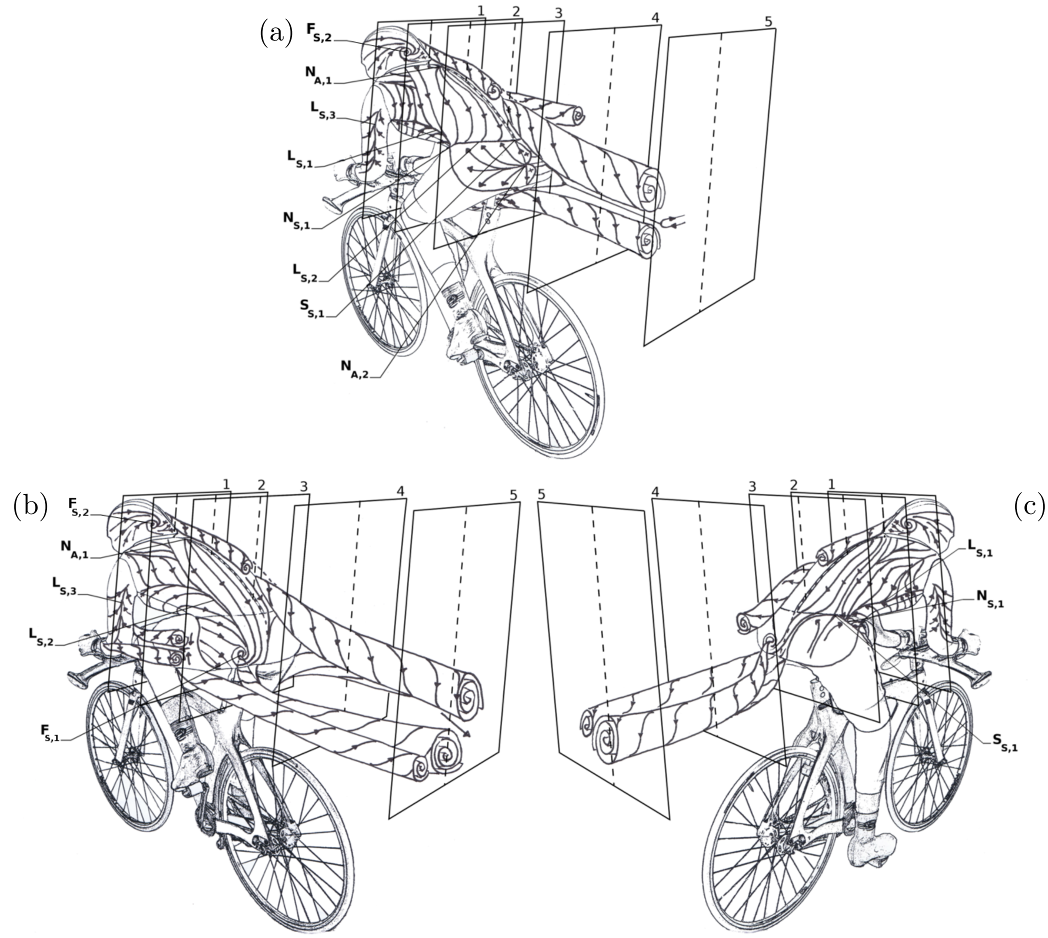

FIGURE 3.8: Flow topology of streamwise vortex system for (a) 15° symmetrical low drag flow regime and 75° asymmetrical high drag flow regime viewed from (b) left-hand side and (c) right-hand side. Symbols L, N, S and F denote major lines, nodes, saddle points and foci respectively with subscript letters S and A indicating if they are associated with separation or attachment. Subscript numbers are used to identify critical points when addressing results in support of the proposed skin-friction patterns.

topologies.

As a result of the 'fragmented' nature of the results used to piece together a grander picture of the overall flow structure, a general picture of the flow topology for each flow regime prior to their explanation aids in the interpretation of results presented in the following sections. Figure 3.8 shows the proposed flow topology for the 15° low drag symmetrical and 75° high drag asymmetrical flow regimes. The schematic highlights the identification of several additional streamwise vortices for each of the characteristic flow regimes, and the location of major separation lines and critical points from which streamwise vortices originate.

In providing evidence in support of the proposed flow topologies depicted in figure 3.8, the multiple streamwise vortices are first identified from the additional streamwise traverses (described in section 2.4.2) labelled 1–5 in figure 3.8 for the low and high drag flow regimes. Time-averaged results are compared for each flow regime and discussed in relation to the time-averaged skin-friction flow visualisations. The formation mechanisms of vortex structures are described using both the quantitative traverse results and the qualitative skin-friction patterns, which are used to deduce the origin of the large-scale flow structures on the body of the mannequin. Skin-friction patterns are discussed in the context of critical point and kinematic principals (Abell *et al.* 1978; Peake & Tobak 1982; Hornung & Perry 1984) to identify critical lines and points of attachment and separation where the wall shear stress is zero. These are depicted in figure 3.8 where the major lines, nodes, saddle points and foci of attachment and separation are denoted with symbols L, N, S and F respectively with subscript letters S and A indicating if they are associated with separation or attachment. Subscript numbers are used to identify critical points when addressing results in support of the proposed skin-friction patterns. As the complete skin-friction topology over the entire body of the mannequin was not investigated, the Poincaré-Bendixson theorem (the 'hairy-sphere' theorem) (Perry & Chong 1987) that stipulates for an isolated three-dimensional body the number of nodes minus the number of saddles must equal two, does not apply to the back of the mannequin where skin-friction flow visualisations were performed.

3.1.3.1 Comparison of Low & High Drag Flow Regimes

The additional streamwise traverses and skin-friction flow visualisations performed for the 15° and 75° leg positions show an added complexity to the wake structure to that previously described for the low and high drag flow regimes. As depicted in figure 3.8 multiple streamwise vortex structures, in addition to the primary vortices previously described in section 3.1.2.2, are identified as being a key feature of the flow around cyclists. Even for the symmetrical low drag flow regime traverse results reveal several areas on the body of the mannequin that provide a strong source of streamwise vorticity of similar magnitude to that of the high drag flow regime. These features were not captured in the previously analysed wake traverses (plane 5). Traverse results not only show the spatial development of the time-averaged flow over the body and into the near wake but also further highlight the significant differences in the low drag symmetrical and high drag asymmetrical flow regimes that account for the large variations in the drag coefficient throughout the crank cycle.

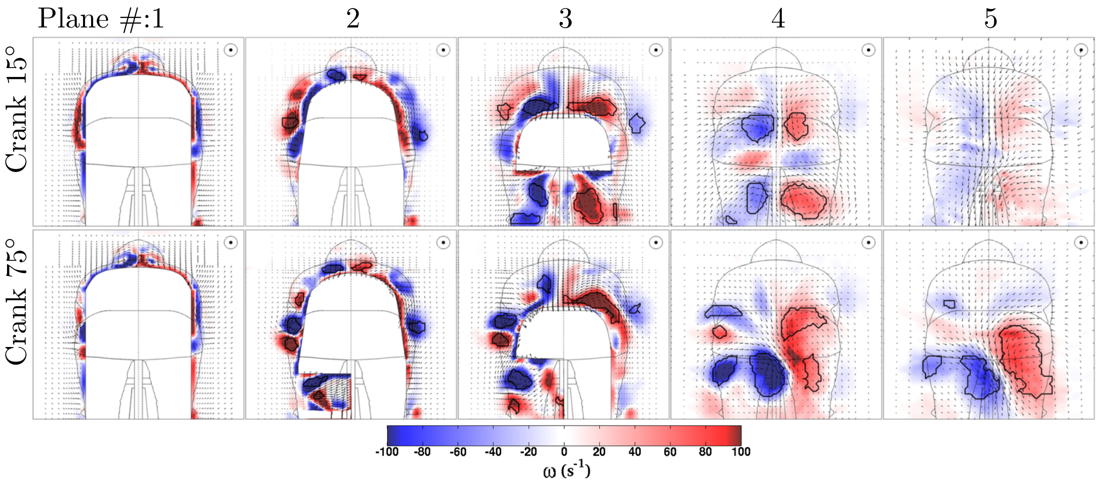

FIGURE 3.9: A comparison of contours of streamwise vorticity for symmetrical and asymmetrical flow regimes at each streamwise traverse plane. Vortex boundaries identified using the swirling strength criterion have been outlined in black.

For the low drag 15° leg position the body traverses show symmetry in the flow not only in the near wake but also over the entire upper body. This is in direct contrast to the 75° high drag leg position where asymmetries in the near wake flow can be seen to develop early on over the body. This is shown in figure 3.9 that compares contours of the out-of-plane streamwise vorticity in planes 1–5 for both flow regimes. Clearly the mechanisms by which the flow develops over the body of the mannequin and into the near wake are very different for each case.

The largest variations between each of the flow regimes shown in figure 3.9 is concerned with the difference in the streamwise vortices present in each of the planes that have been identified using the swirling strength criterion previously discussed in section 3.1.2.2. These streamwise vortices were visualised and are labelled in figures 3.10 and 3.11. Figure 3.10 compares iso-surfaces of the primary vortices for each flow regime and figure 3.11 compares iso-surfaces of the smaller secondary vortex structures that either merge with the primary vortices or decay by cross-diffusive annihilation close to the rear of the mannequin in the near wake. The origin of the major flow structures on the body of the mannequin in each flow regime has being visualised in figures 3.12 and 3.13, which shows images of skin-friction flow visualisations for the low and high drag flow regimes respectively.

For the 15° symmetrical low drag flow regime in figure 3.10(a) a large vortex pair can be seen to develop evenly over the upper hips on both sides of the body. This streamwise vortex pair is analogous to streamwise vortices that develop over low aspect

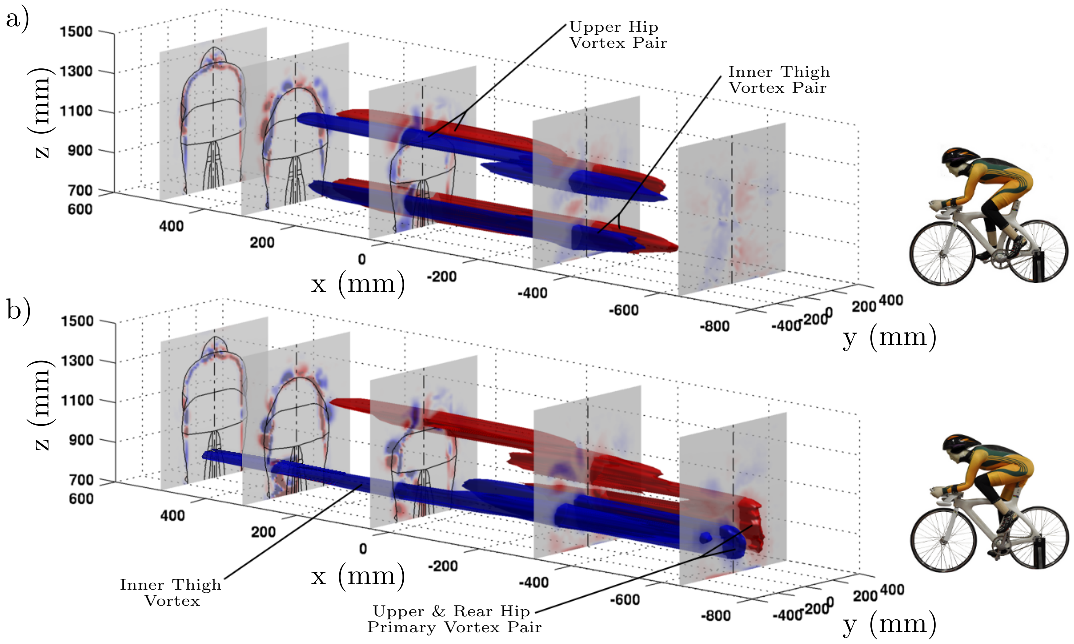

FIGURE 3.10: Spatial development of primary vortex structures over the body of the mannequin for a) 15° symmetrical low drag flow regime and b) 75° asymmetrical high drag flow regime.

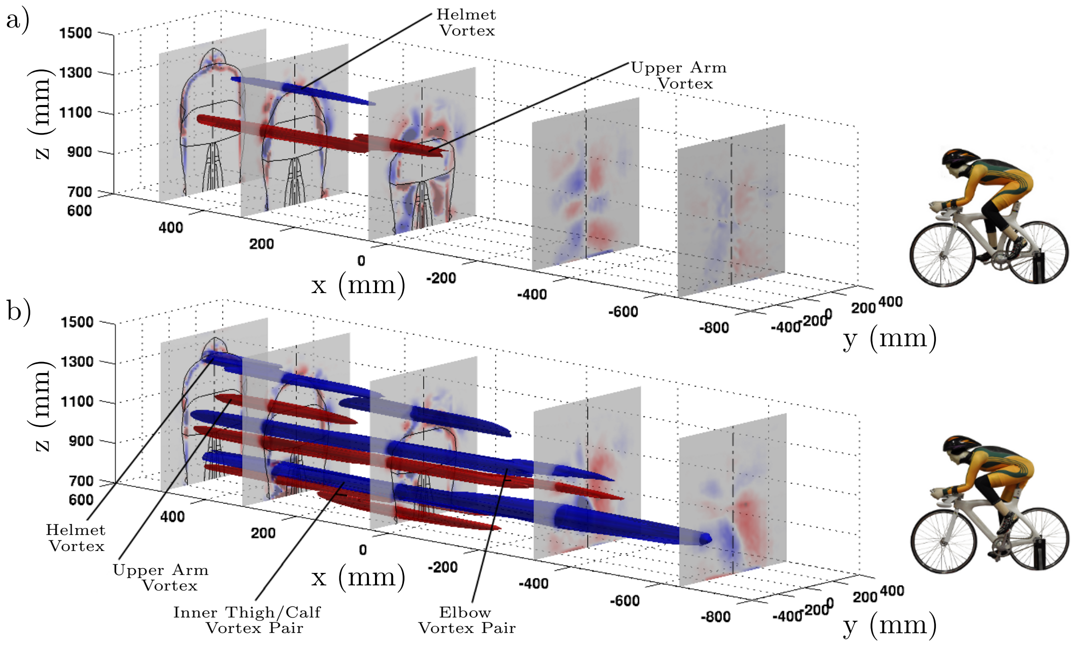

FIGURE 3.11: Spatial development of secondary vortex structures over the left-hand side of the mannequin for a) 15° symmetrical low drag flow regime and b) 75° asymmetrical high drag flow regime. On the right-hand side of the body similar secondary vortices (of opposite sign) exist as those shown in the symmetrical flow regime of (a) for both the 15° and 75° leg positions.

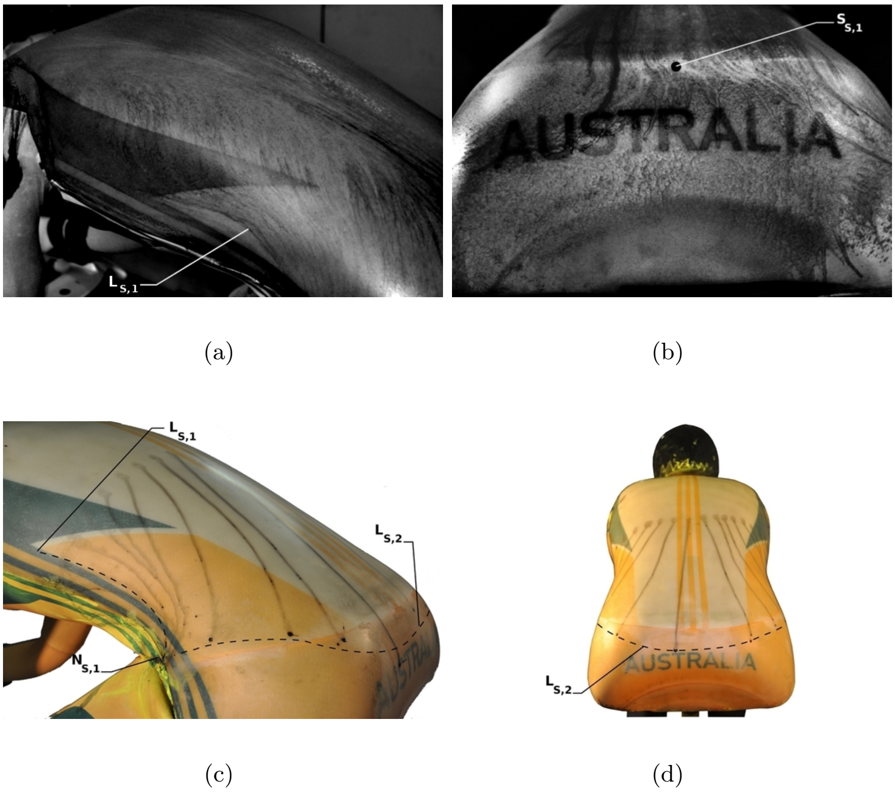

FIGURE 3.12: Skin-friction flow patterns on the suction surface of the mannequin's back for the 15° symmetrical low drag flow regime.

ratio wings due to a pressure differential between the underside of the torso and the suction surfaces of the back. This pressure differential generates a strong flow that is directed up around sides of the torso and hips where flow separates and the shear layers roll up from both sides of the body. This can be seen in figure 3.14 for the 15° leg position that shows contour levels of the in-plane vertical component of velocity reach 50% of the freestream velocity around the sides of the torso where this vortex pair starts to form at plane 2. Flow that is directed up around the sides of the torso and hips separates along the '$L_{S,1}$' separation line, which were visualised using the fluorescent oil and ink-dot method in figure 3.12(a) and (c), respectively. The separated shear layers that roll up to form the upper hip vortex pair cover the entire span of the hips and remain attached to the centre line of the back until they detach from the body at the separation saddle '$S_{S,1}$', shown in figure 3.12(b), and along the major separation line, labelled '$L_{S,2}$'. This separation line is also identified in figures 3.12(c) and (d) using the ink-dot method, where tracer dots finish due to the zero wall shear stress along lines of separation. As this vortex pair develops over the back, figure 3.14 shows a strong

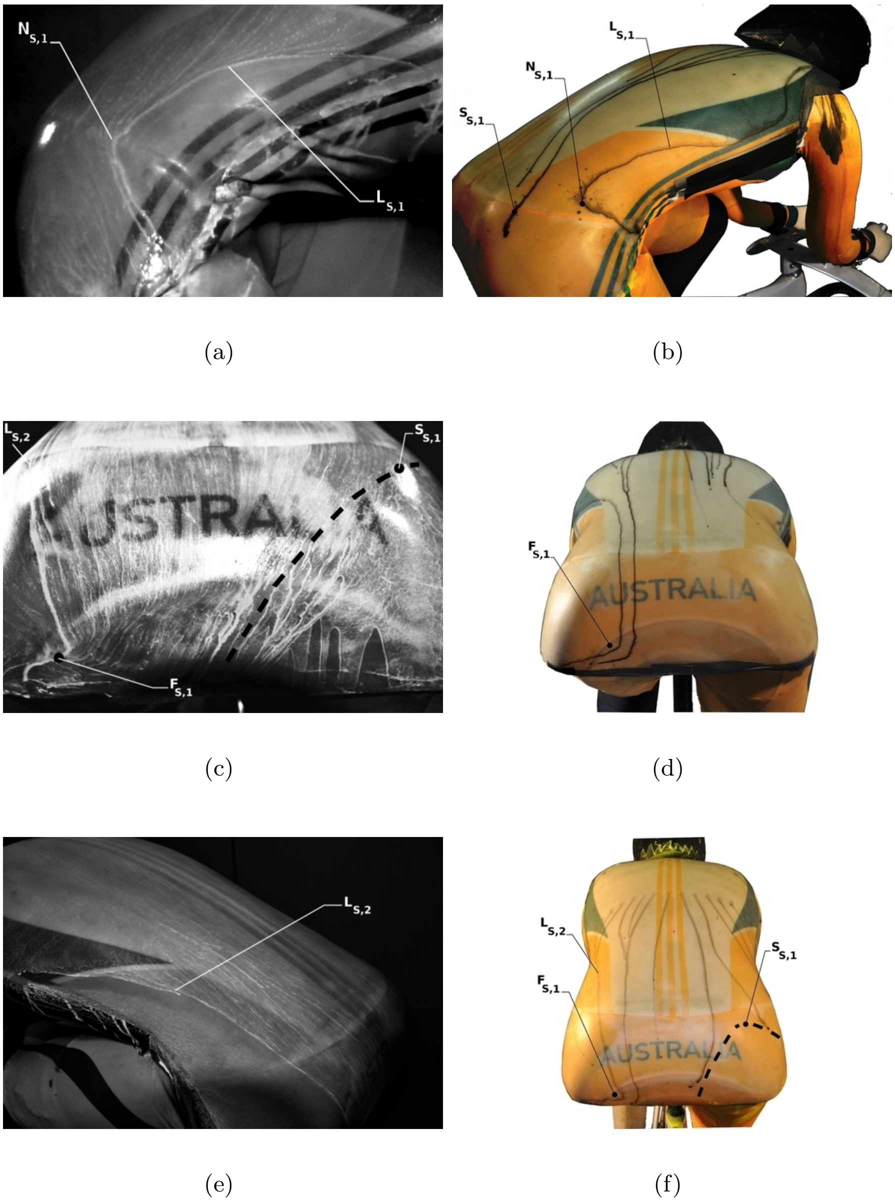

FIGURE 3.13: Skin-friction flow patterns on the suction surface of the mannequin's back for the 75° asymmetrical high drag flow regime.

downwash is generated in between them, aiding in the attachment of the flow down the centreline of the back for the 15° leg position.

A second primary streamwise vortex pair can be seen between the upper legs below the hips in plane 3 of figure 3.9 for the symmetrical 15° flow regime. This vortex pair, of the same sign as the upper hip vortex pair above, forms when flow separates along the inner thighs of both upper legs. With the upper legs aligned, the strength of both vortex pairs are of similar magnitude. As these vortices leave the body of the mannequin they are drawn together in the near wake, which occurs between planes 3 and 4 of figure 3.9. This forms a quadruple structure with upper and lower vortex pairs both exhibiting a downwash with a high shear flow in between. Between planes 4 and 5 there is a significant contraction in the size of the wake as vortices of similar strength and opposite sign on either side of the centreline mutually interact. This results in the cross annihilation of streamwise vorticity and the absence of large in-plane velocity gradients in the flow field measurements performed at plane 5 for the 15° leg position. This is similar to that observed for trailing streamwise vortex systems behind wall mounted rectangular cylinders (Sau *et al.* 2003) and other surface-mounted bluff body obstacles (Mason & Morton 1987).

For the 75° leg position, figure 3.10(b) shows where the primary vortex structures of the asymmetrical flow regime, which have previously been identified and analysed in sections 3.1.2.2 and 3.1.2.3, originate and develop over the body of the mannequin. On the right side of the body for the 75° leg position where the hip angle is open, the upper hip vortex develops in a manner comparable with that of the upper hip vortices that span the lower back in the 15° leg position. The large streamwise vortex is clearly evident in plane three on the right hand side of figure 3.9 for the 75° leg position. Although this is analogous to flow separation on the sides of the torso and hips for the low drag case, flow separation along the primary '$L_{S,1}$' separation line occurs much higher on this side of the torso for the 75° leg position, as shown in figure 3.13(a). The vertical component of velocity on the sides of the torso where this structure develops is also higher for the 75° leg position, which reaches over 50% of the free stream velocity as shown in plane 2 of figure 3.14 for the 75° leg position. Around the hip joint area a large 'kink' in this separation line can be seen which is associated with the node-saddle point combination of ($N_{S,1}$) and ($S_{S,1}$) shown in figure 3.13(a–b) and (f), which marks the location where the upper hip vortex detaches from the lower back. As the upper hip vortex advects downstream the time-averaged results show that it elongates. The near wake traverses indicate that this is a result of its merging with vorticity of the same sign that is fed into the wake behind the straightened upper leg. This elongated hip vortex is visualised further downstream in the iso-surfaces shown in figure 3.10(b).

Although there are similarities between the development of the upper hip vortices in both flow regimes, this is where the similarities between the two flow regimes end. With the hip angle closed the higher pressure flow from the underside of the torso is restricted from accelerating around its curved side. This results in the absence of the high vertical component of velocity on this side of the torso as shown in figure 3.15 on the left-hand side of plane 2 for the 75° leg position. Flow that is directed under the torso is split around the extended leg and either progresses up around the torso on this side of the body or out under the raised leg where the flow separates from the inner thigh forming the inner thigh vortex visualised in figure 3.10. The development of this structure is clearly captured under the raised leg in traverse plane 2 performed at the mid-torso chord. Unlike the development of the inner thigh vortices of the symmetrical flow regime, this vortex develops further out from the centreline of the mannequin. It also develops in combination with a smaller secondary vortex that originates from the inner calf of the lower leg to form the counter-rotating vortex pair (inner thigh/calf vortex pair) labelled in figure 3.11(b). This is a result of the strong flow component that is channelled out under the raised upper leg due to the high blockage of the straightened leg as well as the bicycle frame. This can be seen in plane 2 of figure 3.15 for the 75° leg position, which shows a large horizontal component of velocity of up to 50% of the freestream velocity that is being directed away from the straightened leg out underneath the raised leg. Compared with the 15° symmetrical flow regime this results in a large low velocity recirculation region between the legs below the hips that extends out from the straightened leg. This is evident in plane 3 of figure 3.16, which compares contours of the non-dimensional freestream velocity for both leg positions. A generalised diagram that depicts this, showing the variation in the flow that originates from underneath the torso for both flow regimes, is shown in figure 3.18.

The restriction imposed by the raised leg not only impacts the flow directed under the torso but all around it. Flow that is directed around the raised leg and torso does not see the full extent of the curvature of the upper leg (which is primarily aligned with the freestream in this position) and the torso sides. As a result of this the flow remains largely attached over this side of the torso, separating along the separation line labelled '$L_{S,2}$' in figure 3.13(e). This separation line begins at the armpit junction and extends the entire length of the back over the upper and rear hip. Below this separation line the oil flow visualisations show a turbulent boundary layer where the high momentum flow near the body surface not only aids in the attachment of the flow around the hip, but also increases the flow rate of the oil fluid in this region, leaving behind a textured pattern that is largely devoid of the fluorescent powder.

As the flow progresses around the torso and under the raised leg, the mean velocity vectors show the flow spiralling around the rear of the hip of the raised leg. This is demonstrated with arrows which have been drawn on the left hip of figures 3.14 and 3.15 showing the circulatory motion of the in-plane velocity components around the raised hip. Skin-friction streamlines on the rear of the raised hip, shown in figure 3.13(c), can also be seen to spiral around the marked focus '$F_{S,1}$'. This marks the origin of the rear hip vortex. Further evidence of this surface flow topology is provided by the localised surface streamlines using the ink-dot method shown in figure 3.13(d) and (f), where in the vicinity of the focus, there is a severe deviation in these lines around the focal point. The focus, which forms in combination with the separation saddle '$S_{S,1}$', also marks the termination point of the separation line '$L_{S,2}$'. The three-dimensional focus on the rear hip explains the sudden increase in vorticity below the hips between planes 3 and 4 in figure 3.9 for the 75° leg position, as a result of the formation the rear hip vortex between these planes.

The formation and development of secondary streamwise vortices that originate upstream of the primary structures is also dependent on the position of the legs. This is clearly shown in the iso-surfaces of these structures shown in figure 3.11, that show large variations in streamwise vortices that originate on the left hand side of the mannequin from the helmet, arms and legs for the 15° and 75° leg positions. For both leg positions contours of streamwise vorticity in the plane at the trailing edge of the helmet show a streamwise vortex pair that originates when shear layers roll up from both sides of the helmet. This has been shown to be a characteristic feature of the flow behind helmets by Chabroux *et al.* (2010) who performed similar wake surveys behind different helmets using particle image velocimetry. Downstream of the tip of the helmet the flow reattaches to the body which is marked by an attachment node ($N_{A,1}$) shown in figure 3.12(c). For the 15° leg position the helmet vortices remain attached down the back where they merge downstream with the primary upper hip streamwise vortices which are of the same sign. For the asymmetrical flow regime vortices that originate from the helmet on the side of the body were a upper hip vortex does not form (side where leg is raised), persist much further into the near wake behind the mannequin which is evident for the 75° position in figure 3.11(b).

Although from a mean flow perspective the flow remains relatively attached down the upper back, flow visualisations and analysis of surface pressure fluctuations reveal that unsteady processes play a major role in the development in the flow over the

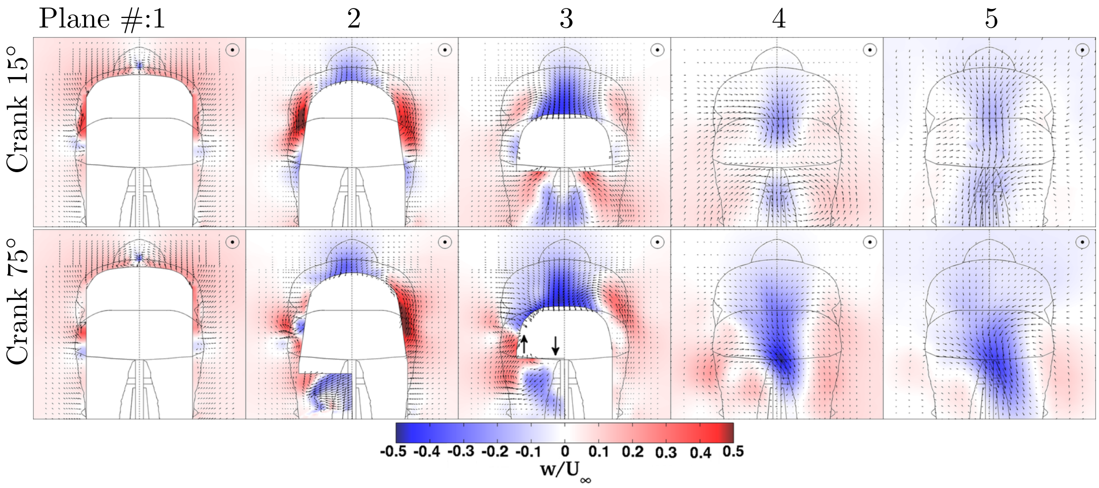

FIGURE 3.14: A comparison of contours of the in-plane non-dimensional vertical component of velocity for symmetrical and asymmetrical flow regimes at each streamwise traverse plane. Blue represents the downward direction and red represents the upward direction.

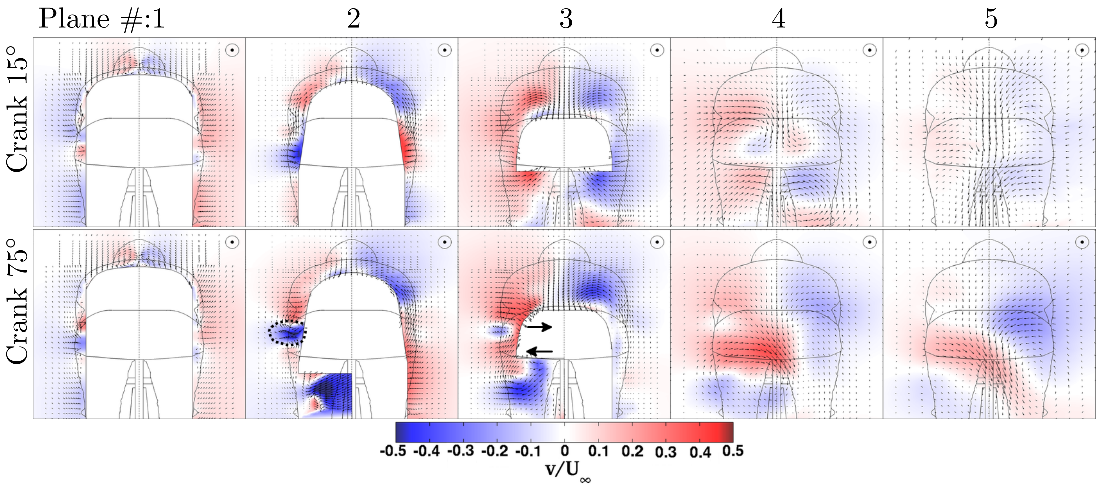

FIGURE 3.15: A comparison of contours of the in-plane non-dimensional spanwise velocity for symmetrical and asymmetrical flow regimes at each streamwise traverse plane. Blue represents the left spanwise direction and red represents the right spanwise direction.

torso. One such area involves flow separation from the shoulders. For all leg positions tested the oil skin-friction lines were observed to converge together over the shoulder as shown in figure 3.20. The converging skin-friction lines show the flow separates behind the helmet approximately around where the gradient of the back transitions to a downwards slope. The unsteady process associated with this separation will be discussed in section 4.1.

With the hip angle closed, the wake from the arms on the side of the body with the leg in a raised position can develop downstream over the body of the mannequin. This is shown in figure 3.11(b) where multiple streamwise vortices are identified in

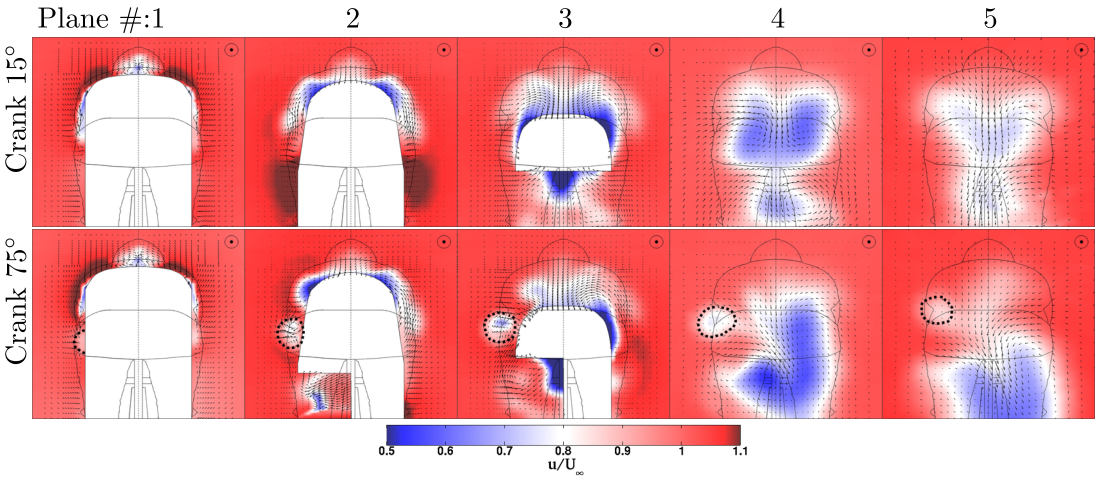

FIGURE 3.16: A comparison of contours of streamwise velocity for symmetrical and asymmetrical flow regimes at each streamwise traverse plane.

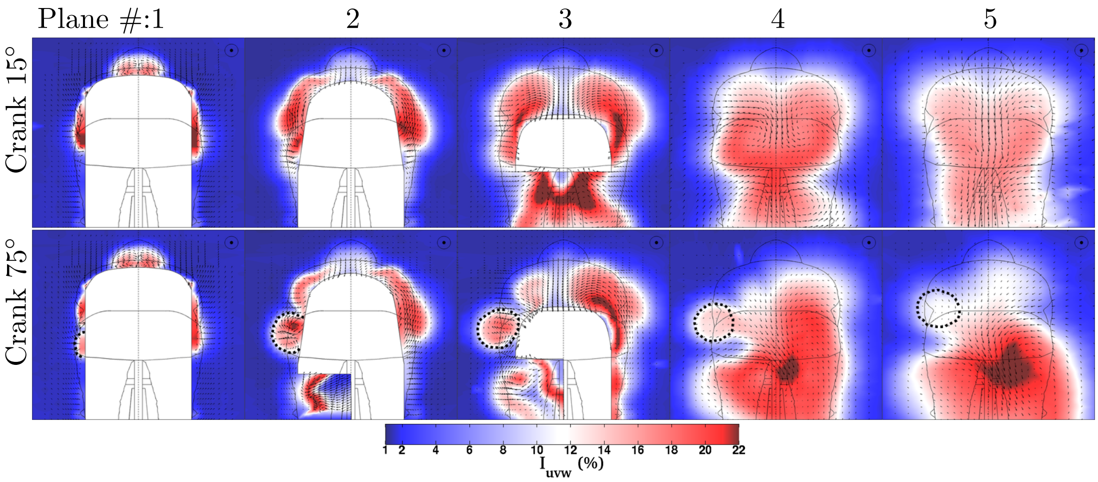

FIGURE 3.17: A comparison of contours of the principal turbulence intensity for symmetrical and asymmetrical flow regimes at each streamwise traverse plane.

the wake of the arms, as opposed to the 15° leg position figure 3.11(a) (and the right hand side of the 75° leg position). On this side of the body the wake flow behind the arms is dominated by the turbulent flow driven up the sides of the torso by the large pressure differential between the underside of the torso and back. A streamwise vortex can be seen in both flow regimes to develop when flow separates from the outside of the upper arm of the mannequin. This generates vorticity that is advected up towards the shoulder due to a strong component of the flow that is directed up the arm. Flow separation from the arms has being visualised by Brownlie *et al.* (2009) using a similar fluorescent china clay technique performed on a mannequin in a time-trail position shown in figure 3.21(a), which identifies the major upper arm separation line marked

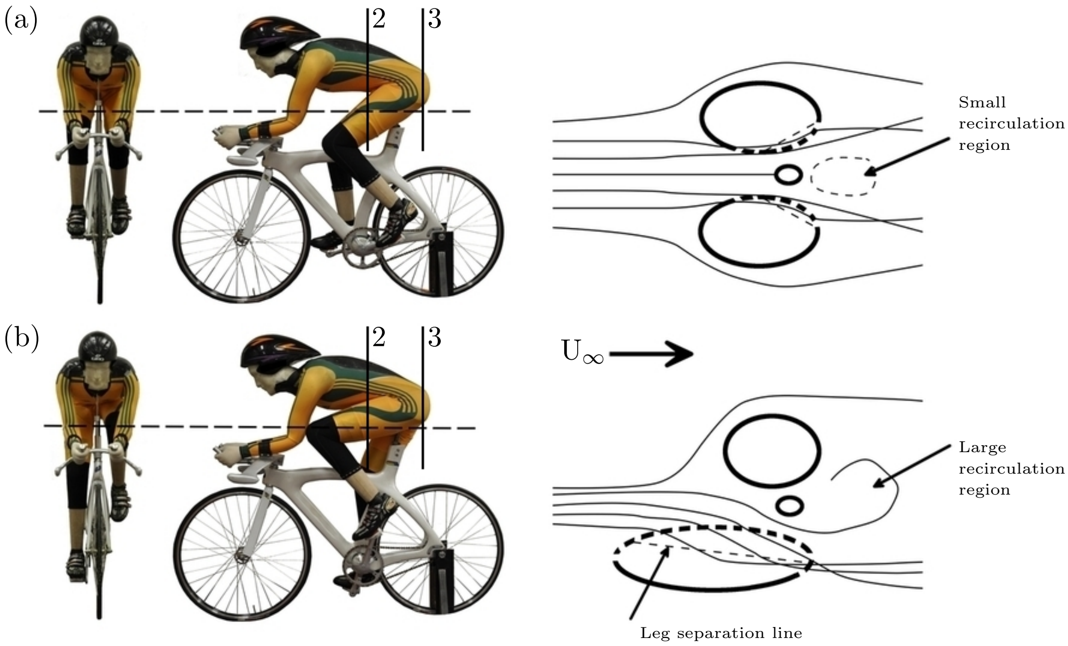

FIGURE 3.18: Schematic showing a cross section of the flow under the torso and through the legs for (a) the low drag 15° and (b) the high drag 75° leg positions.

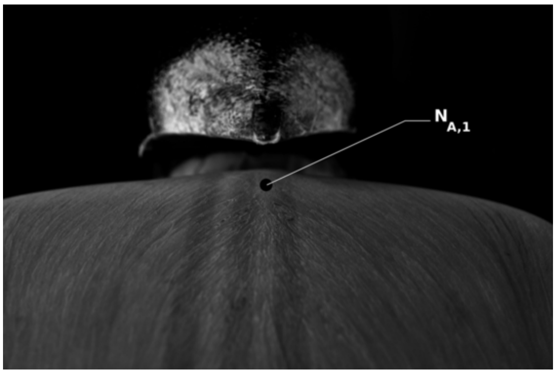

FIGURE 3.19: Oil skin-friction visualisation of the attachment point of flow behind the helmet.

by '$L_{S,3}$'. This separation line is also indicated in figure 3.21(b) by short wool-tufts placed on the upper arm of the mannequin. The wool-tufts are deflected up along the separation line and show that there is a strong local flow component of velocity that is direction up the arms.

Around the armpit junction the separated shear layers from the upper arm are turned and advected downstream by the mean flow resulting in the upper arm vortex. The trajectory of this vortex over the back is similar to that of the separation line '$L_{S,2}$' that originates behind the armpit on the side of the torso, identified in figure 3.12 (b) from the oil flow visualisations. Due the sign and the close proximity of this streamwise

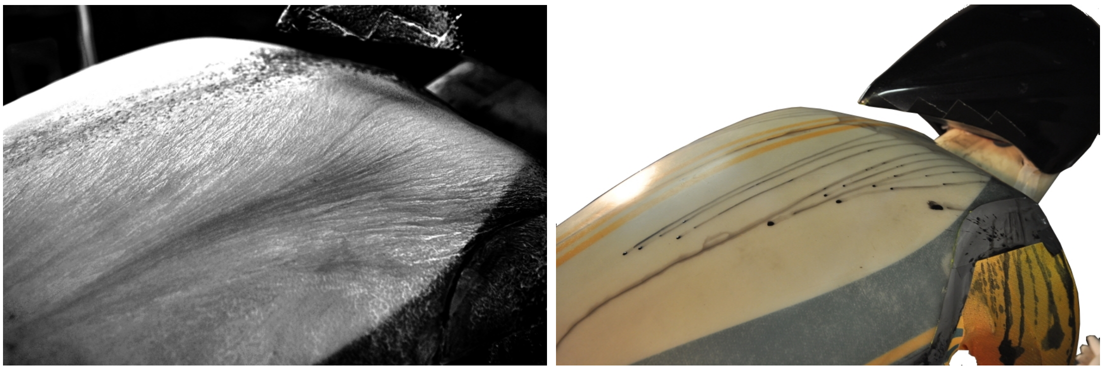

(a) (b)

FIGURE 3.20: Oil skin-friction and ink-dot flow visualisations of flow separation from the shoulders.

(a) (b)

FIGURE 3.21: a) China clay flow visualisation showing separation along the upper arm by Brownlie *et al.* (2009). (b) Wool-tufts highlighting separation line on upper arms of the mannequin.

vortex to the body of the mannequin, it has the effect of 'lifting' the flow from the surface of the model, aiding in flow separating from this side of the torso along the separation line '$L_{S,2}$'.

A strong streamwise vortex pair also develops behind the left elbow joint in plane 1 and is clearly identified in planes 2–4 of figure 3.9 for the 75° leg position. This vortex pair is labelled the 'elbow vortex pair' in the iso-surface of the secondary structures shown in figure 3.11(b). As this vortex pair is advected down along the side of the torso a strong horizontal jet is generated outwards from the side of the torso in between the vortex pair. This is highlighted by the dashed circle in the contours of the spanwise component of velocity in plane 2 of figure 3.15 for the 75° leg position. In tracing the trajectory of this vortex pair from the elbow joint into the near wake we find that it is responsible for the isolated turbulent velocity deficit region previously described in sections 3.1.2.1 and 3.1.2.3. This is further emphasised, in the contour plots of streamwise velocity and turbulence intensity, by the dashed circles that isolate the velocity defect regions associated with the elbow vortex pair in planes 1–5 of figures 3.16 and 3.17. The highlighted regions show that the elbow vortex pair follows an upwards trajectory into the wake behind the mannequin.

3.1.3.2 Smoke & Wool-Tuft Flow Visualisations

Further evidence in support of the proposed time-averaged flow topologies for symmetrical and asymmetrical flow regimes is found in the smoke and wool-tuft flow visualisation studies. High resolution still images and video recordings of smoke patterns do not clearly depict coherent vortex structures. Clearer images of the smoke patterns where achieved by illuminating two-dimensional slices of the flow over the body of the mannequin and in the wake using a laser sheet and increasing the frame rate at which the smoke patterns were recorded. Although the smoke patterns using this technique are in good agreement with the velocity field wake surveys, the rotational motion of streamwise vortices remained unclear. The issue lies in the high diffusion rate of the smoke particles, which acts to mask vortices as well as delivering an appropriate concentration of smoke directly into the core of vortex structures. The ability to vary the concentration of smoke delivered by the smoke wand is limited, and as smoke is built up in the return circuit wind tunnel throughout flow visualisations, the image quality of smoke patterns decreased. The heated tip at the end of the wand, which vaporises the mineral oil to produce the smoke, also meant that injection of smoke right at the surface of the body could not be achieved as it would cause a potential fire hazard. Despite this, smoke and wool-tuft patterns, when interpreted in the context of the asymmetrical and symmetrical flow regimes, are in very good agreement and highlight the dominating influence that large-scale flow structures have on the flow.

The smoke visualisations highlight different aspects of the flow through the injection of smoke at specific points around the body of mannequin for varying leg positions. Figure 3.22 shows the smoke injection points on the left-hand side of the mannequin that are located in areas close to where streamwise vortices of symmetrical and asymmetrical flow regimes originate. Smoke was also injected at the same locations on the right-hand side of the body so that any asymmetries in the flow over the body of the mannequin

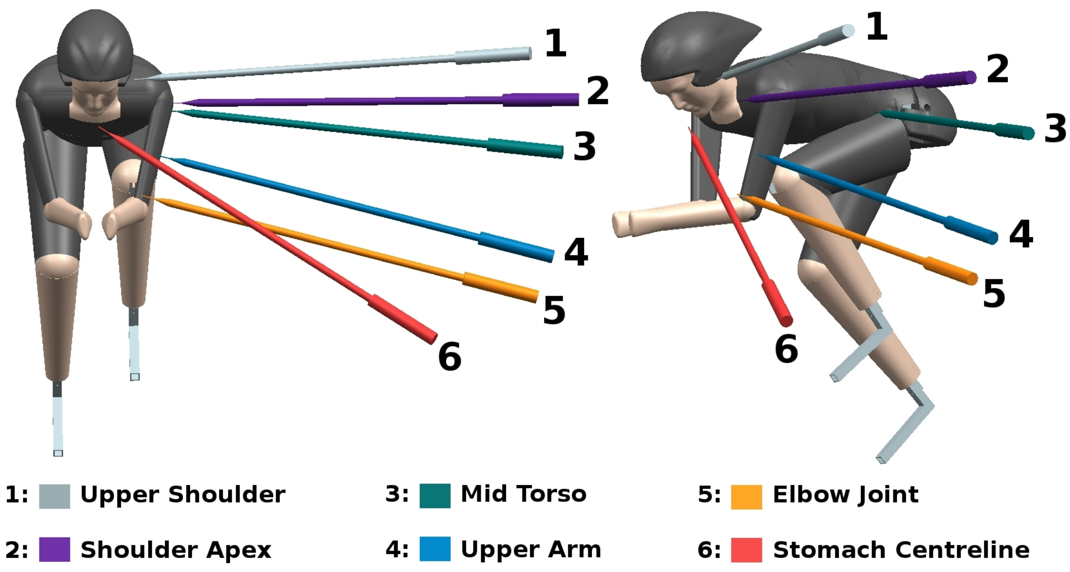

FIGURE 3.22: Smoke release points around body of mannequin.

could be identified for varying leg positions. Due to the highly three-dimensional nature of the flow around a cyclist, high definition video footage of smoke patterns was obtained from side above and rear view perspectives. Video footage from the different perspectives was recorded at 15 frames/second for 12 seconds. For smoke visualisations involving illumination of sections of the wake with a laser sheet this was increased to 60 frames/second for 20 seconds. Upon analysing the video footage it was found that the sampling rate was too slow or images were not clear enough to provide any conclusive information on the frequency of vortex formation and on the detailed dynamics of the vortex wake. Photographs that freeze the motion of the smoke in the image (exposure time 1/800 seconds) identify the dominant features of the time-averaged flow field for both flow regimes. Dominant shedding frequencies in the wake will be investigated through the analysis of fluctuating surface pressure and velocity field components in section 4.1.

As individual video snapshots of smoke flow visualisations did not provide a clear image of the smoke around the model, a novel image processing technique was developed to obtain a clearer picture of the smoke patterns that depict a better representation of the mean flow. This involved reconstruction of a single image from the video footage of each smoke flow visualisation to simulate a ‘long-time exposure’ effect by:

1. converting individual frames of the video footage (for each perspective view) to grey-scale images (video at 15 Hz for 12 seconds = 180 frames),

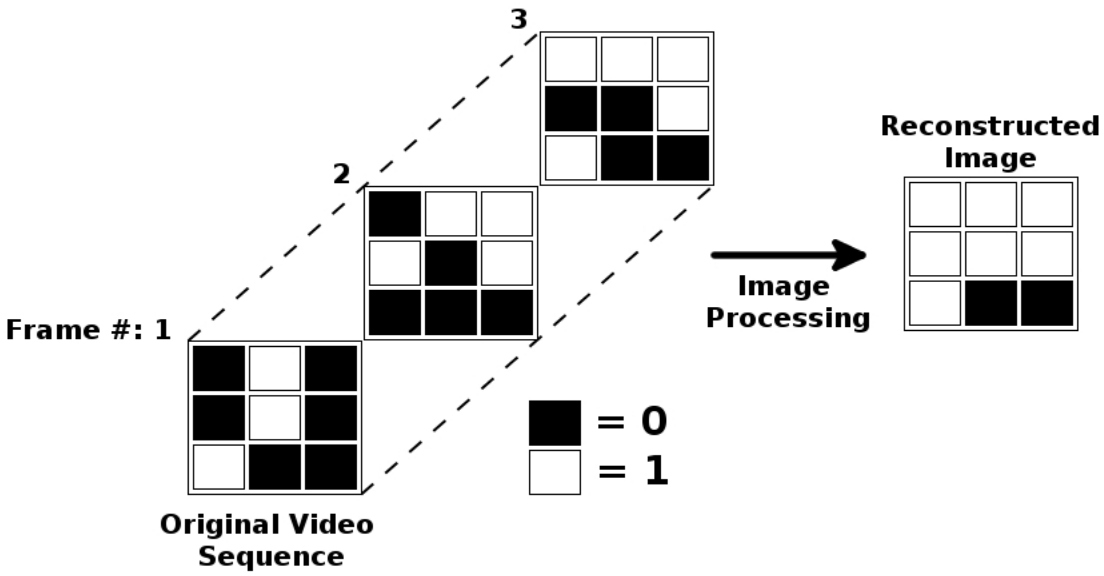

FIGURE 3.23: Diagram of image processing technique used to processes videos of flow visualisations.

2. for each pixel location identifying the maximum pixel value (0–1 for grey scale images, where 0 is black and 1 is white) in the sequence of grey-scale images that comprise the video footage,

3. reconstructing a single image from the maximum pixel values at each pixel location.

A simplified black and white image representation of this process is depicted in figure 3.23. This technique highlights the spread of the smoke and also where the smoke was concentrated as it flows around the body of the mannequin and into the wake flow. Although video footage was processed for all leg positions around the crank cycle only processed images and snapshots of selected leg positions are discussed in this section. These are representative of the smoke patterns observed for each of the symmetrical and asymmetrical flow regimes.

In comparing flow visualisations from left and right sides of the body between the high and low drag leg positions smoke patterns are consistent with symmetrical and asymmetrical flow regimes identified from the velocity field wake surveys. All visualisations for 0°, 15° and opposite 180°, 195° leg positions show symmetrical flow patterns from left and right-hand sides of the body. As a result of this flow symmetry, visualisations for these leg positions are depicted from only one side of the body. Flow visualisations for leg positions characteristic of the asymmetrical flow regime are shown

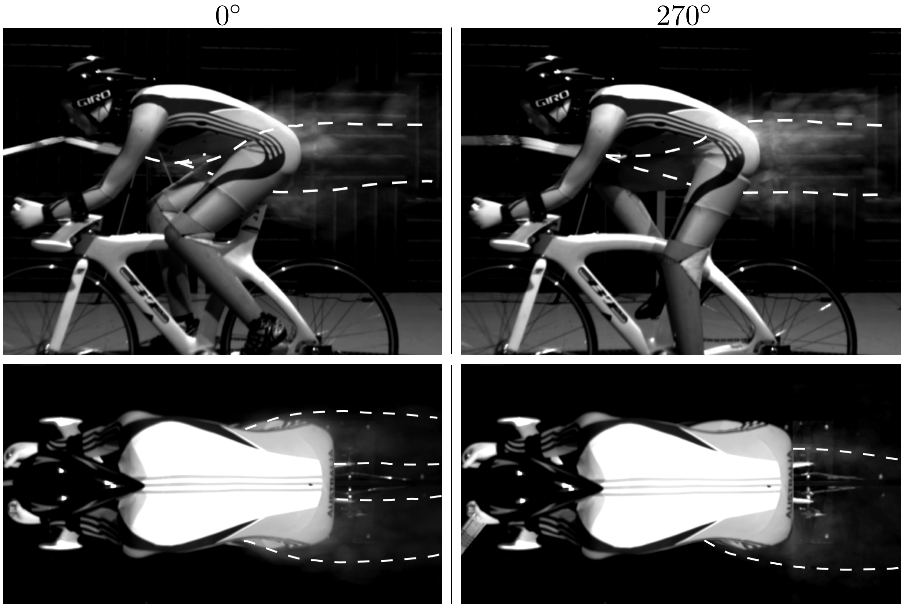

FIGURE 3.24: Flow visualisation of smoke injected along stomach centreline for low drag 0° and high drag 270° leg positions.

from both left and right sides, to show the large asymmetries in the flow over the body.

Smoke released under the chin along the stomach centreline of the mannequin highlights the main differences between low and high drag flow regimes, which can be seen in figure 3.24 for 0° and 270° leg positions. For the 0° leg position, smoke under the stomach is split over the hips of both legs where the upper hip vortices form, and in between the inner thighs of both legs where the inner thigh vortex pair originates. With the right leg raised for the 270° leg position only two distinct smoke paths emerge in the near wake. One is a result of the smoke flowing up from underneath the torso over the right hip of the extended leg. The second is a result of the smoke being split around the extended leg out underneath the raised leg where the inner thigh vortex forms. Smoke coming out from underneath the raised leg is concentrated in the rear hip vortex regions of the wake. This is consistent with smoke being entrained into the low pressure cores of the rear hip and inner thigh vortices.

Further evidence that smoke injected down the centreline of the stomach rolls up into the primary vortices is provided by visualisations of the smoke patterns that are illuminated by a laser sheet perpendicular to the freestream a torso chord length in the wake. Figure 3.25 shows high resolution photographs of these smoke patterns from perspective and rear views for the low 15° and high 75°, 255° leg positions. Many similarities can be drawn between these smoke patterns and qualitative characteristics of the wake, determined from the mean flow field measurements performed at the same imaging location for these leg positions (traverse plane 5). Snapshots of the 15° leg position reveal a symmetrical smoke pattern about the centre plane of the mannequin. Smoke is more widely and evenly distributed throughout the laser sheet compared to the high drag leg positions. This is consistent with a large degree of mixing between the smoke that is contained within the vortex dominated regions of the near wake as a result of the strong mutual interaction of the upper hip and inner thigh vortex pairs, which occurs between traverse planes 4 and 5 in the wake. This results in a high turbulent diffusion rate and mixing of the smoke particles within the turbulent regions of the laser plane.

In contrast to the low drag leg positions, the smoke visualisations of high drag leg positions show large asymmetries in the flow, with smoke flow confined to specific areas of the wake. Although high resolution images and video footage did not conclusively show individual 'vortex cores', smoke released under the chin is concentrated within areas of the laser sheet where the large-scale vortex structures lie in this section of the wake. The smoke patterns are consistent with smoke being drawn into the low pressure core regions of the primary upper and rear hip vortex pair, as well as the smaller inner thigh vortex.

Smoke released at the other injection points around the mannequin focus on visualising the effect leg position has on flow separation around the back, hips and arms. Figure 3.26 shows large variations in smoke patterns result when smoke is released at the sides of the mid torso ($0.5c$) for 180° and 270° leg positions. For both leg positions smoke released just upstream of where the upper hip vortices originate, shows flow coming up from underneath the torso and separating along its sides. The upwards trajectory of the smoke into the wake highlights the high vertical component of velocity that was measured on the sides of the torso just prior to the formation of the upper hip vortex in both flow regimes. In this region of the torso ($0.5c$–$0.6c$), flow is shed much higher into the wake compared to vortex shedding that occurs towards the hip junction. This results in the majority of the smoke released in this area tracing a path into the wake above where the upper hip vortex is located, especially for the 270° position in figure 3.26.

In contrast to this smoke released on the right-hand side of the torso for the 270° leg position shows the smoke flows around the hip of the raised leg and is drawn across

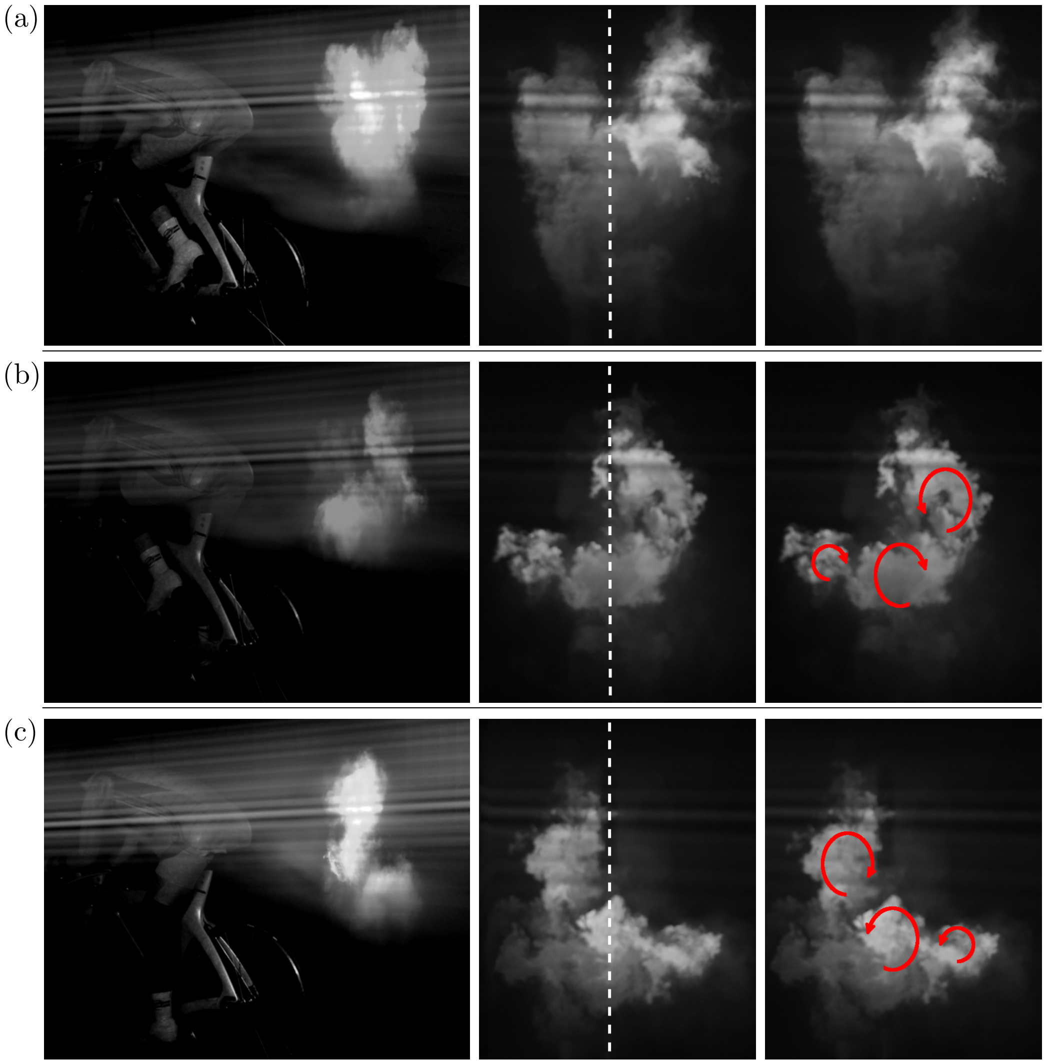

FIGURE 3.25: Snapshots of smoke flow visualisations from perspective and rear views of smoke injected along stomach centreline using a laser sheet to illuminate a plane normal to the mean flow 640mm (torso chord length) in the near wake for low drag (a) 15° and high drag (b) 75° and (c) 255° leg positions. Far right images show rear view smoke patterns with arrows indicating rotation and location of the primary wake structures. Note timing of perspective and rear view images are not synchronised.

the back towards the centre plane. This is consistent with the flow remaining attached around the hip of the raised leg. Behind the rear base of the hips smoke particles trace a sharp downwards trajectory into the wake. The downwards path behind the hips is a result of the large downwash that is generated between the rear and upper hip vortex pair, which is located close to the centre plane of the mannequin in the asymmetrical flow regime.

The differences in the wake flow between the two flow regimes is further highlighted by smoke patterns visualised in cross sections of the wake using a laser sheet. Figure 3.27 shows snapshots of smoke released over the left shoulder for 15°, 75° and 330° leg

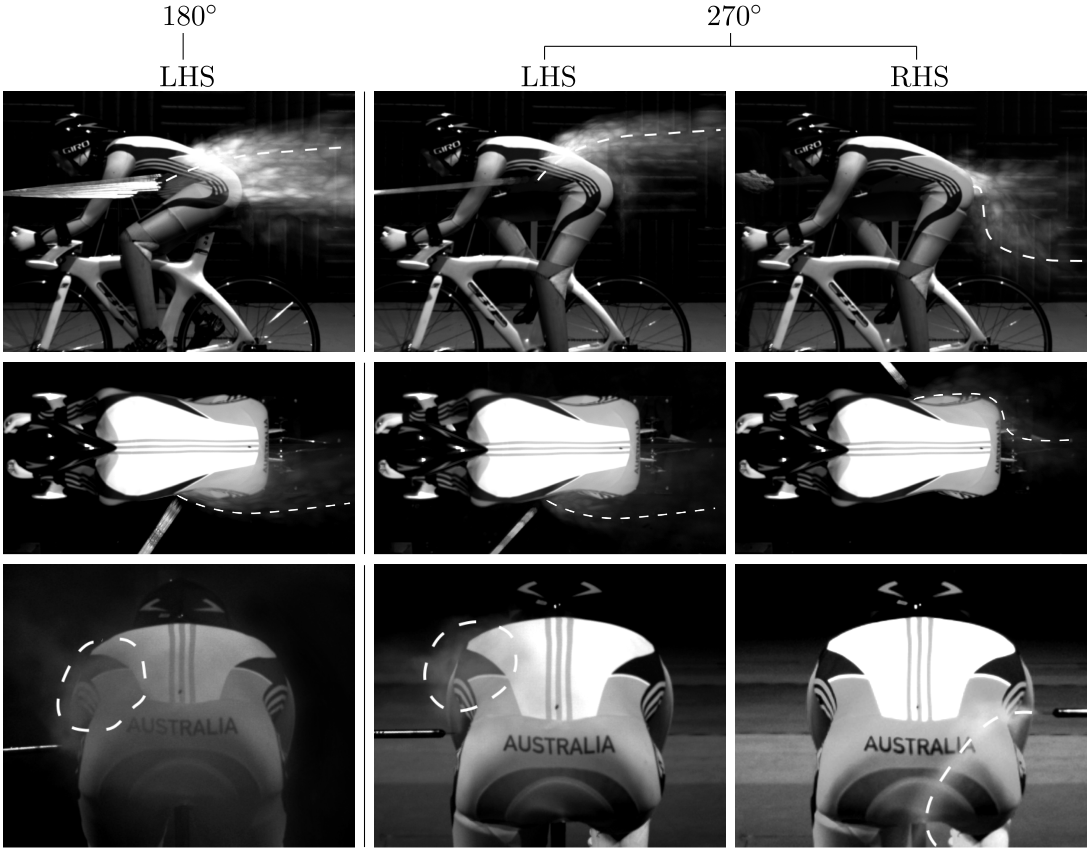

FIGURE 3.26: Flow visualisation of smoke injected at the side of the mid torso for low drag 180° and high drag 270° leg positions.

positions, that is visualised using a laser sheet to illuminate the centre plane of the mannequin. For the low drag 15° position, the smoke released over the back is confined to the upper wake regions projected behind the torso as a result of the flow separation from the lower back, which divides flow coming up from underneath the torso and legs. Below the lower back separation point video footage reveals a small closed recirculation region behind the hips which is shown by the dashed line in figure 3.27(a). In contrast to this, for the asymmetrical leg positions, the smoke flows over the back and takes a sharp downwards trajectory into the wake below the base of the lower hips as a result of the downwash that is generated between the primary upper and rear hip vortices. The strong downwards motion of the smoke into the wake behind the mannequin was observed throughout all leg positions in the asymmetrical flow regime. This was found even for leg positions approaching the transition point to the symmetrical flow regime, which is highlighted in the figure 3.27(c) for the 330° leg position.

Visualisations of the flow over the back show that leg position not only affects the flow in the wake of the mannequin but also over the entire upper body. As the left

(a) 15°

(b) 75°

(c) 330°

FIGURE 3.27: Flow visualisation snapshots of smoke injected over the upper left shoulder using a laser sheet to illuminate the centre plane of the mannequin for low drag (a) 15° and high drag (b) 75° and (c) 330° leg positions.

hip angle opened, smoke released over the upper left shoulder is drawn across to the centre plane of the back as depicted in figure 3.28 for the 270° leg position. As the hip angle is closed up, the smoke takes a straighter trajectory over the back and into the wake flow. Smoke visualisations showed the flow separated from the shoulders for all leg positions tested, around where the skin-friction lines from the oil flow visualisations on the shoulder were observed to converge together. Results presented in Chapter 4 show that this is a very unsteady process that involves the separation and subsequent reattachment of the flow further down the back. For the asymmetrical leg positions this unsteady process results in the smoke being spread over a wide area of the wake as indicated by the two dashed lines drawn on figure 3.28 for the 270° leg position. When the flow separates from the shoulders the smoke takes a high trajectory into the wake. Flowing the reattachment of the flow, smoke takes a downwards trajectory into the wake.

Asymmetries in the flow over the back are also observed in wool-tuft flow visualisations. Figure 3.29(a)–(c) shows instantaneous images of the wool-tufts for 0°,90° and 270° leg positions, whereas figures (d)–(f) show images reconstructed from processing video footage of wool-tufts. The processed images were produced using the same technique previously described at the beginning of this section. Again, they simulate a time exposure image of the motion of the tufts throughout the duration of video footage. Like the processed images of the smoke visualisations, these images provide additional information about range of motion of the tufts, aiding in the interpretation of tuft flow visualisation. The centreline long wool-tuft attached to the trailing edge of the helmet, depicts both symmetrical and asymmetrical flow regimes over the upper body of the mannequin, as the legs were stepped in 10° increments around the crank cycle. For the 0° leg position, figures 3.29(a) and (d) show the movement of the long wool-tuft is constrained to a symmetrical pattern about the centreline of the back. For leg positions in the asymmetrical flow regime, in the first half of the crank cycle the long tuft follows a 'S' pattern over the back and in the second half a reflected 'Ƨ' pattern is observed. This can be seen in both the video snapshots and the processed images of wool-tuft flow visualisations for the 90° and 270° leg positions in figure 3.29.

Shorter tufts placed on the hips and mid torso show the major separated regions that influence the flow symmetry over the back. Similar to the smoke patterns, the chaotic motion of the tufts attached to both sides of the mid torso and hips for the 0° leg position show the flow is completely separated. In contrast to this video snap shots and processed images of the 90° and 270° leg positions show large asymmetries in flow separation from left and right sides of the torso. These asymmetries are consistent with surface oil flow visualisations and results in the 'S' and 'Ƨ' patterns of the long

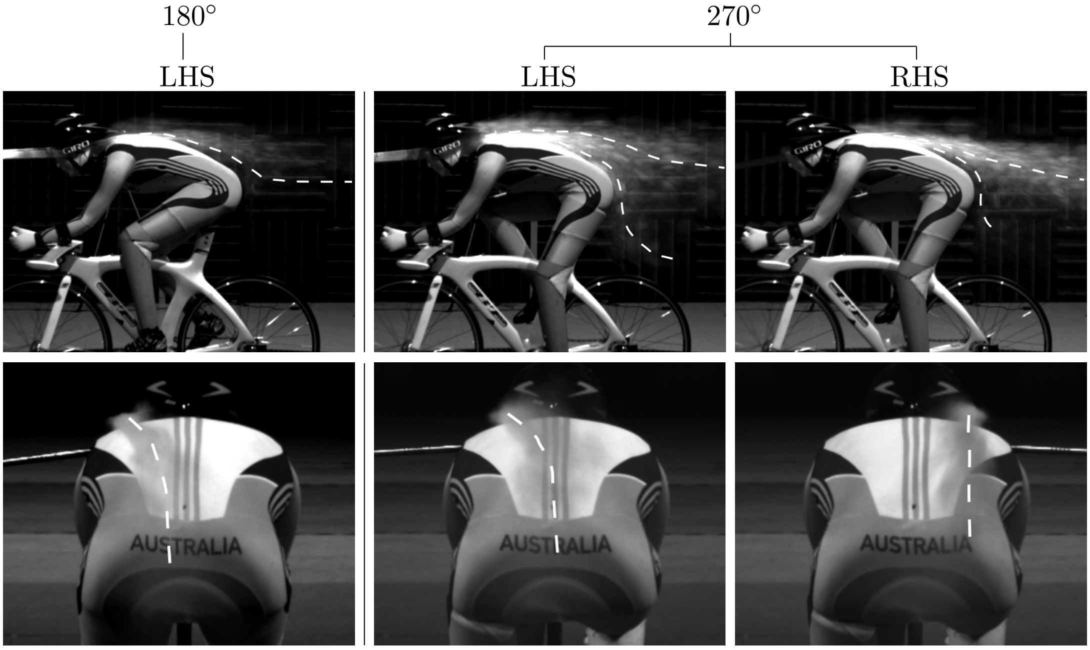

FIGURE 3.28: Flow visualisation of smoke injected to the left-hand side of the helmet for low drag 0° and high drag 270° leg positions.

centreline tuft. On the side of the body where the leg is in an extended position, the rapid motion and 'lifting' of the tufts from the surface of the mid torso shows that the flow is separated. On the opposite side of the body, where the leg is in a raised position, tufts fixed to the mid torso exhibit small fluctuations and do not lift from the body, showing the flow is attached.

The chaotic motion of tufts fixed to the hips highlight the turbulent wake that develops behind the rear base of the mannequin. As expected, the tufts show that the size of the wake increases behind the legs as the hip angle is opened. Chaotic fluctuations (indicated by the bar showing the range of motion of the tuft) of the tuft behind the extended leg for the high drag leg positions are approximately twice as large as that observed in the wake of the hips for the lower drag leg positions, where the hip angle of both legs is much smaller. For the high drag leg positions tufts positioned on the hip of the raised leg show a very different motion and indicate the presence of the rear hip focus with the tufts wrapping around the raised hip in a circular pattern. The low pressures associated with the rear hip focus results in the free end of the long centreline tuft being drawn across the base of the lower back. Video footage reveals that the free end of the long tuft and the rear hip tuft would often curl around each other in a circular pattern. This is a result of both tufts being drawn into the core regions of the rear hip vortex, and is depicted in the snapshot shown in figure 3.29(c)

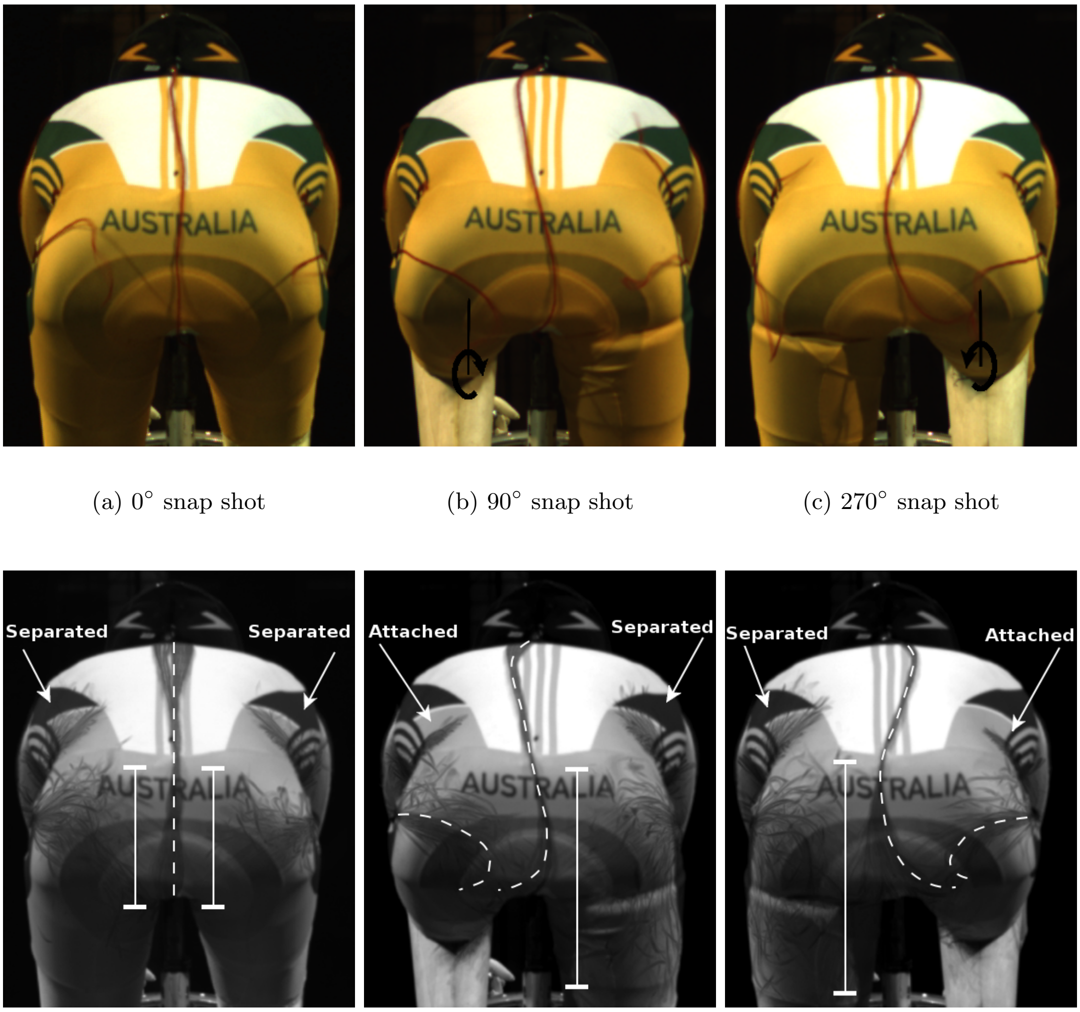

(a) 0° snap shot (b) 90° snap shot (c) 270° snap shot

(d) 0° path history (e) 90° path history (f) 270° path history

Figure 3.29: Long wool-tuft flow visualisations showing instantaneous snapshots of tufts for (a) 180°, (b) 90° and (c) 270° leg positions. Lower images (d) 0°, (e) 90°, (f) 270° show path histories of wool-tufts, from video recordings.

for the 270° leg position.

Visualisations of smoke released over the arms show how leg position affects the flow that develops downstream of the shoulder, upper arm and elbow for both symmetrical and asymmetrical flow regimes. Smoke released over the shoulder apex for 180° and 270° leg positions is visualised in figure 3.30. The smoke patterns outline the shear layer that divides the separated regions in the wake of the shoulder (a combination of both the wake shed from the shoulder and flow separation from the side of the torso) and the streamlines associated with the higher momentum flow that are deflected around the shoulder. The left shoulder smoke pattern for both leg positions is similar and

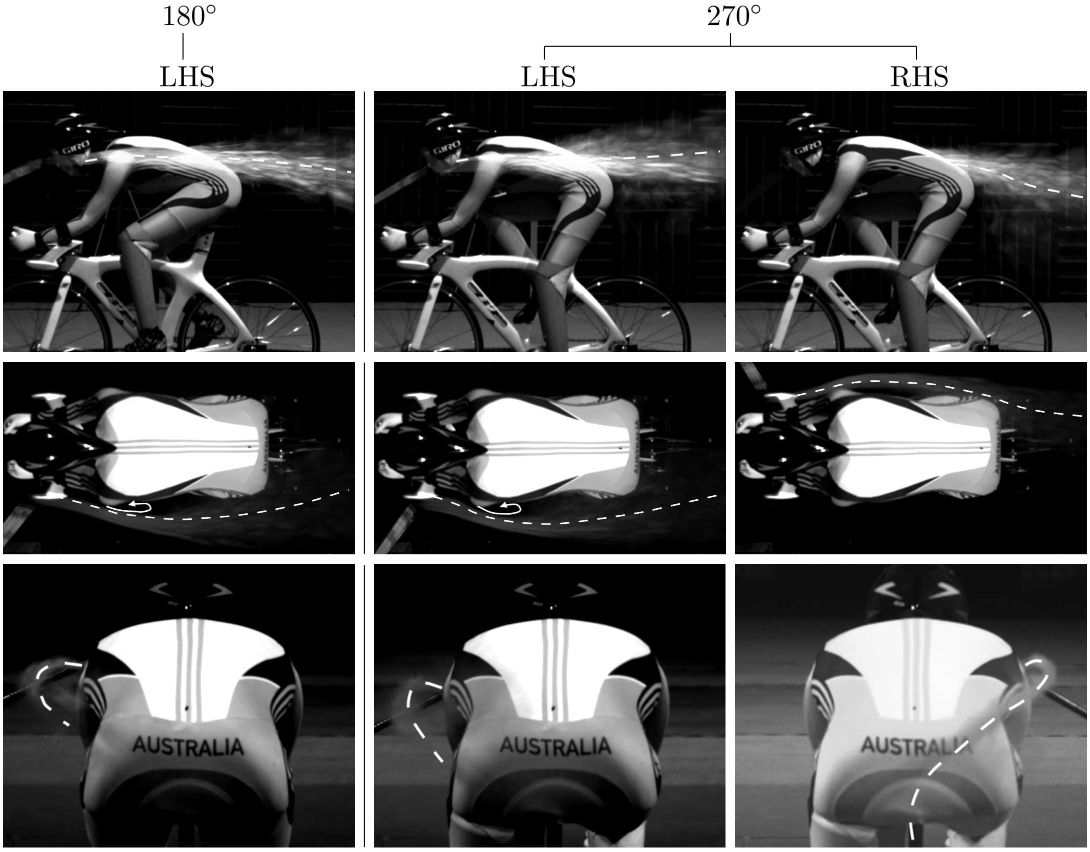

FIGURE 3.30: Flow visualisation of smoke injected at shoulder apex for low drag 180° and high drag 270° leg positions.

shows a relatively large separation region behind the shoulder. Smoke released over the right shoulder for the 270° leg position, where the leg is in a raised position, remains concentrated very close to the right side of the torso, showing a much smaller wake region downstream of the arms.

As the smoke is released closer to the surface of the upper arm (in-line with the armpit) more of the smoke is entrained into the separated flow regions and highlights the wake downstream of the arm. As we have already seen, smoke released close to the left arm of the 180° and 270° leg positions (hip angle is open) visualised in figure 3.31 shows the flow is completely separated and is shed high into the wake. Smoke released close to the arms on the side of the body where the leg is in a raised position however, shows the smoke flows around the sides of the torso and over the lower back towards the centre plane of the mannequin where the smoke then traces a sharp downwards path into the near wake. This flow pattern is visualised in figure 3.31 for smoke injected close to the right upper arm of the 270° leg position. The smoke trajectory over the body follows the '$L_{S,2}$' separation line traced by the surface oil flow visualisations on the side

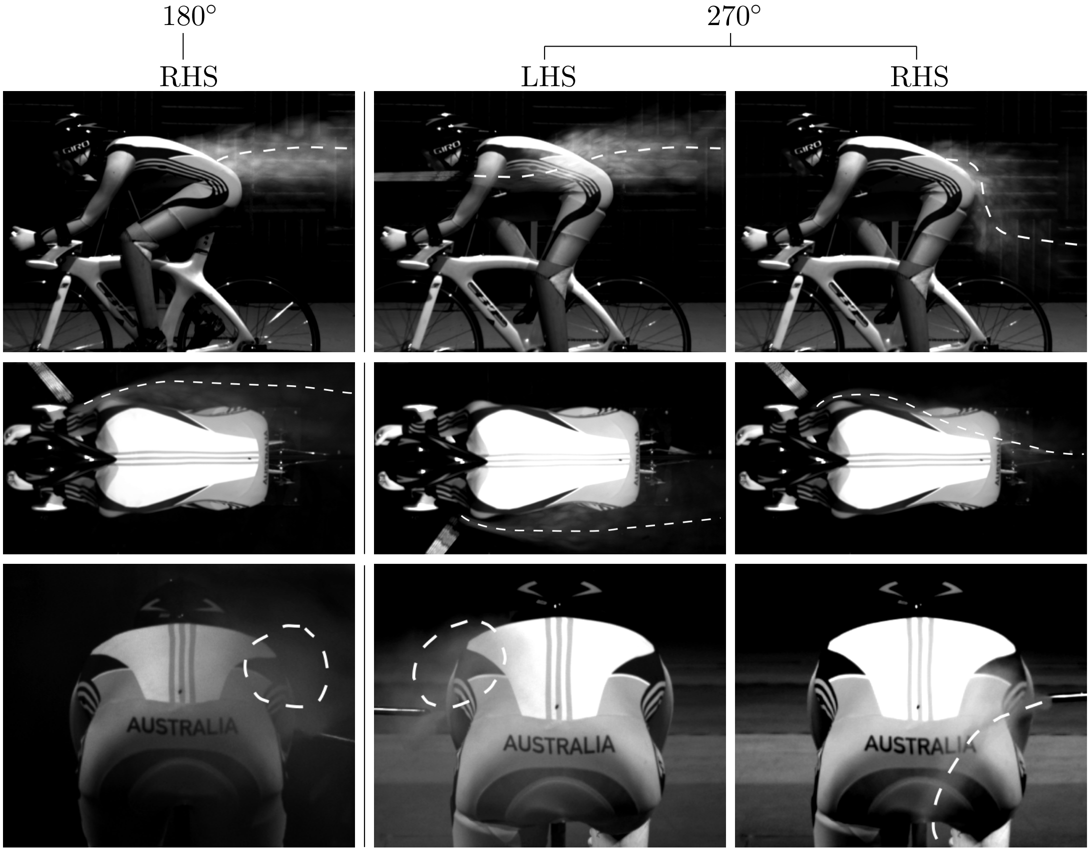

FIGURE 3.31: Flow visualisation of smoke injected at upper arm for low drag 180° and high drag 270° leg positions.

of the torso where the leg was raised. This is consistent with smoke being concentrated within the low pressure core of the upper arm vortex that was described in the previous section and was hypothesised to have a large effect on flow separation from the side of the torso where the leg was raised. Further evidence in support of this is provided by visualising the smoke released over the upper arm close to the body of the mannequin using a laser sheet to illuminate a slice of the flow at the mid torso, which is shown in figure 3.32. Smoke released over the upper left arm, where the left leg is raised for the high drag 75° leg position, shows the smoke remains concentrated very close to the body of the mannequin in the laser sheet. For the 15° and 255° leg positions, smoke visualised in the mid torso plane shows the flow from the arms does not reattach to the body at all, remaining divided from the body by flow wrapping around the side of the torso from underneath the stomach. Scattered light from the smoke illuminated in the laser sheet also highlights the downward smoke path across the hip of the raised leg, once again showing the large influence the upper and rear hip vortices have on the near wake flow and flow structures that develop upstream of the hips.

(a) 15°　　(b) 255°　　(c) 75°

FIGURE 3.32: Flow visualisation of smoke injected at upper arm for low drag and high drag leg positions using a laser sheet to illuminate the mid torso plane.

The influence of the upper arm vortex on smoke patterns was also observed when smoke was injected around the elbow joint of the mannequin. This can be seen in figure 3.33, which shows snapshots of smoke split around the left elbow joint illuminated by central, mid torso and near wake laser sheets, for the low drag (15°) and high drag (75°, 255°) leg positions. From the different slices, the development of smoke patterns over the body and into the wake can be analysed for each flow regime. Although smoke on the sides of the torso was not concentrated in the central plane, light scattered by the smoke in the sheet was adequate to visualise the smoke around the side of the torso (dashed lines are drawn to aid in interpretation of these smoke patterns). For all leg positions the snapshots show that as the smoke is split around the elbow joint, smoke entrained into the upper arm vortex resulted in the transport of smoke from the elbow joint up the arm. This is a result of vorticity generated on the upper arm being convected up towards the shoulder apex. This had the effect of creating a 'smoke curtain' effect along the whole side of the left torso, as smoke concentrated in the wake along the length of the arm was shed downstream over the sides of the torso and into the wake flow behind the mannequin. This was ideal for visualising secondary vortex structures that develop along the side of the torso.

Smoke patterns downstream of the elbow joint are once again characteristic of symmetrical and asymmetrical flow regimes. For the 15° and 255° leg positions a similar smoke pattern is observed in the mid torso plane in figures 3.33(a) and (c). Smoke that was split round the outside of the elbow once again highlights the separated flow from

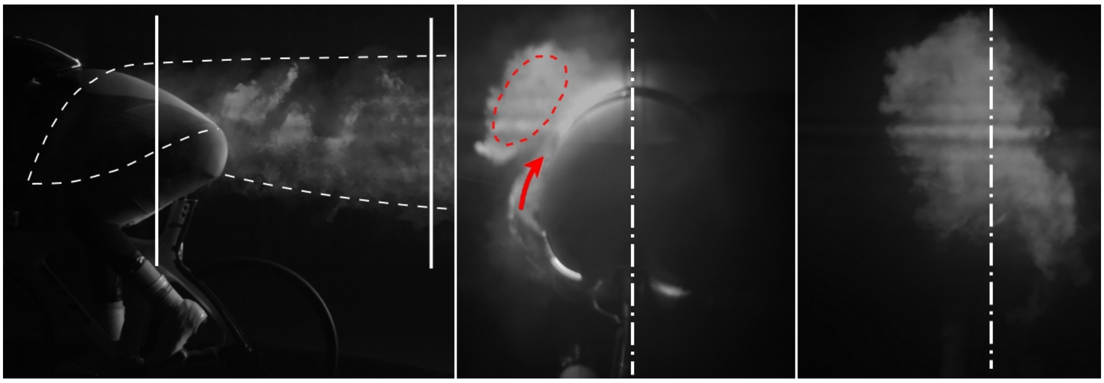

(a) 15°

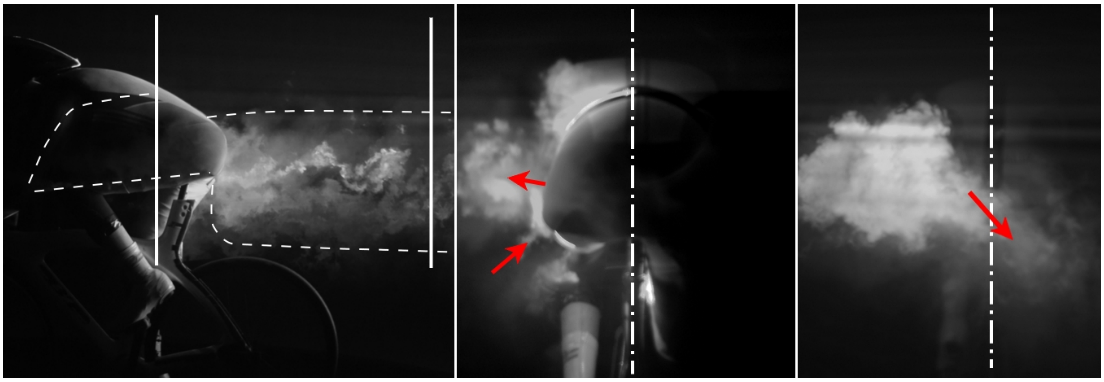

(b) 75°

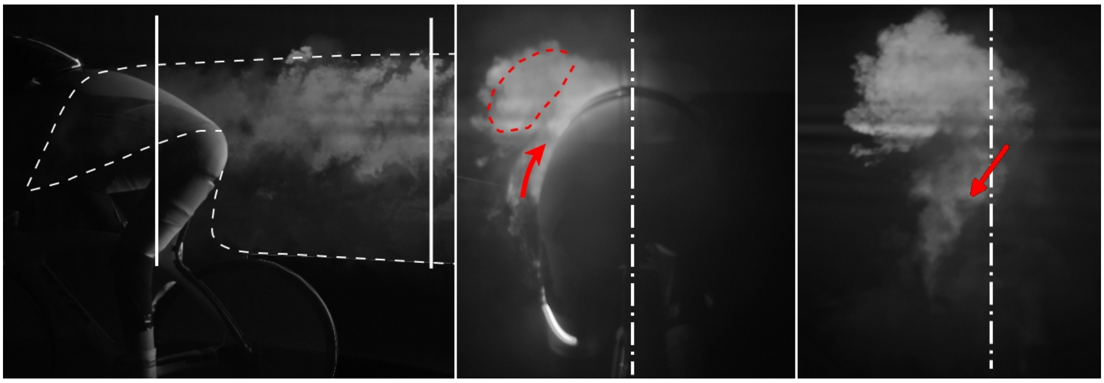

(c) 255°

FIGURE 3.33: Flow visualisation snap shots of smoke injected at elbow joint using a laser sheet to illuminate central, mid torso (plane 2) and wake planes (torso chord length: plane 5) for low drag (a) 15° and high drag (b) 75° and (c) 255° leg positions.

the arms that is carried up into the wake above the torso and is highlighted by the dashed lines enclosing the separated region. Smoke divided on the inside of the elbow however can be seen to flow up around the sides of the torso, as indicated by the curved arrows. For the 75° position, the smoke pattern shows that smoke divided around the outside of the elbow is concentrated within elbow and the upper arm vortex regions, and smoke divided on the inside of the elbow is concentrated in the inner thigh vortex under the raised leg. Video footage and photographs of smoke flow visualisations at the mid torso plane show two 'jets' of smoke on the hip of the raised leg, which are indicated with arrows in figure 3.33(b) for the 75° leg position. The arrow directed away from the hip is consistent with a jet generated between the elbow vortex pair, whereas the arrow directed towards the lower corner of the hip indicates smoke was concentrated within a jet between the inner thigh vortex and the lower vortex of the elbow vortex pair.

As the flow develops in the wake of the mannequin, figure 3.33 shows very different smoke patterns arise in the laser sheet orientated in the wake (plane 5: one torso chord in the wake) between all of the leg positions. For the 15° position, despite the smoke being released on the left side of the body, the smoke pattern in the wake laser sheet is evenly distributed about the centre plane of the mannequin. This further highlights significant mixing of flow and interaction of flow structures that originate from both sides of the body in the symmetrical flow regime. For the high drag 75° and 255° leg positions, smoke released around the left elbow joint predominantly remains concentrated on the left side of the body. When the hip angle is open smoke released around the elbow is shed high into the wake, when the angle is closed smoke remains concentrated in the lower regions of the wake. Unlike the symmetrical leg positions, for the asymmetrical leg positions smoke traces the characteristic downwards path into the wake behind the hips. This is once again due to the large down wash that is generated between the primary rear and upper hip vortices. The downwards path of the smoke in the wake behind the hips is represented by the bottom dashed line just above the rear wheel in the snapshot of the smoke pattern illuminated by the centre plane light sheet for the two high drag leg positions.

3.1.4 Cycling Computational Fluid Dynamics

With improvements in meshing methods, increases in computing power and advances in turbulence modelling and prediction of flow separation, computational fluid dynamics (CFD) is now capable of being practically utilised to investigate viscous flows around complex three-dimensional geometries such as a cyclist. As outlined in a review of the impact of CFD in sport by Hanna (2002), CFD is being increasingly used to solve aerodynamics problems in sports ranging from car racing such as formula one, yacht racing, swimming, soccer, cricket and cycling, to name a few. In recent years numerical codes have been used to simulate flows around bicycle components such as wheels (Godo *et al.* 2009, 2010), and investigate the aerodynamics of different rider positions (Defraeye *et al.* 2010a,b, 2011). There are many benefits to using CFD to investigate rider aerodynamics as it enables information about the flow field around a cyclist system to be obtained which would otherwise be a extremely difficult or prohibitively time consuming process to obtain experimentally. CFD has the potential to solve for the entire flow field that is resolved not only in space but in the time domain as well. Also numerical simulations allow for the aerodynamic forces acting on a cyclist system to be decomposed into the viscous and pressure force components, which can be evaluated independently. Large parametric studies of the effect of position/equipment can be performed by running multiple simulations in parallel and the relative contribution to the overall drag of aerodynamic forces acting on specific parts of the cyclist system, such as the helmet, arms, torso, legs and bicycle, can also be calculated.

Paramount to the successful application of CFD in cycling is the means to ensure that numerical codes accurately capture the fundamental flow physics that determines the aerodynamics of the system been modelled. Currently there is very little research published on CFD in cycling with direct comparison to experimental results or the use of CFD to investigate the flow structure in the wake of a cyclist. In order for computational fluid dynamics to progress in cycling, researchers and sports scientists must have confidence in results obtained from CFD simulations. As part of the wider research program into cycling aerodynamics that includes this thesis research work, the flow around the cycling mannequin has being modelled using numerical methods by a post-doctoral fellow Griffith *et al.* (2012). This work, together with wind tunnel experiments has contributed to the interpretation of the flow topology around a cyclist. These simulations were performed in parallel with mannequin wind tunnel experiments for static leg positions around a complete crank cycle so that numerical results could be directly compared with experiments. This section provides a brief overview of how our new understanding of the flow topology around a cyclist, developed in the previous sections, has contributed to the refinement and validation of numerical simulations. In comparing numerical simulations, which solves for the entire flow field, with the wind tunnel experiments a greater appreciation for the structure of the wake is gained.

3.1.4.1 Validation of Numerical Simulations

Numerical investigations into the flow around the mannequin using Reynolds-Averaged Navier-Stokes (RANS) based models were performed using the commercially available ANSYS-CFX solver and modelling package by Griffith *et al.* (2012). The geometry of the rider and bicycle frame, shown in figure 3.34, is representative of the mannequin cycling system. A computational model of the mannequins head and helmet has been obtained from scanned data, and the torso, arms and legs are based on the CAD models originally developed in the construction phase of the mannequin. The bicycle model is based on a simplified model of the frame with major dimensions matching those of the track bike used in wind tunnel experiments.

The numerical domain size was large enough so that it had negligible effect on results and a comprehensive grid resolution study resulted in simulations using approximately 27 million elements. Simulations were consistent with wind tunnel experiments, modelling the flow around the mannequin for a range of static leg positions at a freestream velocity of 16 m/s. Both steady state and transient simulations have being compared with experimental results using a range of turbulence models, however only numerical results obtained using the Shear Stress Transport (SST) and the Scale-Adaptive Simulation Shear Stress Transport (SAS-SST) are discussed here. These particular turbulence models have been shown to be well suited for strongly three-dimensional flows without geometrically fixed separation points, and have also been found to produce reasonable agreement with experiments when used in numerical simulations of flows around rider geometries (Defraeye *et al.* 2010a). Comparing results between these turbulence models and experimental results shows one example of how mannequin wind tunnel testing has resulted in the identification of numerical modelling techniques that provide the most accurate description of the flow around a cyclist. For a more detailed description of the numerical simulations of the flow around the mannequin see Griffith *et al.* (2012).

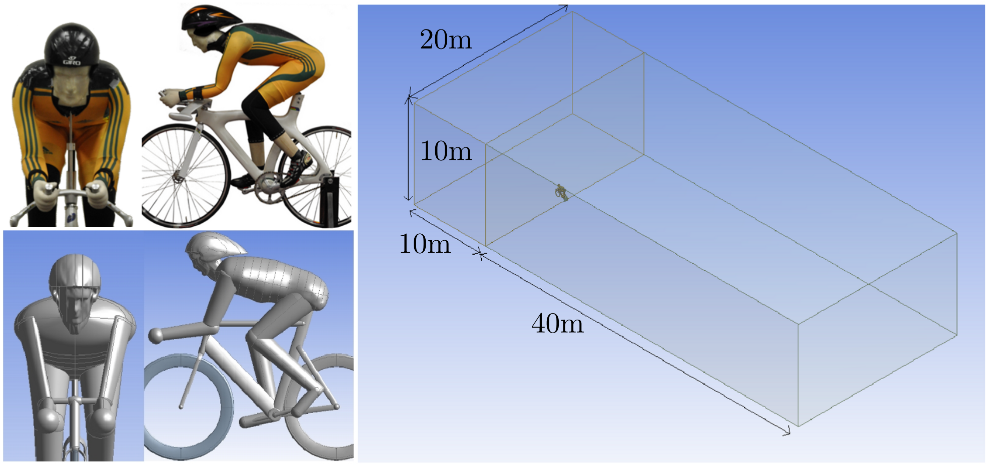

FIGURE 3.34: A sketch of the geometry used in the numerical model, along with the computational domain, from Griffith *et al.* (2012).

Figure 3.35 compares the variation in drag area obtained from time independent SST numerical simulations with that measured with the force balance in the MLWT. The most obvious difference between the experiments and the numerics is that the simulations under-predict the drag area values by $\approx$ 13–14%. Several possible reasons have been identified, and are listed below, that may account for the lower drag results:

1. The geometry of the simulated model is not an exact replica of the mannequin used in the wind tunnel experiments.

2. The bicycle frame and wheels in the numerical simulation is of a much simpler design and rear wheel mounting struts used in the experiments were not modelled (SST model).

3. The effect of surface roughness on the boundary layer that develops over the mannequin is not modelled in the numerical simulations.

4. Variations in the inlet boundary conditions from those present in the wind tunnel.

5. Transient effects and numerical difficulties in simulating a high Reynolds number turbulent flow with a highly three-dimensional geometry.

In isolation all of these differences are likely to have relatively small effects, however the cumulative effect may lead to significant differences in the measured drag.

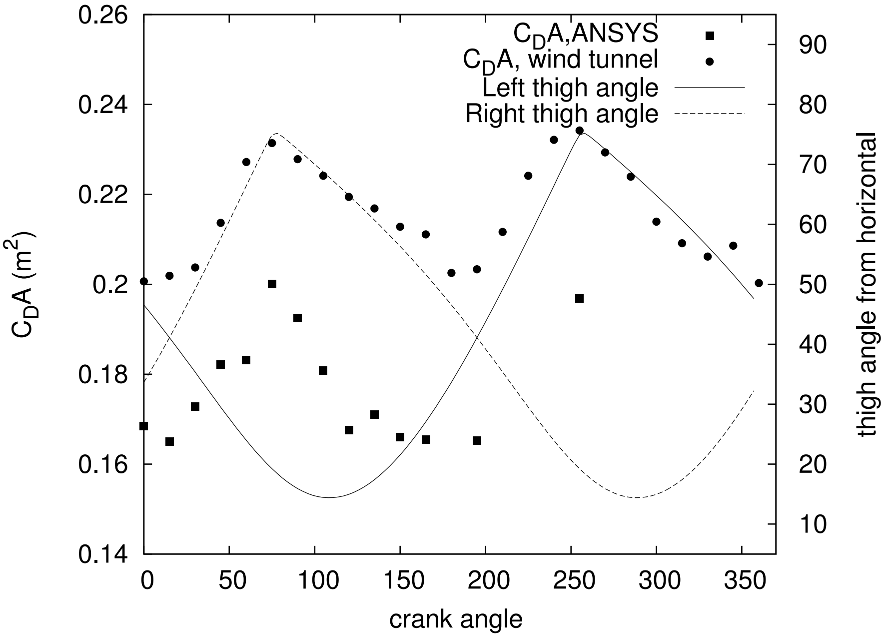

FIGURE 3.35: Plot of C_DA against crank angle for both wind tunnel measurements and ANSYS numerical simulations (points). Also plotted are the angles of each of the thighs from the horizontal (also known as hip angle ϕ), through the crank angle cycle (lines), from Griffith *et al.* (2012).

Although the exact values of the numerical drag area results are lower, the variation in drag over the course of the pedal stroke matches the experimental variation very well. The maximum and minimum drag values occur at the low and high drag leg positions in line with the experiments and the range of drag values determined around the pedal stroke also matches well that measured experimentally. The similar variation in the drag between the numerics and experiments suggests that the numerical simulations have captured the essential physics of the flow that results in the large variations in drag throughout the course of the pedal stroke.

From the mannequin wind tunnel investigations it was shown that the large variations in drag with leg position is primarily a result of a global change in the flow structure in the wake of the mannequin. To see if the numerical simulations accurately capture the primary flow structures, wind tunnel traverses performed in the wake of the mannequin with the four-hole pressure probe are compared with the simulated flow field at the same traverse locations. This can be seen in figure 3.36, which compares contours of the streamwise vorticity field obtained from the steady-state and time-averaged transient simulations with time-averaged wind tunnel traverses performed at planes 3 (hips), 4 (half a torso length in the wake of mannequin) and 5 (torso length in the wake of mannequin), for the 15° low drag and 75° high drag leg positions. Comparisons between the steady state SST simulations (top of figure 3.36) with experiments (bottom of figure 3.36) show mixed results for the two low and high drag leg positions. For the 75° leg position the SST model captures the asymmetries and the bias of the flow to the side of the body where the leg is in an extended position. The primary upper/rear hip counter-rotating vortex pair is also clearly evident in the numerical results. Comparisons for the 15° leg position however, show large variations in the wake structures between the numerically simulated and experimental results. The symmetrical flow regime for the 15° leg position is not observed in the time-mean simulations, with the wake more closely resembling that of the asymmetrical flow regime with the wake biased to one side. It was found that as the solution was iterated further towards convergence, the wake would flip to the other side of the body, never actually settling down, indicating a very unstable flow. This highlights a limitation of the time-mean solver, in that it is sometimes difficult to achieve a converged solution.

As a result of the large discrepancies in flow structures between experiments and the CFD model, numerical simulations were extended further to use the time-dependent SAS-SST solver. The time-average of these simulations provides a more accurate representation of the experimental results, however they are much more computationally expensive compared to obtaining time-mean solutions, requiring 10–15 times the computing time. The time-averaged drag values obtained using the transient model were not significantly different to those from the time-mean (SST) model, however the time-averaged wake structure compares much better (middle of figure 3.36) with experimental findings. For the 15° leg position, the transient solver reasonably simulates the time-averaged symmetrical low drag wake pattern and vortex structures. For the 75° leg position an improvement can be seen in the location, magnitude and size of the primary upper/rear hip vortex pair, as well as the inner thigh vortex that can be seen developing under the raised upper left leg.

As the CFD simulations solve for the entire flow field, a much more detailed structure of the wake flow can be obtained, which complements mannequin wind tunnel experiments where the nature of the time-averaged flow has to be derived from fragmented or incomplete information. Figure 3.37 shows isosurfaces of streamwise vortices for the low and high drag leg positions, where vortex structures have been identified using the 'Q' criterion from time-averaged transient flow simulations. Similar to the

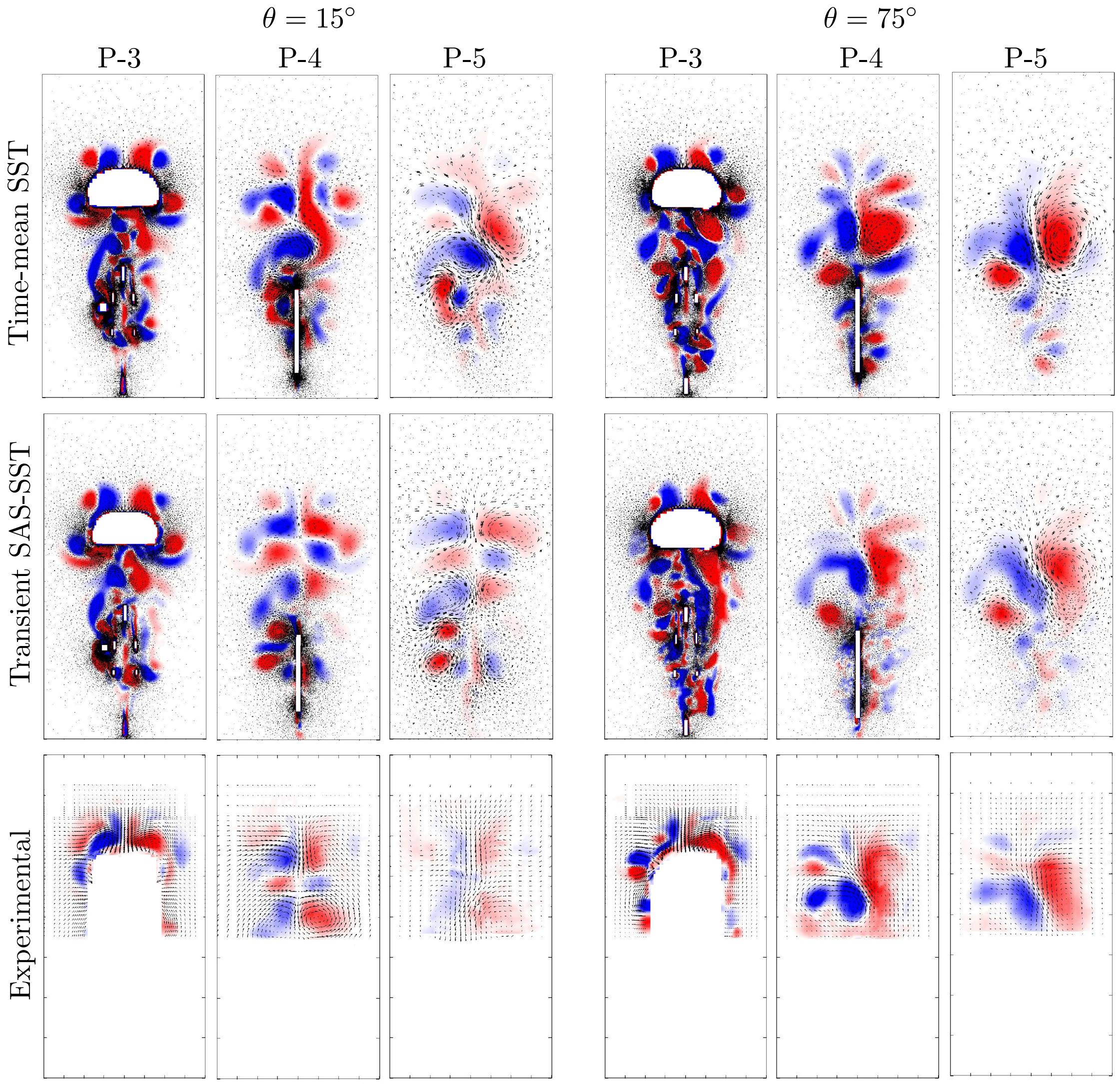

FIGURE 3.36: A comparison of contours of streamwise vorticity for steady state (top) and transient (middle) numerical simulations with the experimentally obtained vorticity fields. Both the simulated and experimental vorticity fields for low 15° (left) and high 75° (right) drag leg positions are shown at planes 3 (hips), 4 (half a torso length into the wake) and 5 (a torso length into the wake). Contours vary across the range $100s^{-1} \leq \omega \leq 100s^{-1}$, where blue is negative and red is positive (from Griffith *et al.* (2012)).

swirling strength criterion used to identify large-scale vortices from traverse data the dimensionally equivalent 'Q' criterion is also a vortex identification scheme based on the velocity gradient tensor (Carmer *et al.* 2008). Due to the significant increase in spatial resolution compared with experiments, the numerical simulations depict a more complete wake structure, resolving vortices of much smaller scale than possible with the experimental data. Despite the more complex wake structure educed from the CFD simulations, the major flow structures that were identified from the mannequin wind tunnel experiments (discussed in section 3.1.3) are consistent in the numerical results.

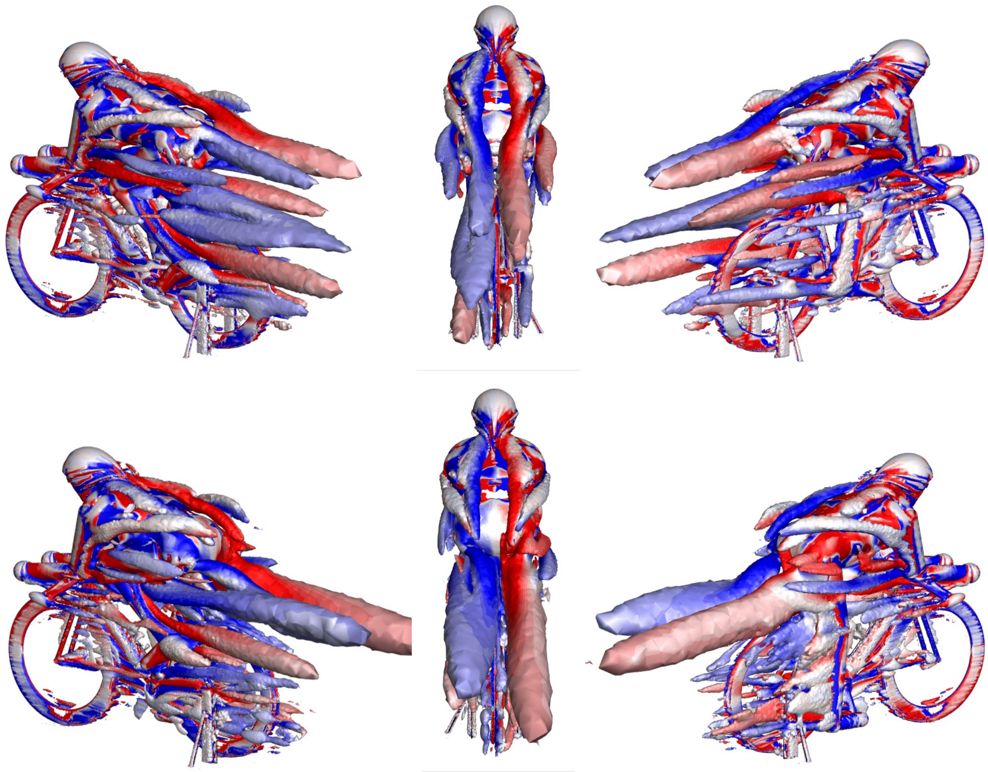

FIGURE 3.37: At top, the case for crank angle of 15 degrees and at bottom for 75°. Shown are left and right perspective views of iso-surfaces for a single value of the Q-criterion, coloured by streamwise vorticity calculated from velocity field transient average, where blue is negative and red is positive (from Griffith *et al.* (2012)).

For the symmetrical low drag 15° leg position figure 3.37 shows an even distribution of streamwise vortices that develop from the left and right sides of the body. As identified from the wind tunnel experiments, the large-scale features of the flow consist of a pair of streamwise vortices that can be seen to detach from the upper left and right upper hips, and a pair of vortices that develop between the legs from the inner left and right thighs that forms a quadruple structure in the wake with the vortices that develop above them. Many similarities are also evident between the numerical and experimental results concerning the smaller secondary vortex structures that are present in the wake of the helmet, upper arm and elbow joints.

As the formation of these flow structures is dependent on where flow separation occurs, it is no surprise that the areas on the body where separation is predicted by the time-averaged SAS-SST simulations compare well with the oil and paint flow visualisation studies. For the 15° leg position, figure 3.38 compares the skin-friction lines (also known as limiting streamlines) drawn on the numerical model with the surface oil flow patterns presented in section 3.1.3. The CFD simulations show the flow separates

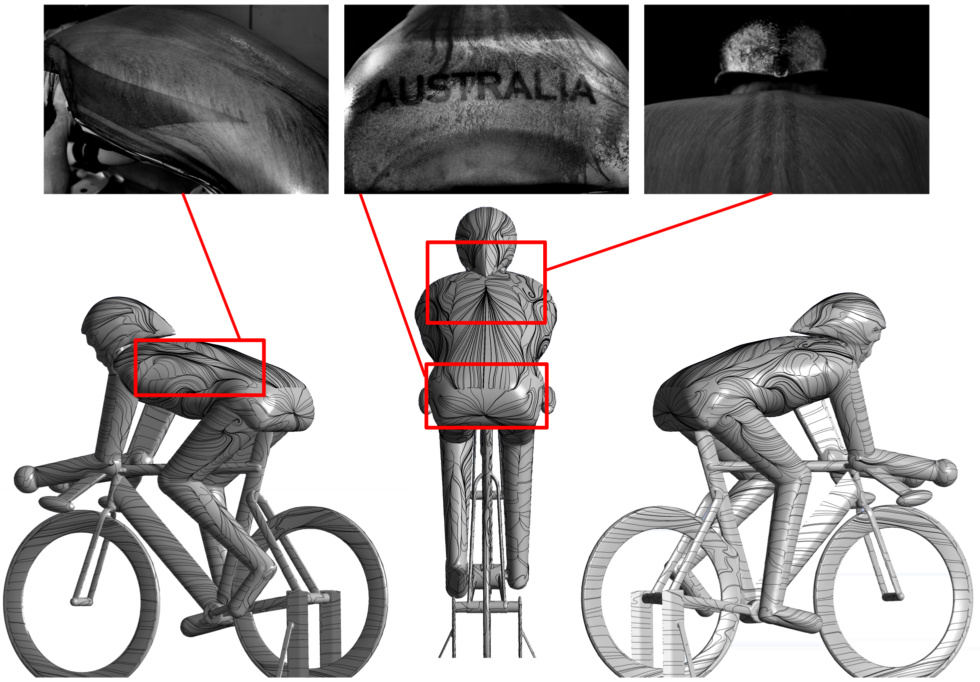

FIGURE 3.38: Comparision of surface oil skin-friction patterns with time-averaged limiting streamlines drawn on the wall boundaries of the numerical SAS-SST model for the low drag 15° leg position.

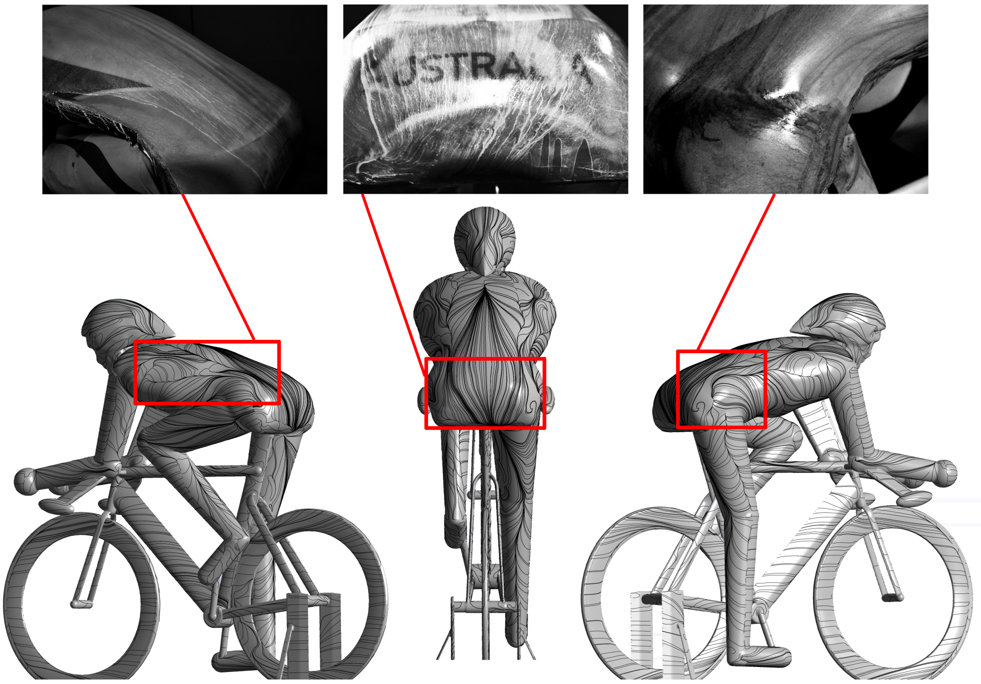

FIGURE 3.39: Comparison of surface oil skin-friction patterns with time-averaged limiting streamlines drawn on the wall boundaries of the numerical SAS-SST model for the high drag 75° leg position.

from both sides of the torso and the lower back where the upper hip vortices originate. Following the separation line from the lower back the limiting streamlines show the flow reattaching to the base of the mannequin on the rear of the hips. The attachment node just downstream of the trailing edge of the helmet is also visible. Apart from filling in many of the gaps in skin-friction patterns over the entire cyclist system, the similarities in numerical skin-friction patterns also builds further confidence in the interpretation of the experimental mannequin flow visualisation studies (i.e., there was negligible effect of gravitational force on the oil and paint pattern on the 3-D surfaces of the mannequin).

For the 75° leg position, similar to the major findings with the mannequin, figure 3.37 shows a large change in the wake structure compared to the low drag 15° leg position, with the simulated wake exhibiting the characteristic high drag asymmetrical flow pattern. The major wake structure is the large counter-rotating vortex pair that is orientated asymmetrically in the wake. Compared with the wake structures of the low drag flow regime, the large-scale vortices for the 75° leg position are stronger and penetrate much further into the wake. This is consistent with the mannequin findings. A comparison between the skin-friction lines and the surface oil flow visualisations for the 75° leg position, shown in figure 3.39, also yields a favourable agreement. The major separation lines on the torso sides and on the hip joint of the extended leg, as well as the asymmetries in the skin-friction distribution on the rear of the numerical model, are in good agreement with results obtained from the surface oil and paint flow visualisation studies.

Some minor differences in wake structures are evident between the numerical and experimental results. The wind tunnel experiments showed a lot more vorticity being shed into the wake higher up on the right hip of the extended leg compared to the CFD simulations. Also the strong elbow vortex pair that was identified in the wake of the elbow joint on the side of the body where the leg was in a raised position (left-hand side for 75° leg position) is not noticeable in figure 3.37 for the 75° leg position. However a similar structure that was not identified in experiments is observed in the numerical results in the wake of both elbow joints for the 15° leg position and in the wake of the right elbow joint for the 75° leg position. The flow around the arms, and the complex interaction between the advancing leg and the spacing between the elbow and knee joint (influenced by geometry, position, skin-suit type and Reynolds number), is an area of particular interest that is currently under further investigation using both numerical and experimental techniques.

3.1.5 Summary of the Time-Averaged Flow Structure Model

A time-averaged model of the wake structure of a cyclist has been proposed based on experimental wind tunnel investigations with a mannequin in a time-trial position. Force measurements showed large variations in the drag force as the mannequin's legs were stepped around the crank cycle. This was found primarily to be a result of a large change in the flow regime, which is dependent on leg position. Two characteristic flow regimes were identified that accounted for the main variation in the structure and topology of the flow throughout the crank cycle. For the leg positions tested these were:

a) the symmetrical low drag flow regime ($0° - 15°$ & $180° - 195°$) and

b) the asymmetrical high drag flow regime ($30° - 165°$ & $210° - 345°$) .

The primary feature of each flow regime consists of a large trailing streamwise vortex system. For the low drag symmetrical flow regime, the primary flow structures consist of a streamwise counter-rotating vortex pair that is formed evenly on both sides of the torso over the upper hip areas, together with a pair of vortices of similar strength and sign that originate between the inner thighs of both legs. The upper hip vortices are analogous to streamwise vortices (lifting) that develop over the tips of low aspect ratio wings as a result of a large pressure differential between the high pressure areas of the chest/stomach and the low pressure suction surfaces of the back. The inner thigh vortex structures form due to the inclination of the upper legs that are cylindrical in shape. As each pair is brought closer together in the wake behind the mannequin this results in a quadruple arrangement of similar sign and strength vortices orientated symmetrically about the centre plane of the mannequin. This symmetrical flow regime results in a beneficial contraction of the wake due to the mutual interaction of similar strength vortices of opposite sign.

As the wake transitions to the high drag asymmetrical flow regime the primary wake structures consists of streamwise vortices that develop when flow separates from the upper hip of the extended leg and the rear of the hip of the raised leg. These vortices form a large counter-rotating vortex pair in the wake that is orientated asymmetrically in the centre plane and constitutes the major source of the large variation in the drag force measured throughout the crank cycle. This primary vortex pair persists much further into the wake flow compared to streamwise vortices formed in the low drag symmetrical flow regime. As the legs progress around the crank cycle a wake integral analysis showed that the strength and interaction of the primary vortex structures is dependent on leg position. This pointed out that the optimisation of cycling aerodynamics cannot be assessed from frontal surface area alone and that the variation in the drag is much better explained through the effect that leg position has on the large-scale flow structures. The high dependence of the drag force on the formation, strength and interaction of the primary vortex structures suggests that there is a great potential to improve rider aerodynamics through a targeted approach at reducing the drag associated with these flow structures.

The development of a model of the wake structure for a cyclists has also been instrumental in the development of numerical simulations of the flow around a cyclist. The mannequin wind tunnel studies have also identified several areas where the model could be improved. Despite minor differences between experiments and the computational results the CFD simulations provided reasonable predictions of the variation in drag around the crank cycle, the major structures of the wake and where the flow will separate from the model. Although the CFD simulations are currently in the developmental stage, they have already helped in the interpretation of experimental findings. They have also aided in developing a more complete picture of what the flow looks like around a cyclist and how the flow is affected by changes in leg position. With confidence in our models provided by this general agreement, this has enabled more detailed investigations of the flow physics associated with the aerodynamics of a cyclist to be pursued, and also the optimisation of rider position and equipment to progress.

3.2 Surface Pressures

3.2.1 Effect of Crank Angle on Surface Pressures

In the previous sections the primary flow structures that develop throughout the crank cycle were identified and analysed, this section looks at the impact they have on time-averaged surface pressures. As the aerodynamic drag force is predominantly a result of the pressure drag, surface pressure distributions can be used to identify areas on the body where most of the drag is generated. Coupled with the flow visualisation studies, surface pressures also reveal the nature of the near wake flow structures and the location of separation and reattachment lines. Large changes in flow regimes and their effect on the drag force is also further emphasised through time-averaged surface pressure distributions, which vary significantly throughout a complete crank cycle.

3.2.1.1 Time-Averaged Results

Figure 3.40 shows contours of the time-averaged surface pressure coefficient on the suction surface of the mannequin's back for a complete crank cycle. Surface pressure distributions were reconstructed from surface pressures measured on the left-hand side of the mannequin for a complete crank cycle to show surface pressures spanning both left and right sides of the torso (i.e., pressure distributions across the centreline for opposing leg positions around the crank cycle are assumed to be symmetric, see section 2.4.4). Surface pressure measurements clearly show that leg position has a dramatic effect on both the magnitude and distribution of mean pressures throughout the crank cycle.

During the symmetrical flow regime, 0° and 15° leg positions display a characteristic symmetrical high pressure recovery distribution. The presences of the low pressure hip vortices on the sides of the torso are apparent. Where the flow separates across the back of the hips ($L_{S,2}$ symmetrical flow regime), there is a slight reduction in surface pressure followed by a significant increase, with the surface pressure peaking in the middle of the lower back. This is consistent with the reattachment of the flow to the base of the mannequin that is marked by an attachment node '$N_{A,2}$'. This is demonstrated in the proposed skin-friction lines that have been overlaid on the contours of the surface pressure coefficient for the 15° leg position.

As the leg progresses around the crank cycle surface pressure distributions become increasingly more asymmetrical with large pressure gradients. As the flow transitions to the asymmetrical flow regime large low pressure regions develop where the primary

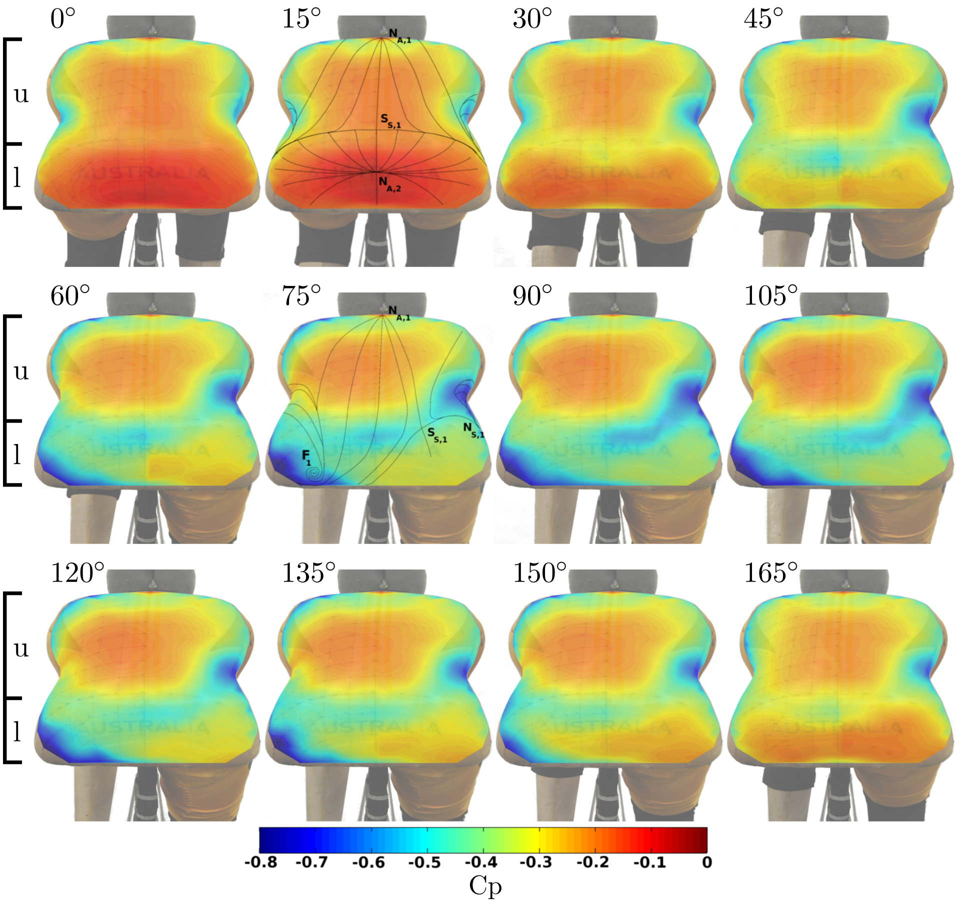

FIGURE 3.40: Surface pressure distributions showing the development of surface pressures throughout the first half of the crank cycle where 'u' and 'l' denote upper and lower regions of the back, respectively.

upper and rear hip vortex pair develop on the surface of the mannequin. This is clearly shown for the 75° leg position in figure 3.40, which also shows the skin-friction flow topology for the asymmetrical flow regime overlaid on the surface pressure contours.

A good indication of the large variation in time-averaged pressures can be found by comparing centreline pressures for the different leg positions. The evolution of the centreline pressure distribution is shown in figure 3.41 for selected leg positions around the first half of the crank cycle. The large differences and 'grouping' behaviour of the distributions for the low and high drag leg positions is clear. Over the first 70% of the back similar trends in the pressure distributions are seen for all leg positions around the crank cycle. The initial favourable pressure gradient between $(0.15 < x/c < 0.30)$ for both low and high drag leg positions is a result of the acceleration of the flow over the shoulders post reattachment behind the helmet. This is followed by a pressure recovery region $(0.30 < x/c < 0.55)$ that begins approximately where the gradient of

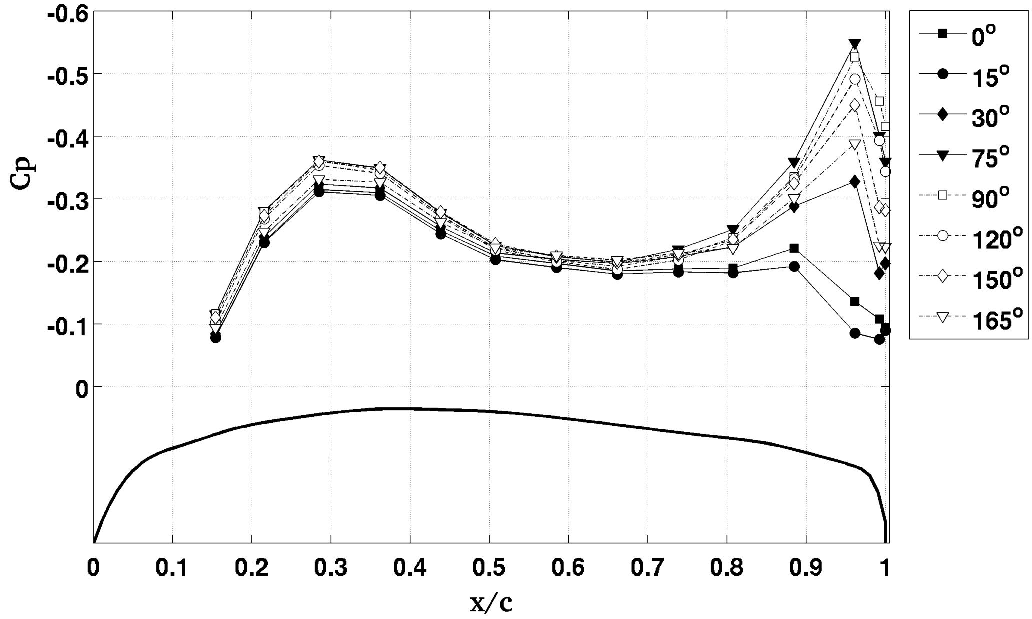

FIGURE 3.41: Centreline pressure distributions for selected leg positions around the first half of the crank cycle. Note back centreline is drawn from a 0° angle-of-attack position.

the back transitions to a downwards slope. For the low drag leg positions pressures remain relatively constant from around where the upper hip vortices begin to form up until the upper hips, where flow separation occurs ($0.55 < x/c < 0.90$). For the high drag leg positions, following the pressure recovery region of the upper to mid back, a gradual increase in the pressure gradient is observed with downstream direction. This is a result of both the curvature of the back and the strong vortex being formed over the upper hip of the extended leg. The favourable pressure gradient extends much further down the lower back for the high drag leg positions, until a strong adverse pressure gradient is observed where the flow separates. This is consistent with the flow visualisations where the flow remained attached much longer down the centreline of the back for the asymmetrical leg positions, compared to leg positions where the upper thighs were more aligned.

For the high drag leg positions all centreline tap locations exhibit low pressures compared to when the upper thighs are more aligned. The largest differences in the distributions are observed in the lower back regions. As the legs are stepped around from the 0° leg position mean pressures initially show a slight increase in the pressures acting on the rear of the mannequin (15°), which is quickly followed by a dramatic reduction in the pressure, as the flow transitions to the asymmetrical flow region at $\approx 30°$. Narrowing

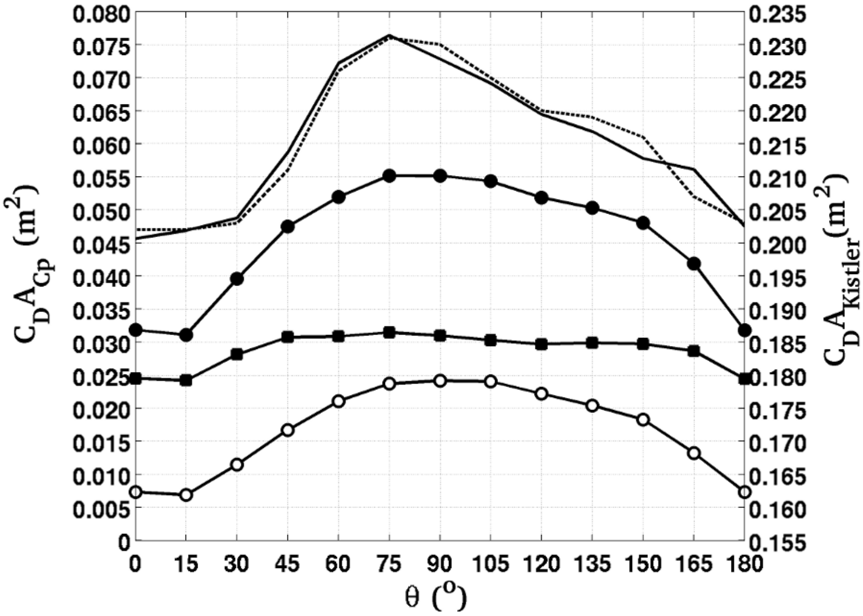

FIGURE 3.42: Left-hand axis: suction drag as a function of crank angle from; back total (–•–), upper back (–■–) and lower back (–○–). Right-hand axis: drag measured by Kistler force balance with standard config. (—) and with fibre-glass config. (···) minus 0.023 m^2 offset. Note both axes are of the same scale.

in on the centreline pressures measured at the tap located approximately in line with the hip joint ($x/c \approx 0.96$), base pressures continue to fall until the high drag 75° leg position. Following this peak in negative pressure a gradual increase in pressure is observed with the general shape of the distribution maintained.

3.2.1.2 Integral Analysis of Surface Pressures

The large differences in the pressure forces acting on the lower back with leg position and the large contribution to the drag from the back is further emphasised by integrating the pressure distributions. The suction drag on the back (with reference to the freestream static pressure) has been calculated by integrating the surface pressure coefficient over the area of the mannequin's back that is normal to the freestream direction. Figure 3.42 compares the suction drag on the back of the mannequin with the drag measured directly using the Kistler force balance. As previously discussed in section 2.4.4 force measurements with the fibreglass configuration resulted in an $\approx 0.023m^2$ increase in the mean drag compared to the standard skin-suit set up. When the mean offset is subtracted from the fibreglass set up however, force measurements with the two different configurations collapse onto one another, suggesting the mechanisms causing the variation in drag with leg position are consistent between the two set ups.

Although the suction drag from the back only accounts for 12–20% of the total drag throughout the crank cycle, its importance arises from the fact that it accounts for more than 60% of the variation in drag between the low and high drag leg positions. The relative contributions of upper and lower back regions, which contain the formation region of each of the primary vortices, to the total back suction drag is also shown where the upper and lower sections of the back have been marked in figure 3.40 with 'u' and 'l' respectively. As a result of the large change in the pressure distribution on the lower back where the rear hip vortex originates, and also the fact that the lower back surfaces are primarily aligned with the drag producing direction, more than 75% of the variation in the back suction drag is a result of the surface pressures acting on the lower back below the upper hips.

3.2.2 Effect of Rider Position on Surface Pressures

As identified in the literature review of cycling aerodynamics small changes in rider position can result in large changes in the drag force. This may suggest that only minor changes in the position the rider are required to complete reorganise the mean structure of the flow. As we have already seen with changing leg position, a major change to the flow topology is usually accompanied by a large change in the pressure distribution and hence the drag force. While also identifying low drag positions (not associated with leg position), in this section the sensitivity of the primary flow structures to changes in rider position is investigated. This is achieved by comparing pressure distributions on the back, where the primary vortices form, for a range of different upper body positions with the 'standard position discussed thus far. In addition to this, Kistler force measurements for new positions are also compared with force measurements of the standard position.

The investigations into rider position have targeted particular position changes that could significantly affect the drag force by altering the formation of the primary flow structures. The first aspect of position investigated is the effect of arm position, achieved by adjusting the spacing between the elbow joints. There is considerable anecdotal evidence and studies into rider position (Kyle 1989; Broker 2003; Oggiano *et al.* 2008) that suggest arm position can have a large effect on drag. The arms are located directly upstream and in line with the hips where primary vortices originate. As a result, the wake that develops downstream of the arms may have a large effect on the formation process of primary vortex structures. This may either be through affecting the development of the boundary layer prior to the major flow separation lines or altering the complex interactions between the wake shed from body parts as the relative positioning between them is altered.

The second change to rider position investigated was angle-of-attack of the torso. As a rider sits up more on the bicycle, apart from the increase in the projected frontal area, the spacing between the upper thighs and stomach is changed. This may have a significant effect on how the flow develops between the legs and up around the sides of the torso and hips. Also, similar to a stalled airfoil at large angle-of-attack, at some point the reattachment process of the flow behind the helmet and shoulders will become less likely to occur due to an increasing adverse pressure gradient. Such large changes in the location at which flow separates from the back are likely to have a significant effect on both the drag and the flow structure. Rather than carry out a detailed parametric study of the effects of these position characteristics, rider arm and torso positions were selected that represent the most extreme positions an elite cyclist in a time-trial position might assume. This section also investigates the effect of Reynolds number over the range of speeds a cyclist would typically travel at in cycling events where a time-trial position is used.

Although a few wind tunnel studies have noted the independence of rider drag with Reynolds number (Kawamura 1953; Kyle 1979; Zdravkovich *et al.* 1996), the forward speed at which a cyclist moves is likely to have some effect on the flow structure. This hypothesis is based on the fact that the shapes of many body components, such as the arms and legs, geometrically resemble cylinders, which are very sensitive to Reynolds number effects (Achenbach 1971). Based on the mean diameter of the arms/legs and the typical range of rider speeds, the local Reynolds number of these body parts ($80{,}000 < Re\# < 400{,}000$) means they operate in the critical Reynolds number ranges at which turbulent transition of the attached boundary layer and transition of the separated shear layer is likely to occur. The sensitivity of the drag force on the transitional process of the boundary layer is also supported by studies that have shown the effectiveness of zoned textured fabric or surface roughness to reduce the drag of cyclists (Kyle *et al.* 2004; Brownlie *et al.* 2009) by inducing a super-critical flow regime (drag crisis).

All investigations into rider position were carried out in the MLWT open-jet test section at a freestream speed of 16m/s unless stated otherwise. To test that force

(a) Arms-out

(b) Arms-in

FIGURE 3.43: Mannequin arm test positions.

measurement did not drift over the testing period of rider position experiments, the low 15° and high 75° drag leg positions in the 'standard' configuration served as a baseline. Baseline Kistler force measurements were recorded before and after a change to rider position and did not show any variations in the drag force that were outside the sensitivity of the measurement system and the repeatability of rider position, as outlined in section 2.3.

3.2.2.1 ArmPosition

Figure 3.43 compares the 'standard' arm position (160 *mm* elbow spacing) with the new arm position where the elbows have been brought closer together (70 *mm* elbow spacing). From this point on the two arm positions will be referred to as the 'arms-out' and 'arms-in' positions. The arms are moved closer together by angling the arms in at the shoulder joint. The handlebars have also been angled in to accommodate the change in hand position.

The effect of angling the arms in on the surface pressure distributions is shown in figure 3.44. This compares time-averaged contours of the surface pressure coefficient between the arms-in and out positions. A distinct reduction in the magnitude of the low pressure regions associated with the primary vortex pair is evident for the arms-in position. Despite a change in the magnitude of the pressures however, the same

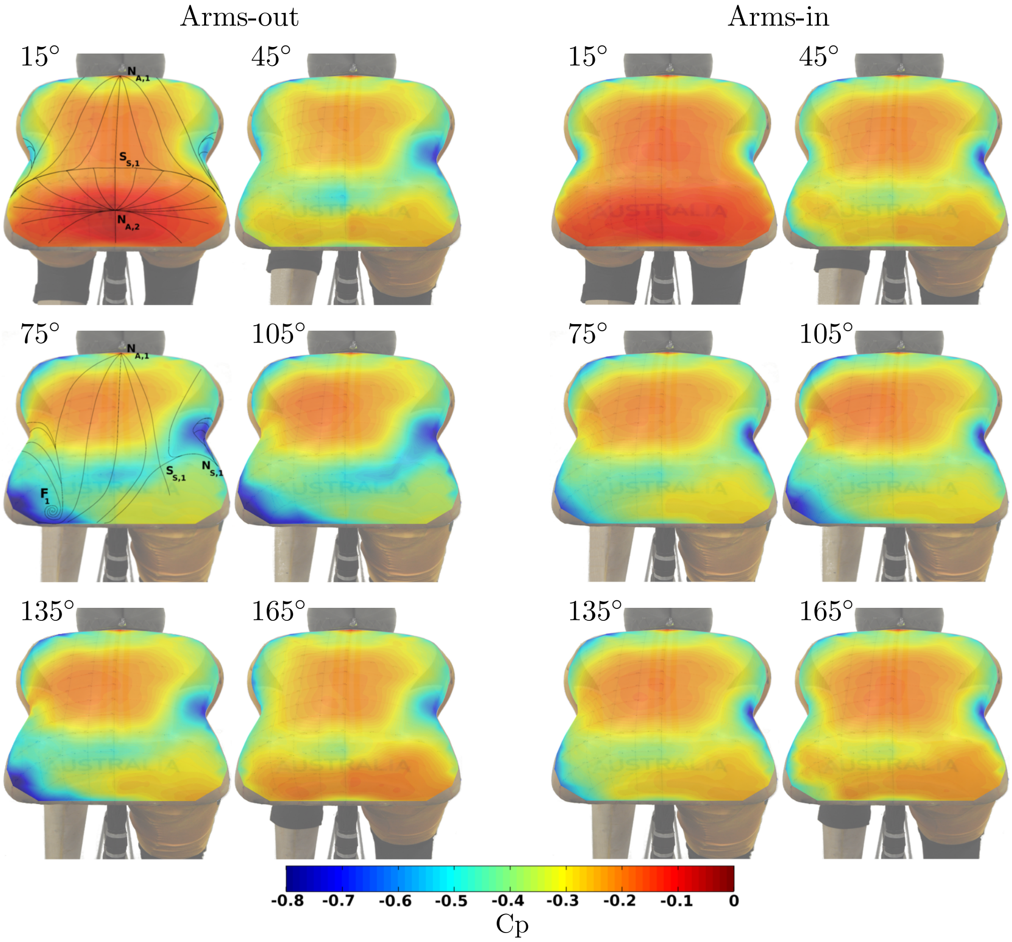

FIGURE 3.44: Variation in surface pressure distributions for arms-out (standard) and arms-in positions.

symmetries and asymmetries in the pressure distributions are observed throughout the crank cycle. The similarities in the global distribution of pressures suggests the same dominant flow structures are responsible for the pressure distribution observed for both arm positions, which appear to be weakened by bringing the arms closer together.

This is reflected in the centreline pressure distributions for both arm positions, which are compared in figure 3.45(a) for the low and high drag leg positions. For the 75° leg position, surface pressures over the upper back are the same. In the lower back regions on the rear base of the mannequin the overall shapes of the distributions are similar, however, a smaller peak in low pressure (around the hip joint) and a better pressure recovery results from having the arms in. For the 15° leg position a better pressure recovery occurs down the mid back regions for the arms-in position, however any benefits that result from this appear to be cancelled out as the pressure recovery over the rear base of the mannequin is lower compared to the standard arms-out

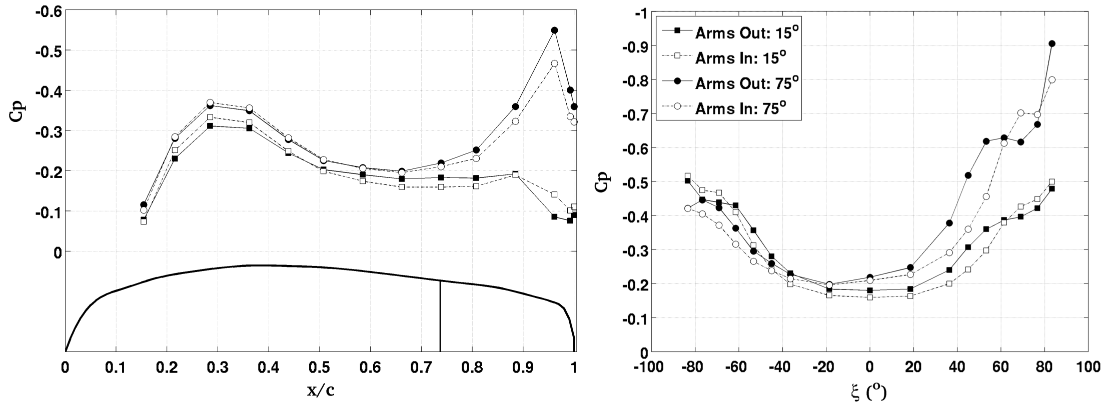

(a) Centreline

(b) Spanwise: 74%

FIGURE 3.45: Centreline and spanwise pressure distributions for arms-in and out positions. Line style and markers used to identify arm and leg position are consistent in both plots of the (a) centreline and (b) spanwise pressure distributions.

position.

Similar trends were also observed for the spanwise pressure distributions along the back where the upper hip vortex is formed. Figure 3.45(b) shows the spanwise pressure distribution for taps located at $\approx 75\%$ of the torso chord. The horizontal axis represents the location of the pressure measurements at the spanwise location with reference to the rib angle 'ξ'. The rib angle denotes the angle made between a line that connects the tap on the surface with the torso central chord location and the vertical drawn through the middle of the torso. Negative angles represent measurements on the left-hand side and positive the right-hand side (note symmetry is assumed here to depict pressures on the right-hand side). For the 75° leg position with the arms in, the majority of surface pressures are higher on the right side of the torso where the upper hip vortex is formed, compared to when the arms are out. For the 15° leg position the higher pressures observed in the mid back regions in the centreline pressure distributions are also reflected in the majority of spanwise measurements across the back.

As expected, a reduction in the magnitude of the major low pressure regions on the body reduces the drag for the majority of the high drag asymmetrical leg positions. This is shown in figure 3.46, which compares Kistler force measurements between the two arm positions, as well as the 'suction drag' estimates determined by integration of the pressure coefficient in the drag producing direction. The similarity in the reduction in the drag coefficient, for most of the asymmetrical leg positions ($30° < \theta < 165°$), for

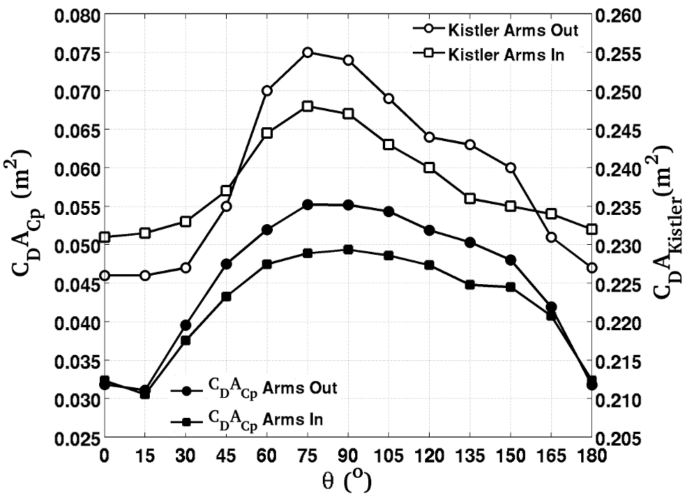

FIGURE 3.46: Left-hand axis: suction drag from back for both arms-out and in positions. Right-hand axis: drag measured by Kistler force balance for both arms-out and in positions (Fibre-glass configuration). Note both vertical axes have the same scale.

the Kistler force measurements and the integration of pressure over the back, suggests that almost all the drag saving arising from the change in arm position arises from the change in pressure forces on the back. This saving comes at a cost however, as an increase in the drag coefficient is observed for the leg positions around the low drag symmetrical flow regime ($0° <= \theta <= 30°$ for the first half of the cycle). When averaged over the pedal stroke the drag for the arms-in position only results in a $< 1\%$ reduction in the integrated mean leg position drag. For leg positions where there is an increase in drag for the arms-in position, there is no significant differences in both the shape and the magnitude of the pressure distributions between the two arm positions. This suggests that the increase in drag arising from the arms-in position over these crank angles is caused by a change in the pressure distribution on surfaces of the body other than the back.

3.2.2.2 Reynolds Number Effects

To test the conflicting findings of previous research into the effects of Reynolds number on the drag of a cyclist, surface pressure and force measurements were repeated with the mannequin in the arms-in position at a low 13 m/s and high 19 m/s freestream test speed. This is considered the minimum and maximum forward cycling speed likely encountered in cycling events where the time-trial position is used.

Interestingly Kistler force measurements for the low and high test speeds, which

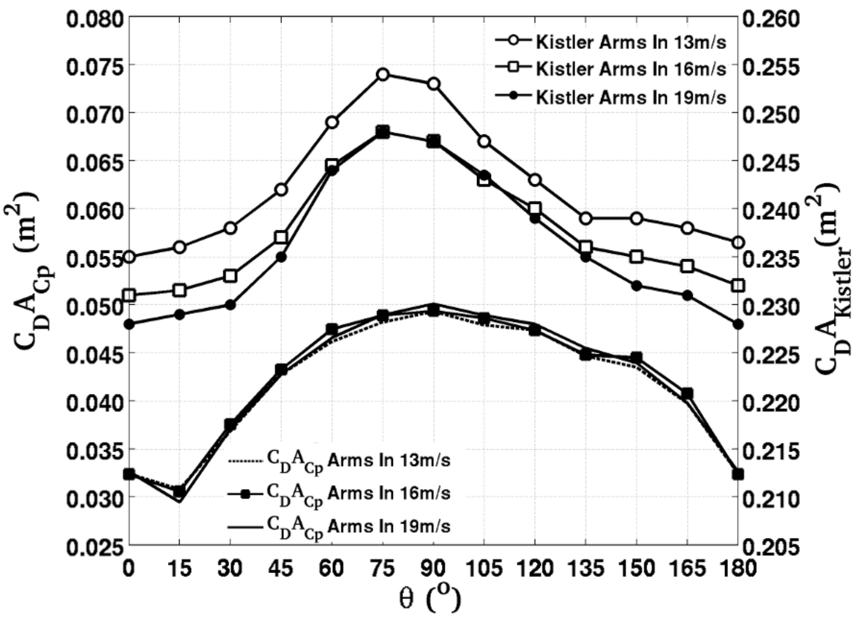

FIGURE 3.47: Left-hand axis: suction drag from back for freestream test velocities of 13 m/s, 16 m/s and 19 m/s, for the mannequin in the arms-in position (Fibre-glass configuration). Right-hand axis: total drag measured by Kistler force balance for the different test speeds. Note both vertical axes have the same scale.

are compared with the reference 16 m/s speed in figure 3.47, show the aerodynamic forces acting on the mannequin are dependent on Reynolds number. Compared with the reference 16 m/s speed, the low test velocity resulted in a consistent increase of approximately 1.85% in the mean drag coefficient across all leg positions. The higher speed resulted in an overall reduction in the mean leg position drag (0.75%), however this reduction is primarily only found for leg positions within the symmetrical flow regime.

The effect of Reynolds number on the shape and magnitude of the surface pressure distribution acting on the back had no noticeable effect. This is evident in figure 3.47 by the suction drag estimated from the integration of the pressure distributions. For all leg positions the suction drag acting on the back collapse onto one another for all the test speeds. This suggests that the variation in drag with Reynolds number is not caused by the pressure forces acting on the back where the primary flow structures originate. This, along with the findings from moving the arm position, highlights the importance of considering the flow around the entire body when optimising the aerodynamics of a cyclist.

(a) AOA = 12.5°, FSA = $0.410m^2$

(b) AOA = 15.0°, FSA = $0.419m^2$

(c) AOA = 18.0°, FSA = $0.429m^2$

FIGURE 3.48: Mannequin torso angle-of-attack test positions for the mannequin in the 180° leg position.

3.2.2.3 Torso Angle-of-Attack

The torso position was changed by angling the torso up from the hip joint. The standard low 12.5° angle-of-attack position as well as the medium 15° and high 18° torso angles are shown in figure 3.48. As the torso was rotated up the hand position was shifted along the handle bars so that the elbow joint angle was maintained. The 15° and 18° positions resulted in an average increase in the total projected area of 1.7% and 4.0%, respectively.

The Kistler force measurements in figure 3.49(a) show that as the torso angle was increased all leg positions tested experienced higher drag. Compared to the low torso angle position the mean drag over the course of the pedal stroke increased by 3.1% and 5.9% for the medium and high torso angle positions respectively. Although there are clearly differences in the magnitude of the pressures acting on the back, as was seen when the arm position was changed, the same global structure of the pressure distributions for the majority of leg positions is observed for the medium and high angles-of-attack. These are compared with the low torso angle for selected leg positions in figure 3.50. Even at the high 18° angle-of-attack, the pressure distribution shows the flow over the back has still not completely separated.

Although reducing the projected frontal area is clearly desirable, it is interesting that frontal area alone does not account for all of the increase in drag measured for higher torso angles. Figure 3.49(b) compares the variation in the drag coefficient throughout the first half of the crank cycle for the three torso positions. There is little difference in the drag coefficient between the low and medium torso angles around the low drag

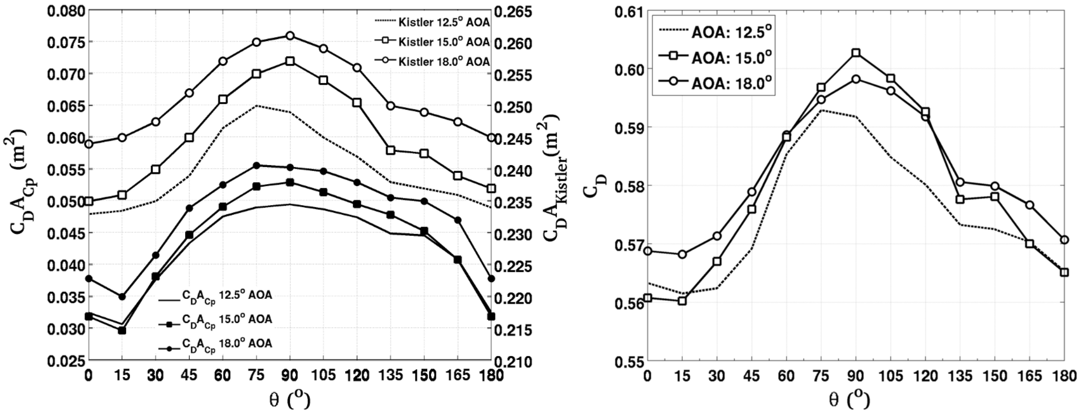

(a) (b)

FIGURE 3.49: (a) Left-hand axis: suction drag from back for 12.5°, 15.0° and 18.0° torso angle-of-attack positions (Fibre-glass configuration). Right-hand axis: total drag measured by the Kistler force balance for the different torso positions. Note both axes are of the same scale. (b) Drag coefficient for different torso angle-of-attack positions.

leg positions ($0° <= \theta <= 15°$ & $165° <= \theta <= 180°$). This is shown in the pressure distributions for these crank angles, as well as the integration of surface pressures for the new torso positions, which are plotted along with the Kistler force measurements in figure 3.49(a). As the torso was angled up, the area over which the integration was performed was held constant (i.e., integrated over same area as the standard low 12° AOA position), so that differences in the distributions over the back could be easily identified. It is worth noting however that when the increase in area over which the integration is performed is taken into account, > 95% of the variation in drag, which is a combination of both the change in frontal area and the drag coefficient, is a result of pressure forces acting on the back.

In contrast to the medium torso angle, an increase in the drag coefficient and pressure integrals between the reference low torso angle and the high torso position for low drag crank angles, is observed. This results from an increase in the magnitude of the low pressure areas on the back for the high torso position, which can be seen in the centreline and spanwise pressure distributions depicted in figures 3.51(a) and (b) respectively, for the low drag 15° leg position. Over the mid to lower back regions, after the initial pressure recovery over the shoulders, the centreline pressure distributions show lower pressures for the high torso angle position, compared to the low and medium torso angles which are very similar. A slight increase in the pressure recovery

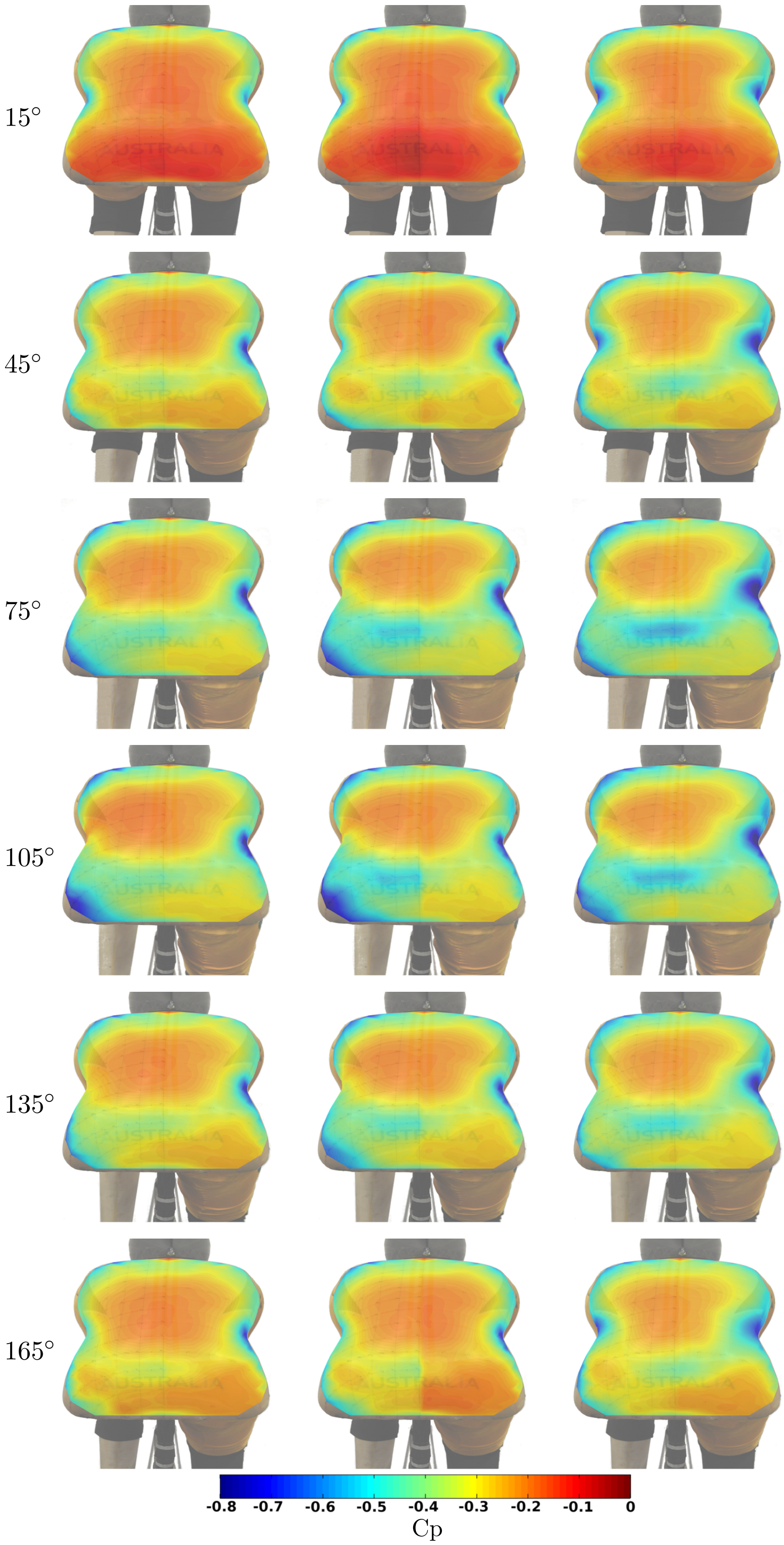

FIGURE 3.50: Variation in surface pressure distributions for 12.5° (left), 15° (middle) and 18° (right) angle-of-attack (mannequin arms-in position).

is observed for the medium 15° torso angle compared to the low angle-of-attack, which partially accounts for the slightly lower drag and pressure integral coefficient for the medium torso position.

The largest differences in the pressure distributions are observed on the sides of the torso. This is evident in the contours of the pressure coefficient in figure 3.50 that show not only a strengthening of the low pressure areas associated with the large-scale vortices that roll up around the sides of the torso, but also these regions of low pressure are initiated much earlier along the sides of the torso. This is more clearly depicted in the spanwise pressure distributions, which are drawn in figure 3.51(b) at 50% of the torso chord line where the major low pressure regions on the torso sides originate for the high angle-of-attack position. A large increase in the magnitude of the low pressures for taps located on the sides of the torso are evident for the 18° torso angle, compared to the two lower positions, which show no significant differences.

It is also apparent in the pressure contours, that as the legs are stepped around from 0°, the low pressure areas on both sides of the torso persist much further into the crank cycle for the high torso angle compared to the low and medium angles. Even at the 45° leg position significant low pressure areas are still present on both sides of the torso. It is hypothesised that this is a result of the larger gap between the upper thigh and stomach for the high torso angle position. As a result of the larger thigh/stomach gap the legs must progress further into the crank cycle in order to achieve the same thigh/stomach spacing as found in the lower torso angle positions. This also explains why we find that the lower pressure areas on the side of the body of the falling leg (left) are initiated much earlier towards the end of the first half of the crank cycle. This can be seen by comparing contours of the pressure coefficient for the three torso angles at the 165° leg position as the flow transitions back to the symmetrical flow regime.

As the legs are stepped around the crank and the flow transitions to a fully developed asymmetrical flow regime, differences in the drag and surface pressure integral coefficients arise for both the medium and high AOA positions compared to the low torso angle. Firstly, there is a distinct shift in the peak drag coefficient away from the 75° towards the 90° leg position. Secondly, an increase in the back surface pressure integral coefficient occurs for both the medium and high angle-of-attack positions. This results in the increase in the drag coefficient for both the medium and high angle-of-attack positions over the asymmetrical high drag crank angles. The centreline pressure

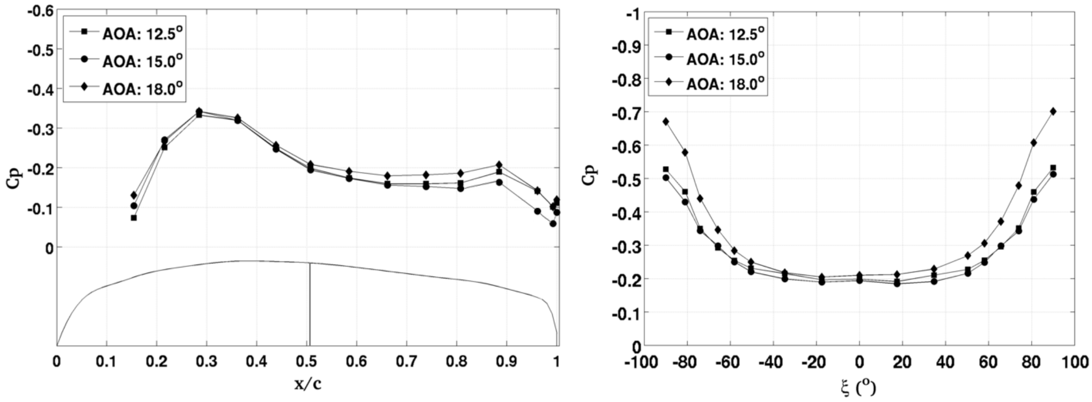

(a) Centreline

(b) Spanwise: 50%

FIGURE 3.51: Centreline (a) and spanwise 50% chord line (b) pressure distributions for low, medium and high torso angles-of-attack for the 15° low drag leg position.

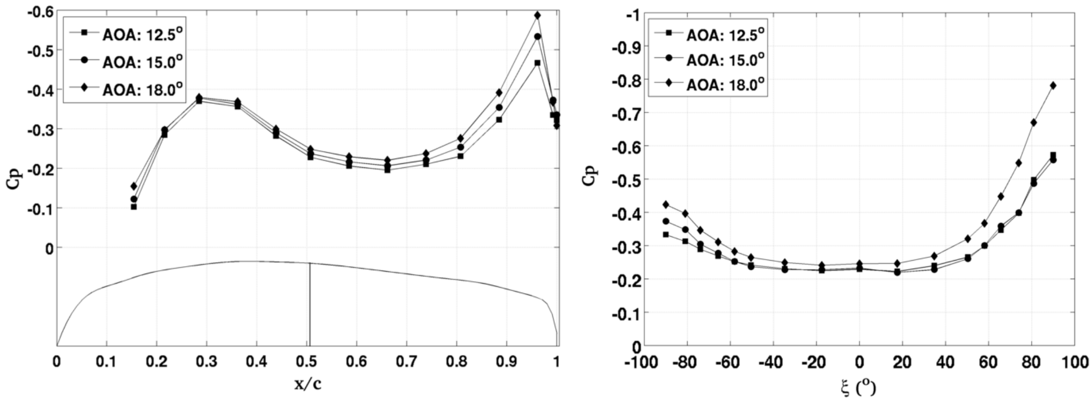

(a) Centreline

(b) Spanwise: 50%

FIGURE 3.52: Centreline (a) and spanwise 50% chord line (b) pressure distributions for low, medium and high torso angles-of-attack for the 75° high drag leg position.

distributions for these leg positions, which are shown for the 75° crank angle case in figure 3.52(a), show a gradual increase in low pressure acting over the mid and lower back as the torso angle is increased. The peak in the centreline low pressure around the hip joint ($x/c \approx 0.96$) also progressively increases with torso angle.

Akin to the 15° spanwise distributions, figure 3.52(b) shows that the spanwise pressure distribution for the 75° leg position at the 50% chord location are similar for the low and medium torso angles. A small reduction in the pressure coefficient is visible on the left side of the torso for the 15° angle-of-attack position. For the high torso angle distributions, the significant increase in the magnitude of the low pressure areas on the side of the torso, where the hip angle is open (right), is the major feature.

3.2.3 Summary of Surface Pressure & Rider Position Investigations

Time-averaged surface pressure distributions have strengthened findings regarding the effect of leg position on the near wake flow structure and the aerodynamic drag force. Surface pressures are characteristic of the symmetrical and asymmetrical flow regimes and clearly identify the major low pressure areas associated with the primary time-averaged flow structures that originate over the back. The global change in the flow structure that was identified in section 3.1 as being the primary mechanism affecting the large variation in drag measured throughout the crank cycle, was reflected in the surface pressure distributions. The majority of the variation in the aerodynamic drag force with leg position, which is dominated by the pressure drag component, can be explained by changes in the pressure distribution acting on the back and not the small variation in the projected frontal surface area that occurs throughout the crank cycle.

In addition to these findings, surface pressure measurements for different arm and torso positions, showed that the surface pressure distributions were relatively resilient to these changes. The major influence of the position changes was to alter the magnitude of the pressure within the low pressure regions where large-scale flow structures originate, however the general shape of the distributions remained unchanged. As the major features of the low and high drag flow topologies can be inferred from the surface pressure distributions, this suggests that the primary flow structures characteristic of the 'standard' position will still be the dominant feature of the flow for these new positions.

Interestingly, the positional changes had a different effect on the surface pressure distributions for each of the symmetrical and asymmetrical flow regimes. A reduction in the magnitude of the low pressure regions associated with the upper and rear hip vortices of the asymmetrical flow regime was the major contributor to the reduction in the total drag force acting on the mannequin for the arms-in position. For the more symmetrical leg positions when the upper thighs were close to being aligned, the surface pressure distributions between the arms-in and out positions did not change significantly. The increase in the total drag measured for this particular region of the crank cycle when the arms were brought closer together must therefore be a result of a change in the pressure distribution acting on body parts other than the back.

This finding highlights the importance of considering multiple flow regimes that occur throughout the crank cycle when optimising the aerodynamics of a cyclist.

The importance of the pressure drag component acting on body components other than the back was also demonstrated when the influence of Reynolds number on the aerodynamic drag force and back surface pressure distributions were investigated. In contrast to much of the literature discussing the influence of Reynolds number effects on the aerodynamics of cyclists, the aerodynamic drag area force was dependent on the Reynolds number. For the three low, medium and high test velocities that span cycling speeds typically experienced by cyclists in events where the time-trial position in used, the Kistler drag force varied by as much as 3.5% at the different leg positions. For the different test speeds the back surface pressure coefficient distribution remained unchanged for all leg positions around the crank cycle. This suggested that the boundary layer that develops over the back is already turbulent, post critical and is therefore unlikely to be effected by changes in the texture of the skin-suit in this region. The variation in the total drag coefficient with Reynolds number is thought to be primarily influenced by pressure forces acting on the head, arms or legs. This is expected given that these particular body components resemble simplified geometries such as spheres and circular cylinders where the drag coefficient is highly dependent on Reynolds number. More importantly however is that based on the local Reynolds number of these body parts, critical and super critical drag regimes (where the drag coefficient varies significantly with small changes in Reynolds number) exist for the simplified geometries.

As expected as the torso was angled up this had a negative effect on drag for all leg positions throughout the pedal stroke. Although this demonstrated the importance of reducing frontal area, the increase in the drag with the higher torso angles was a result of both the change in the projected frontal area and the drag coefficient. The relative contribution of the projected frontal area and the drag coefficient to the increase in drag, varied throughout the crank cycle and was dependent on the angle of the torso.

Once again, the affect the position change of the torso angle had on the pressure distribution acting on the back, which accounted for almost all the variation in the drag with torso position, was dependent on which part of the crank cycle the legs were positioned in. For the medium torso angle, surface pressures were very similar to the reference low torso position for the symmetrical leg positions. The higher drag measured for these leg positions is primarily a result of the increase in the area over which the pressure force acts in the drag direction. For asymmetrical leg positions, a reduction in the pressure coefficient over the lower back resulted in an increase in the drag coefficient, which accounted for much of the increase in the total drag. For the high torso angle the low pressure regions that occur on the side of the torso were strengthened throughout the whole crank cycle resulting in an increase in the drag coefficient. This is analogous to low aspect ratio wings where the strengthening of low pressure streamwise vortices with increasing angle-of-attack (prior to stall) results in lower pressures on the upper suction surface of the wing.

Chapter 4

Unsteady Experimental Results & Discussion

4.1 Cyclist Unsteady Aerodynamics

Analysis of velocity field and surface pressure measurements have thus far revealed how the major time-averaged flow structures affect the mean drag over the course of a pedal stroke. This has shed light on where and how the greatest drag savings can be effectively achieved. This chapter analyses the fluctuating component of surface pressure, and wake velocity field measurements, for the mannequin in the standard arms-out position. The wake of a cyclist is unsteady meaning the aerodynamic drag forces vary with time. Although it is the time-averaged drag force that is of most practical interest to cyclists, previous investigations into unsteady bluff body flows have shown that near wake unsteadiness is related to the overall drag force. Studies have shown, for more simplified bluff body geometries, that the aerodynamic drag force can be reduced through altering the formation of the unsteady flow structures associated with the large-scale vortical motions in the near wake (Roshko 1955; Bearman 1965; Zdravkovich *et al.* 1989).

In this investigation into cycling aerodynamics, the time scales associated with the unsteady flow structures are also important to the validity of a quasi-steady assumption. If the pedalling frequency of a cyclist is of the same order of magnitude as the frequency of periodic high-energy fluctuations found in the wake of the static mannequin, then it can no longer be assumed that the same unsteady structures associated with these frequencies will develop over the course of the pedal stroke. If that were the case then a quasi-steady approximation could depart significantly from the real flow found around cyclists under pedalling conditions.

As might be expected given how little work has been published on the time-averaged wake structures, there is even less known about the unsteady nature of the cyclist wake. A frequency analysis of wake probe data and time-accurate surface pressure measurements have revealed a complex wake exhibiting a variety of time and length scales associated with unsteady wake structures. This is expected given the complex three-dimensional geometry of the mannequin is composed of a wide range of body parts of varying shapes and sizes. At typical cycling speeds the local Reynolds numbers of the major body parts (upper/lower arms, legs, torso and head), many of which exhibit cylindrical (tapered) or spherical geometries, are sufficiently high that a turbulent boundary layer would be expected over the majority of the body surfaces. For more generic three-dimensional bodies, such as circular cylinders, transition to a turbulent boundary layer not only results in a reduction in the size of the wake but also a loss in the periodicity of the flow and shedding behaviour (Roshko 1993). This is in contrast with other bluff bodies where the separation points are more or less fixed (i.e., geometries with sharp edges, such as square cylinders and flat plates) and have well defined shedding behaviour for much higher Reynolds numbers.

Although the unsteady pressure and velocity fluctuations of the flow around the mannequin exhibit a broad frequency spectrum, of primary importance are the unsteady components that contain the majority of the energy of the fluctuations. By analysing the time histories of measurements made at discrete locations in the wake and on the surface of the mannequin, regions of high unsteadiness exhibiting distinct spectral peaks are identified. Unsteady surface pressures and wake velocity components are directly compared so that areas of similar spectral content can be identified, building a more complete picture of how unsteady flow structures develop while also strengthening findings. Due to the broad nature of the frequency spectrum these regions were decomposed into low, medium and high frequency bands. Although there is still much work to be completed to obtain a comprehensive description of the true unsteady nature of the wake of a cyclist, the dominant shedding frequencies found are at the higher end of the spectrum (an order of magnitude higher than typical pedalling frequencies). This provides further evidence that a quasi-steady approximation of the flow for moving legs will likely be valid for a wide range of cycling speeds.

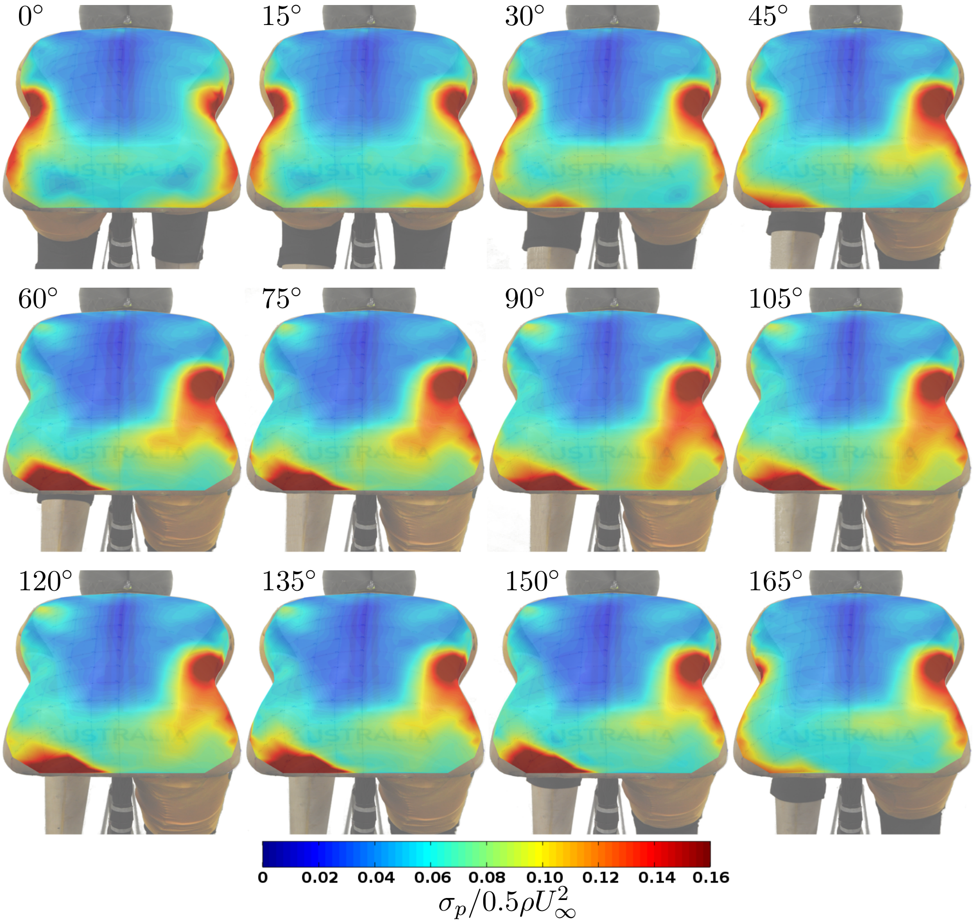

FIGURE 4.1: Contours of the fluctuating surface pressure coefficient.

4.1.1 Areas of high surface pressure and wake unsteadiness

4.1.1.1 Surface pressure fluctuations

Because of the unsteady nature of separated flows, it is expected that the largest pressure and velocity fluctuations will occur in the separated areas on the surface and in the near wake of the mannequin. Figure 4.1 shows contour plots of the fluctuating surface pressure coefficient (standard deviation of surface pressure measurements 'σ_p' normalised by the freestream dynamic pressure) for leg positions in the first half of the crank cycle. The low pressure areas on the surface of the mannequin, where the primary flow structures originate, corresponds with areas of large surface pressure fluctuations. Areas where the flow remains attached over the majority of the upper back exhibit low surface pressure fluctuations.

Similar asymmetries in the distribution and magnitude of the surface pressure fluctuations to those observed in the time-averaged surface pressure distributions as the legs are moved around the crank cycle are seen. Figure 4.2 shows the variation in the

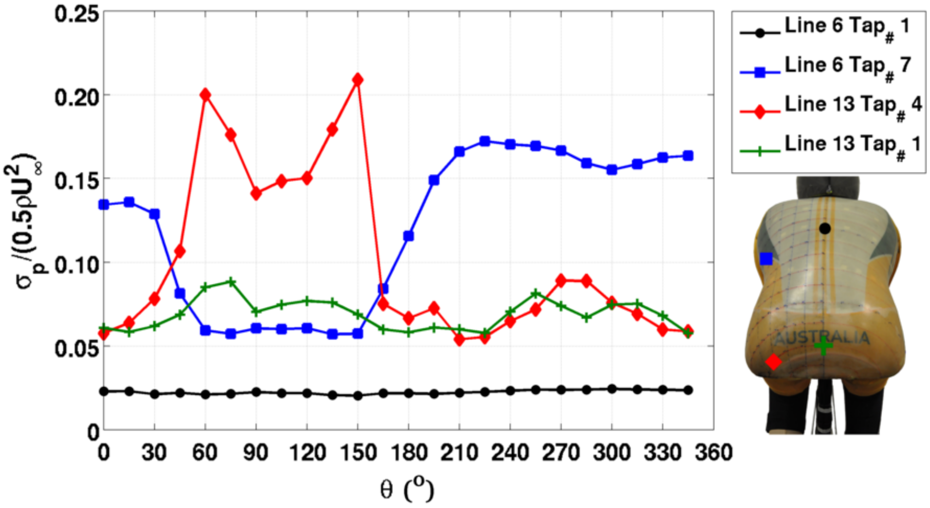

FIGURE 4.2: Variation in fluctuation pressure coefficient with crank angle at selected tap locations.

fluctuating surface pressure coefficient throughout the complete crank cycle for selected pressure taps located in separated and attached regions of the back. Also shown for these selected pressure taps are probability density functions (PDFs) for low and high drag leg positions. These describe how the pressure fluctuations are distributed about the local mean pressure. The PDFs in figure 4.3 are shown in the standardised format with the random variable represented in the reduced form with zero mean and unitary standard deviation. For surface pressures measured at the tap located on the centreline of the mid back (Line 6 $Tap_{\#}1$), changes in leg position have little effect on pressure fluctuations, which are low. Pressure fluctuations in these areas are typical of those observed in an attached turbulent boundary layer. Figure 4.3(a) and (b) shows PDFs representative of these low fluctuation coefficient regions on the back for the low and high drag leg positions. Pressure fluctuations in these areas closely match a Gaussian distribution about the mean pressure (standard normal distribution).

In separated areas of the back the local fluctuating surface pressure coefficient and PDFs depend on the position of the legs. Figure 4.2 shows how the magnitude of the largest pressure fluctuations vary throughout the crank cycle on the side of the torso and on the base of the mannequin, where the low pressure regions occur. The largest fluctuations are observed on the rear of the hips on the side of the body when the leg is in a raised position where the rear hip vortex originates. This can be seen for the tap located on the rear of the left hip (Line 13 $Tap_{\#}4$) where in the first half of the crank cycle pressure fluctuations increase rapidly from the 0° and 15° low drag leg positions as

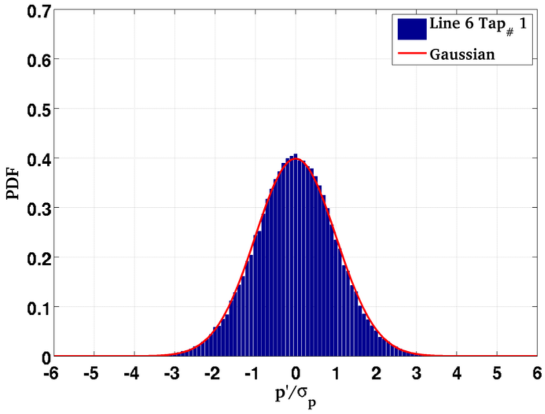

(a) $\theta = 15^\circ$, $\sigma_p = 3.3pa, S = -0.01$

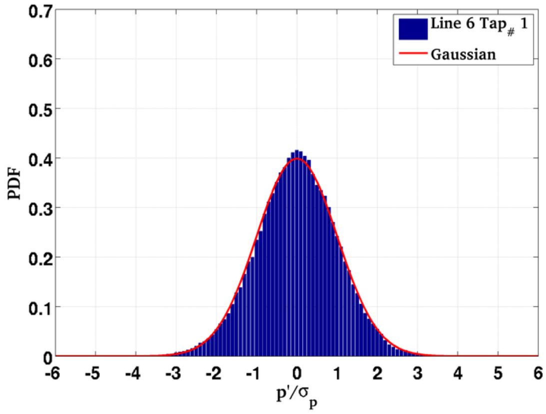

(b) $\theta = 75^\circ$, $\sigma_p = 3.04pa, S = -0.05$

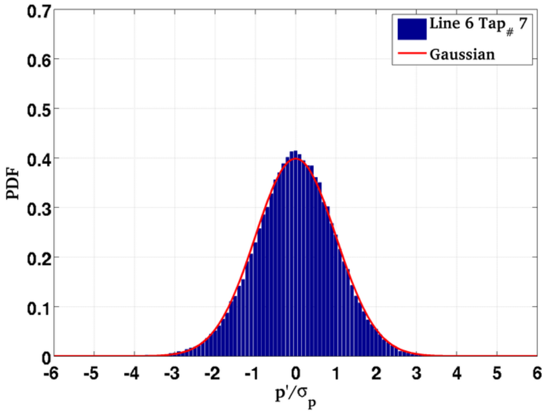

(c) $\theta = 75^\circ$, $\sigma_p = 8.10pa, S = -0.12$

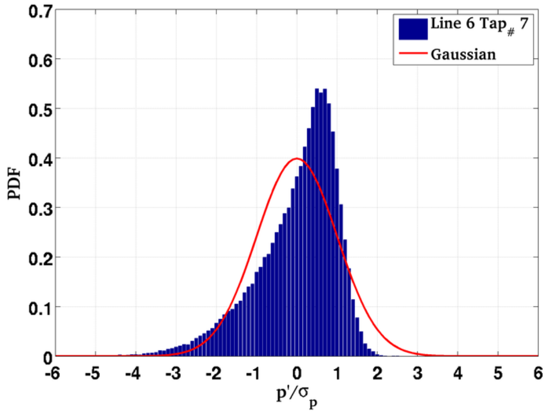

(d) $\theta = 255^\circ$, $\sigma_p = 23.7pa, S = -1.10$

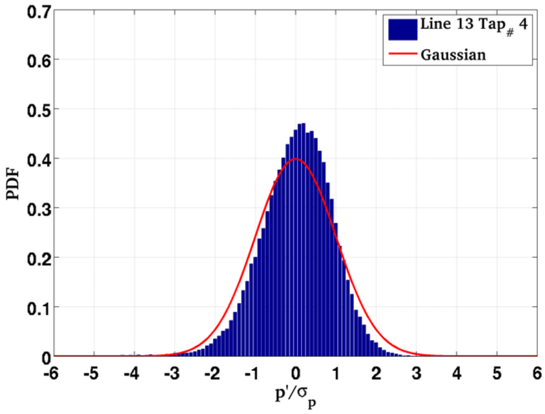

(e) $\theta = 75^\circ$, $\sigma_p = 25.58pa, S = -2.30$

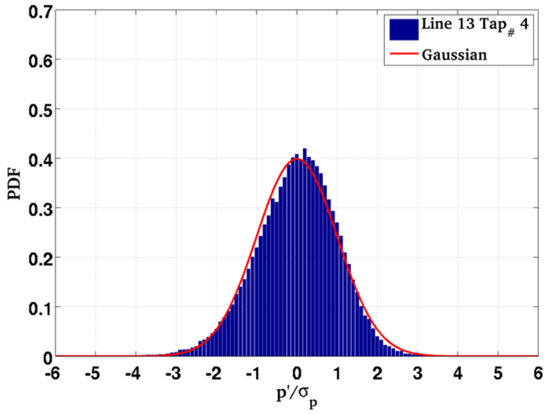

(f) $\theta = 255^\circ$, $\sigma_p = 10.10pa, S = -0.28$

the transition to the asymmetrical flow regime occurs. Two distinct peaks are found at the 60° and 150° leg positions after which the fluctuating pressure coefficient drops, as

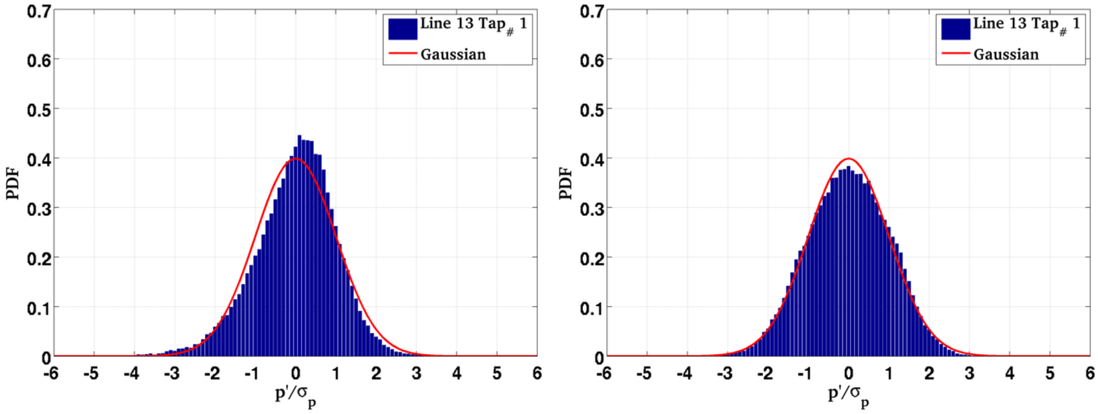

(g) $\theta = 15°$, $\sigma_p = 8.32pa, S = -0.40$

(h) $\theta = 75°$, $\sigma_p = 12.54pa, S = -0.08$

FIGURE 4.3: Probability density function histograms (PDF) at selected taps for low drag and high drag leg positions.

the wake transitions to the asymmetrical flow regime on the opposite side of the body. In contrast to these measurements, for surface pressure measurements located on the side of the left torso, as the left leg raises up to close the gap between the torso, a drop in the fluctuating pressure coefficient can be seen at the 60° and 150° leg positions. As the hip angle is opened in the second half of the crank cycle a significant increase in the magnitude of the pressure fluctuations can be seen on the side of the left torso. Compared to the magnitude of the pressure fluctuations in these large separated areas, pressure fluctuations in the middle of the base of the lower back (Line 13 $Tap_{\#}1$) are much smaller and vary less throughout the pedal stroke.

Figures 4.3(c–h) show how the PDFs vary between taps located on the left side of the torso, left rear hip and the middle of the base of the lower back for high drag 75°, 255° and low drag 15° leg positions. It is clear that when flow separates from the base of the lower back and sides of the torso the PDF's are biased towards negative values, and a departure from the reference Gaussian curve is observed. A measure of this is given by the skewness level 'S', which is shown below the PDFs, along with the standard deviation of the raw pressures signals 'σ_p'. As the flow separates from the base of the hips and sides of the torso throughout the crank cycle pressure fluctuations are skewed towards negative values as a result of large negative peaks in the time series of the pressure signals.

The surface pressure measurements exhibiting the largest skewness levels were concentrated where the flow separates from the rear hip of the raised leg. This is seen in

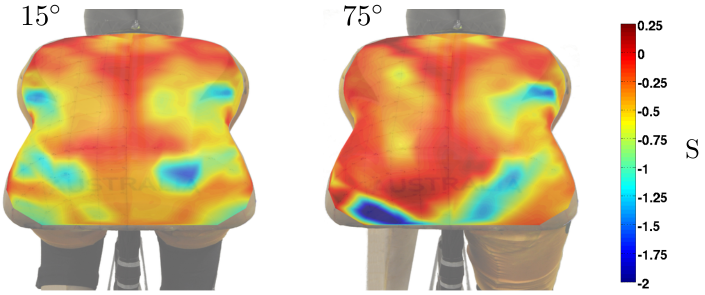

FIGURE 4.4: Contours of skewness levels for the low and high drag leg positions.

the contours of the skewness levels shown in figure 4.4 for the symmetrical low drag 15° and asymmetrical high drag 75° leg positions. These types of large negative pressure fluctuations are consistent with the intermittent rolling up of the separated shear layers. Similarly, skewed distributions have also been found to correspond with large surface pressure fluctuations in the separated zones measured on the rearward faces of square prisms (Kawai 1983; Bearman & Obasaju 1982), blunt flat plates (Kiya & Sasaki 1983), and close to the leading edges on the sides of low rise buildings (Ginger & Letchford 1993).

4.1.1.2 Fluctuating velocity components

As flow separates from the body large fluctuations in surface pressures result from the unsteady velocity fluctuations near the surface and in the wake of the mannequin. It was previously shown in section 3.1.2.1 that areas of high turbulence intensity in the wake corresponds to regions of large axial velocity deficits and high streamwise vorticity where the large-scale primary vortices exist. By breaking the velocity fluctuations up into the three components (streamwise, spanwise and vertical), velocities containing the largest fluctuations can be identified. By identifying areas of high turbulent velocity fluctuations the nature of unsteady processes, such as vortex shedding, can be investigated and compared with high energy surface pressure fluctuations. Figures 4.5 and 4.6 show contours of the three turbulence intensity components for the 15° and 75° leg positions in traverse planes 1–5.

Turbulence levels in the wake behind the mannequin (P4 and P5) are significantly lower in all three velocity components for the low drag 15° leg position compared to the high drag 75° position. They are evenly distributed about the centre plane of the mannequin in all wake measurements for the low drag 15° leg position, whereas asymmetries in turbulence levels can be seen to develop early in the velocity field

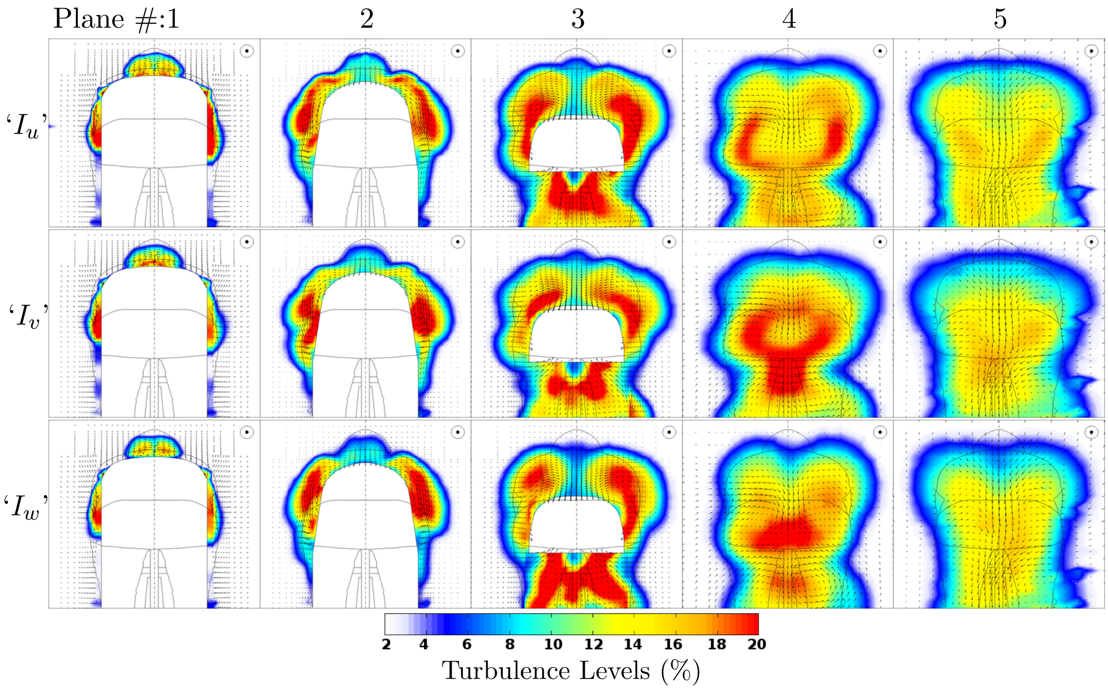

FIGURE 4.5: Contours of turbulence intensity levels in traverse planes 1–5 for u (top), v (middle) and w (bottom) velocity components for the low drag 15° leg position.

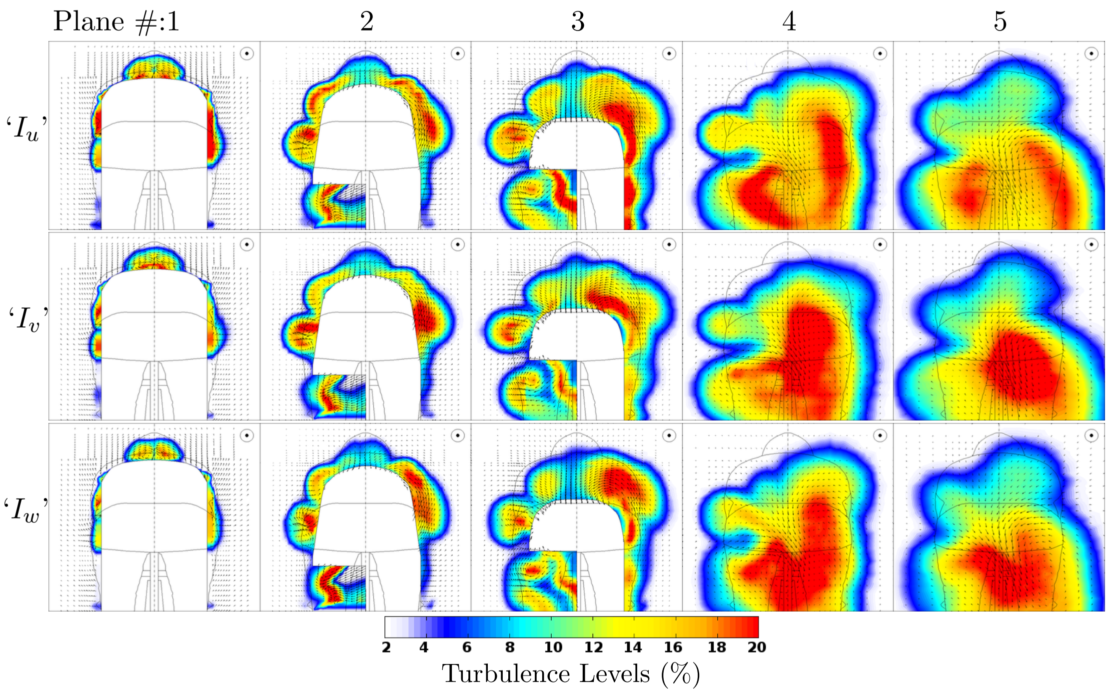

FIGURE 4.6: Contours of turbulence intensity levels in traverse planes 1–5 for u (top), v (middle) and w (bottom) velocity components for the high drag 75° leg position.

measurements performed in the plane at the trailing edge of the helmet (P1) for the 75° position. For both high and low drag leg positions all three turbulence level components have a similar distribution in the velocity field measurements upstream of the base of the hips (P1–P3). High turbulence levels are initially found in the wake of the helmet, and then a reduction in these levels is observed as the flow reattaches to the centreline of the back, between planes one and two. On the sides of the torso, where the low mean pressure and high surface pressure fluctuations were identified, large turbulence levels are observed in all velocity components for the 15° and 75° positions. High turbulence levels can also be seen in the core regions of the time-averaged vortex structures that were identified in the wake of the elbow, upper arms and in between the legs.

As the flow develops in the wake behind the hips (P4 and P5) large differences can be seen in the distribution of the turbulent velocity components for both the 15° and 75° leg positions. Velocity fluctuations measured in traverse plane 4 (50% torso chord length behind mannequin) show distinct areas of unsteadiness associated with a particular velocity component. For the 15° leg position the streamwise 'u'' velocity fluctuations are mainly concentrated near the edges of the left and right hips. The highest levels are observed in the spanwise 'v'' and vertical 'w'' fluctuating velocity components. These are concentrated behind the left/right hips and in between the legs for the spanwise velocity component, and behind the middle rear base of the hips/lower-back for the vertical component.

For the 75° leg position high turbulence levels in the streamwise component of velocity are located close to the outer edges of the upper hip/thigh of the right extended leg and below the hip of the raised left leg. In the spanwise component high turbulence levels are primarily contained below the upper hips on the side of the body where the leg is in an extended position, which is where the time-averaged upper hip vortex structure is located. In the vertical component turbulence levels are much more evenly distributed about the centre plane covering areas of the wake dominated by both the upper/rear hip vortex pair.

4.1.2 Frequency analysis

In this section, frequency spectra of surface pressures and velocity components in the wake region are examined to determine if dominant frequencies in regions of high unsteadiness are associated with vortex shedding from the body of the mannequin. Major conclusions are drawn from the frequency analysis of fluctuating surface pressures measured in the MLWT for various leg positions throughout the crank cycle. Compared with point velocity field measurements, all surface pressures on the back were measured simultaneously for each leg position. Sampling times of surface pressures (three repeated tests at 1500Hz for 60 seconds) were also twelve times that of point velocity measurements with the Cobra Probe, allowing much higher spectral resolution. Despite these differences, dominant frequencies in the wake of the mannequin in the high turbulent areas were analysed and compared with the frequency analysis of surface pressure fluctuations. Unsteady findings of wake velocity components measured in the 450kW wind tunnel are consistent with findings in the MLWT. Surface pressure measurements, which were repeated in the smaller 450kW wind tunnel, are also compared to ensure that final conclusions are independent of the wind tunnel used. Similarities in the results from the two wind tunnels indicates that wind tunnel background noise levels, which differ between the two wind tunnels (presented in section 2.2.1.2), have not compromised the final conclusions. Potential sources of error in the frequency analysis of pressure and velocity signals are identified and discussed in this section.

The basic equations used in the Fourier analysis of the fluctuating surface pressure and wake velocity components can be seen in equations 4.1 – 4.7 after Bendat & Piersol (1980). Over the finite sampling time 'T_s', the spectral content of pressure or wake velocity signals '$x(t)$', is found by converting the measured signal from the time domain into the frequency domain using the Fast Fourier Transform (FFT)

$$X_{f,T_s}(f) = \int_0^{T_s} x(t)\, e^{-i2\pi f t} dt. \tag{4.1}$$

The energy contribution per frequency band in the Power Spectral Density (PSD) function was calculated using equation 4.2, where 'n' denotes the number of samples recorded over the finite sampling time 'T_s' that are averaged. The area under the PSD function is equivalent to the variance of the measured signal (Parseval Theorem). By integrating the PSD function between frequency limits an estimate of the contribution to the variance of the signal between the frequency limits can be obtained.

$$G_{xx}(f) = \frac{2}{n.T_s} \sum_{k=1}^{n} |X_k(f, T_s)|^2. \tag{4.2}$$

As surface pressure measurements were recorded simultaneously for each leg position tested, fluctuating pressures recorded at different locations on the back could be directly compared for spectral coherence and phase relationships. The Cross Power Spectral Density (CPSD) function given in equation 4.3 below provides a measure of the spectral content and phase relationship between two signals '$x(t)$' and '$y(t)$', where '$X_k^*(f, T_s)$' is the complex conjugate of the FFT of the time signal '$x(t)$' and '$Y_k(f, T_s)$' is the FFT of the time signal '$y(t)$'. The magnitude and phase '$\theta_{xy}(f)$' relationship of the two signals are found from the real '$C_{xy}(f)$' and imaginary '$Q_{xy}(f)$' components of the CPSD function using equations 4.4 and 4.5. The phase angle between the two signals provides information on the time delay between to two signals at discrete frequencies. For simultaneous surface pressure measurements, given the time delay (or lag) and the spacing 'd' between the two pressure taps, the propagation velocity over the surface (convection velocity) can be calculated using either the phase angle or gradient $\theta'_{xy}(f)$ using equation 4.6, where 'f' is the frequency component in radians at which the convection velocity '$c_{xy}(f)$' is calculated. The key governing equations are

$$G_{xy}(f) = \frac{2}{n.T_s} \sum_{k=1}^{n} X_k^*(f, T_s).Y_k(f, T_s), \tag{4.3}$$

$$|G_{xy}(f)| = \sqrt{C_{xy}^2(f) + Q_{xy}^2(f)}, \tag{4.4}$$

$$\theta_{xy}(f) = tan^{-1}\left(\frac{Q_{xy}(f)}{C_{xy}(f)}\right), \tag{4.5}$$

$$c_{xy}(f) = \frac{2.\pi.f.d}{\theta_{xy}(f)} = \frac{2.\pi.d}{\theta'_{xy}(f)}. \tag{4.6}$$

The coherence function given in equation 4.7 provides a direct measure of how well the two signals are correlated. For two perfectly correlated signals the function is equal to one and for two complete uncorrelated signals the function is zero.

$$\gamma_{xy}^2 = \frac{|G_{xy}(f)|^2}{G_{xx}(f).G_{yy}(f)}. \tag{4.7}$$

When performing a Fourier analysis on time series from experimental wind tunnel measurements, the external influences of the wind tunnel testing environment on measurements and the limitations of the Fourier analysis need to be considered so that any potential error sources can be identified. The major sources of error affecting the frequency analysis of surface pressure and wake velocity field signals are listed below.

1. Wind tunnel background noise (MLWT - Surface Pressures) (450kW - Wake Traverses).
2. Electrical/System noise (DPMS - Surface Pressures) (Cobra Probe - Wake Traverses).
3. Vibrations (Mannequin - Surface Pressures) (Cobra Probe / Mannequin - Wake Traverses).
4. Fourier Analysis (Aliasing, Spectral Leakage).

Background noise levels of the MLWT, 450kW wind tunnel and the measurement systems were presented in section 2.2.1.2. Due to the relatively low energy contained in the background noise levels inherent to the wind tunnel and equipment used, these noise sources should not significantly affect the spectral content of pressure and velocity signals in high energy areas of spectral activity. If, however, background noise levels are amplified in the unsteady regions of the wake the effect of background noise levels on measurements must be considered. As surface pressure measurements were repeated in the 450kW wind tunnel, and background noise characteristics are specific to the wind tunnel tested in, the spectral content of similar surface pressure measurements can be compared between the two wind tunnels to check the sensitivity of surface pressures to the external influences of the wind tunnel testing environments. In areas where surface pressure fluctuations are only weakly periodic in the attached areas of the body, the effect of the wind tunnel background noise levels becomes more prominent, especially at the lower end of the spectrum. The influence of background noise on the frequency analysis will be discussed in the following sections, where that power spectra of surface pressures in distinct areas of spectral activity are directly compared with wind tunnel background noise levels.

During testing slight 'shaking' movements of the mannequin were observed. Although only characterised visually, these movements were generally high frequency in nature and were not periodic, randomly coming and going throughout the duration of a test. To investigate the effect of these movements, surface pressure measurements in the 450kW wind tunnel were performed at selected leg positions with piano wire fastened to the wind tunnel walls and attached to the arms of the mannequin and handle bars of the bicycle frame to eliminate the majority of the movement of the mannequin throughout testing. Comparing measurements between tests with and without the extra wire supports resulted in no appreciable differences between mean pressures and the spectral content of the fluctuating pressures. As the same support system was used to fix the mannequin to the floor of the MLWT, this result is expected to hold true for the surface pressure measurements performed in both wind tunnels.

Errors arising due to aliasing are expected to be small as frequencies above the Nyquist frequency (750 Hz i.e. half the sampling rate) are not expected to play a dominant role in spectra. To reduce the effects of 'leakage' on the frequency spectrum various windowing functions were investigated. Spectral 'leakage' is a result of the Fourier transform assuming that signals are perfectly periodic in nature and are repeated throughout the entire signal (or window) being analysed. For non-periodic behaviour however, spectral leakage distorts the spectra and results in the signal's energy being artificially smeared out over a wide frequency range in the FFT. To reduce the effects of 'leakage', windowing functions were utilised to provide a cleaner and better representation of the frequency spectrum.

Many windowing functions have been developed to suit specific types of signals, and have advantages and disadvantages in terms of improvements to frequency and amplitude resolution. For the analysis of surface pressure and wake traverse data it was found that a Hanning window function provided the best compromise between frequency and amplitude resolution with reduced spectral leakage. Although windowing functions improve a signal's noise-amplitude ratio, they cause distortion as they change the overall amplitude of the signal across all frequencies (i.e., area under the PSD function is no longer equal to the variance of the signal). To correct for this, all PSD estimates are multiplied by a constant scaling factor 'k' (Note: 'k' is a constant irrespective of tap/traverse location and the choice of the window size).

Power spectral densities using the Hanning window were evaluated using Welch's averaged periodogram method (Welch 1967). Welch's method splits the time series up into segments 'n' samples long with a 50% overlap and then computes the PSD function of the overlapping segments. The PSDs for each segment are then averaged to produce the power spectral density estimate. This method effectively reduces the random error associated with a finite noisy signal (by a factor of $1/\sqrt{\frac{9}{11}n}$ for 50% overlap) in exchange for a slight reduction in the frequency resolution. Over the frequency range most relevant to surface pressure fluctuations ($> 15Hz$) a window length of approximately

3 seconds (4500 samples) was sufficient to accurately define dominant peaks contained within spectral estimates of surface pressure data and may be assumed unless otherwise stated. For a summary of the random errors associated with the frequency analysis of unsteady surface pressure measurements see Appendix F.

4.1.2.1 Areas of distinct spectral activity

As noted at the beginning of this chapter, spectra of unsteady surface pressures and velocity components measured in the wake traverses show very broadband characteristics. Despite this, pressure fluctuations on the back and in the wake of the mannequin exhibit regions of distinct spectral activity. These regions were identified by determining the energy content of surface pressure spectra in low (0–8 Hz), medium (11–24 Hz) and high (40–60 Hz) frequency bands. The energy contained within these frequency bands was calculated by integrating the area under the PSD function within these frequency limits. Areas associated with a particular frequency band can then be further scrutinised by analysing spectra at discrete locations on the body and in the wake of the mannequin.

The energy content of surface pressure fluctuations contained within low, medium and high frequency bands expressed as a ratio of the total variance of the signal (total area under PSD function) is shown as contours in figures 4.7 and 4.8 for the low and high drag leg positions respectively. It is evident the majority of the energy of the surface pressure fluctuations fall into a particular frequency range depending on which region of the back and leg position is analysed. Also shown to the far left of figures 4.7 and 4.8 are contours of the variance, so that areas previously identified with large surface pressure fluctuations can be compared with areas that display distinct spectral activity.

In areas where the highest pressure fluctuations occur on the sides of the torso for both high and low drag leg positions, the energy of these fluctuations is concentrated in the high 40–50 Hz frequency range. This was also seen in the fluctuating surface pressures in the 450kW tunnel, which compare very well with those measured in the MLWT. This can be seen in Appendix G, which shows a copy of figures 4.7 and 4.8 for time-accurate surface pressure measured in the 450kW tunnel. Other areas of lower energy pressure fluctuations associated with low and medium frequency bands are also noticeable on the lower back of the mannequin. Based on these findings surface pressure fluctuations were further scrutinised in the areas of high 40–50 Hz, medium 16–24 Hz

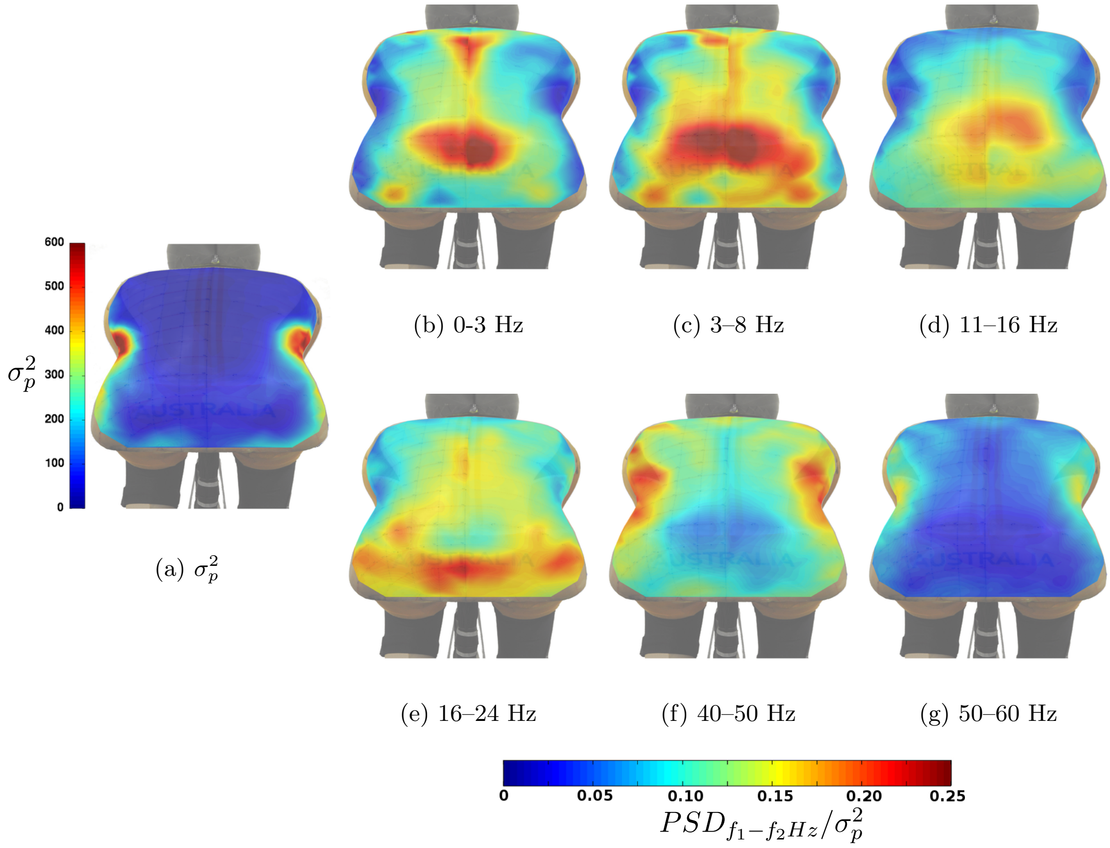

(a) σ_p^2 (b) 0-3 Hz (c) 3–8 Hz (d) 11–16 Hz (e) 16–24 Hz (f) 40–50 Hz (g) 50–60 Hz

FIGURE 4.7: Contours of energy levels contained in discrete frequency bands compared with total variance of surface pressure fluctuations for the low drag 15° leg position.

and low 0–8 Hz frequency spectral content for all leg positions around the crank cycle. The nature of these pressure fluctuations is examined using band-pass filtering, real-time animations of pressure fluctuations and cross-spectral analysis. Surface pressure fluctuations on the back are also compared with areas of the wake exhibiting the low, medium and high frequency velocity fluctuations.

4.1.2.2 High frequency spectral content

Figure 4.9 shows the contribution of energy contained in the high frequency band 40–50 Hz to the total energy of surface pressure fluctuations for leg positions in the first half of the crank cycle. For positions 15° either side of the low drag 15° and 195° leg positions, high frequency fluctuations are concentrated on both sides of the torso. As the gap between the upper thigh and chest is closed, and the flow transitions to the asymmetrical flow regime, these high frequency fluctuations are only observed on the side of the torso where the leg is in an extended position.

Spectra in the high frequency areas of the torso for both low and high drag leg

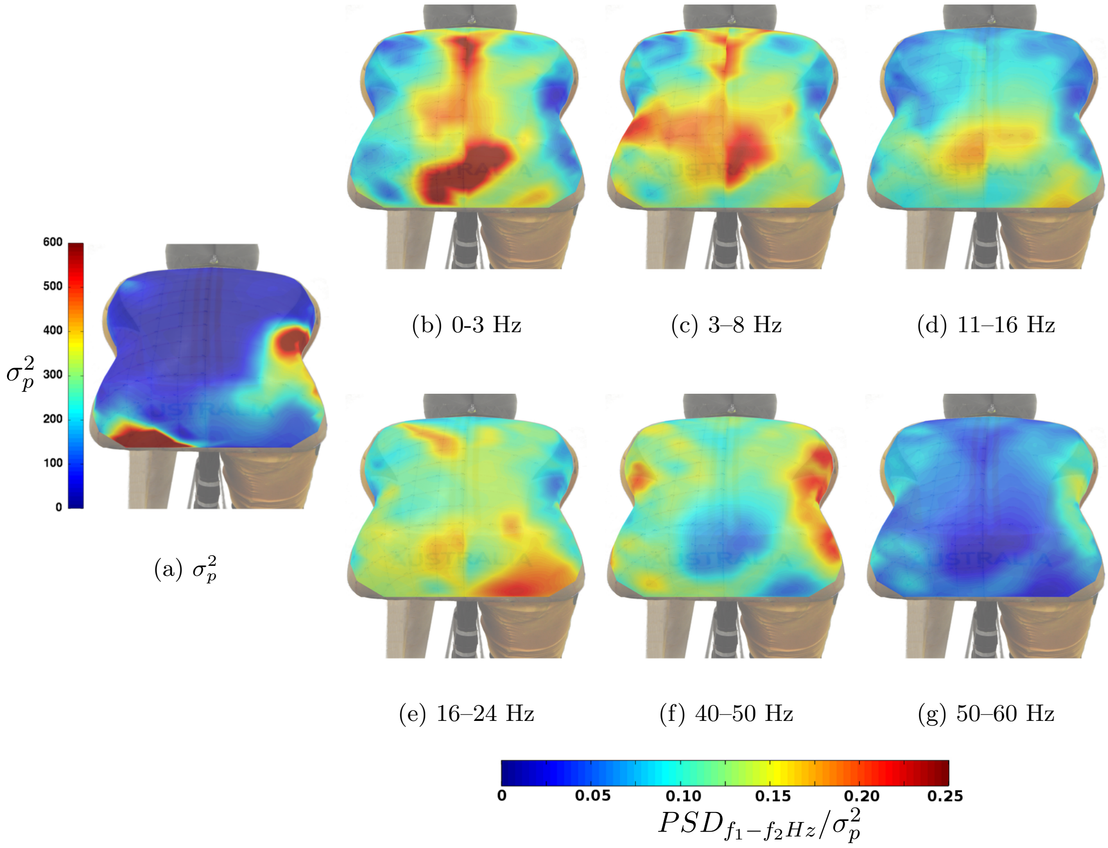

(a) σ_p^2 (b) 0-3 Hz (c) 3–8 Hz (d) 11–16 Hz (e) 16–24 Hz (f) 40–50 Hz (g) 50–60 Hz

FIGURE 4.8: Contours of energy levels contained in discrete frequency bands compared with total variance of surface pressure fluctuations for the high drag 75° leg position.

positions are shown in figures 4.10 and 4.11. For both positions when the upper thighs are aligned (15° and 195°) and when the hip angle is open on the left side (255°), a broad spectral peak can be seen at the higher end of the spectrum (40–50 Hz). For leg positions in the asymmetrical flow regime on the side of the body where the hip angle is open, the largest pressure fluctuation in the 40–50 Hz frequency range are found at the mid torso upstream of where the rear hip vortex originates. The energy content of the high frequency pressure fluctuations diminishes with incremental tap spacing downstream of the mid-torso ($\approx 50mm$), as shown in figure 4.10(d). This suggests that the large pressure fluctuations occurring on the sides of the torso are not associated with shedding phenomena of the primary rear hip vortex that is formed further downstream at the hip junction where lower pressure fluctuations are observed. Instead, it is hypothesised that the unsteadiness associated with this frequency is primarily associated with vortex shedding from the arms. Further evidence in support of this hypothesis will be discussed when investigating the influence of arm position on surface pressure and velocity fluctuations in the wake of the arms.

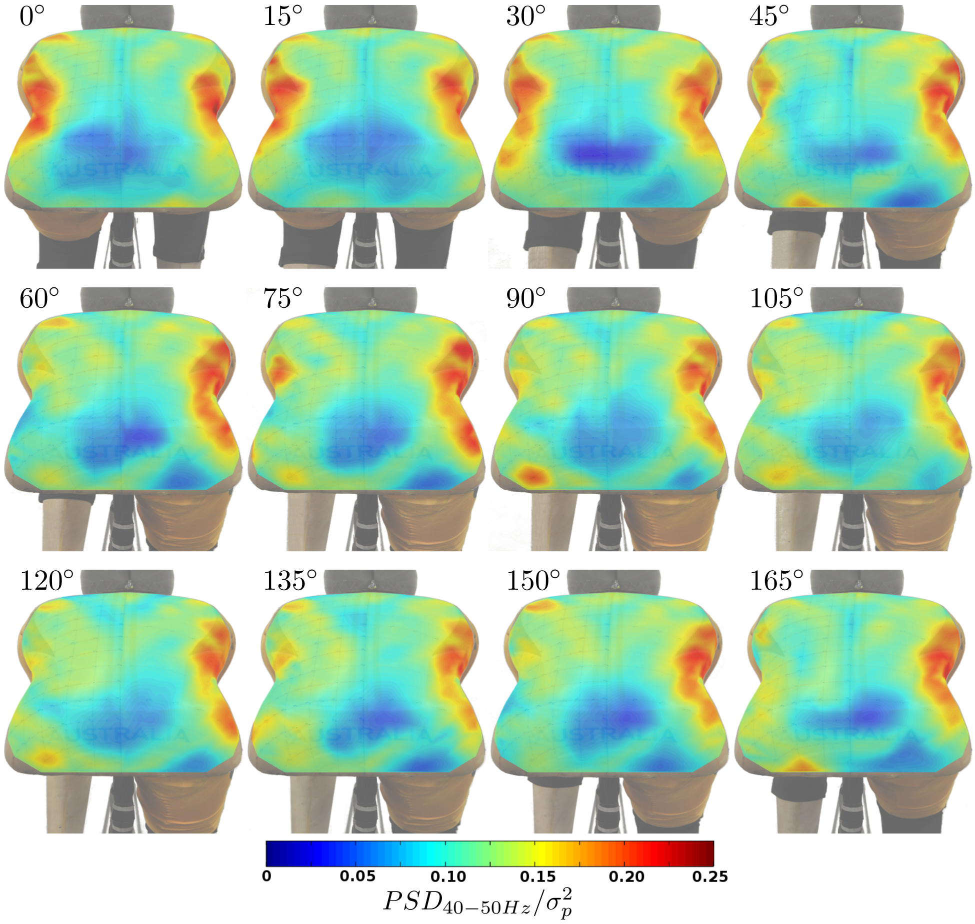

FIGURE 4.9: Contours of the PSD function integrated between 40–50 Hz expressed as a ratio of the total variance of the surface pressure fluctuations (total area under PSD function).

As the legs move around the crank cycle, the defining characteristics of high frequency pressure fluctuations show little variation with leg position. This can be seen in figure 4.11, which shows the PSD functions of the selected taps (marked in figure 4.10) in 30° increments around the complete crank cycle. Also notable are the crank angles where a distinct drop in the PSD function is observed across all frequencies as the flow reattaches to the left side of the torso between 45°–150° in the first half of the crank cycle (i.e., when the leg is raised).

Averaging of the PSD spectra at specific locations on the body over a range of crank angles provides a good indication of the mean spectral behaviour of pressure fluctuations throughout the pedal stroke. Figure 4.12 shows the spectrum on the left side of the torso, which has been averaged over the second half of the cycle (i.e., when the left hip angle is open). This is compared with the frequency spectrum at the same location for the high drag 255° leg position and also the averaged spectrum for the fluctuating pressures measured in the 450kW wind tunnel. Measurements in both

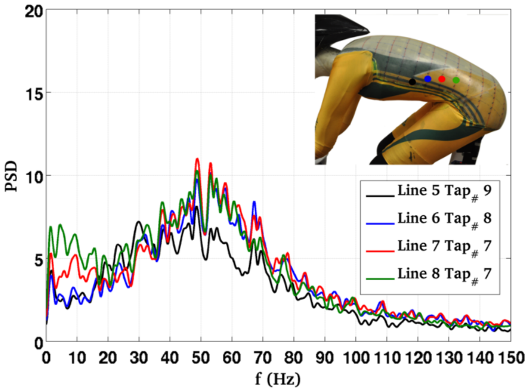

(a) $\theta = 15°$

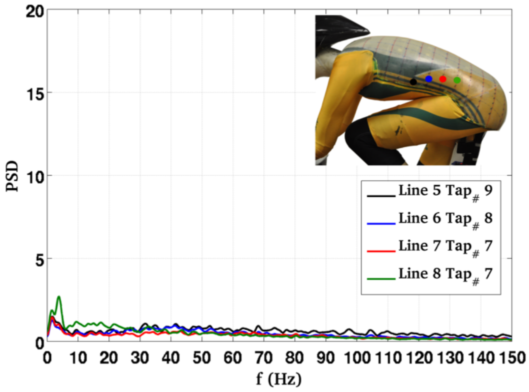

(b) $\theta = 75°$

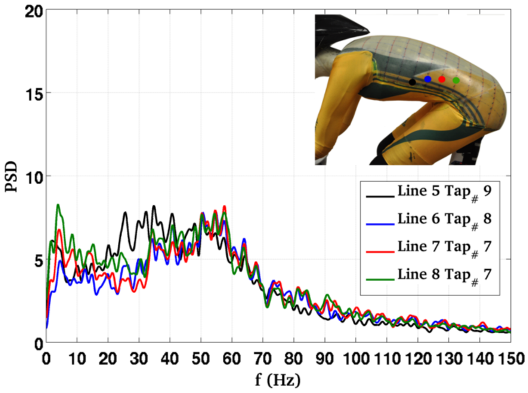

(c) $\theta = 195°$

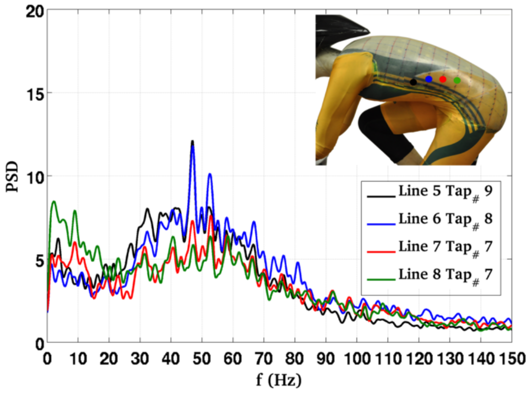

(d) $\theta = 255°$

FIGURE 4.10: Spectra of surface pressure fluctuations measured at pressure taps located on the side of the torso for low and high drag leg positions.

wind tunnels show the same global broadband nature of the pressure fluctuations over these particular crank angles, again suggesting that these particular frequencies are not significantly affected by background wind tunnel noise or blockage constraints.

Analysis of the group behaviour of time-accurate pressure measurements in high frequency areas show how these pressure fluctuations propagate over the torso. Figure 4.13 shows the cross-spectral magnitude/phase relationship between surface pressure measurements where high frequency pressure fluctuations are first observed to occur (reference marked by a red cross) and measurements downstream that span the area where a spectral peak between 40–50 Hz was observed (marked by coloured dots). The broad frequency spectrum is more clearly defined compared with single PSD estimates at these measurement locations, with cross spectra peaking in the 40–50 Hz high

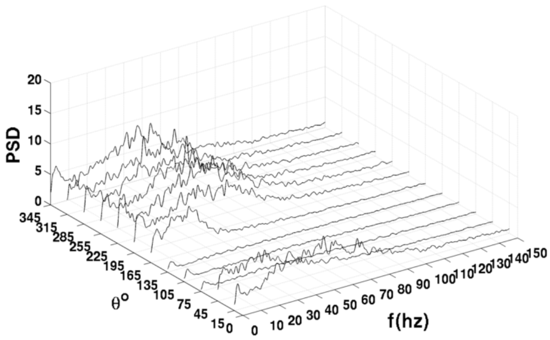

(a) Line 5 $Tap_{\#}$ 9

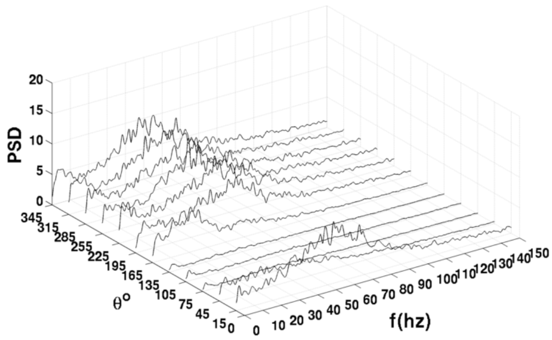

(b) Line 6 $Tap_{\#}$ 8

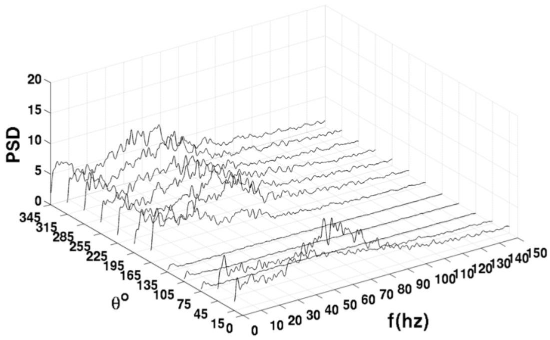

(c) Line 7 $Tap_{\#}$ 7

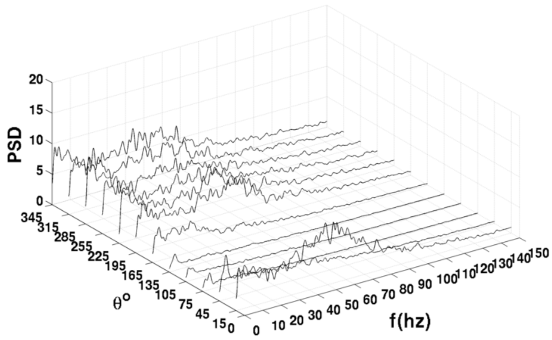

(d) Line 8 $Tap_{\#}$ 7

FIGURE 4.11: Variation in spectra of surface pressures measurements located on the side of the torso throughout the course of the pedal stroke.

frequency band at ≈ 48 Hz. No significant variations in cross spectra are observed in this region for crank angles between 0°–30° and 180°–360°, when flow separation occurs on the left side of the torso.

Phase estimates are also shown. These show that for frequencies that range across the broad cross spectral peak a linear phase/frequency relationship exists. This is consistent with Taylor's hypothesis of non-dispersive propagation, where the convection velocity is independent of both frequency and wave number, and is equal to the local mean velocity Moin (2009). The gradient of this linear portion of the phase relationship increases as pressure fluctuations at the mid torso are progressively compared with pressures measured at taps located further downstream. As expected the increase in the gradient is directly proportional to the increase in the spatial separation between taps. The phase relationship between fluctuating pressures is consistent with vortex shedding, with vortices being formed and connecting downstream along the side of the

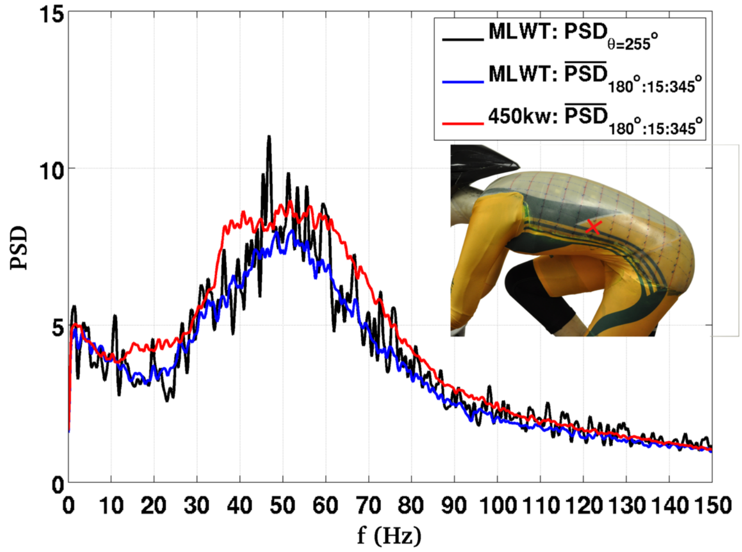

FIGURE 4.12: Average spectra in both the MLWT and 450kW wind tunnels over crank angles in the second half of the crank cycle, for the tap positioned on the side of the torso at the mid torso chord location (Line 6 $Tap_{\#}8$).

torso with the local mean velocity. The convection velocity of vortices shed over the sides of the torso (calculated by the phase relationship of separated taps in this region) is approximately 60% of the freestream velocity. This is comparable with the local mean velocity that was measured around the sides of the torso in the wake traverse measurements (see figure 3.16).

Where vortices are shed around the side of the torso the surrounding pressure measurements in these regions are well correlated. This can be seen in figure 4.14, which shows contours of the coherence coefficient and phase lag of surrounding pressure measurements referenced to where the high frequency 40–50 Hz fluctuations are first observed on the torso (marked by red dot). From the time lag of pressure fluctuations in highly correlated areas we get a sense of the path taken by vortices over the torso as they are convected downstream for the 15° and 255° leg positions shown. Pressure fluctuations that arrive in phase can be seen where the same 'lag time' is measured between fluctuating pressures measured at the different tap locations. The graduated contours of the time lag shows distinct bands, which have being highlighted with bold black lines, where pressure fluctuations arrive in phase at the same time. Comparing figure 4.14(b) and (d), it is evident that the pressure fluctuations, that are driven by the shedding of low pressure vortices, take a slightly higher trajectory over the torso

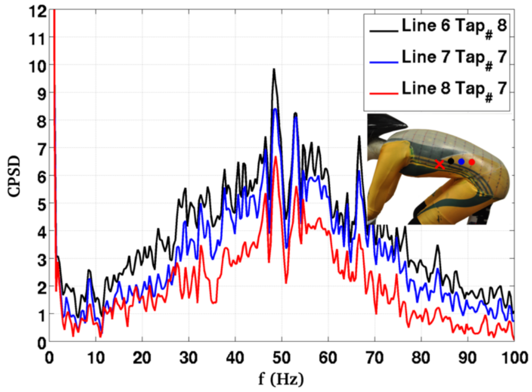

(a) CPSD: $\theta = 15°$

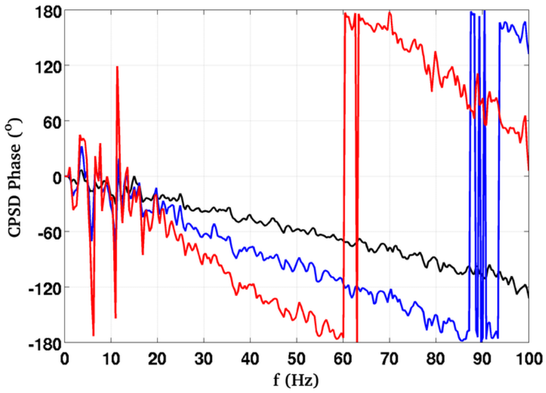

(b) Phase: $\theta = 15°$

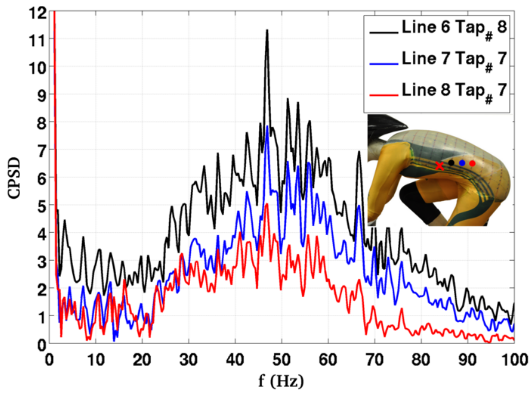

(c) CPSD: $\theta = 255°$

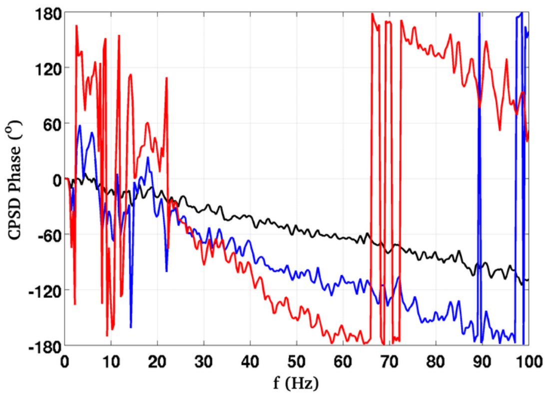

(d) Phase: $\theta = 255°$

FIGURE 4.13: Cross spectra and cross-phase relationships for fluctuating pressures measured on the left side of the torso for 15° and 255° leg positions. All spectra are compared with the tap located at the mid torso (Line 6 $Tap_{\#}8$) marked by the red cross in the images of the two positions.

for the 255° leg position where the hip angle is at a maximum. The orientation of the pressure fluctuations is comparable with that of the path taken by smoke released at the mid torso that was shed high into the wake.

The propagation of fluctuating surface pressures in the separated regions on the sides of the torso has also being further characterised by visualising surface pressures in real time. Attached to Appendix H is a CD that contains animations of contours, of both the instantaneous surface pressure coefficient, and the fluctuating pressure component with the mean pressure subtracted. These animations are viewed in slow motion from side and rear view perspectives for the low (15°) and high (75°, 255°) drag leg positions. From these animations periodic high frequency pressure fluctuations are identified on

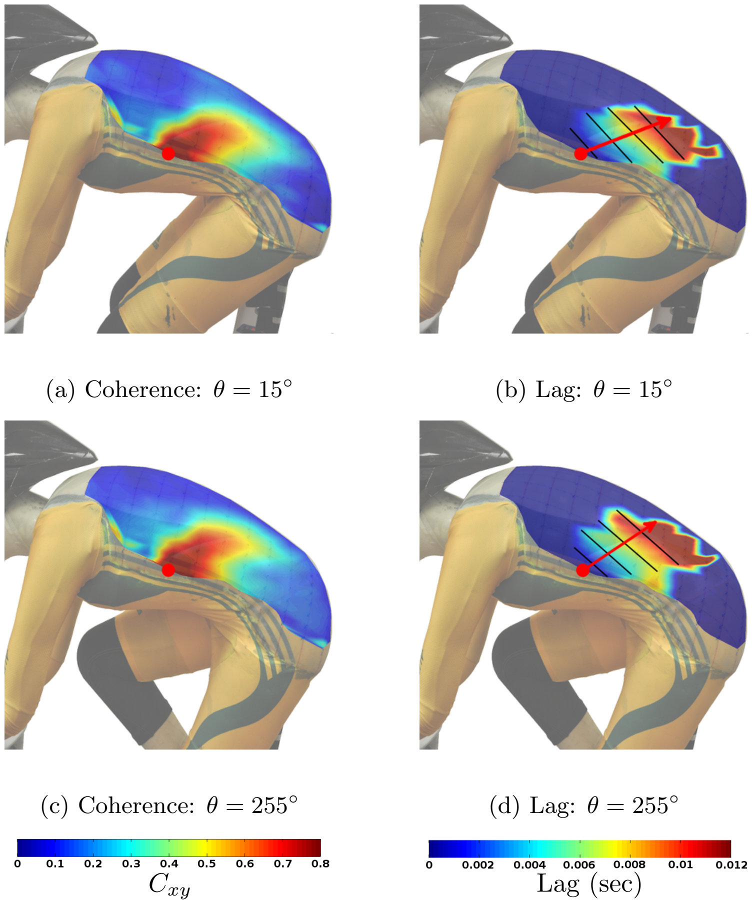

(a) Coherence: $\theta = 15°$ (b) Lag: $\theta = 15°$

(c) Coherence: $\theta = 255°$ (d) Lag: $\theta = 255°$

FIGURE 4.14: Contours of the cross-correlation coefficient and time lag for 15° and 255° leg positions. Contours show correlation between back surface pressures and fluctuating pressures measured at the mid torso (Line 6 $Tap_{\#}8$), where high frequency pressure fluctuations are first observed (marked by the red dot in the images).

the torso sides where the largest pressure fluctuations occur. To highlight these pressure fluctuations, band-pass filtering was applied to surface pressure measurements using a third-order Butterworth filter. Along with the raw surface pressure fluctuations, animations of fluctuating surface pressures band-pass filtered between the 3–8 Hz, 16–24 Hz and 40–50 Hz can also be found on the CD in Appendix H for side and rear view perspectives.

For both low and high drag leg positions the 40–50 Hz band-pass filter clearly captures the vortex shedding cycle from the side of the torso, despite the broad band spectral nature of the pressure fluctuations. Figure 4.15 shows a sequence of instantaneous pressure coefficient contours from the 40–50 Hz band-pass filtered animations. The contours show one shedding cycle for low and high drag leg positions. The size and magnitude of pressure fluctuations on the side of the torso when the hip angle is at

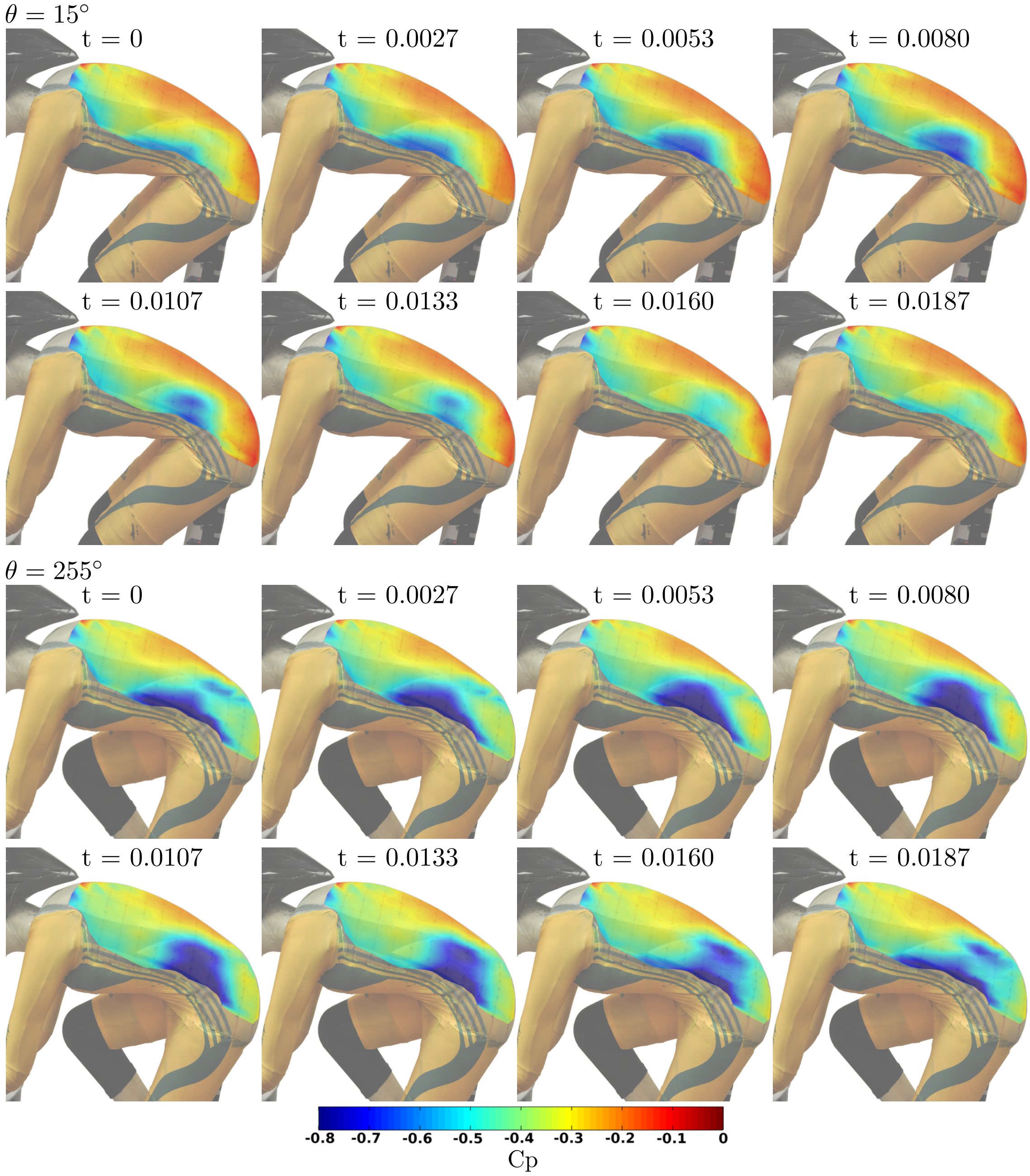

FIGURE 4.15: Instantaneous pressure distributions band-pass filtered between 40–50 Hz for low 15° (Top) and high drag 255° (Bottom) leg positions. Time (t) is in seconds.

a maximum are clearly greater than the low drag leg positions. On closer inspection of the animations that depict this shedding process, periods of regular periodic motions are also coupled with time periods where other complex pressure motions are evident and appear at random time intervals in the signal. This suggests competing modes of surface pressure fluctuations, which are more noticeable in the animations that show fluctuating pressure with the mean component subtracted. The transient nature of these dominant periodic motions contributes to the broadband characteristics of the pressure fluctuations in these areas.

Although the primary focus of this section is the characterisation of the unsteady aerodynamics associated with the standard arms-out position, it is worth noting how arm positions influence the surface pressure fluctuations measured at the sides of the torso. Section 3.2.2.1 has shown that arm position has a large influence on the magnitude of the mean pressures acting on the torso sides. It is found that arm position also influences the magnitude of the unsteady pressure fluctuations in these areas. Figure 4.16 shows spectra for leg positions around the crank cycle for the mannequin in the arms-in position, for the four selected pressure taps that were previously used to characterise pressure fluctuations for the standard arms-out position. Also shown in figure 4.16 are spectra at each tap location that was averaged over the crank angles where the high frequency content has been identified. Average spectra are shown for both arm positions so that the global characteristics of the pressure fluctuations throughout the crank cycle can be compared. The major difference between the two arm positions is that there is a significant increase and a more clearly defined high-frequency peak for the arms-in position.

Interestingly, surface pressure fluctuations in the 40–50 Hz high frequency range are at a frequency consistent with vortex shedding from the upper arms. At the local Reynolds number of $\approx$ 87,000 based on the mean upper arm diameter (0.08 m), a shedding frequency of 42 Hz would be expected. This is based on the well established Strouhal number of 0.21 for circular cylinders Roshko (1955). If vortex shedding from the arms is driving the high frequency fluctuation then this may explain the increase in energy associated with these frequencies for the arms-in position. As the arms are brought closer together the wake that develops downstream is more likely to impinge on or to buffet the sides of the torso. It was also found that the Strouhal number associated with these pressure fluctuations remained relatively constant over the three test speeds. This is shown in figure 4.17, which shows spectra of surface pressure fluctuations on the side of the torso as a function of the Strouhal number based on the mean diameter of the upper arms. All spectra shown for the three test velocities were averaged over crank angles where the high frequency fluctuations were present on the left side of the torso.

Further evidence in support of this hypothesis was gained by investigating the spectral content of velocity fluctuations measured using the Cobra Probe for wake traverses.

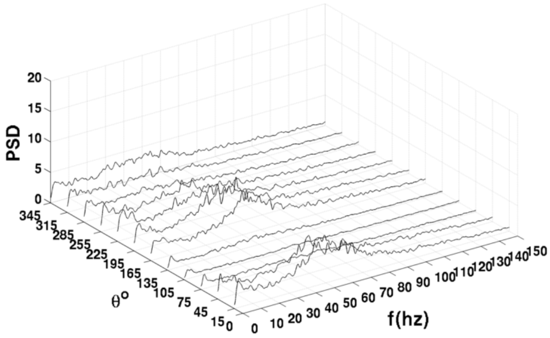

(a) Arms-in: Line 5 $Tap_{\#}$ 9

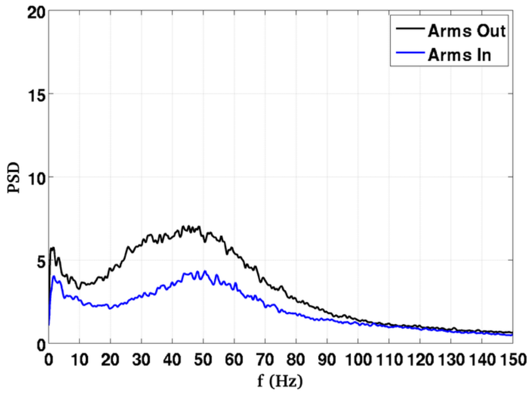

(b) Line 5 $Tap_{\#}$ 9: $\overline{PSD}_{\{0°,15°\}\cap\{180°:15:345°\}}$

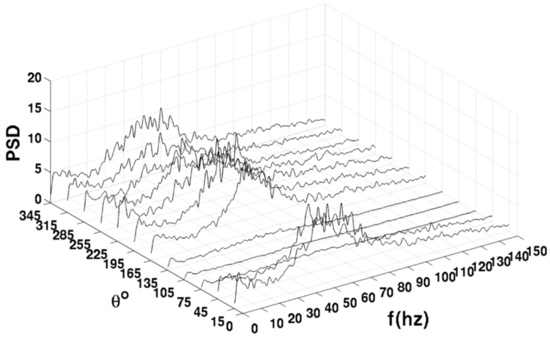

(c) Arms-in: Line 6 $Tap_{\#}$ 8

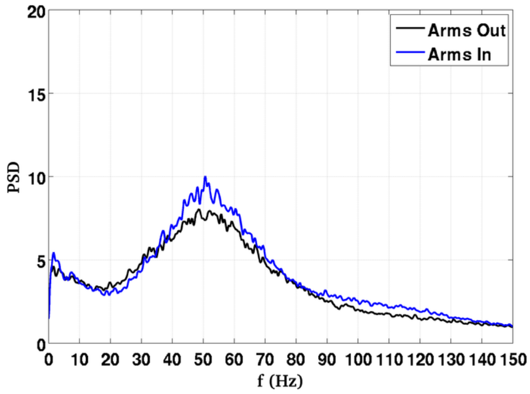

(d) Line 6 $Tap_{\#}$ 8: $\overline{PSD}_{\{0°,15°\}\cap\{180°:15:345°\}}$

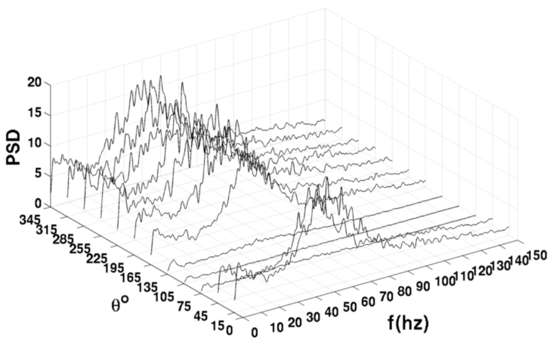

(e) Arms-in: Line 7 $Tap_{\#}$ 7

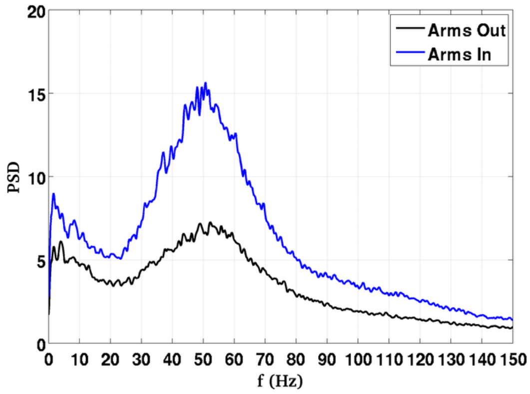

(f) Line 7 $Tap_{\#}$ 7: $\overline{PSD}_{\{0°,15°\}\cap\{180°:15:345°\}}$

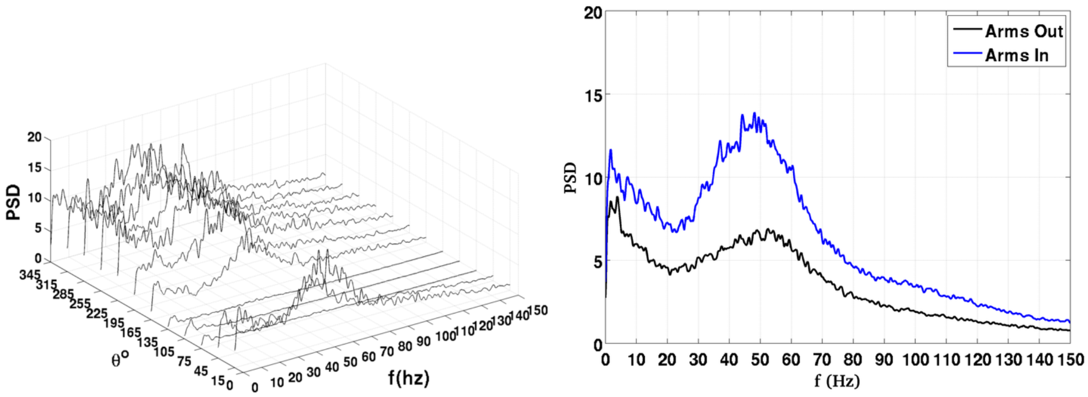

(g) Arms-in: Line 8 $Tap_{\#}$ 7 (h) Line 8 $Tap_{\#}$ 7: $\overline{PSD}_{\{0°,15°\}\cap\{180°:15:345°\}}$

FIGURE 4.16: Variation in spectra of surface pressures measurements located on the side of the torso throughout the course of the pedal stroke for the arms-in position. Spectra averaged over the course of the pedal stroke where high frequency fluctuations are prominent, are shown alongside the PSD functions depicted around the crank cycle at each tap location.

In the wake of the arms on the sides of the torso, probe measurements show distinct areas where a peak frequency between the high 40–50 Hz band is found in the PSD functions of both the spanwise 'v' and vertical 'w' fluctuating velocity components. These areas are identified in figures 4.18(a–b), which show contours of the peak value of the PSD function for 'v' and 'w' components for the five traverse planes for both the low (15°) and high (75°) drag leg positions. Traverse measurements where the peak values of the PSD function was between 40–50 Hz have been marked with a black dot. The largest concentration of probe measurements that identify a high peak frequency is found in the 'w' component of velocity fluctuations measured in the upper regions of the wake in line with the shoulders in the traverse plane performed at the hip joint (P3). This finding suggests much of the flow forward of the hip/torso junction does not roll up into the primary rear hip vortex but instead is shed high up into the wake behind the mannequin above the hips. This is supported by the smoke flow visualisations presented in section 3.1.3.2, where an upwards trajectory of smoke particles into the wake was observed for smoke released at the mid torso and arms.

Although the large pressure fluctuations on the sides of the torso are characterised by frequencies in the 40–50 Hz range, the energy of velocity fluctuations prominent in this frequency band are significantly lower compared to the much higher energy velocity fluctuations that occur lower in the wake below the upper hips. This was found not

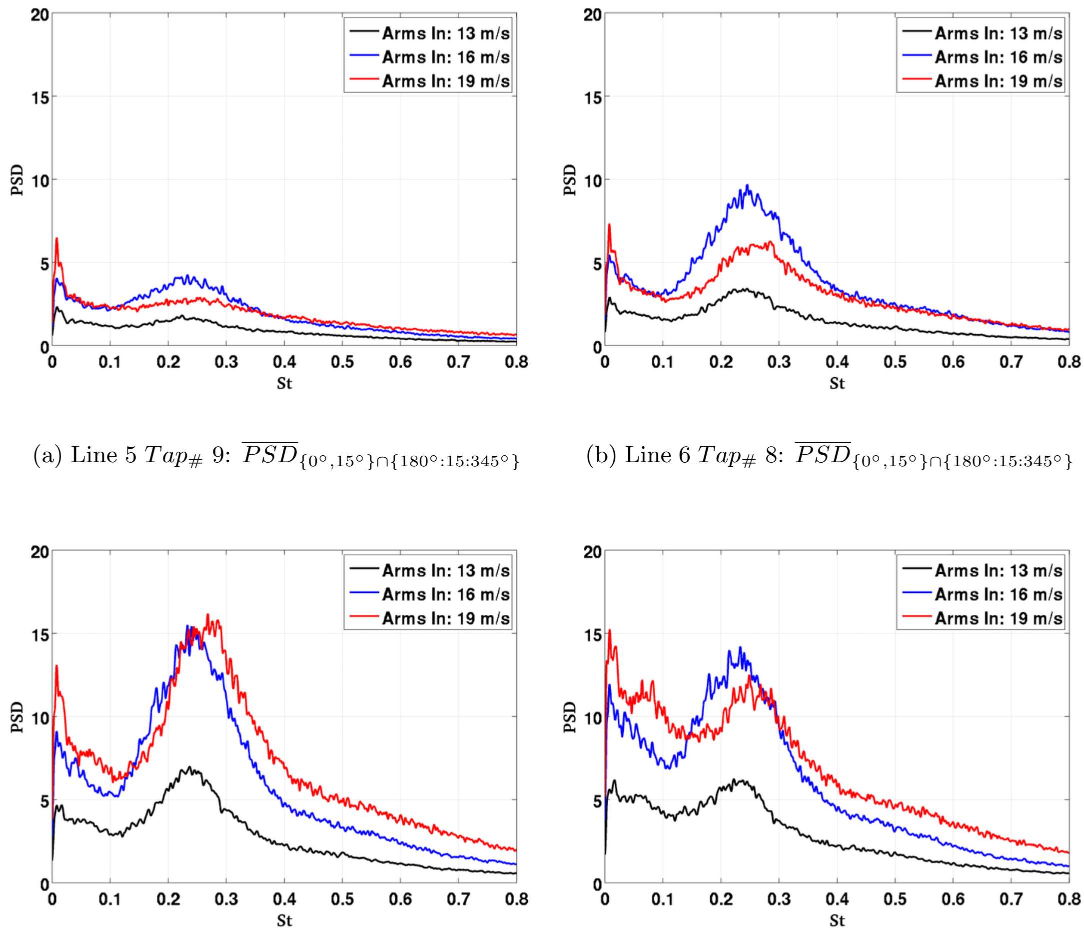

(a) Line 5 $Tap_{\#}$ 9: $\overline{PSD}_{\{0°,15°\}\cap\{180°:15:345°\}}$

(b) Line 6 $Tap_{\#}$ 8: $\overline{PSD}_{\{0°,15°\}\cap\{180°:15:345°\}}$

(c) Line 7 $Tap_{\#}$ 7: $\overline{PSD}_{\{0°,15°\}\cap\{180°:15:345°\}}$

(d) Line 8 $Tap_{\#}$ 7: $\overline{PSD}_{\{0°,15°\}\cap\{180°:15:345°\}}$

FIGURE 4.17: Spectra of surface pressures measurements located on the side of the torso as a function of the Strouhal number based on the mean upper arm diameter.

only for the 15° and 75° leg positions but for all leg positions around the crank cycle. For the ‘w’ velocity fluctuations, figure 4.19 shows that as the areas associated with the high frequency velocity fluctuations are traced from the upper arms back into the wake, the energy content of these frequencies components quickly diminishes. This shows that structures associated with these frequencies decay relatively rapidly in the near wake and are not characteristic of the much higher energy velocity fluctuations that occur lower down in the wake.

4.1.2.3 Medium frequency spectral content

Compared with sides of the torso, spectra of surface pressure fluctuations that occur on other areas of the back are less coherent and have lower energy. Regions where surface

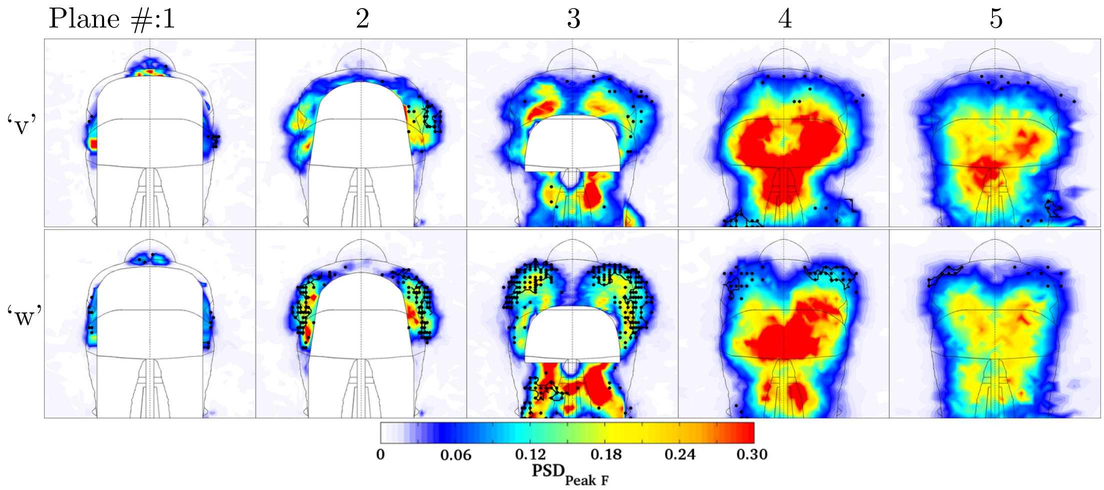

(a) $\theta = 15°$

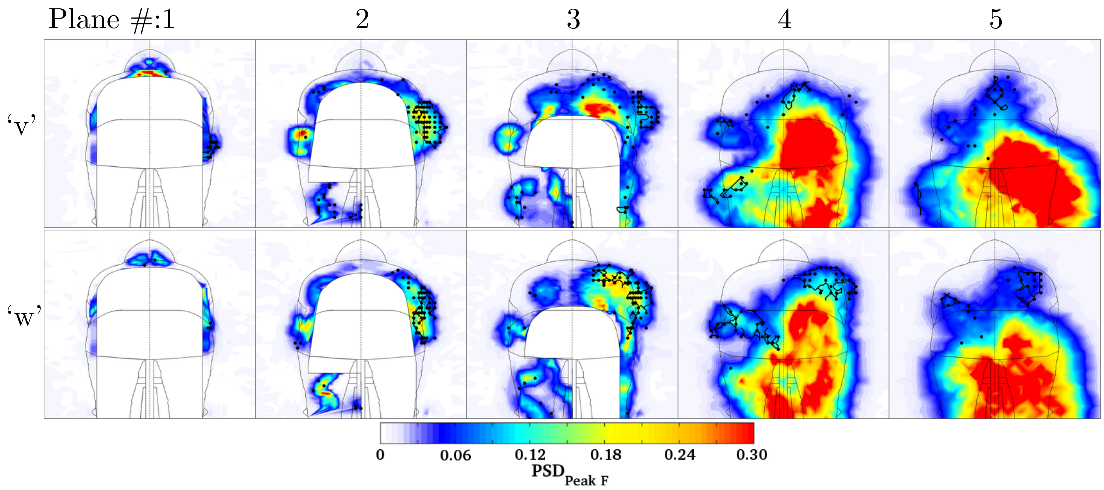

(b) $\theta = 75°$

FIGURE 4.18: Frequency analysis of 'v' and 'w' components of velocity, for Cobra Probe measurements in planes 1–5 for (a) the 15° and (b) 75° crank positions. Contours are of the PSD function at the peak frequency. Velocity measurements in the traverse planes whose peak frequency lies between 41–46 Hz are marked '•', with black lines outlining measurements that are concentrated within this frequency band.

pressure fluctuations on the back are concentrated in the medium 16–24 Hz frequency band are identified in figure 4.20 for leg positions in the first half of the crank cycle. The largest areas of spectral activity in the medium frequency band arise on the rear base of the mannequin for all leg positions. For the low drag positions (0°, 15°), a band of medium frequency activity spans across the lower hip region on the rear base. For the higher drag leg positions, the energy in the medium frequency band is primarily concentrated on the rear hip of the extended leg (right leg in first half of the cycle). This area, which is highlighted for the 75° leg position in figure 4.20 by the dashed line, closely matches up with the separation region that was identified in the surface

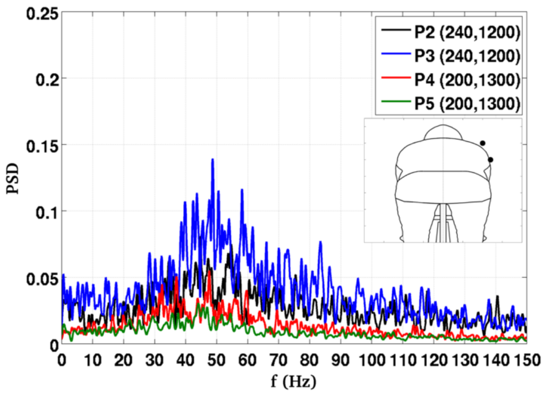

(a) $\theta = 15°$

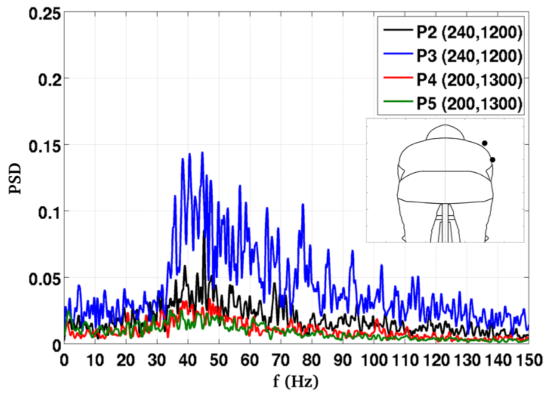

(b) $\theta = 75°$

FIGURE 4.19: Power spectra of 'w' component of velocity measured in traverse planes 2–5 (P2,P3,P4,P5), showing high frequency velocity fluctuations at (P2 and P3 (240 mm,1200 mm)) and (P3 and P4 (200 mm,1300 mm)) coordinate points.

skin-friction flow visualisations (see figure 3.13 in section 3.1.3.2). Other notable areas characteristic of this frequency range occur on the shoulders, especially the left shoulder for the asymmetrical leg positions in the first half of the crank cycle.

As in the higher frequency fluctuations, fluctuating pressures characteristic of the medium frequency band also display broadband spectral behaviour. This is shown in figure 4.21, which shows the PSD functions for pressure measurements located on the rear base. Energy concentrated in the medium frequency band was particularly evident for both low (15°) and high (255°) drag leg positions. For the 15° position, a peak in the spectrum is found between 16–24 Hz for pressure fluctuations measured on the middle of the base of the lower back in both the MLWT and the 450kW wind tunnels. For the high drag 255° position, a very broad peak is found for surface pressure fluctuations measured in the separated area on the rear of the hip of the extended left leg. This broad spectral behaviour was observed for all leg positions in the asymmetrical flow regime. This is indicated by spectra which were averaged over the second half of the crank cycle for the tap located by the red cross in figure 4.21. The averaged spectrum for pressure fluctuations measured at the same tap location in the 450kW wind tunnel is also shown. The two averaged spectra once again compare very well, showing the same global nature of the pressure fluctuations in this region was consistent for both tunnels.

Fluctuating velocity components measured in the wake traverses show that signif-

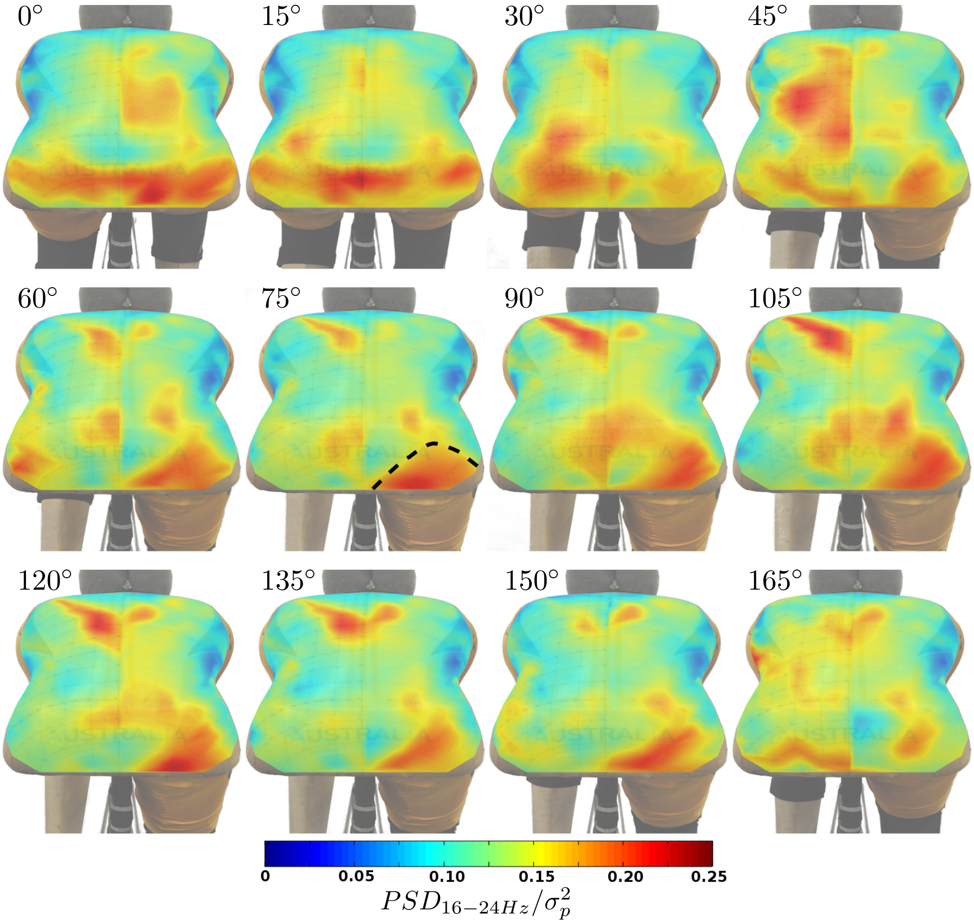

FIGURE 4.20: Contours of the PSD function integrated between 16–24 Hz expressed as a ratio of the total variance of the surface pressure fluctuations (total area under PSD function).

icant portions of the wake are characterised by areas of high unsteadiness associated with the medium frequency band. Figure 4.22(a–b) show contours of the peak value of the PSD function of fluctuating 'v' and 'w' velocity components measured in the five traverse planes, for the 15° and 75° leg positions. The black dots on the contours mark probe locations where the peak value of the PSD function was between the 16–24 Hz limits. Only measurement locations that were within the acceptable working limits of the Cobra Probe (see section 2.4.1 for details) are included in this analysis. For both leg positions, areas of the wake where the highest energy fluctuations occur correspond to this 16–24 Hz range. Although there is clearly spectral activity in the medium frequency band in the vertical 'w' components, it is much stronger in the spanwise 'v' component. This was typical for the majority of leg positions around the crank cycle. Figure 4.23 identifies the measurement locations in the wake, for leg positions around the complete crank cycle, where the fluctuating 'v' component showed a medium-band peak for the wake traverse performed a torso length behind the mannequin. The high

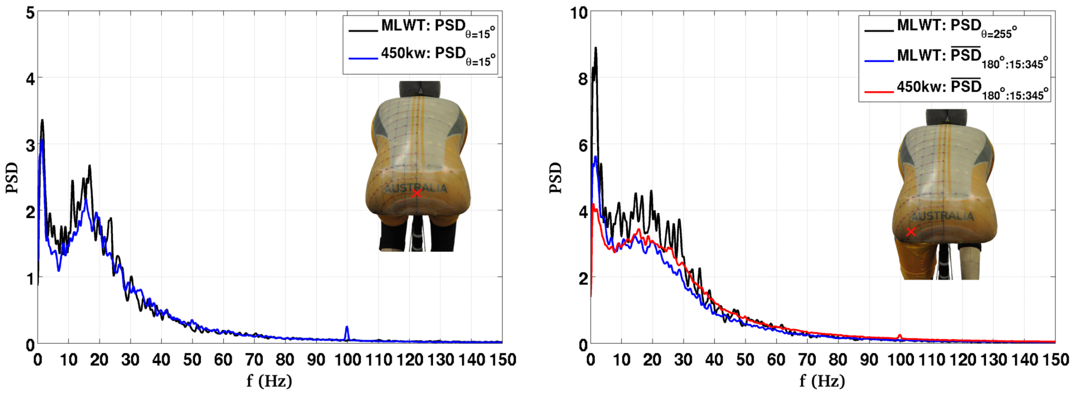

(a) (b)

FIGURE 4.21: (a) Spectra for surface pressures measured in the middle separated area on the rear base of the mannequin (Line 13 $Tap_{\#}1$) for the 15° leg position and (b) spectra averaged over crank angles in the second half of the crank cycle, for the tap positioned behind the left extended leg (Line 13 $Tap_{\#}4$). Note vertical scale in figure (a) is half of that shown in (b).

concentration of peak medium frequency band measurements where the largest velocity fluctuations occur in the wake is clearly evident.

Figure 4.24 shows PSD functions for point measurements of the 'v' velocity component located behind the middle of both left and right hip joints in the traverse plane one torso length in the wake. For the measurement locations behind the right leg, figure 4.24(a) shows the evolution of the PSD spectra in 30° increments for a full crank cycle. A gradual increase in the energy content contained in the 16–24 Hz frequency band can be seen in the first half of the crank cycle, where it peaks when the right hip angle is at a maximum between 90° and 120°. (See figure 2.8 for variation in hip angle with crank angle). The spectrum for the 90° leg position shown in figure 4.24(b), has a spectral peak in the 16–24 Hz frequency band that is particularly evident. Also shown in this figure, is the spectrum at this measurement location in the wake averaged over crank angles 45° to 165°. The mean behaviour of the velocity fluctuations throughout this portion of the crank cycle clearly exhibits the medium frequency spectral behaviour. As the legs progress around the crank cycle and the wake flips over to the other side of the body, the energy in the spectrum of spanwise velocity fluctuations measured behind the right leg drops. In the second half of the crank cycle figure 4.24(c–d) shows the same 16–24 Hz spanwise velocity fluctuations now occur behind the extending left leg on the opposite side of the body.

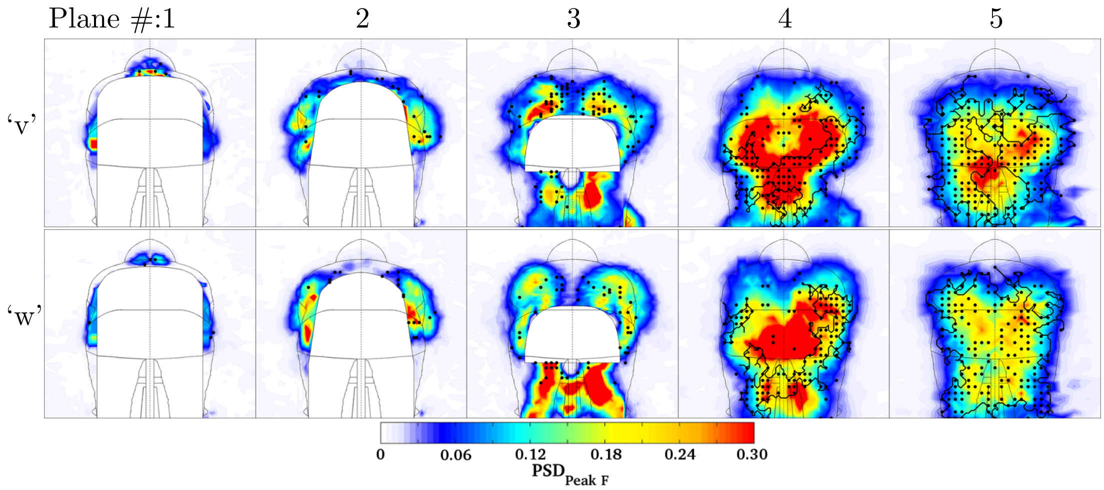

(a) $\theta = 15°$

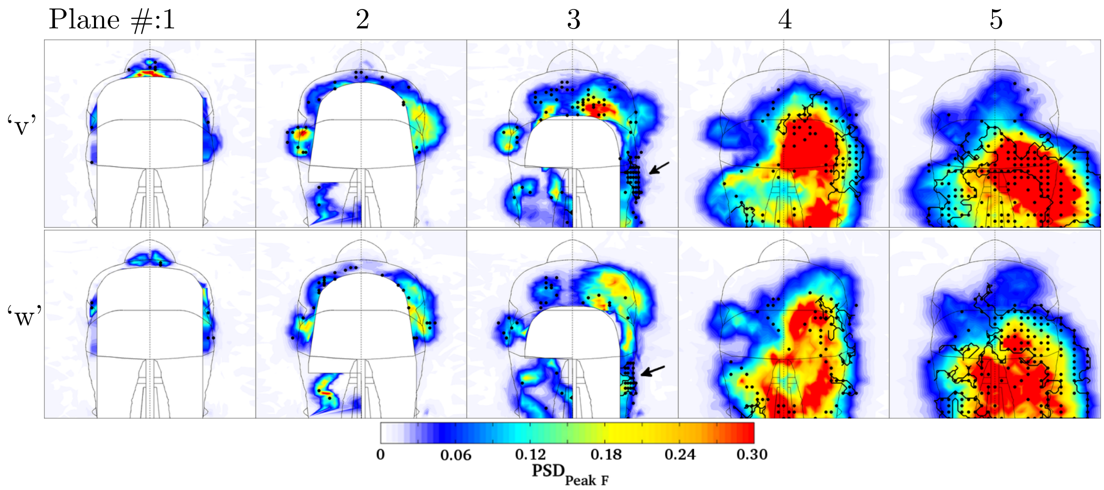

(b) $\theta = 75°$

FIGURE 4.22: Frequency analysis of 'v' and 'w' components of velocity, for Cobra Probe measurements in planes 1–5 for (a) the 15° and (b) the 75° crank positions. Contours are of the PSD function at the peak frequency. Velocity measurements in the traverse planes whose peak frequency lies between 17–22 Hz are marked '•', with black lines outlining measurements that are concentrated within this frequency band.

Interestingly, a dominant peak in the spanwise velocity component located behind the legs is consistent with alternating Kármán-like vortices being shed from the inner and outer thighs. Like the arms, one might also expect the legs to exhibit Kármán-like shedding, given that the legs were modelled on tapered cylindrical sections. Based on a mean upper leg diameter of 0.15 m and an expected Strouhal number of ≈ 0.2, a vortex shedding frequency of ≈ 21 Hz could be expected. This is consistent with the dominant frequencies that were identified in the fluctuating velocity components. It is hypothesised that vortices are predominately initiated along the lower regions of the upper thighs, where the legs more closely resemble a cylinder in a pure cross flow. This

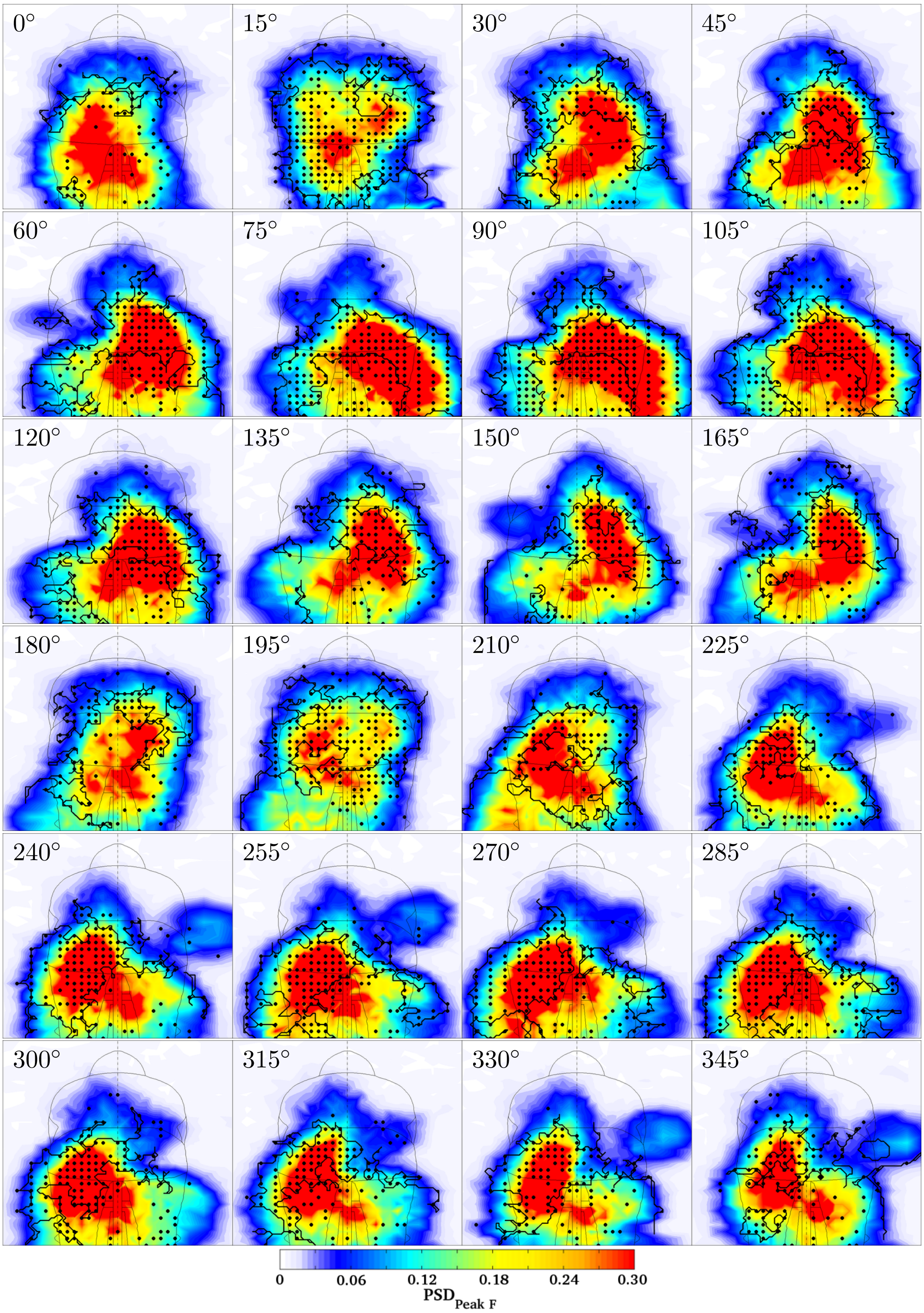

FIGURE 4.23: Frequency analysis of 'v' component of velocity for Cobra Probe measurements in planes 5 (Torso chord length in wake) for leg positions around a complete crank cycle; Contours are of the PSD function at the peak frequency. Measurements in the traverse planes (> 90% good data) whose peak frequency lies between 16–24 Hz are marked '•', with black lines outlining measurements that are concentrated within this frequency band.

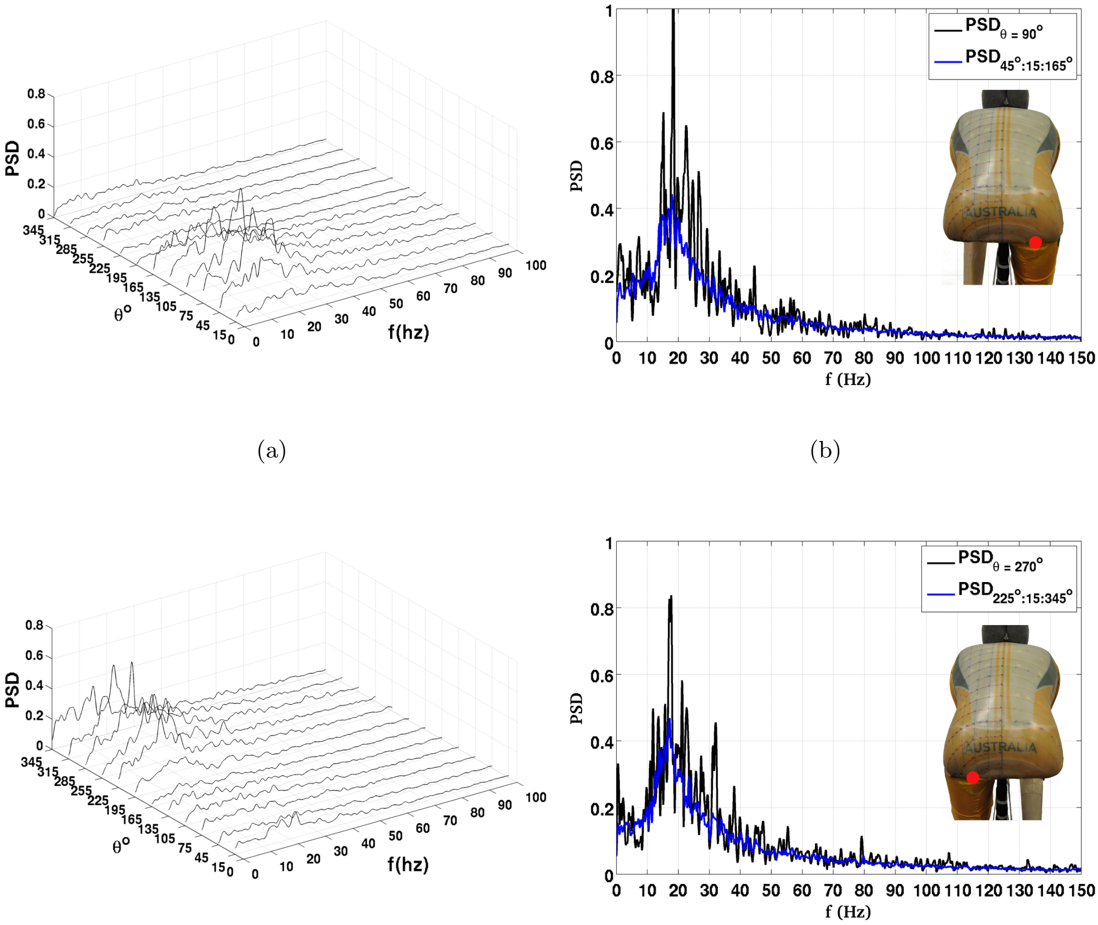

(a) (b)

(c) (d)

FIGURE 4.24: Evolution of spanwise velocity spectra at P5 for 30° increments in crank angle around the complete cycle measured at (a) behind right leg (100 *mm*, 950 *mm*) and (c) behind left leg (-100 *mm*, 950 *mm*). Spectra at these two measurement locations averaged over crank angles where high energy in the medium 16–24 Hz band is observed is shown alongside these figures.

is also suggested in figure 4.22, where probe measurements performed at the hip traverse plane (Plane 3) first identify concentrated measurements associated with the 16–24 Hz band along the upper extended thigh below the lower hips (marked by an arrow). As surface pressure have only be measured on the upper-body regions, this may partially explain the relatively weak spectral behaviour of surface pressure fluctuations in this frequency range observed on the upper regions of the leg (hips). Also, as the axis of the upper legs is always aligned at some angle to the freestream direction (i.e., the max hip angle referenced to the horizontal is $\phi \approx 70°$) the initial alignment of vortex tubes shed from the legs will also be yawed to the flow, as found for cylinders at moderate yaw angles (Ramberg 1983; Thakur *et al.* 2004; Zhao *et al.* 2009). This may explain the spectral peaks observed in both inplane velocity components, as vortices shed at similar angles to the axis of the legs, will result in fluctuations in both the spanwise and vertical velocity components.

Further analysis of smoke flow visualisations and pressure fluctuations over the upper back show that flow separation upstream from the shoulders has a significant effect on the unsteady aerodynamics further downstream. Figure 4.25 shows a sequence of video snapshots that were recorded at 15 Hz for smoke released over the left shoulder for the low 0° and high 240° drag leg positions. (Note that for smoke injected over the right shoulder for the asymmetrical 240° leg position no noticeable change in the smoke patterns was observed). Although the visualisations are somewhat coarse, with a much higher frame rate being required to observe any finer-scale details, it is clear that flow separation occurs around the shoulders followed by the subsequent reattachment further downstream. This results in a wavy smoke pattern in the vertical direction in the wake. The location on the back where smoke is observed to leave the surface of the mannequin approximately corresponds with where the skin-friction lines converge together in the oil and ink-dot surface flow visualisations, which indicate separation of the mean flow.

The location on the upper back where flow separates also corresponds with the concentration of energy contained in the 16–24 Hz frequency over the shoulders. Although the shedding frequency cannot accurately be determined from the video footage alone, based on the time period for one shedding cycle depicted in the video snapshots, this equates to a shedding frequency of $\approx$ 3.8 Hz at the flow visualisation test speed of 4.1 m/s. Assuming the Strouhal number remains relatively constant over the Reynolds number range of interest this corresponds to a shedding frequency of $\approx$ 15 Hz based on the cycling speed of 16 m/s tested, which is comparable with the frequency of surface pressure fluctuations on the upper back.

Although figure 4.20 shows that the energy concentrated in the medium frequency band is much stronger on the side of the body where the leg is in a raised position, a peak in the frequency spectrum was observed on the shoulder for the majority of the leg positions around the crank cycle. This can be seen in figure 4.26 which shows the spectrum averaged over the complete crank cycle for fluctuating surface pressures measured on the left shoulder in both the MLWT and the 450kW wind tunnels. The PSD function for the 90° leg position, where the maximum peak occurred between the

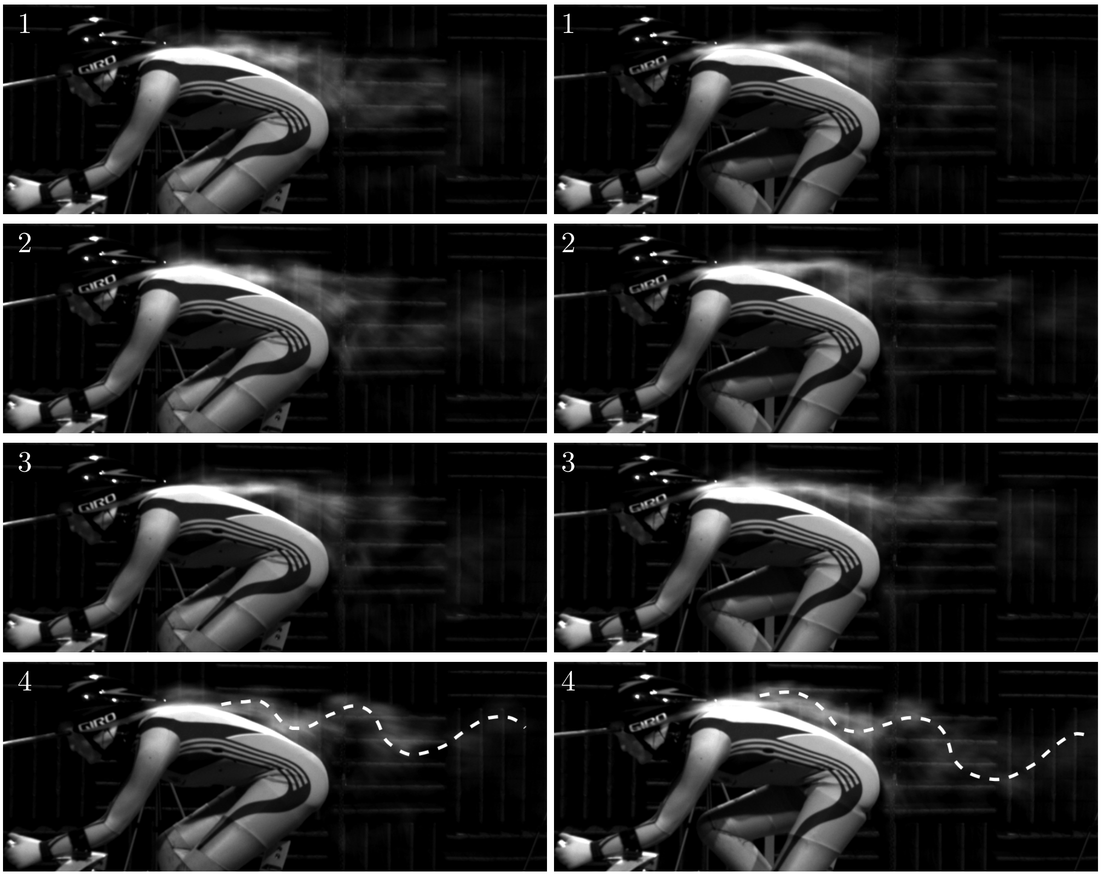

(a) 0° (b) 240°

FIGURE 4.25: Sequence of snapshots taken from video recordings of smoke separating from the left shoulder for low (a) and high (b) drag leg positions.

medium frequency band at this tap location is also shown. The location of the peak in the 16–24 Hz frequency band in the averaged spectra is consistent for the surface pressure fluctuations measured in both wind tunnels. It is expected that the major differences between the two spectra is caused by background wind tunnel noise, which differs between the two wind tunnels. This is particularly evident at the lower end of the spectrum where there is a peak at 1.6 Hz in the MLWT and not the 450kW tunnel. This low frequency matches the peak measured in the background static pressure fluctuations in the MLWT (see section 2.2.1.2) and will be discussed more extensively in the following section, which addresses low frequency surface pressure fluctuations.

Despite the relatively low energy and broadband nature of the spectrum associated with these frequencies, real time animations of surface pressure fluctuations reveals evidence of coherent spanwise vortex structures propagating down the back. The video files in Appendix H show the fluctuating component of surface pressures band-pass filtered between the medium 16–24 Hz frequency range. They show distinct bands of

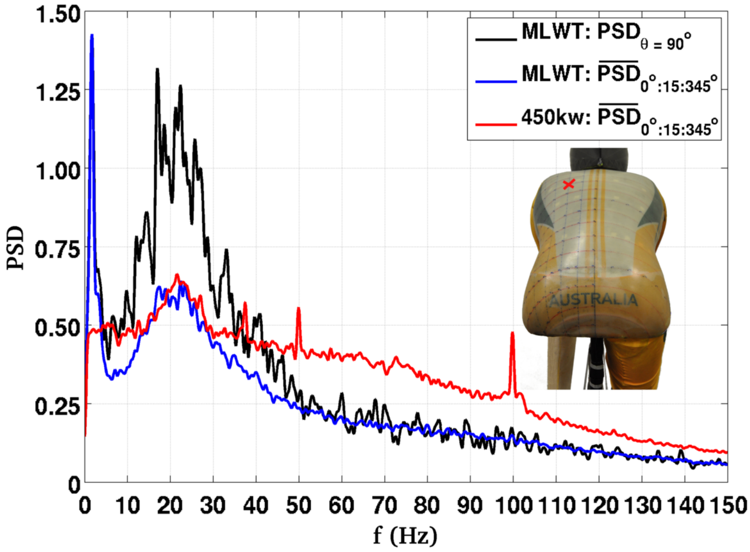

FIGURE 4.26: Average spectra around full crank cycle for pressures measured on the left shoulder (Line 6 $Tap_{\#}$ 8) in both the MLWT and 450kW wind tunnel. Spectrum at 90° leg position where a peak in the energy contained in the 16–24 Hz frequency band occurs is also shown.

low pressure that originate from the shoulders and propagate down the centreline of the back. As these low pressure regions propagate down the back they interact with the unsteady areas on the rear base of the mannequin. Figure 4.27 shows a sequence of contours from these animations, which depicts this motion of the alternating low and high pressure bands originating around shoulders and spanning the majority of the back.

The low pressure suction peaks across the torso are observed for all leg positions around the crank cycle and are more clearly defined in figure 4.28, which shows space-time contour plots of centreline pressure taps (spaced in 50 mm increments down the back) numbered 1 (trailing edge of helmet) to 14 (rear base of hips) for the two low and high drag leg positions. The top images shows the space-time relationship of centreline pressure fluctuations for the first ten seconds of surface pressures sampled at 1500 Hz. The mid-back centreline tap locations (taps 3–11) show streaky lines of alternating low and high pressure bands. This feature becomes more pronounced as we zoom in on sections of the time series, such as those shown in the middle images, which depict centreline pressure fluctuations measured over the 7–8 second interval. The downstream convection of low pressure vortices is marked by the angled pattern of the contours, which is clearly identified in the bottom images that show the propagation

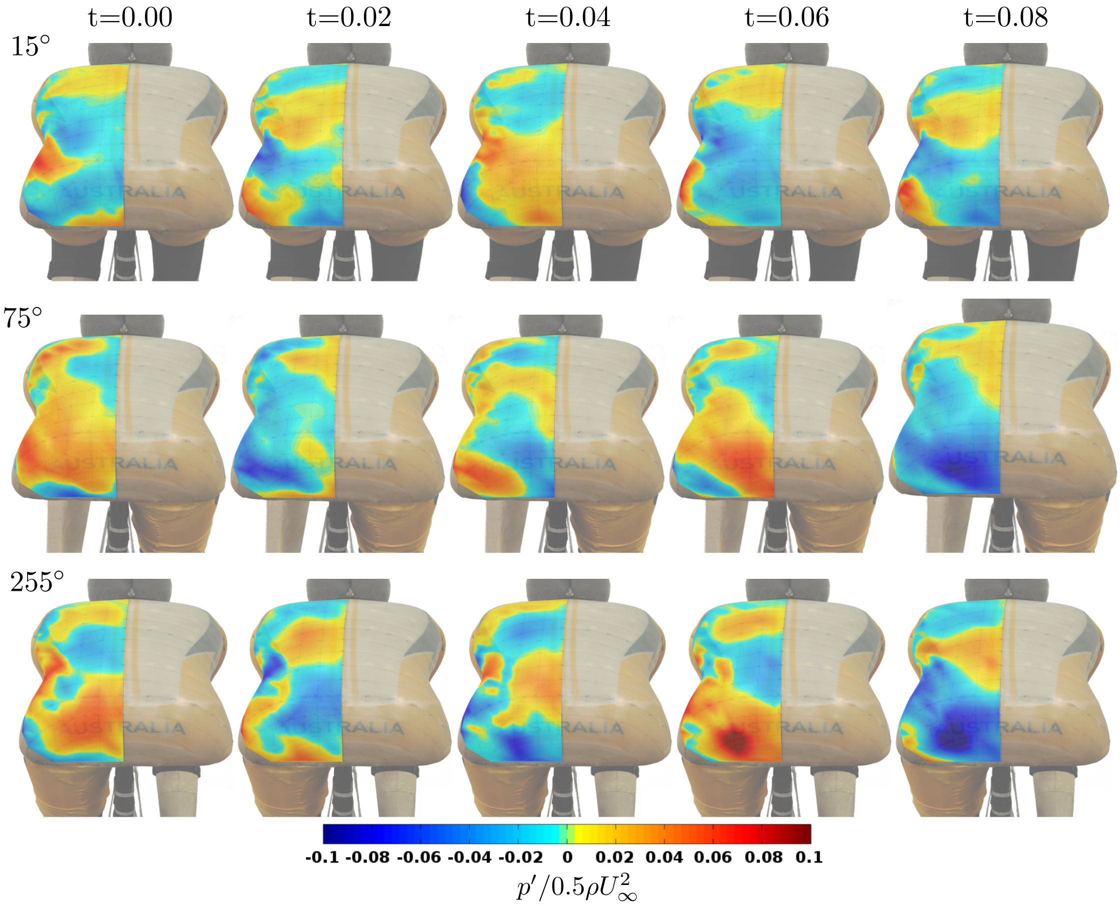

FIGURE 4.27: Contours of the fluctuating pressure component band-pass filtered between 16–24 Hz, showing low pressure bands that develop on the left-hand side of the back for 15°, 75° and 255° leg positions.

of centreline pressure fluctuations band-pass filtered between 16–24 Hz. Despite the intermittent nature of the pressure fluctuations the 'pseudo-periodic' shedding process is captured in the band-pass filtered contours (also evident in the animations). The phase relationship between spatially separated pressure fluctuations recorded simultaneously on the centreline, which is covered in detail in the section that follows, shows pressures propagating down the back in this frequency range with a convection velocity of $0.4U_\infty$.

Cherry *et al.* (1984) have shown that spanwise vortices shed behind a backward-facing step are responsible for the observed pressure fluctuations; it is hypothesised that vortex structures originating around the shoulder and propagating down the back analogously cause the pressure fluctuations seen here. It is well know that the progression of near wall large-scale vortices is primarily responsible for the instantaneous negative peaks in the surface pressure fluctuations. Backward-facing steps are just one example of a separating/reattaching flow where surface pressure fluctuations downstream of sep-

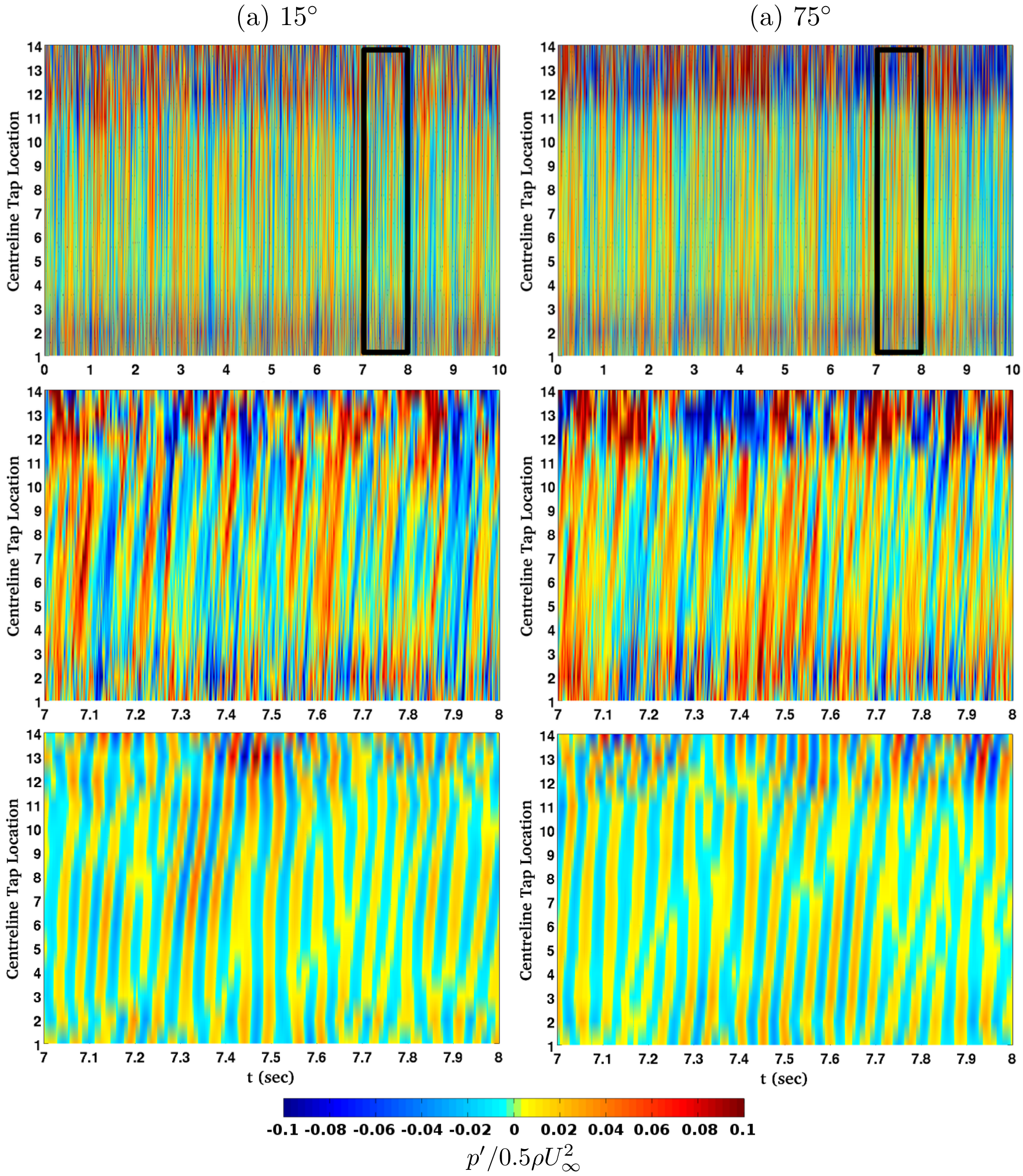

FIGURE 4.28: Space-time contour plots of centreline pressure fluctuations for (a) low and (b) high drag leg positions. Top and middle figures show space-time relationships for raw unfiltered data whereas the bottom figures show contours of pressure fluctuations that were band-pass filtered between 16–24 Hz.

aration are primarily driven by vortical structures in the shear layer. Although flows over sharp discontinuities such as steps have well defined separation points, it has been shown that for flows over complex curved three-dimensional bluff bodies, such as that over the rear of sedan type vehicles (Gilhome 2002), there are also large-scale spanwise flow structures that are similar to those of a backward-facing step, despite the flow being highly three-dimensional. Although the reattachment process behind a step re-

(a) 15°

(b) 75°

FIGURE 4.29: Instantaneous snapshots of smoke illuminated by a laser sheet orientated down the centreline of the back for (a) low and (b) high drag leg positions. Scale is in meters.

sults in a number of processes with different frequency components (Lee & Sung 2002), the Strouhal number associated with the large-scale vortices has been shown to be between 0.5–0.8 based on the reattachment length x_r being the characteristic length scale (Mabey 1972; Driver *et al.* 1987; Lee & Sung 2001). For the 16–24 Hz frequency band, where an increase in energy over the shoulders was observed, the separation length over the back would be roughly 0.4–0.6 m, which seems reasonable given the length of the back. Also the scale of vortex structures associated with the 16–24 Hz frequency band is in agreement with that expected for the large-scale vortices shed behind a step, which have been shown to be between $0.5x_r - 0.6x_r$ (Kiya & Sasaki 1985; Lee & Sung 2002). From the animations and the centreline space-time contours of figure 4.28 based on a convection velocity of $0.4U_\infty$, the spacing between the low pressure valleys is approximately 0.25–0.30 m. Although discrete vortex structures were not clearly captured in the flow visualisations, figure 4.29 shows evidence of similar scale turbulent motions in the instantaneous high resolution snapshots of smoke released over the left shoulder and illuminated by a centreline laser sheet.

Many questions remain about the exact nature of the unsteady separation and reattachment process over the back and more detailed investigations targeting specific aspects of the unsteady separation and reattachment process are required. As a result of the low aspect ratio of the torso and highly three-dimensional nature of the flow over the back, fine-scale observations and simultaneous measurements of multiple (surface pressure and velocity) flow quantities are required to construct a complete picture of the relationship between surface pressure fluctuations and large-scale flow structures. Unsteady processes that originate from other parts of the body must also be considered as these appear to influence the unsteady aerodynamics over the back. It is also worth noting the potential impact of unsteady processes associated with the flow over the helmet. As a result of the low aspect ratio of the torso and the position of the helmet upstream of the torso the surface pressure and velocity fluctuations that result from unsteady processes associated with flow separation from the helmet (identified in section 3.1.3.2) are likely to influence the velocity and surface pressure fluctuations over the back. The helmet shares some of the properties of the simpler geometry of a sphere. Over the Reynolds number range of interest, the shedding of vortices from spheres occurs at a Strouhal number of 0.2 (Achenbach 1972, 1974; Taneda 1978), and based on the maximum width of the mannequin's helmet (0.2 m) we might expect vortices to be shed from the helmet with a frequency of about 16 Hz at the wind tunnel test speed. This provides yet another potential flow mechanism for the increase in energy found in the medium frequency band over the back. At this stage the relationship between unsteady processes associated with flow separation from the shoulders and the helmet remains unclear and is likely to be a fruitful area for future research.

4.1.2.4 Low frequency spectral content

From figure 4.30 it is evident that the centreline of the back passes through areas where the pressure fluctuations are at the lower end of the spectrum. This occurs in both the upper back and separated regions of the lower back. Comparing power spectra of centreline taps with low frequency pressure and velocity fluctuations identified in the MLWT in section 2.2.1.2, low frequency background noise is identified in pressure measurements. Figure 4.31 compares power spectra of centreline pressure taps on the upper back, where the effects of background noise are particularly evident, with Cobra Probe background noise measurements (Note: the window size used in the analysis of low frequencies was extended to 10 seconds worth of data, 15,000 samples). There is clearly a spectral peak at 1.6 Hz, which corresponds to the peak in spectra of static pressure fluctuations in the clean (without the mannequin) MLWT test section. This source of low frequency noise is responsible for the majority of the energy contained in the low frequency band in the upper regions of the back centreline. Figure 4.32 shows normalised PSD functions for pressure measurements all the way down the centreline of the back. In the separated areas at the rear of the mannequin, where there is an increase in the magnitude of the unsteady pressure fluctuations, the spectral peak at 1.6 Hz is less well defined.

The other lower energy spectral peaks in the background static pressure fluctuations between 11–15 Hz and 200 Hz are not evident in attached or separated areas of surface pressure measurements for all leg positions tested. Compared with the majority of the pressure fluctuations measured over the back, i.e., in the separated areas on the sides of the torso and rear hips, the energy content of background pressure and velocity fluctuations is weak, and the background noise levels would not be expected to have a significant impact on the dominant pressure fluctuations. This is further supported in Appendix G, which compares centreline spectra of surface pressure measurements preformed in the both the MLWT and the 450kW wind tunnel, which has very different background noise characteristics. It is clear that spectral peaks associated with background noise in the MLWT (such as at 1.6 Hz) are not present in the 450kW tunnel measurements. Apart from these differences however, similar to the mean pressures, the defining global characteristics such as the decay of spectra are independent of the wind tunnel. Instantaneous contours of unfiltered and filtered pressure fluctuations over the back have also been compared between the two tunnels and show no large differences

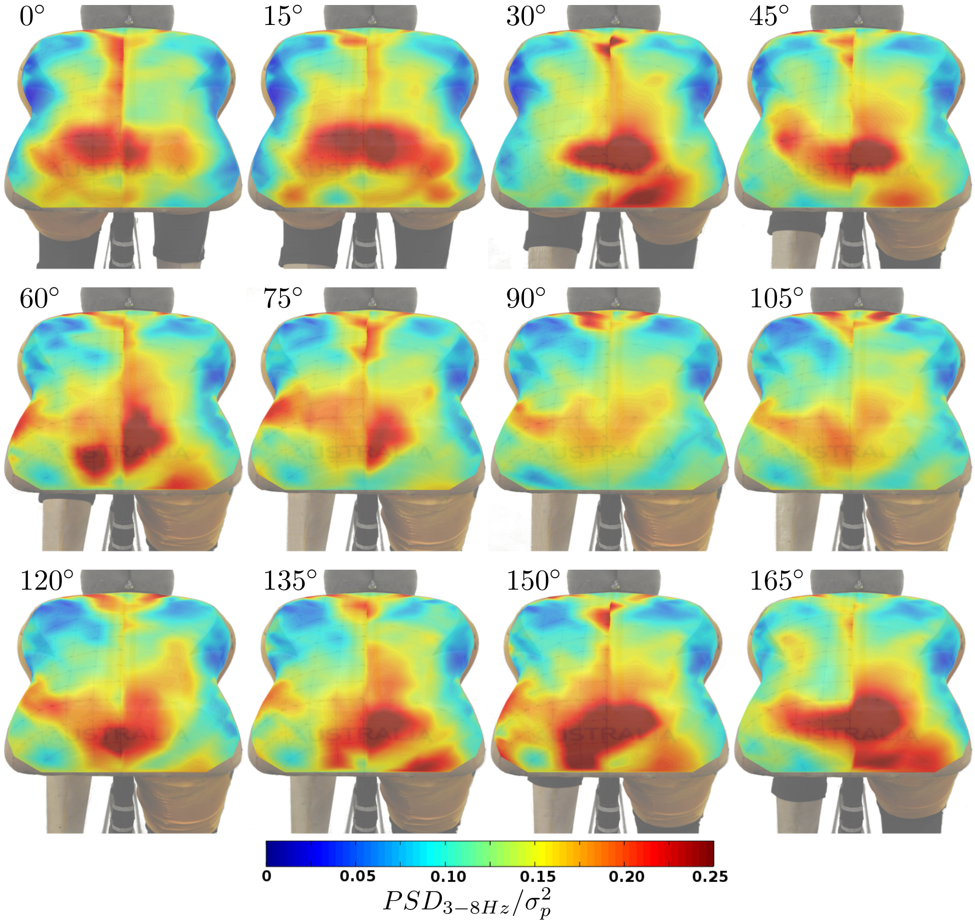

FIGURE 4.30: Contours of the PSD function integrated between 3–8 Hz expressed as a ratio of the total variance of the surface pressure fluctuations (total area under PSD function).

in the pressure fluctuations over a range of scales.

Although detailed measurements in the boundary layer are outside the scope of this investigation, is interesting to note the nature of the surface pressure fluctuations, which are driven by pressure fluctuations associated with the boundary layer. The normalised PSD functions shown in figure 4.32 for all centreline pressure measurements, reveal information about the evolution the boundary layer down the middle of the back. For both the low and high drag leg positions, the centreline pressure spectra are very similar as the flow develops down the back. Approaching the base, surface pressure spectra between the two leg positions no longer collapse on to one another.

In the favourable pressure gradient region after the trailing edge of the helmet, following the 1.6 Hz peak in the spectra shown in figure 4.32(a) and (b), the functional variation exhibits a f^{-1} power-law dependence (refer to figure 3.41 for the centreline pressure gradient). This type of decay is attributed to turbulence activity in the log-law region of the boundary layer and is typical for attached two-dimensional tur-

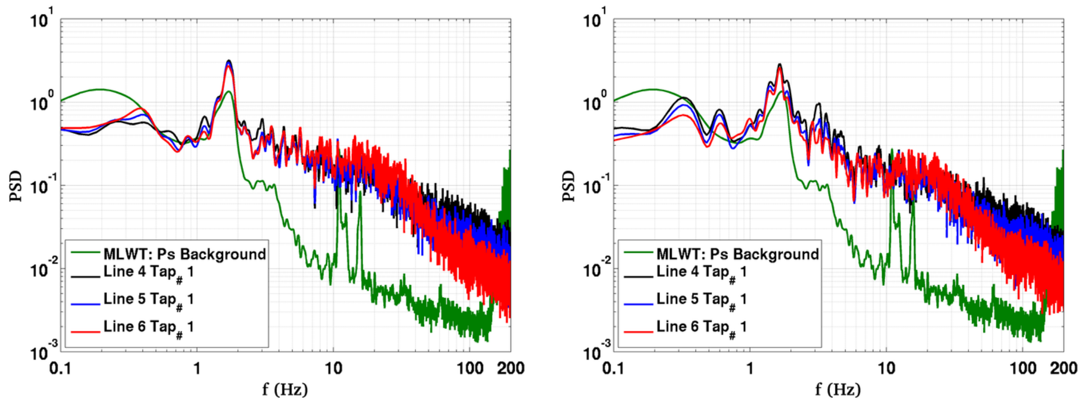

(a) 15° (b) 75°

FIGURE 4.31: Comparison of surface pressure spectra with MLTW background static pressure fluctuations.

bulent boundary layers in zero pressure gradient and accelerating flow regions for high Reynolds numbers (Bradshaw 1967; Perry & Chong 1987; Perry & Li 1990; Panton & Linebarger 1974). Bradshaw (1967) was the first to show the f^{-1} dependence on wall pressure spectra, which Perry & Chong (1987) called the overlap region as a result of both inner layer (viscous region) and outer layer (largest eddies) scaling holding in this region.

As the flow accelerates over the shoulders and enters the pressure recovery region of the mid back a distinct shift towards the classical high Reynolds number Kolmogorov $f^{-5/3}$ power law is observed for frequencies > 20 Hz, where isotropic motions are responsible for the dissipation of turbulent kinetic energy. Following this transition, the $f^{-5/3}$ power law decay is observed over the majority of the back where the mean pressure gradient flattened out for the low drag leg positions and transitioned to a favourable pressure gradient for the asymmetrical higher drag leg positions. This can be seen in figure 4.32(e) and (f), where power spectra in this region of the back collapse onto one another until the base of the lower back is approached.

Although there are many examples of this type of spectral behaviour in turbulent flows a good example in the context of this investigation is that of Castro & Epik (1998), who investigated the development of a turbulent boundary layer post separation and reattachment along a flat plate. Castro & Epik (1998) note the $f^{-5/3}$ decay downstream of the separated region (separation bubble) at the leading edge of a blunt flat plate where transition occurs in the separated shear layer prior to reattachment of the flow. The

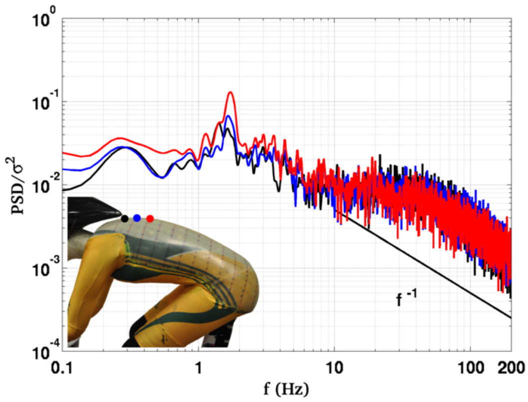

(a) 15°

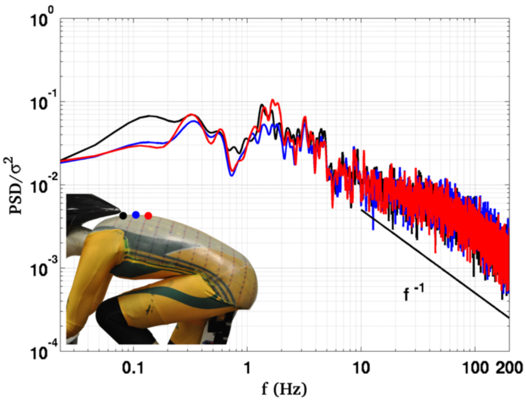

(b) 75°

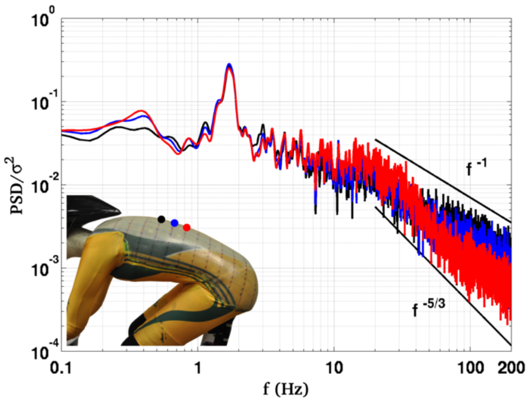

(c) 15°

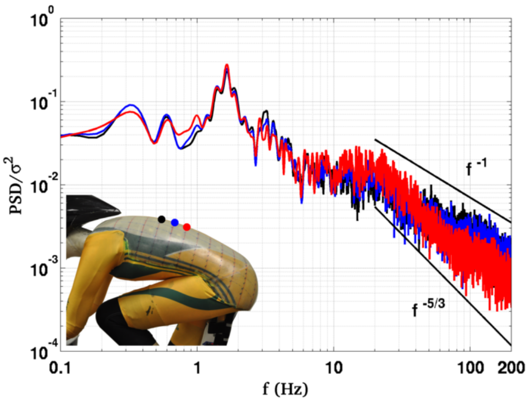

(d) 75°

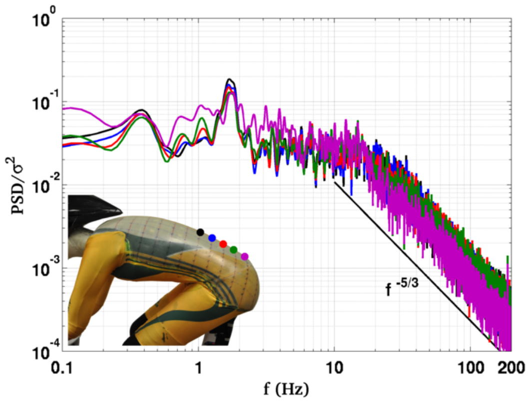

(e) 15°

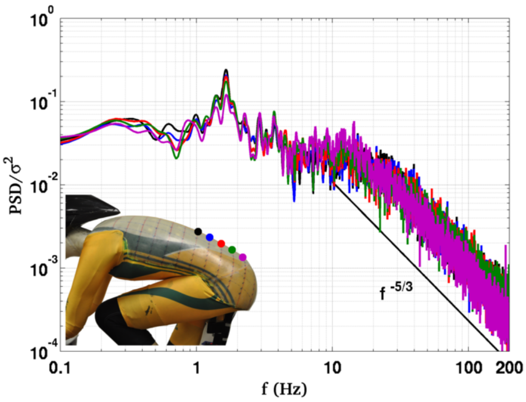

(f) 75°

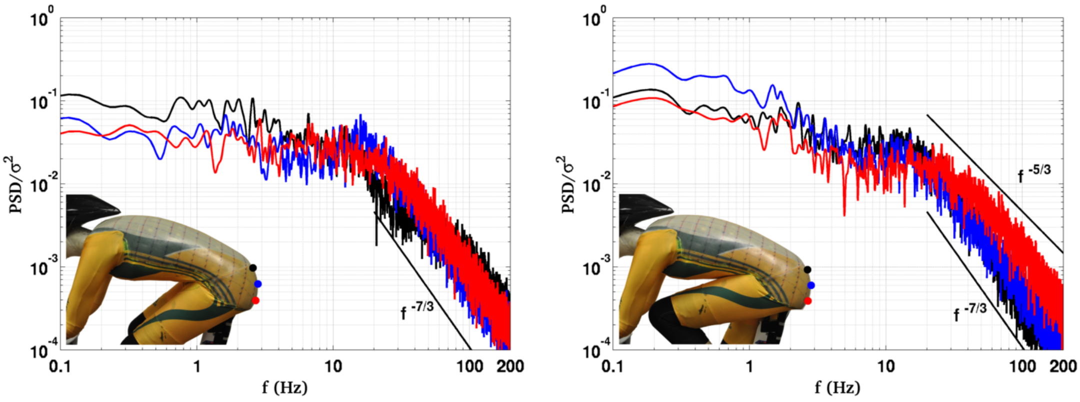

(g) 15°

(h) 75°

FIGURE 4.32: Centreline Spectra for low 15° and high 75° drag leg positions.

transition to turbulence coupled with a favourable pressure gradient, which is primarily a result of the large downwash component induced by the upper hip vortices, is ideal for maintaining attached flow down the centreline of the back. The fact that a turbulent boundary layer is present over the majority of the back is consistent with findings presented in section 3.2.2.2, which showed mean surface pressures on the back were independent of the Reynolds number range at which cyclists would typically travel. The fact that spectra typical of a turbulent boundary layer are present on the smooth fibreglass skin suggests that the transition to turbulence will take place regardless of the texture of the skin-suit. This is not surprising given the unsteadiness associated with flow separation from the shoulders and the wake of the helmet being shed immediately upstream of the back centreline.

As the lower back region is approached the centreline spectra show a steepening of the decay to a $f^{-7/3}$ power law as large-scale motions in the separation region on the rear become more prominent. The transition to the $f^{-7/3}$ decay corresponds to the area on the base of the lower back where there is an increase in the energy concentrated in the low frequency band, which can be seen in figure 4.30. This was also observed in surface pressure fluctuations measured in the 450kW wind tunnel, which can be seen in the low frequency band contours for the 450kW wind tunnel shown in Appendix G. For the low drag 15° leg position, the energy in this frequency band is concentrated in the region that immediately follows where the mean flow separates from the upper hips. (See the oil flow visualisation showing this separation in figure 3.12). For the high

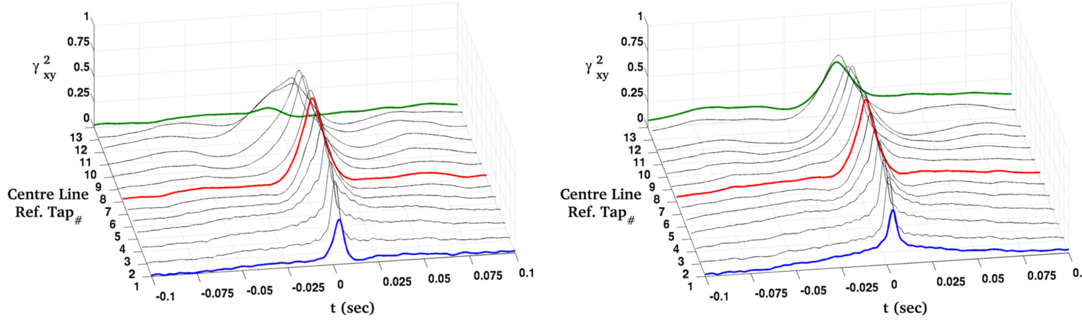

(a) 15°

(b) 75°

FIGURE 4.33: Evolution of coherence functions for pairs of adjacent centreline surface pressure measurements separated by 50 mm. The location of the coherence function is referenced to the upstream measurement location where tap locations are numbered 1–13 from the trailing edge of the helmet.

drag 75° leg position the low frequency energy is concentrated along the separation line associated with the separated region at the rear of the hips of the extended leg. (See the oil flow visualisation in figure 3.13). This suggests that the low frequency pressure fluctuations in these areas are strongly related to the developing shear layer in this region.

In separated regions shed vortices are largely responsible for pressure fluctuations and a faster spectral decay is commonly observed with respect to an attached turbulent boundary layer as the power of the fluctuations decays more quickly as the size of the eddies increases. A good example of this type of behaviour can be found in surface pressure fluctuations commonly observed in the separation regions of forward- and backward-facing steps. Camussi *et al.* (2006b) and Lee & Sung (2001) both observed a $f^{-7/3}$ decay in fluctuating surface pressures measured in the separated regions immediately trailing a backward-facing step, where the energy distribution in the surface pressure spectrum was dominated by the effects of flow separation. Camussi *et al.* (2008) showed that as the separation region was approached in front of a forward-facing step, surface pressure fluctuations showed a drop off in the decay of spectra towards the $f^{-7/3}$ power law. It was also noted by Camussi *et al.* (2006a) that from a global point of view there is little difference in surface pressure spectra in the separated region in the front of forward-facing steps and the rear of a backward-facing step.

Unlike the separated areas on the sides of the torso, as the separation region on the

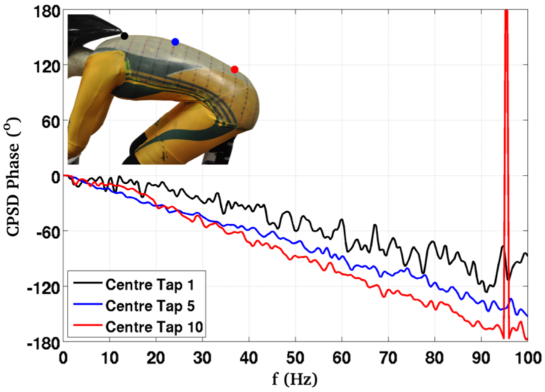

(a) 15°

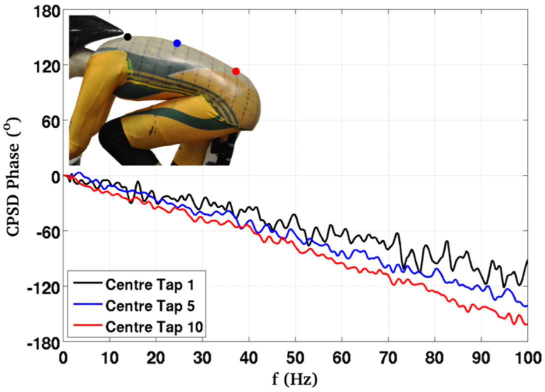

(b) 75°

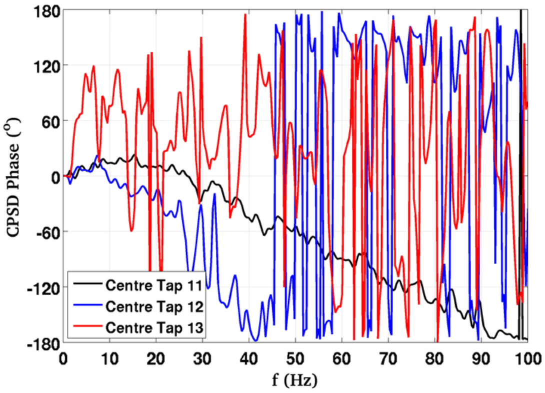

(c) 15°

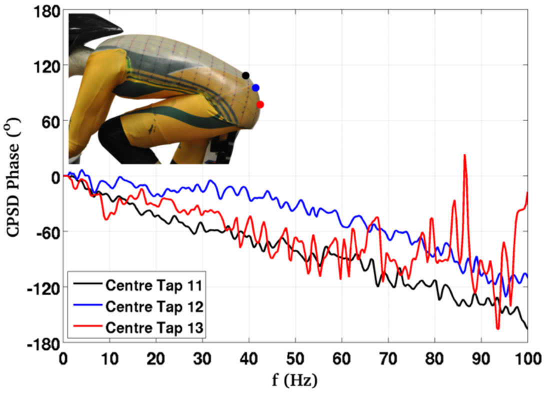

(d) 75°

FIGURE 4.34: Cross-phase spectrum for selected pairs of adjacent centreline pressure measurements separated by 50 mm. The upstream reference tap locations are marked by dots on the mannequin with the corresponding colours of the CPSD phase spectra.

rear of the mannequin is approached surface pressures become increasingly less correlated, indicating the highly unsteady turbulent nature of the flow in this region. This is demonstrated in figure 4.33, which shows the evolution of the correlation coefficient down the back for the 15° and 75° leg positions. The correlation coefficient has been calculated between pairs of surface pressure fluctuations measured at centreline tap locations that are adjacent to one another (i.e., separated by 50 mm), with the reference tap location being the upstream measurement. This is also reflected in the CPSD phase plots in figure 4.34, which are shown for selected adjacent tap pairs down the back for the two leg positions (note only the reference upstream tap is marked). In the separated regions on the rear for the 15° leg position pressures are less correlated compared to the

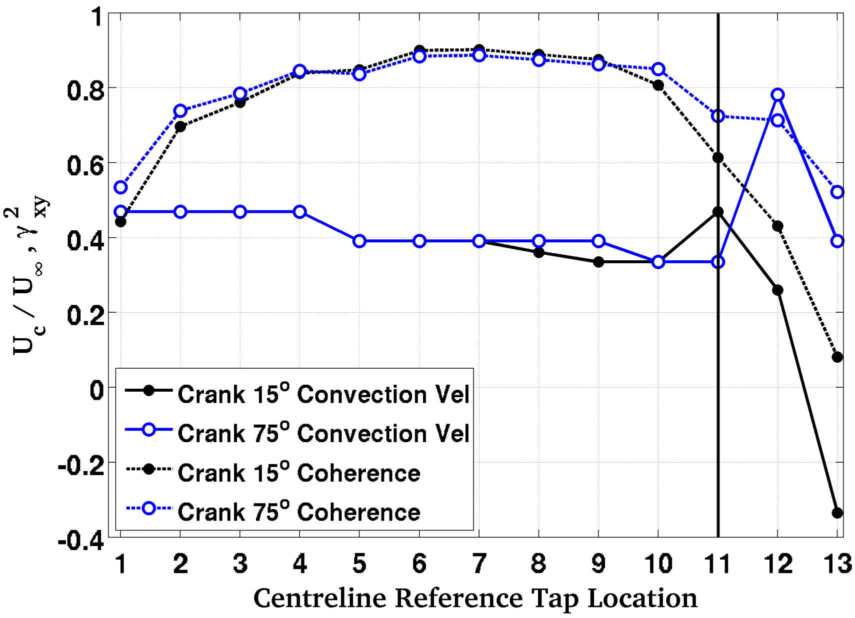

FIGURE 4.35: Variation in the coherence coefficient and the convection velocity calculated down the centreline of the back for 15° and 75° leg positions.

asymmetrical leg positions where the flow remains more attached down the centreline in the lower back regions.

In the upper regions of the back, where surface pressures are well correlated for all leg positions, cross spectra show a linear frequency-phase relationship between adjacent taps for both leg positions. This is what one would expect from Taylor's proposal of 'frozen turbulence', where all turbulent length scales are convected downstream at the same convection velocity. From the positive inclined nature of the centreline space-time relationship of pressure fluctuations, as was previously shown in figure 4.28 both the positive lag at the peak coherence value and the linear gradient of the CPSD phase spectra show a positive convection velocity of around $0.4U_\infty$ for the upper-mid back areas. For the areas of back above the rear base of the mannequin, calculation of the convection velocity from the lag time at the peak coherence coefficient and the gradient of the phase cross spectrum are equal. The lag time between adjacent centreline pressure measurements gradually increases down the back from the trailing edge of the helmet to the hips, which is also indicated by the increase in the gradient of the cross-phase spectrum in figures 4.34(a) and (b). Figure 4.35 shows the variation in the coherence coefficient and the convection velocity calculated from the lag time at the peak value

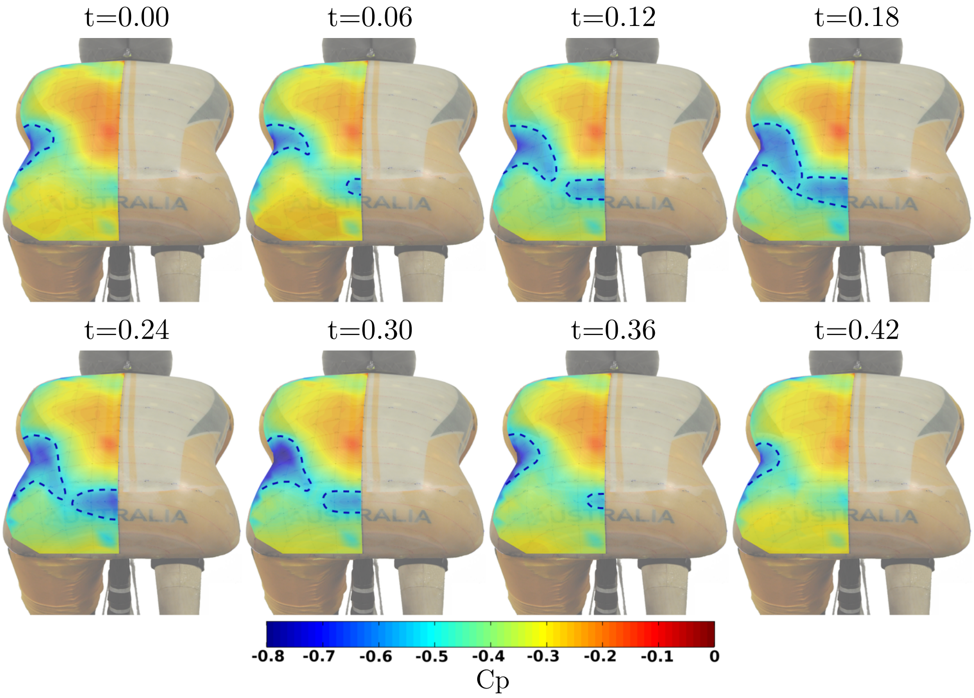

FIGURE 4.36: Contours of the instantaneous surface pressure coefficient low pass filtered at 8 Hz, showing spanwise low pressure fluctuations on the rear base of the mannequin for the 255° asymmetrical leg position.

of the coherence coefficient for the 15° and 75° leg positions. From the trailing edge of the helmet to the hips, the convection velocity reduces from approximately $0.45U_\infty$ to $0.35U_\infty$. On the rear base of the mannequin, due to the low coherence and messy phase cross spectrum, a particular convection velocity cannot accurately be determined.

As the rear base of the mannequin is approached, cross spectra of centreline taps located around where the flow separates from the upper hips for the 15° leg position (centre tap 11) display an initially positive gradient for low frequencies, as expected in regions of flow reversal. For the high drag leg positions animations of the surface pressure fluctuations for the 75° and 255° leg positions show around the top of the hips in the middle of the lower back, that the largest surface pressure fluctuations in this region are primarily orientated in the spanwise direction and not the freestream direction. In the animations it appears that surface pressure fluctuations that originate on the side of the torso with the leg extended influence the pressure fluctuation on the rear base of the mannequin for the high drag leg positions. This is indicated by the sequence of snapshots taken from the 0–8 Hz low pass filtered animations of surface pressures in figure 4.36. This image sequence shows low pressure regions that develop on the side of the hips 'joining' up with low pressure regions in the middle of the lower back. These relatively low energy, low frequency pressure fluctuations are very unsteady and intermittent. The exact nature of these fluctuations and the influence of the separated shear layer that develops from the sides of the torso and that which develops from the rear base of the mannequin is still a matter of speculation.

4.1.3 Summary of Unsteady Results

Although this study has primarily targeted developing the structure of the mean flow, progress has also been made on identifying the primary unsteady flow features of a cyclist's wake. A frequency analysis of time-resolved surface pressure measurements and velocity fluctuations in the wake revealed a complex array of time and length scales associated with unsteady flow structures. Some of these can be traced to vortex shedding from various parts of the cyclist, while others are consistent with broader turbulence behaviours seen in other, more generic, flows. Surface pressure measurements, which formed the basis for the bulk of the analysis, were repeated in the 450kW wind tunnel and demonstrated that unsteady flow features and mechanisms were consistent in both wind tunnels. Comparison of both wind tunnel data sets also showed that background noise levels were unlikely to have compromised robust unsteady flow features.

Despite velocity and pressure fluctuations displaying intermittent and broadband spectral behaviour, areas of high unsteadiness on the back and in the wake of the mannequin are associated with specific frequency bands of spectral activity. Surface pressure fluctuations with the highest energy that were concentrated around a particular frequency band were found to occur on the separated areas at the mid torso. These surface pressure fluctuations are in the high 40–50 Hz frequency band. Animations of pressure fluctuations on the torso coupled with flow visualisations and wake probe data support the hypothesis that this region of high unsteadiness is closely connected with vortex shedding that originates from the upper arms. The Strouhal number found is similar to that expected for simple circular cylinder geometries based on the mean diameter of the upper arms. It was also shown that as the elbow spacing was reduced, bringing the arms more in line with the sides of the torso, the magnitude of the pressure fluctuations found in the 40–50 Hz frequency band increased.

In the wake of the mannequin, the largest velocity fluctuations are found in the spanwise and vertical fluctuating velocity components in the medium i.e. 16–24 Hz frequency band. These frequencies are consistent with Kármán vortex shedding from the upper thighs. Other sources that might contribute to these wake frequencies were also found in the surface pressure fluctuations originating over the shoulders. In this region of the back, surface pressures revealed evidence of spanwise roller type vortices propagating down the back with a mean convection speed of $0.4U_\infty$. Although the exact nature of the unsteady flow mechanisms over the back has not been fully resolved, low pressure regions that propagate down the back from the shoulder and the sides of the torso were observed to interact with the unsteady areas on the rear base of the mannequin. Only the dominant pressure fluctuations were investigated, however multiple modes of pressure fluctuation could be seen in animations of time-resolved pressure fields, which showed that the unsteady aerodynamics over the back is a pseudo-periodic but very unstable process. This is likely to be result of the high Reynolds number and the multiple areas over which flow separates around the upper body and the torso, which is of a very low aspect ratio.

Apart from the fact that the forward speed of a cyclist is much higher than the speed of the legs under race conditions, the dominant frequencies near the body and in the wake also support a quasi-steady assumption. Surface pressure and velocity fluctuations with the highest energies occur at a much higher frequency (by an order of magnitude) than the pedalling frequency of a cyclist in a time-trial position. Although there is still work required to fully uncover the detailed aerodynamics and wake flow dynamics when the legs are actually pedalling, it is expected that the dominant flow structures identified in this study will exist for a large range of the pedalling frequencies typically used by elite athletes.

Chapter 5

Conclusions & Recommendations

This section summarises the major findings pertaining to the primary objectives outlined in the Introduction of this thesis. Additional findings that resulted from the experiments are also summarised. Based on these findings, recommendations are made for future research directions.

5.1 Major Findings

1. Multiple flow regimes must be considered when optimising the aerodynamics of elite cyclists in a time-trial position. Two major flow regimes were identified as the legs progressed around the crank cycle which consisted of a:

- Symmetrical low drag flow regime ($0° - 15°$ & $180° - 195°$)
- Asymmetrical high drag flow regime ($30° - 165°$ & $210° - 345°$).

Changes in flow regime were found to cause the large changes in aerodynamic drag (up to 20% around the crank cycle), rather than the small variation in frontal area associated with the positioning of the legs.

2. The large-scale flow structures associated with each flow regime consist of multiple trailing streamwise vortices:

The variation in the aerodynamic drag force that occurs throughout the crank cycle is dependent on the strength of the large-scale flow structures associated with the low and high drag flow regimes.

- The primary feature of the low drag flow regime consists of streamwise vortices that originate from the upper and inner thighs forming a quadruple arrangement of similar sign vortex pairs orientated symmetrically in the centre plane of the mannequin.

- For the high drag flow regime the large-scale flow structures consist of streamwise vortices that originate when flow separates from the upper hip of the extended leg and the rear of the hip of the raised leg. The upper and rear hip vortex pair is orientated asymmetrically in the centre plane and persists much further into the wake flow compared to the primary vortices of the symmetrical, low drag regime.

3. A general picture of the flow topology around a rider in a time-trial position was developed and used to validate and refine numerical simulations of the flow around a simulated rider of similar geometry and position. When care is taken in the numerical modelling and choosing the initial conditions, computational fluid dynamics can be used with confidence as a tool to investigate flows around rider geometries and to optimise the aerodynamics of cyclists.

4. The primary flow structures are responsible for the large low pressure regions on the cyclist's back, which accounts for 12–20% of the total aerodynamic drag force throughout the crank cycle. Major separated low pressure regions occur on the upper body of the mannequin. These arise from flow structures originating on the sides of the torso/hips and the rear base of the hips, depending on leg position. Over 60% of the variation in drag with leg position could be accounted for solely by the large change in the pressure distribution that occurs on the back throughout the crank cycle.

5. Both arm position and the angle of the torso influences the mean pressure forces acting on the back. Although the magnitude of pressures acting on the back are influenced by these positional changes, low pressure regions associated with the primary vortices are always present. There were also no observable effects on back surface pressure distributions for Reynolds numbers that spanned the range of typical cycling speeds travelled in road and track events.

6. The base pressure on the back could be increased, resulting in lower drag, by reducing the strength or altering the formation of primary vortices. This could be done by changing the rider position or equipment. The wake developing behind the arms forms directly upstream of where the hip vortices form and consequently has a large impact on their formation. It is also evident that the flow from between the legs is critical to the formation of the primary wake structures of both the low and high drag flow regimes. This suggests that changing variables such as leg spacing and equipment design could provide effective means of affecting the flow in this region. In particular, redesign of the bicycle frame and the area around the seat post could reduce drag.

However any changes that alter the formation of the primary wake structures must also consider the effect on the aerodynamic drag force acting on the complete rider system for the different flow regimes. This was demonstrated in changing the positioning of the arms by bringing the elbows closer together. When the legs were in positions representative of the asymmetrical flow regime, bringing the arms together resulted in a reduction in drag, which was primarily a result of an increase in base pressure associated with the upper hip vortices. However for symmetrical leg positions bringing the arms together resulted in an increase in drag which was not a result of a change in the pressure distribution acting on the back. This suggests that the increases in drag can also result from the pressure forces acting on areas of the body other than the back. There were similar findings from studies investigating rider speed, which showed the drag coefficient depends on Reynolds number but that back surface pressure coefficients are relatively insensitive to Reynolds number effects. This implies that the total rider drag's dependence on Reynolds number must also result from a change in the pressure distribution acting on areas of the body other than the back.

7. Similar to the time-averaged flow structure, unsteady wake structures were also found to depend on leg position and showed symmetrical and asymmetrical flow regimes. Two dominant shedding frequencies were found in the wake and on the body of the mannequin were associated with vortex shedding from the upper arms and legs. Vortex shedding from the upper arms in the 40–50 Hz range was associated with fluctuating velocity components in the wake and large surface pressure fluctuations on the side of the torso directly downstream of the arms. The dominant frequencies in the near wake were associated with vortex shedding from the upper legs in the 16–24 Hz range and were strongest on the side of the body where the leg was fully extended. Dominant frequencies in the fluctuating components of near wake velocities and back surface pressures are more than ten times typical pedalling frequencies. This, along with the high cycling velocity compared to the speed of the legs around the crank cycle suggests that the quasi-steady approach used to identify dominant wake structures should hold for a wide range of typical pedalling frequencies and riding speeds under racing conditions.

5.2 Secondary Findings

1. In addition to the primary wake structures, several smaller secondary wake structures were also identified around the mannequin. The formation, strength and interaction of these vortices with the primary wake structures also depends on leg position. These include:

- A streamwise counter-rotating vortex pair in the wake of the helmet which is of the same sign and merges with primary flow structures in the near wake.
- A strong streamwise vortex that develops along the inner thigh of the raised leg in the asymmetrical flow regime. Due to the close proximity of this structure to the rear hip vortex, which are of similar sign, they interact strongly. A similar streamwise vortex also forms along the inner calf of the lower leg, which is of opposite sign to the inner thigh vortex that forms directly above it.
- A vortex pair that develops around the elbow joint and is particularly prominent on the side of the body where the leg is raised. Along with primary vortices, this structure is also responsible for significant deficits in velocity and pressure in the near wake for the asymmetrical flow regime.
- As flow separates along the length of the upper arm, another streamwise vortex is generated on the arms and originates around the shoulder joint. When the leg is raised this structure develops downstream and convects over the sides of the torso.

2. A fully developed turbulent boundary layer exists over the back behind the helmet. This explains why there is no observable effect on the pressure distribution over the back when the Reynolds number changes. This suggests that means of changing the flow by passive methods, such as textured fabrics on the back sections of skin suits, which might be expected to induce transition are likely to be ineffective. Further investigations should focus on reducing the pressure drag by inducing transition to a turbulent boundary layer on other parts of the body.

3. Higher torso angles resulted in an increase in aerodynamic drag. However, this increase was a result of both an increase in the projected frontal area and a change in the drag coefficient. Again, pressures acting on the back of the mannequin could explain most of the variation in the aerodynamic drag with increasing torso angle-of-attack.

4. Rider arm position not only influences the magnitude of the mean pressure forces acting on the sides of the torso but also the unsteady pressures. As the arms are brought closer together, the magnitude of the fluctuating pressures on the sides of the torso increases as a result of the alignment with the torso and vortex shedding from the arms.

5. Unsteady flow characteristics associated with separating and reattaching flows were identified over the upper back. This results in the formation of roller type vortices propagating down the back similar to separating reattaching flows behind backwards facing steps.

5.3 Recommendations for future studies

1. Compare wind tunnel tests to on-road and track environments. This should focus on characterising and investigating the influence of natural free stream turbulence levels, length scales and other wind conditions (i.e., yawed flow) on the primary wake structures and aerodynamic drag force.

2. Wind tunnel testing of a mannequin with moving legs. Further studies are required to address how pedalling frequency influences the aerodynamic forces and at what point a quasi-steady assumption will no longer provide a valid approximation of moving legs.

3. Complete characterisation of all of the near wake flow and body surface pressures, instead of the upper torso/legs regions focused on in this study.

4. Compare mannequin findings with a range of athlete shapes to focus on the influence of rider geometry/position and equipment on the formation of large-scale flow structures. These include:

- Torso aspect ratio and shoulder and hip widths.
- Shape of the back especially lower back angles.
- Upper leg size and spacing.
- Crank length, which the hip and lower leg angles are dependent on.
- Design of the seat post region of the bicycle frame, which are in close proximity to where large-scale vortices from the upper legs/thighs originate.
- Influence of surface roughness on arms and helmet position/geometry on the wake that develops downstream over the sides of the torso and back.

Appendix A

Athlete Back-Profiles

Rider torso profiles from (Crouch *et al.* 2010), showing the shape of athletes' backs during wind tunnel force measurements of static and dynamics pedalling conditions.

Subject 1

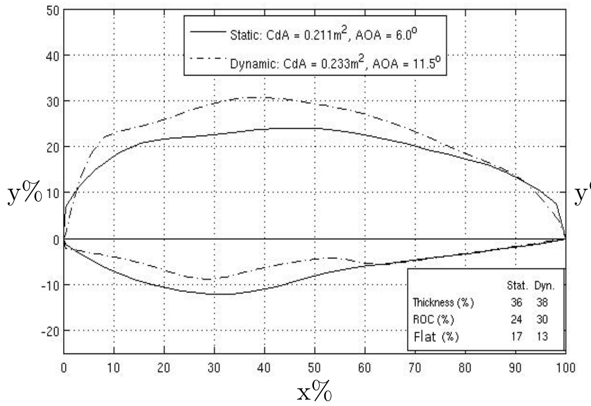

Subject 2

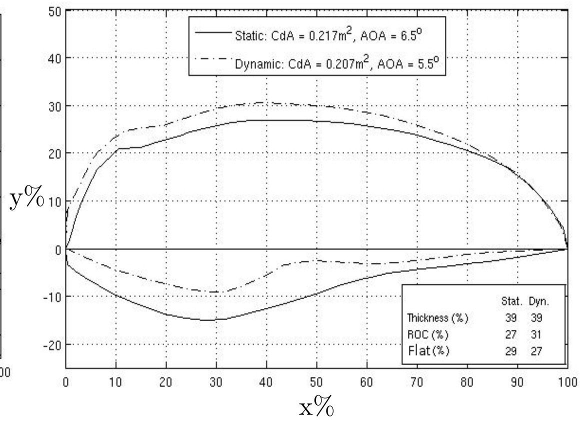

Subject 3

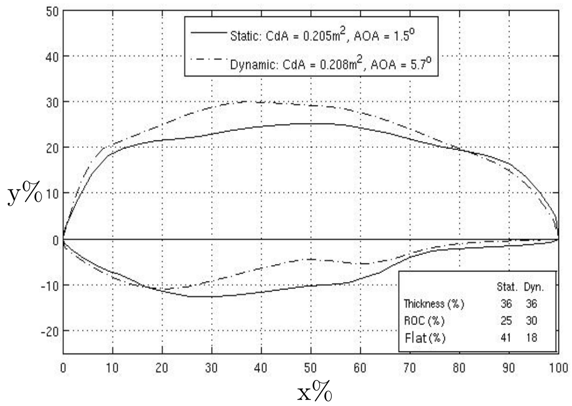

Subject 4

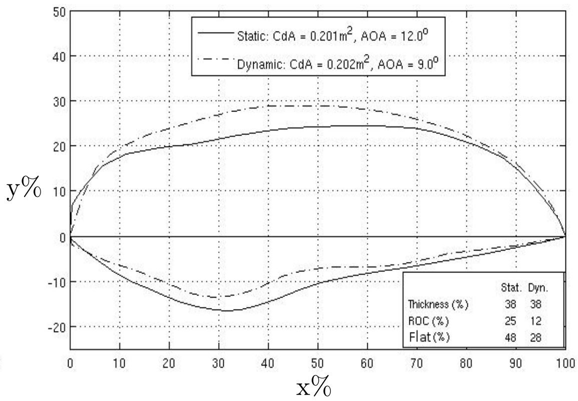

Subject 5

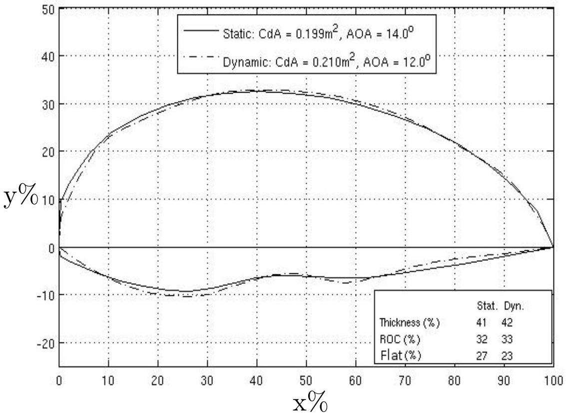

Subject 6

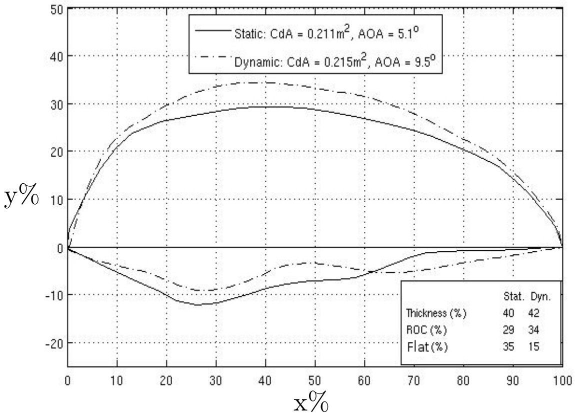

Subject 7

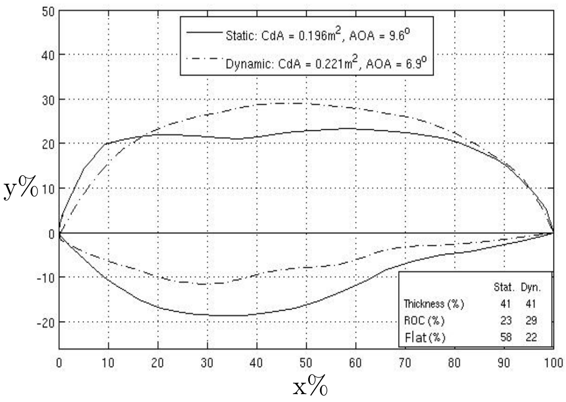

Subject 8

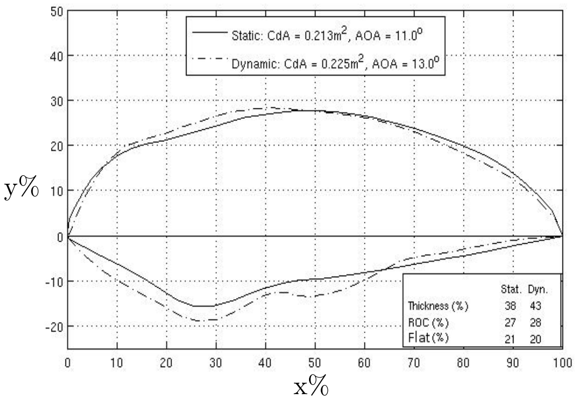

Subject 9

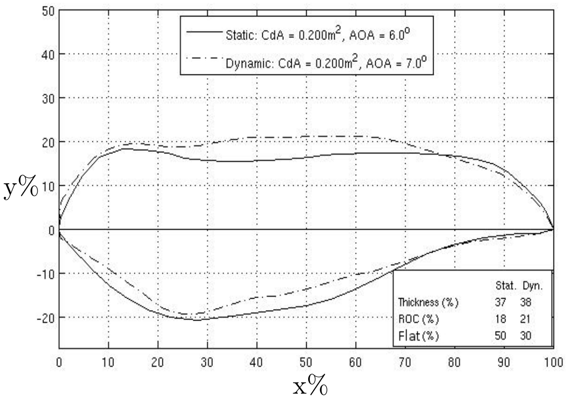

Subject 10

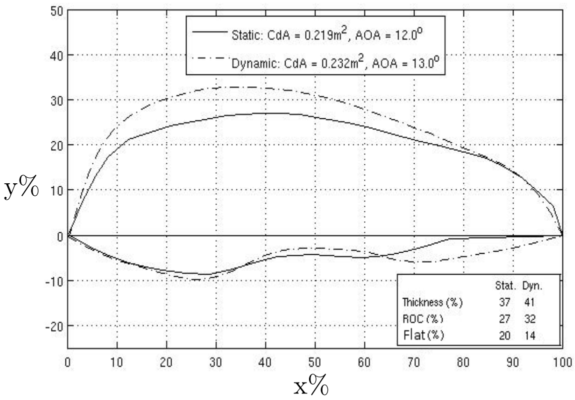

Subject 11

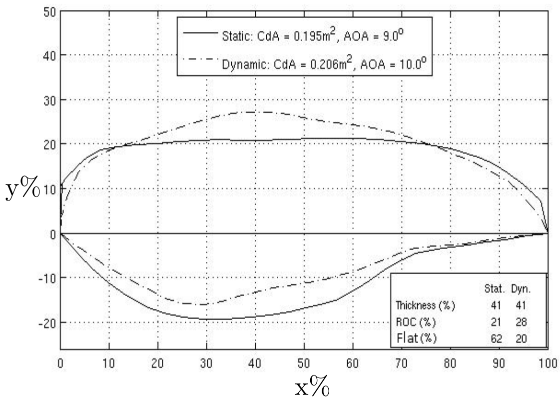

Subject 12

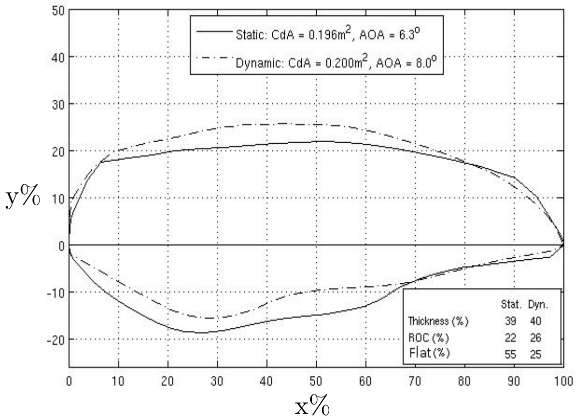

Subject 13

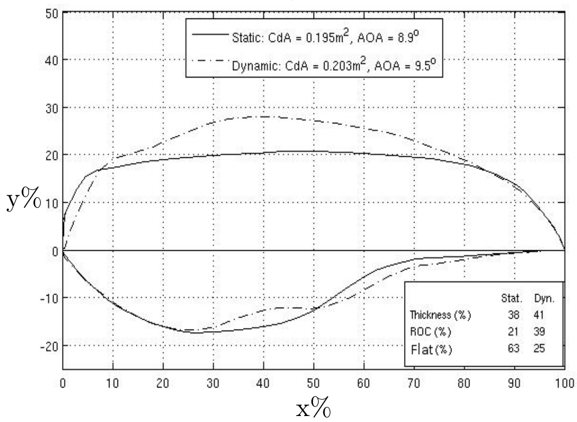

Appendix B

Mannequin Geometry Development

The geometry of the torso and legs has been defined using a combination of simple two-dimensional ellipse and circle shapes using the following methods.

1. Athlete torso and legs were divided up into sections for profiling. The torso into upper (back above the chord line) and lower halves (stomach/chest below the chord line) and the upper and lower legs into front (quads in front of a line connecting the hip-knee joints and shins in front of a line connecting knee-ankle joints) and back halves (rear hamstring-calf sections). Profile slices were taken at 10% intervals of the length of the torso, upper leg and lower leg sections.

2. High resolution images taken of athlete profiles to convert rider geometry into a digital format. An example of an image taken of a profile of the top half of an athlete's torso at 80% chord line is shown in figure B.1. Note the following methods will be described with reference to this particular rib section however they apply equally to the bottom half of the torso (stomach chest) and the leg profiles.

3. Images converted to grey scale and edge detection methods used in Matlab (Prewitt, Sobel, Roberts or Canny methods) to define the boundary of rib edges and check symmetry of the profiled rib section (see figure B.2). Pixel width and height locations serve as rib (x, y) coordinates with known mm/pixels x and y scale factors.

4. The aspect ratio the rib section determined for the minor and major axis lengths of the upper back rib section elliptic fit.

5. Where the ellipse doesn't fit the rib sections well a circle is used to provide a better fit on the sides of the torso. The overall shape of the profiles section is defined as a combination of the ellipse fit and the circular fit to the sides of the torso. A line drawn tangent to the ellipse and circular sections is used to connect the two. The circular fit is defined in terms of the radius 'r' of the circle and the (x_c, y_c) location of the circle centre with reference to the rib profile. The circular fit is referred to as the radius of curvature of the rib profile. The (x_c, y_c) location is determined by drawing lines normal to the section of the profile to be fit by the circle 'normal lines' and finding the focus of the interception of these lines as shown in figure B.3. The focus is found by:

   - finding the intercept of the normal lines with lines $y = c$ where c is a constant.
   - y_c is defined as the point where the standard deviation of x coordinate of the intercept points is minimised as shown in figure B.4. Note x intercept coordinates that are greater than two standard deviations of the mean intercept location are excluded.
   - x_c is defined as the average interception location along the $y = y_c$ line.
   - The radius of the circle 'r' is defined as the mean length of the lines that connect the rib with the point (x_c, y_c).

   This process is repeated for the second half of the profiled section and the results of the circular fit averaged.

6. Elliptical and circular fits are then found for both the upper and lower halves of the torso to complete the geometry of a particular slice of the torso.

FIGURE B.1: Photograph of a profile of an upper torso rib section.

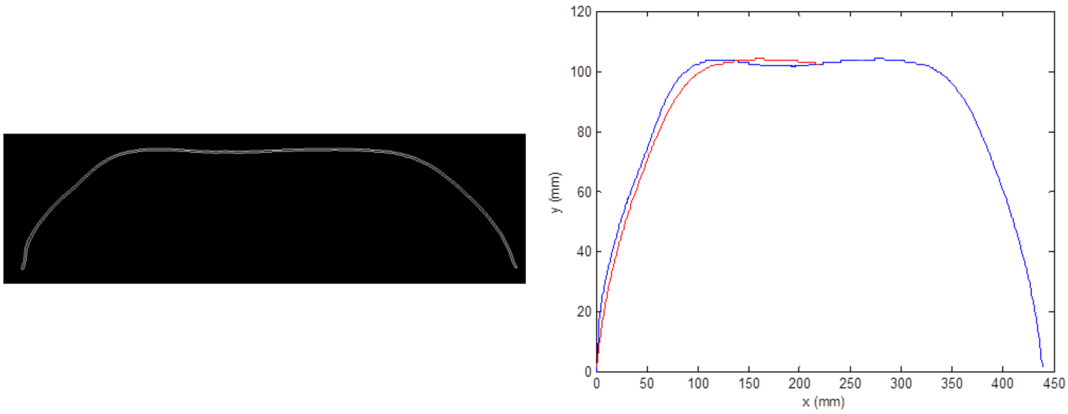

(a) (b)

FIGURE B.2: Detection of rib edges and comparison of rib symmetry.

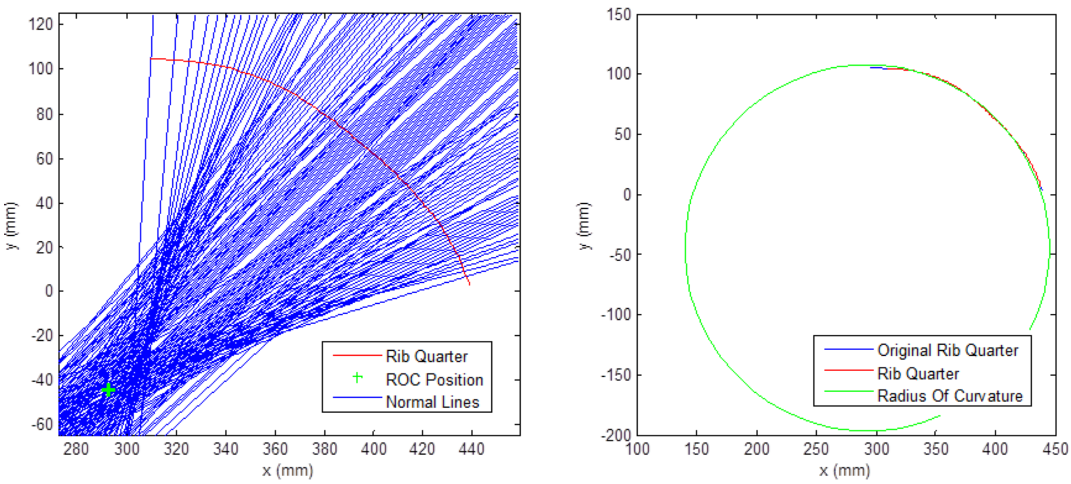

(a) (b)

FIGURE B.3: Determination of circular fit to the rib section.

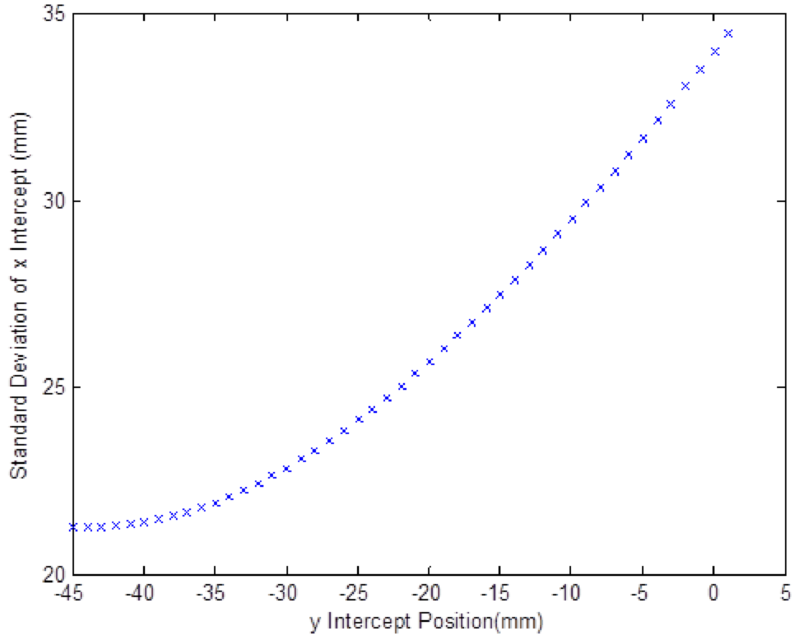

(a)

FIGURE B.4: Determination of y_c position of the circular fit to rib section.

Appendix C

Calibration of Measurement Systems

Typical calibrations and calibration checks of instrumentation used in mannequin wind tunnel studies.

1) MLWT Differential Pressure Transducer Calibration

Raw MLWT Transducer Calibration Factor $= 1284.2 Pa/Volt$

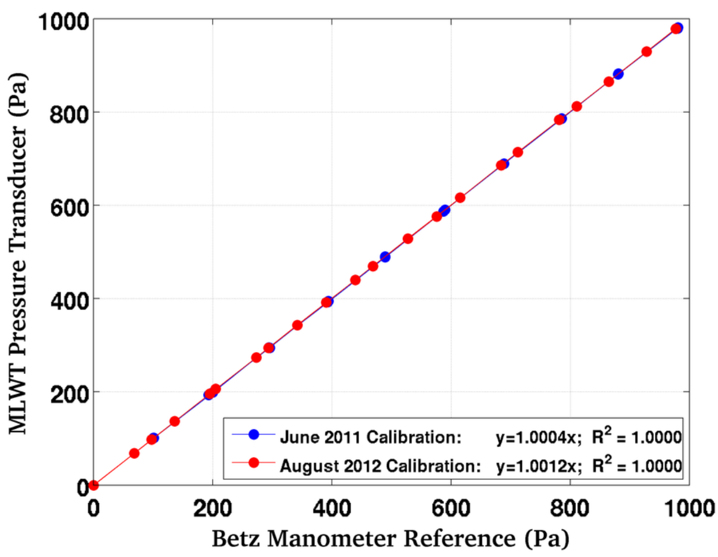

Figure C.1: Pitot-static tube pressure transducer calibration check.

2) MLWT Velocity-Factor Calibration

Velocity Factor = 0.9848

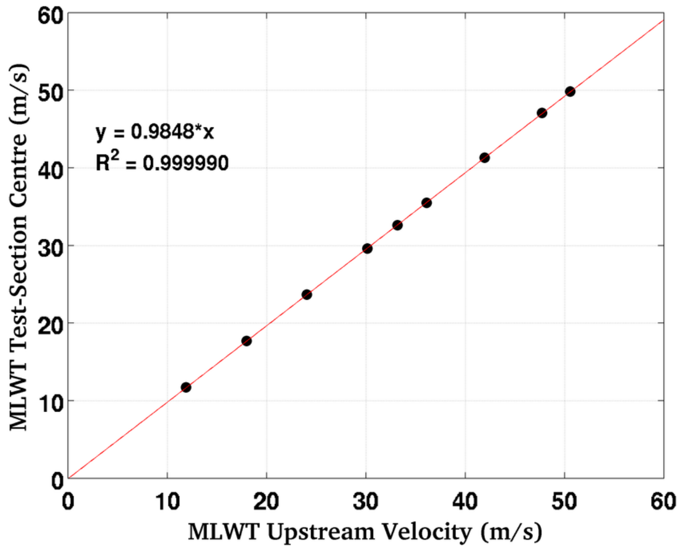

FIGURE C.2: Determination of wind tunnel velocity factor.

3) Kistler Force Calibration

Raw Kistler Calibration Factor $= -124.198 N/Volt$

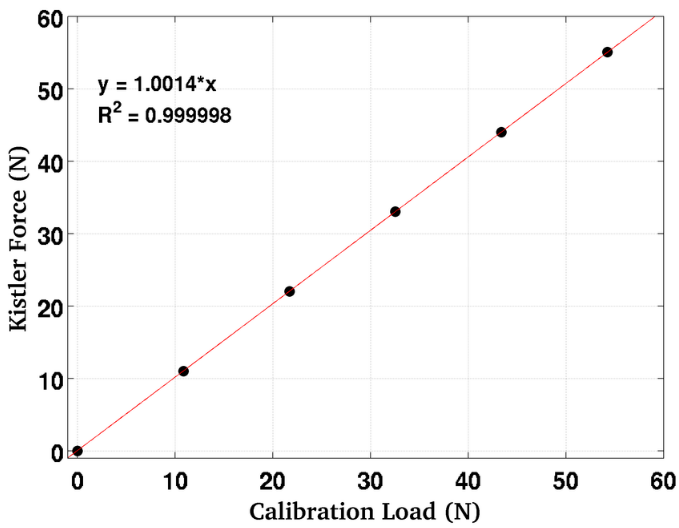

FIGURE C.3: Typical Kistler calibration for the x-component of force measurements.

4) DPMS Calibration

- Raw DPMS-1335 Calibration Factor $\approx 305 Pa/Volt$ (varies slightly depending on channel)
- Raw DPMS-1336 Calibration Factor $\approx 690 Pa/Volt$ (varies slightly depending on channel)

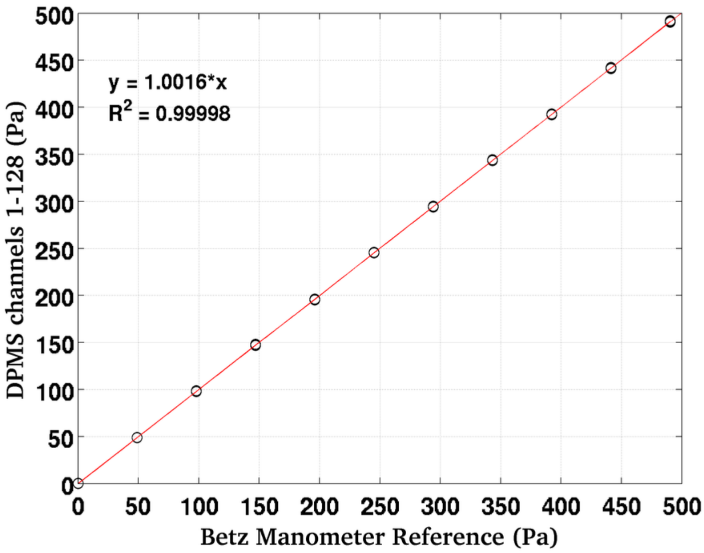

FIGURE C.4: Calibration check of DPMS differential pressure transducer channels.

Appendix D

Measurement Uncertainties

The major uncertainties associated with measurements presented in this thesis can be characterised as follows:

- Uncertainty test section conditions (temperature, pressure, density).
- Wind tunnel test speed.
- Force measurement uncertainties.
- Surface pressure measurement uncertainties.
- Wake velocity measurement uncertainties.
- Data-Acquisition errors.

If all errors are assumed independent then the total uncertainty in a measurement point associated with both bias 'B' and precision errors 'P' can be estimated as

$$U_{Total} = \pm\sqrt{B^2 + P^2}. \tag{D.1}$$

Temperature: The temperature is determined from the average of two T-type thermocouples located inside the test section. The estimated data acquisition error (see table D.3) and precession error of temperature measurements is $\pm 2.33°C$.

Barometric Pressure: Barometric pressure was measured using a Blackart BAA-46 Reference Barometer. The combined precision and data acquisition error of the barometer is estimated at $\pm 3mmHg$.

Density: Air density is affected by humidity, barometric pressure and the ambient air temperature. Errors in the measurement of these parameters result in error in the calculation of the air density. The estimated uncertainty in the calculation of air density is ±7.2%.

Wind Speed: The wind tunnel flow velocity is calculated from the dynamic pressure measured at the upstream pitot-static tubes. Therefore, the uncertainty associated with the wind tunnel flow speed is a result of errors in the measurement of the dynamic pressure, the air density and the velocity calibration factor (between the test section centre and upstream pitot-static tube measurements). The total uncertainty of the wind tunnel flow velocity is estimated at ±5.0%. The maximum variation in the time averaged wind tunnel speed during repeated measurements with the mannequin was $\pm 0.15 m/s$.

Kistler Drag Force: The aerodynamic drag measurement error is dependent on errors induced in the calibration of the force measurement system 'E_C', data acquisition error 'E_A' and the uncertainty associated with the mean due to the variability in the force data (precision error '$P_{\overline{x}}$'). For force results at each leg position, which are taken as the mean result of multiple separate samples the precision limit can be estimated by

$$P_{\overline{x}} = \frac{t_{0.95}\sigma_{\overline{x}}}{\sqrt{M}}, \tag{D.2}$$

where 'σ' is the standard deviation of the 'M' sample results and 't' is found from the Student-t distribution for '$c\%$' confidence level. Assuming that the error is normally distributed, for $M - 1$ degrees of freedom, $t = 2.92$ for 95% confidence for the minimum of three measurements sampled at each leg position (worst case scenario). The estimated total uncertainty in a force measurement is

$$U_{\overline{x}} = \sqrt{E_C^2 + E_A^2 + P_{\overline{x}}^2}. \tag{D.3}$$

The maximum measurement error (95% confidence) for force and drag area results is $\pm 0.77N$ and $\pm 0.003m^2$ respectively. These errors do not included that associated with repositioning of the mannequin. When the variability in force measurements due to repositioning the mannequin is included the total uncertainty in the drag area is estimated to be ±2.5% of the mean drag area at each leg position tested.

DPMS:

Table D.1 shows the uncertainty associated with mean surface pressures and coefficients determined from mannequin wind tunnel tests using the two DPMS modules (mean of three separate tests). The uncertainty in measured surface pressures is as-

DPMS	DPMS-1335 $\pm 3kPa$	$\pm 7kPa$
Pressure (Pa)	$\pm 3.0Pa$	$\pm 7.0Pa$
Pressure Coefficient (C_P)	± 0.02	± 0.04

TABLE D.1: Estimated total uncertainty in mean surface pressure measurements for the worst case scenario.

Flow Quantity	Error
Velocities (U, V, W)	±1% of total velocity
Yaw and Pitch angles	±0.5°
Static Pressure	±1% of dynamic head
Turbulence Intensity	±5% of total turbulence level

TABLE D.2: Estimated errors of Cobra Probe stated by manufacturer TFI Pty. Ltd

sumed to be equal to the uncertainty stated by the manufacturer being ±0.1% $F.S.O$. The standard error of mean surface pressure measurements was found to be insignificant.

Cobra Probe:

The uncertainty in Cobra Probe measurements shown in table D.2 is assumed to be equal to the uncertainty stated by the manufacture.

Data-Acquisition Systems/Cards:

Measurement	Card Type	Card Range	Volts/Unit	Card Acc.	Calibration Acc.	Measurement Acc.
Barometric Pressure ($mmHg$)	PXI-6255	$\pm 10V$	$7.53\times^{-3}$	$\pm 1.924mV$	$\pm 1.630mV$	$\pm 0.333mmHg$
Temperature 1 ($^{\circ}C$)	SCXI-1102	$\pm 0.1V$	$40.26\times^{-6}$	$\pm 0.045mV$	$\pm 0.046mV$	$\pm 1.60^{\circ}C$
Temperature 2 ($^{\circ}C$)	PXI-6221	$\pm 0.1V$	$40.26\times^{-6}$	$\pm 0.031mV$	$\pm 0.046mV$	$\pm 1.38^{\circ}C$
Combined Temperature 1 + 2 ($^{\circ}C$)	Combined	$\pm 0.1V$				$\pm 2.11^{\circ}C$
Force (Kistlers 'x' component)	PXI-6284	$\pm 10V$	0.008	$\pm 0.980mV$	$\pm 4.56mV$	$\pm 0.565N$

TABLE D.3: Data acquisition errors.

Appendix E

MLWT Resonant Modes

The following equations from Arnette *et al.* (1999) have been used to calculate the various theoretical resonant modes in the MLWT test section using values outlined in table E.1.

Tube Response:

$$f_{tube} = \frac{C.n}{2.L_{Total}}. \tag{E.1}$$

where n is the mode number (1,2,3...).

Test-leg Response:

$$f_{test-leg} = \frac{C(2.n-1)}{4.L_0}. \tag{E.2}$$

where n is the mode number (1,2,3...).

Plenum Resonance:

$$f_{plenum} = \frac{C.\beta.\alpha}{2.D_n} \tag{E.3}$$

where

$$\alpha = \left[\left(\frac{n_x}{(\frac{L_P}{D_n})}\right)^2 + \left(\frac{n_y}{(\frac{W_P}{D_n})}\right)^2 + \left(\frac{n_z}{(\frac{H_P}{D_n})}\right)^2\right]^{0.5} \tag{E.4}$$

and n_x, n_y, n_z are the mode numbers $(0,1,2,3...)$ associated with each of the x, y, z directions. For the lowest plenum resonant frequency ($n_x = 0$,$n_y = 1$,$n_z = 0$).

Jet Shear Layer Frequency:

$$\alpha = \frac{U_\infty}{(\frac{L}{D_n})}\left[\frac{(n-a)}{(\frac{M}{\beta}+k_v)D_n}\right] \tag{E.5}$$

where $a = 0.25$ and $k_v = 1.75$.

MLWT	Symbol	Value
Speed of sound	C	343 m/s
Test-section velocity	U_∞	16 m/s
Mach Number	M	0.05
β ($\beta = \sqrt{1 - 0.2M^2}$)	β	0.9998
Nozzle hydraulic diameter	D_n	2.57 m
Duct length	L_{Total}	94 m
Open-Jet Length (Nozzle exit to collector)	L	10.0 m
Open-Jet Length (Nozzle exit to first corner)	L_0	21.5 m
Plenum length	L_P	9.0 m
Plenum width	W_P	12.0 m
Plenum height	H_P	5.2 m

TABLE E.1: Wind tunnel test conditions and major geometric parameters influencing resonant modes in the MLWT.

Appendix F

Surface Pressure Spectral Uncertainties

Based on the repeatability of real-time surface pressure measurements the random error associated with the analysis of fluctuating surface pressures has been determined (95% confidence). Bias errors associated with the spectral characteristics of peak frequencies are expected to be negligible compared with the random error.

Power Spectral Density: The maximum uncertainty in the magnitude of the low, medium and high frequency peaks identified in the spectral analysis of fluctuating surface pressures is $\pm 8.6\%$. The uncertainty in the location of peak frequencies is estimated to be $\pm 10.0\%$.

Cross-Spectrum: The maximum uncertainty in cross power spectral density estimates analysed in areas of high coherence is $\pm 12.2\%$.

Phase Angle: The uncertainty associated with phase angle estimates between pressure taps located on the back for the peak frequencies is estimated at $\pm 6.5°$.

Appendix G

450kW Spectral Characteristics

Appendix G shows results from unsteady surface pressure measurements performed in the 450kW wind tunnel. Areas of distinct spectral activity and peak frequencies compare very well for unsteady surface pressure measured in both wind tunnels for all leg positions investigated. The main differences in the spectral analysis of pressures measured in each wind tunnel is a result of low frequency background pressure fluctuations which differ between the two wind tunnel testing environments.

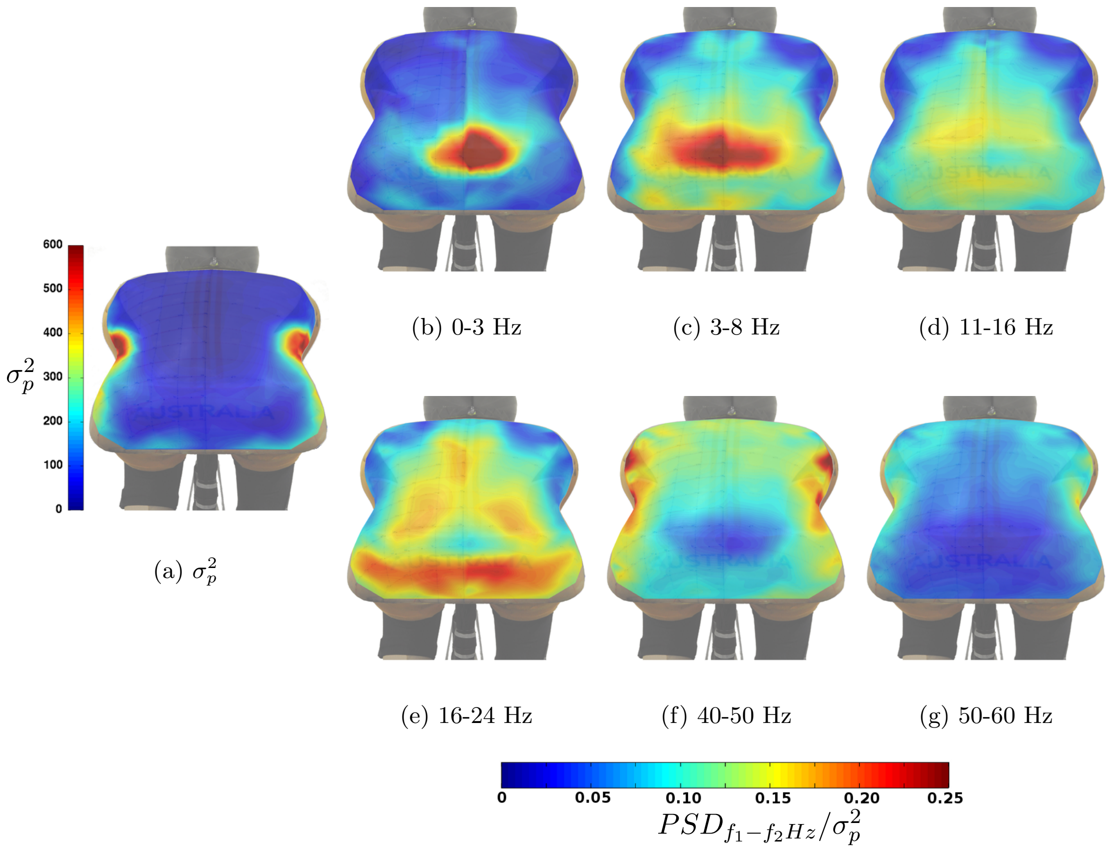

(a) σ_p^2 (b) 0-3 Hz (c) 3-8 Hz (d) 11-16 Hz (e) 16-24 Hz (f) 40-50 Hz (g) 50-60 Hz

FIGURE G.1: Contours showing areas of distinct spectral activity determined from fluctuating surface pressure measured in the 450kW wind tunnel for the low drag 15° leg position.

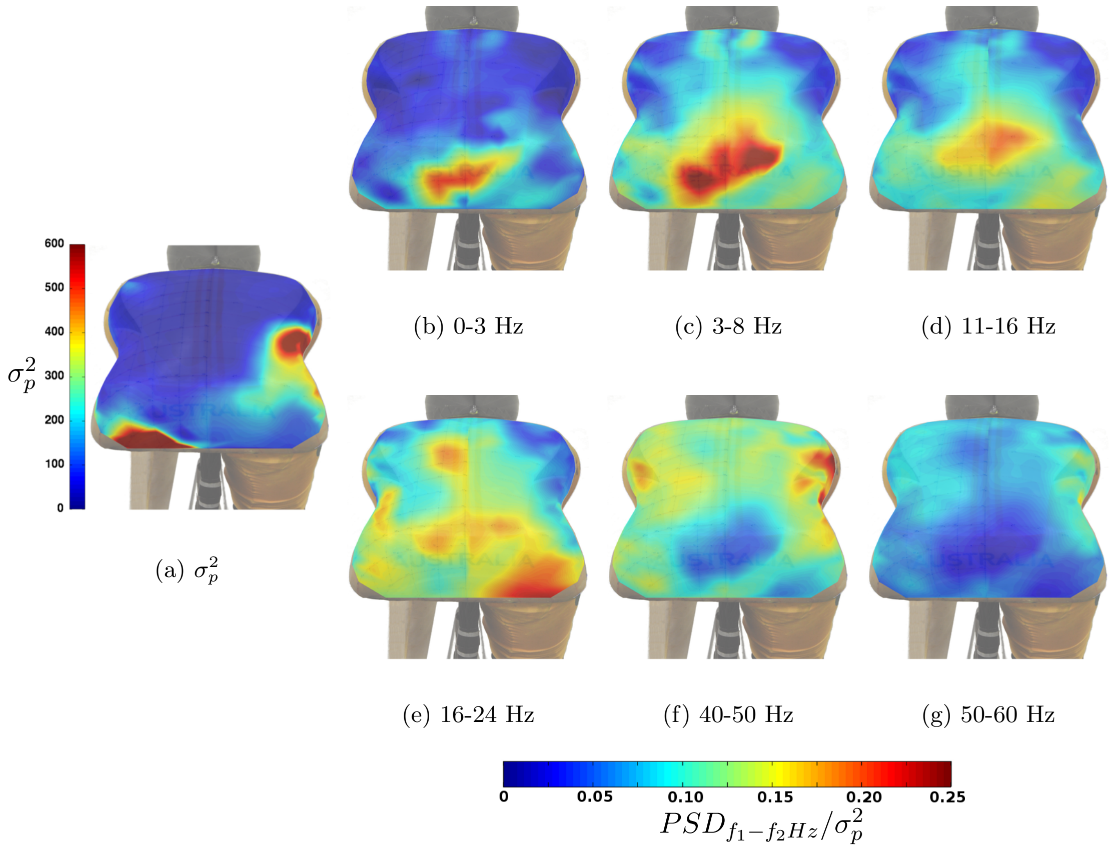

FIGURE G.2: Contours showing areas of distinct spectral activity determined from fluctuating surface pressure measured in the 450kW wind tunnel for the high drag 75° leg position.

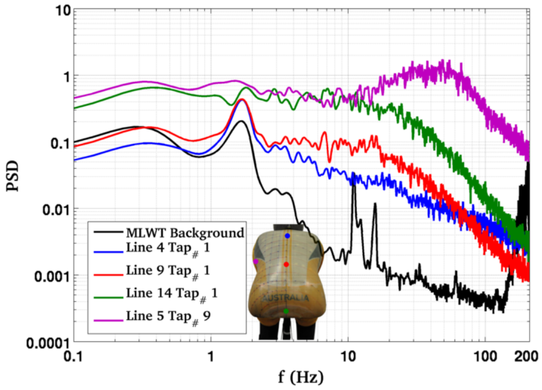

(a) MLWT $\theta = 15°$

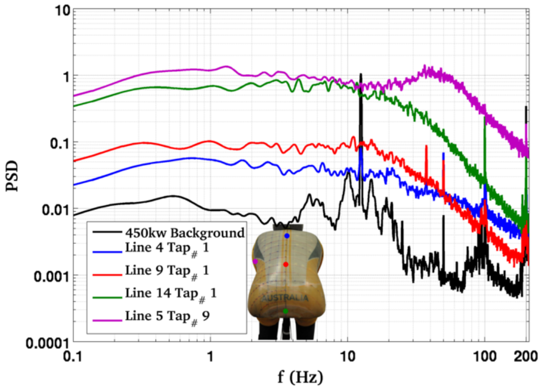

(b) 450Kw $\theta = 15°$

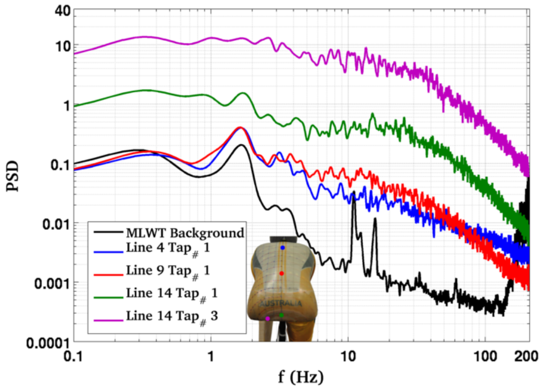

(c) MLWT $\theta = 75°$

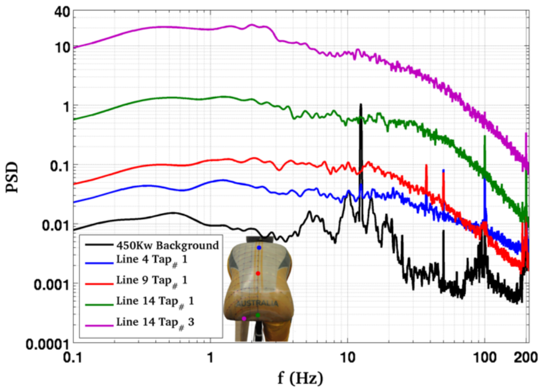

(d) 450Kw $\theta = 75°$

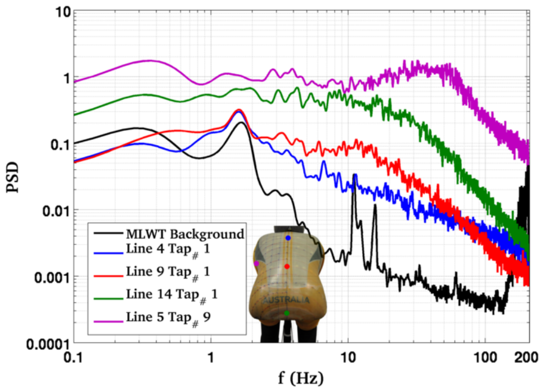

(e) MLWT $\theta = 195°$

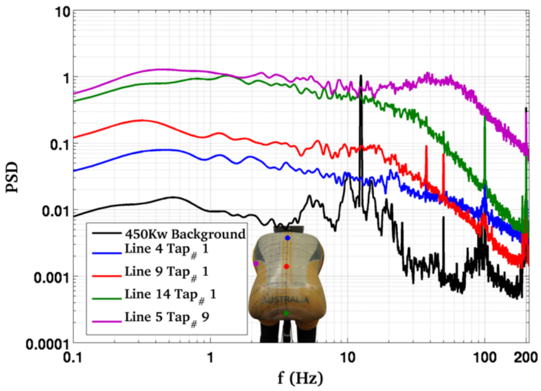

(f) 450Kw $\theta = 195°$

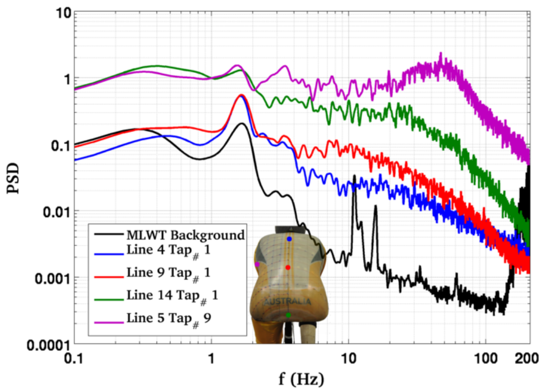

(g) MLWT $\theta = 255^{\circ}$

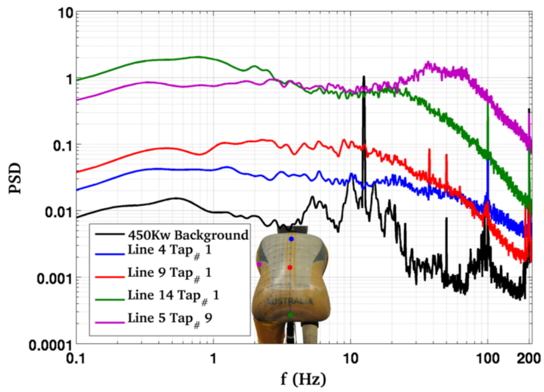

(h) 450Kw $\theta = 255^{\circ}$

FIGURE G.3: Comparison of surface pressure spectra at selected taps with wind tunnel (MLWT and 450kW) background static pressure fluctuations.

Appendix H

Annimations

A DVD containing animations of time-averaged and unsteady velocity field and surface pressure measurements is attached to the back cover of this thesis.

Bibliography

Abell, C., Peterka, J. & Woo, H. 1978 Kinematical studies of the flows around free or surface-mounted obstacles; applying topology to flow visualization. *J. Fluid Mech* **86** (part 1), 179–200.

Achenbach, E. 1971 Influence of surface roughness on the cross-flow around a circular cylinder. *Journal of Fluid Mechanics* **46** (2), 321–335.

Achenbach, E. 1972 Experiments on the flow past spheres at very high reynolds numbers. *Journal of Fluid Mechanics* **54** (03), 565–575.

Achenbach, E. 1974 Vortex shedding from spheres. *J. Fluid Mech.* **62**, 209–221.

Ahmed, S. 1983 Influence of base slant on the wake structure and drag of road vehicles. *Journal of fluids engineering* **105** (4), 429–434.

Ahmed, S., Gawthorpe, R. & Mackrodt, P.-A. 1985 Aerodynamics of road-and rail vehicles. *Vehicle System Dynamics* **14** (4-6), 319–392.

Ahmed, S., Ramm, G. & Faitin, G. 1984 Some salient features of the time-averaged ground vehicle wake. *Tech. Rep.*. Society of Automotive Engineers, Inc., Warrendale, PA.

Aider, J., Beaudoin, J. & Wesfreid, J. 2010 Drag and lift reduction of a 3d bluff-body using active vortex generators. *Experiments in fluids* **48** (5), 771–789.

Arnette, S. A., Buchanan, T. D. & Zabat, M. 1999 On low-frequency pressure pulsations and static pressure distribution in open jet automotive wind tunnels. *SAE paper* (1999-01), 0813.

Awbi, H. 1974 The investigation of wind tunnel wall interference on bluff body models.". PhD thesis, Ph. D Thesis, Trent Polytechnic, Nottingham.

Awbi, H. 1978 Wind-tunnel-wall constraint on two-dimensional rectangular-section prisms. *Journal of Wind Engineering and Industrial Aerodynamics* **3** (4), 285–306.

Barlow, J. B., Rae, W. H. & Pope, A. 1999 Low-speed wind tunnel testing .

Bassett JR, D., Kyle, C., Passfield, L., Broker, J. & Burke, E. 1999 Comparing cycling world hour records, 1967-1996: modeling with empirical data. *Medicine & Science in Sports & Exercise* **31** (11), 1665–1676.

Bearman, P. 1965 Investigation of the flow behind a two-dimensional model with a blunt trailing edge and fitted with splitter plates. *J. Fluid Mech* **21** (part 2), 241–256.

Bearman, P. 1984 Some observations on road vehicle wakes. *Tech. Rep.*. Society of Automotive Engineers, Inc., Warrendale, PA.

Bearman, P. 1997 Near wake flows behind two-and three-dimensional bluff bodies. *Journal of wind engineering and industrial aerodynamics* **69**, 33–54.

Bearman, P. & Obasaju, E. 1982 An experimental study of pressure fluctuations on fixed and oscillating square-section cylinders. *Journal of Fluid Mechanics* **119**, 297–321.

Beaudoin, J., Cadot, O., Aider, J., Gosse, K., Paranthoën, P., Hamelin, B., Tissier, M., Allano, D., Mutabazi, I., Gonzales, M. *et al.* 2004 Cavitation as a complementary tool for automotive aerodynamics. *Experiments in fluids* **37** (5), 763–768.

Bendat, J. S. & Piersol, A. G. 1980 Engineering applications of correlation and spectral analysis. *New York, Wiley-Interscience, 1980. 315 p.* **1**.

Blair, K. & Sidelko, S. 2008 Aerodynamic performance of cycling time trial helmets. *The Engineering of Sport 7* pp. 371–377.

Bradshaw, P. 1967 Inactive motion and pressure fluctuations in turbulent boundary layers. *J. Fluid Mech* **30** (2), 241–258.

Broker, J. 2003 Cycling power: road and mountain. *High-Tech Cycling: The Science of Riding Faster* pp. 147–174.

Brownlie, L., Kyle, C., Carbo, J., Demarest, N., Harber, E., MacDonald, R. & Nordstrom, M. 2009 Streamlining the time trial apparel of cyclists: the nike swift spin project. *Sports Technology* **2** (1-2), 53–60.

Camussi, R., Felli, M., Pereira, F., Aloisio, G. & Di Marco, A. 2008 Statistical properties of wall pressure fluctuations over a forward-facing step. *Physics of fluids* **20**, 075113.

Camussi, R., Guj, G., Di Marco, A. & Ragni, A. 2006a Propagation of wall pressure perturbations in a large aspect ratio shallow cavity. *Experiments in fluids* **40** (4), 612–620.

Camussi, R., Guj, G. & Ragni, A. 2006b Wall pressure fluctuations induced by turbulent boundary layers over surface discontinuities. *Journal of sound and vibration* **294** (1), 177–204.

Candau, R., Grappe, F., Ménard, M., Barbier, B., Millet, G., Hoffman, M., Belli, A. & Rouillon, J. 1999 Simplified deceleration method for assessment of resistive forces in cycling. *Medicine & Science in Sports & Exercise* **31** (10), 1441–1447.

Carmer, C., Konrath, R., Schröder, A. & Monnier, J. 2008 Identification of vortex pairs in aircraft wakes from sectional velocity data. *Experiments in Fluids* **44** (3), 367–380.

Castro, I. P. & Epik, E. 1998 Boundary layer development after a separated region. *Journal of Fluid Mechanics* **374** (1), 91–116.

Chabroux, V., Barelle, C. & Favier, D. 2008 Aerodynamics of time trial bicycle helmets. *The Engineering of Sport 7* pp. 401–410.

Chabroux, V., Mba, M., Sainton, P. & Favier, D. 2010 Wake characteristics of time trial helmets using piv-3c technique .

Chakraborty, P., Balachandar, S. & Adrian, R. 2005 On the relationships between local vortex identification schemes. *Journal of Fluid Mechanics* **535** (1), 189–214.

Cherry, N., Hillier, R. & Latour, M. 1984 Unsteady measurements in a separated and reattaching flow. *Journal of Fluid Mechanics* **144**, 13–46.

Cooper, K. 1998 Bluff-body blockage correction in closed and open test section wind tunnels. *AGARD, AG-336, NTIS, Springfield, VA* p. 6.

Crouch, T., Sheridan, J., Thompson, M. & Brown, N. A. 2010 Effect of cyclist shape and position on aerodynamic drag. *Tech. Rep.*. Department of Mechanical and Aerospace Engineering Monash University.

Defraeye, T., Blocken, B., Koninckx, E., Hespel, P. & Carmeliet, J. 2010a Computational fluid dynamics analysis of cyclist aerodynamics: Performance of different turbulence-modelling and boundary-layer modelling approaches. *Journal of biomechanics* **43** (12), 2281–2287.

Defraeye, T., Blocken, B., Koninckx, E., Hespel, P. & Carmeliet, J. 2010b Computational fluid dynamics analysis of cyclist aerodynamics: Performance of different turbulence-modelling and boundary-layer modelling approaches. *Journal of biomechanics* **43** (12), 2281–2287.

Defraeye, T., Blocken, B., Koninckx, E., Hespel, P. & Carmeliet, J. 2011 Computational fluid dynamics analysis of drag and convective heat transfer of individual body segments for different cyclist positions. *Journal of biomechanics* **44** (9), 1695–1701.

Délery, J. 2001 Robert legendre and henri werlé: Toward the elucidation of three-dimensional separation. *Annual review of fluid mechanics* **33** (1), 129–154.

Driver, D. M., Seegmiller, H. L. & Marvin, J. G. 1987 Time-dependent behavior of a reattaching shear layer. *AIAA journal* **25** (7), 914–919.

Duell, E., Kharazi, A., Muller, S., Ebeling, W. & Mercker, E. 2010 The bmw avz wind tunnel center. *SAE Technical Paper* pp. 01–0118.

García-López, J., Rodríguez-Marroyo, J. A., Juneau, C.-E., Peleteiro, J., Martínez, A. C. & Villa, J. G. 2008 Reference values and improvement of aerodynamic drag in professional cyclists. *Journal of sports sciences* **26** (3), 277–286.

Garner, H. C., Rogers, E., Acum, W. & Maskell, E. 1966 Subsonic wind tunnel wall corrections. *Tech. Rep.*. DTIC Document.

Gerhand, W., Wilhelm, V. & Stephen, W. 2000 Wind tunnel pulsation and their active suppression. *Social Automotive Engineering.[SL]: SAE* pp. 01–0869.

Gibertini, G. & Grassi, D. 2008 Cycling aerodynamics. *Sport Aerodynamics* pp. 23–47.

Gilhome, B. 2002 Unsteady and time-averaged near-wake flow over the rear of sedan autombiles. PhD thesis, Monash University Department of Mechanical Engineering, Melbourne, Australia.

Ginger, J. & Letchford, C. 1993 Characteristics of large pressures in regions of flow separation. *Journal of Wind Engineering and Industrial Aerodynamics* **49** (1), 301–310.

Glauert, H. 1933 Wind tunnel interference on wings, bodies and airscrews.

Godo, M. N., Corson, D. & Legensky, S. M. 2009 An aerodynamic study of bicycle wheel performance using cfd. In *47th AIAA Aerospace Sciences Annual Meeting, Orlando, FL, USA*, pp. 5–8.

Godo, M. N., Corson, D. & Legensky, S. M. 2010 A comparative aerodynamic study of commercial bicycle wheels using cfd. In *48th AIAA Aerospace Sciences Annual Meeting, Orlando, FL, USA*, pp. 4–7.

Griffith, M., Crouch, T., Thompson, M., Burton, D. & Sheridan, J. 2012 Elite cycling aerodynamics: Wind tunnel experiments and cfd. In *18th Australasian Fluid Mechanics Conference*.

Gross, A., Kyle, C. & Malewicki, D. 1983 The aerodynamics of human-powered land vehicles. *Scientific American* **249** (6), 142–152.

Hackett, J. & Sugavanam, A. 1984 Evaluation of a complete wake integral for the drag of a car-like shape. *SAE paper* **840577**.

Hanna, R. 2002 Can cfd make a performance difference in sport. *The engineering of sport* **4**, 17–30.

Hoerner, S. 1965 *Fluid-dynamic drag: practical information on aerodynamic drag and hydrodynamic resistance*. Hoerner Fluid Dynamics.

Holmes, J. & Lewis, R. 1987 Optimization of dynamic-pressure-measurement systems. i. single point measurements. *Journal of Wind Engineering and Industrial Aerodynamics* **25** (3), 249–273.

Hooper, J. & Musgrove, A. 1997 Reynolds stress, mean velocity, and dynamic static pressure measurement by a four-hole pressure probe. *Experimental thermal and fluid science* **15** (4), 375–383.

Hornung, H. & Perry, A. 1984 Some aspects of three-dimensional separation. i-streamsurface bifurcations. *Zeitschrift fur Flugwissenschaften und Weltraumforschung* **8**, 77–87.

Hucho, W. & Sovran, G. 1993 Aerodynamics of road vehicles. *Annual review of fluid mechanics* **25** (1), 485–537.

Hucho, W.-H. 1987 *Aerodynamics of road vehicles: From fluid mechanics to vehicle engineering*. Butterworth Publishers, Stoneham, MA.

Irwin, H., Cooper, K. & Girard, R. 1979 Correction of distortion effects caused by tubing systems in measurements of fluctuating pressures. *Journal of Wind Engineering and Industrial Aerodynamics* **5** (1), 93–107.

Janssen, L. & Hucho, W. 1975 Aerodynamische formoptimierung von vw golf und vw scirocco. *AUTOMOBILTECHN Z* **77** (11).

Jeukendrup, A. & Martin, J. 2001 Improving cycling performance: how should we spend our time and money. *Sports Medicine* **31** (7), 559–569.

Kawai, H. 1983 Pressure fluctuations on square prisms-applicability of strip and quasi-steady theories. *Journal of Wind Engineering and Industrial Aerodynamics* **13** (1), 197–208.

KAWAMURA, T. 1953 Wind drag of bicycles. *Tokyo University, Tokyo, Japan* .

KIYA, M. & SASAKI, K. 1983 Free-stream turbulence effects on a separation bubble. *Journal of Wind Engineering and Industrial Aerodynamics* **14** (1), 375–386.

KIYA, M. & SASAKI, K. 1985 Structure of large-scale vortices and unsteady reverse flow in the reattaching zone of a turbulent separation bubble. *Journal of Fluid Mechanics* **154** (1), 463–491.

KYLE, C. 1979 Reduction of wind resistance and power output of racing cyclists and runners travelling in groups. *Ergonomics* **22** (4), 387–397.

KYLE, C. 1989 The aerodynamics of helmets and handlebars. *Cycling Science* **1** (1), 122–125.

KYLE, C. 2003 Selecting cycling equipment. *High-Tech Cycling: The Science of Riding Faster* pp. 1–48.

KYLE, C., BROWNLIE, L., HARBER, E., MACDONALD, R. & NORSTROM, M. 2004 The nike swift spin cycling project: reducing the aerodynamic drag of bicycle racing clothing by using zoned fabrics. *The engineering of sport* **5** (1).

KYLE, C. & BURKE, E. 1984 Improving the racing bicycle. *Mechanical engineering* **106** (9), 34–45.

LE GOOD, G. M. & GARRY, K. P. 2004 On the use of reference models in automotive aerodynamics. *SAE Technical Paper* pp. 01–1308.

LEE, I. & SUNG, H. 2001 Characteristics of wall pressure fluctuations in separated and reattaching flows over a backward-facing step: Part i. time-mean statistics and cross-spectral analyses. *Experiments in fluids* **30** (3), 262–272.

LEE, I. & SUNG, H. J. 2002 Multiple-arrayed pressure measurement for investigation of the unsteady flow structure of a reattaching shear layer. *Journal of Fluid Mechanics* **463** (1), 377–402.

LUCA, O., SÆTRAN, L., LEIRDAL, S. & ETTEMA, G. 2008 Aerodynamic optimization and energy saving of cycling postures for international elite level cyclists. *The Engineeeing of Sport 7* pp. 597–604.

MABEY, D. G. 1972 Analysis and correlation of data on pressure fluctuations in separated flow. *Journal of Aircraft* **9** (9), 642–645.

MALTBY, R. 1962 Flow visualization in wind tunnels using indicators. *Tech. Rep.*. DTIC Document.

MARTIN, J., DAVIDSON, C. & PARDYJAK, E. 2007 Understanding sprint-cycling performance: the integration of muscle power, resistance, and modeling. *International journal of sports physiology and performance* **2** (1), 5.

MARTIN, J., MILLIKEN, D., COBB, J., MCFADDEN, K. & COGGAN, A. 1998 Validation of a mathematical model for road cycling power. *Journal of Applied Biomechanics* **14**, 276–291.

MASKELL, E. 1963 A theory of the blockage effects on bluff bodies and stalled wings in a closed wind tunnel. *Tech. Rep.*. DTIC Document.

MASKELL, E. 1973 *Progress Towards a Method for the Measurement of the Components of the Drag of a Wing of Finite Span*. Procurement Executive, Min. of Defence.

MASON, P. & MORTON, B. 1987 Trailing vortices in the wakes of surface-mounted obstacles. *Journal of Fluid Mechanics* **175** (1), 247–293.

MCLEAN, B., DANAHER, R., THOMPSON, L., FORBES, A. & COCO, G. 1994 Aerodynamic characteristics of cycle wheels and racing cyclists. *Journal of Biomechanics* **27** (6), 675–675.

MERCKER, E., COOPER, K., FISCHER, O. & WIEDEMANN, J. 2005 The influence of a horizontal pressure distribution on aerodynamic drag in open and closed wind tunnels. *SAE transactions* **114** (6), 921–938.

MERCKER, E., WICKERN, G. & WIEDEMANN, J. 1997 Contemplation of nozzle blockage in open-jet wind tunnels in view of different'q' determination techniques. *SAE paper* .

MERCKER, E. & WIEDEMANN, J. 1996a On the correction of interference effects in open jet wind tunnels. *SAE paper* **105** (6), 795–809.

MERCKER, E. & WIEDEMANN, J. 1996b On the correction of interference effects in open-jet wind tunnels. *SAE paper* .

MOIN, P. 2009 Revisiting taylor's hypothesis. *Journal of Fluid Mechanics* **640**, 1.

MOREL, T. 1978a Aerodynamic drag of bluff body shapes characteristics of hatch-back cars. *Tech. Rep.*.

MOREL, T. 1978b The effect of base slant on the flow pattern and drag of three-dimensional bodies with blunt ends. In *Aerodynamic Drag Mechanisms of Bluff Bodies and Road Vehicles*, pp. 191–226. Springer.

OGGIANO, L., LEIRDAL, S., SAETRAN, L. & ETTEMA, G. 2008 Aerodynamic optimization and energy saving of cycling postures for international elite level cyclists. *The engineering of sport* **7**, 597–604.

Onorato, M., Costelli, A. & Garrone, A. 1984 Drag measurement through wake analysis. *Tech. Rep.*. Society of Automotive Engineers, Inc., Warrendale, PA.

Padilla, S., Mujika, I., Angulo, F. & Goiriena, J. J. 2000 Scientific approach to the 1-h cycling world record: a case study. *Journal of Applied Physiology* **89** (4), 1522–1527.

Panton, R. L. & Linebarger, J. H. 1974 Wall pressure spectra calculations for equilibrium boundary layers. *Journal of Fluid Mechanics* **65** (2), 261–287.

Parker, B., Franke, M. & Elledge, A. 1996 Bicycle aerodynamics and recent testing. *AIAA* .

Peake, D. & Tobak, M. 1982 *Three-dimensional separation and reattachment*, , vol. 84221. DTIC Document.

Perry, A. & Chong, M. 1987 A description of eddying motions and flow patterns using critical-point concepts. *Annual Review of Fluid Mechanics* **19** (1), 125–155.

Perry, A. & Li, J. 1990 Experimental support for the attached-eddy hypothesis in zero-pressure- gradient turbulent boundary layers. *Journal of Fluid Mechanics* **218**, 405–438.

Ramberg, S. 1983 The effects of yaw and finite length upon the vortex wakes of stationary and vibrating circular cylinders. *Journal of Fluid Mechanics* **128** (1), 81–107.

Rennie, M., Kim, M.-S., Lee, J. & Kee, J. 2004 Suppression of open-jet pressure fluctuations in the hyundai aeroacoustic wind tunnel. *SAE Paper* (2004-01), 0803.

Roshko, A. 1955 On the wake and drag of bluff bodies. *J. Aero. Sc.* **22**, 124–132.

Roshko, A. 1993 Perspectives on bluff body aerodynamics. *Journal of Wind Engineering and Industrial Aerodynamics* **49**, 79–100.

Rouméas, M., Gilliéron, P. & Kourta, A. 2009 Drag reduction by flow separation control on a car after body. *International journal for numerical methods in fluids* **60** (11), 1222–1240.

Sau, A., Hwang, R., Sheu, T. & Yang, W. 2003 Interaction of trailing vortices in the wake of a wall-mounted rectangular cylinder. *Physical Review E* **68** (5), 056303.

Schlichting, H., Kestin, J., Schlichting, H. & Schlichting, H. 1968 *Boundary-layer theory*, , vol. 539. McGraw-Hill New York.

Shepherd, I. 1981 A four hole pressure probe for fluid flow measurements in three dimensions. *Journal of Fluids Engineering* **103**, 590.

Taneda, S. 1978 Visual observations of the flow past a sphere at Reynolds numbers between 10^4 and 10^6. *J. Fluid Mech.* **85**, 187–192.

TFI 2011 *Getting Started Series 100 Cobra Probe*. Turbulent Flow Instrumentation Pty Ltd.

Thakur, A., Liu, X. & Marshall, J. 2004 Wake flow of single and multiple yawed cylinders. *Journal of fluids engineering* **126** (5), 861–870.

Underwood, L. & Jermy, M. 2010 Optimal hand position for individual pursuit athletes. *Procedia Engineering* **2** (2), 2425–2429.

Underwood, L. & Jermy, M. 2013 Optimal handlebar position for track cyclists. *Sports Engineering* pp. 1–10.

Von Kármán, T. 1948 Progress in the statistical theory of turbulence. *Proceedings of the National Academy of Sciences of the United States of America* **34** (11), 530.

Welch, P. 1967 The use of fast fourier transform for the estimation of power spectra: a method based on time averaging over short, modified periodograms. *Audio and Electroacoustics, IEEE Transactions on* **15** (2), 70–73.

Wickern, G. 2001 On the application of classical wind tunnel corrections for automotive bodies. *SAE paper* pp. 01–0633.

Wickern, G. & Lindener, N. 2000 The audi aeroacoustic wind tunnel: Final design and first operational experience. *SAE transactions* **109** (6), 1387–1402.

Zdravkovich, M., Ashcroft, M., Chisholm, S. & Hicks, N. 1996 Effect of cyclists[U+02BC] posture and vicinity of another cyclists on aerodynamic drag. *The Engineering of Sport* **1**, 21–28.

Zdravkovich, M., Brand, V., Mathew, G. & Weston, A. 1989 Flow past short circular cylinders with two free ends. *Journal of Fluid Mechanics* **203** (1), 557–575.

Zhao, M., Cheng, L. & Zhou, T. 2009 Direct numerical simulation of three-dimensional flow past a yawed circular cylinder of infinite length. *Journal of Fluids and Structures* **25** (5), 831–847.

Zhou, J., Adrian, R., Balachandar, S. & Kendall, T. 1999 Mechanisms for generating coherent packets of hairpin vortices in channel flow. *Journal of Fluid Mechanics* **387** (1), 353–396.